12-2017

Experimental Study of Global Luminescent Oil-Film (GLOF) Skin-Friction Meter on Delta Wings

Patrick Nicholas Wewengkang
Western Michigan University

EXPERIMENTAL STUDY OF GLOBAL LUMINESCENT OIL-FILM (GLOF) SKIN-FRICTION METER ON DELTA WINGS

by

Patrick Nicholas Wewengkang

A thesis submitted to the Graduate College
in partial fulfillment of the requirements
for the Degree of Master of Science in Engineering (Aerospace)
Department of Mechanical and Aerospace Engineering
Western Michigan University
December 2017

Thesis Committee:

Tianshu Liu, Ph.D., Chair
Parviz Merati, Ph.D.
Javier Montefort, Ph.D.

EXPERIMENTAL STUDY OF GLOBAL LUMINESCENT OIL-FILM (GLOF) SKIN-FRICTION METER ON DELTA WINGS

Patrick Nicholas Wewengkang, M.S.E.

Western Michigan University, 2017

This thesis describes how the Global Luminescent Oil-Film (GLOF) Skin-Friction Meter can be applied experimentally to extract skin-friction from a set of images. In this study, the effect of oil viscosity, experimental sample size, and step size were considered to see how they would affect the extracted skin-friction using the GLOF method. These results were then compared to published literature on skin-friction diagnostics of delta wings, based on observations of critical characteristics such as reattachment and separation lines. Delta wings of 50°, 55°, 60°, 65°, and 70° sweep angles were built and placed in the Small Wind Tunnel (SWT) at the Applied Aerodynamics Laboratory (AAL) in Western Michigan University (WMU). Luminescent oil was then applied to the surface of the delta wings and images were taken at different angle of attacks. All experiments were performed with a freestream velocity of 20 meters per second, and a corresponding Reynolds number of 250,000.

A study of step size, sample size, and oil viscosity showed that the extracted skin-friction fields are sensitive to these variables and that they are not mutually independent. The lack of numerical simulations and experiments performed at the same Reynolds and Mach number, means that the discussion in this thesis was largely observational in nature. In a nutshell, GLOF has the ability to quantitatively measure skin-friction on a global scale, which is desirable when trying to understand the interaction between the flow and the surface boundary layer for complex flows.

ACKNOWLEDGMENTS

I would like to begin by extending my heartfelt gratitude to Dr. Tianshu Liu, my advisor, for giving me an opportunity to work on this project. Without his support and guidance, this thesis would not have been possible. His work in this topic inspired me to pursue the subject, and ultimately led to the work contained in this thesis.

Secondly, I would like to thank the members of my graduate committee, Dr. Parviz Merati, and Dr. Javier Montefort for taking the time to review my work. The past four years of working together on a multitude of projects have provided me with the skills and analytical mindset that solidified my passion for applied fluid dynamics and experimental aerodynamics. I sincerely thank them for all their guidance and patience through the years.

Lastly, I would like to thank my parents, family, and friends for their constant support and encouragement. I would not have been able to complete my studies without them.

Patrick Nicholas Wewengkang

TABLE OF CONTENTS

LIST OF FIGURES

List of Figures - - Continued

List of Figures - - Continued

List of Figures - - Continued

List of Figures - - Continued

List of Figures - - Continued

List of Figures - - Continued

List of Figures - - Continued

List of Figures - - Continued

List of Figures - - Continued

INTRODUCTION

Drag is one of the most important parameters in aerodynamics. To increase efficiency, aircrafts are designed to have the lowest drag possible. Drag consists of two components, parasite and induced drag. Figure 1 below shows the relationship between the two forms of drag with respect to flight velocity.

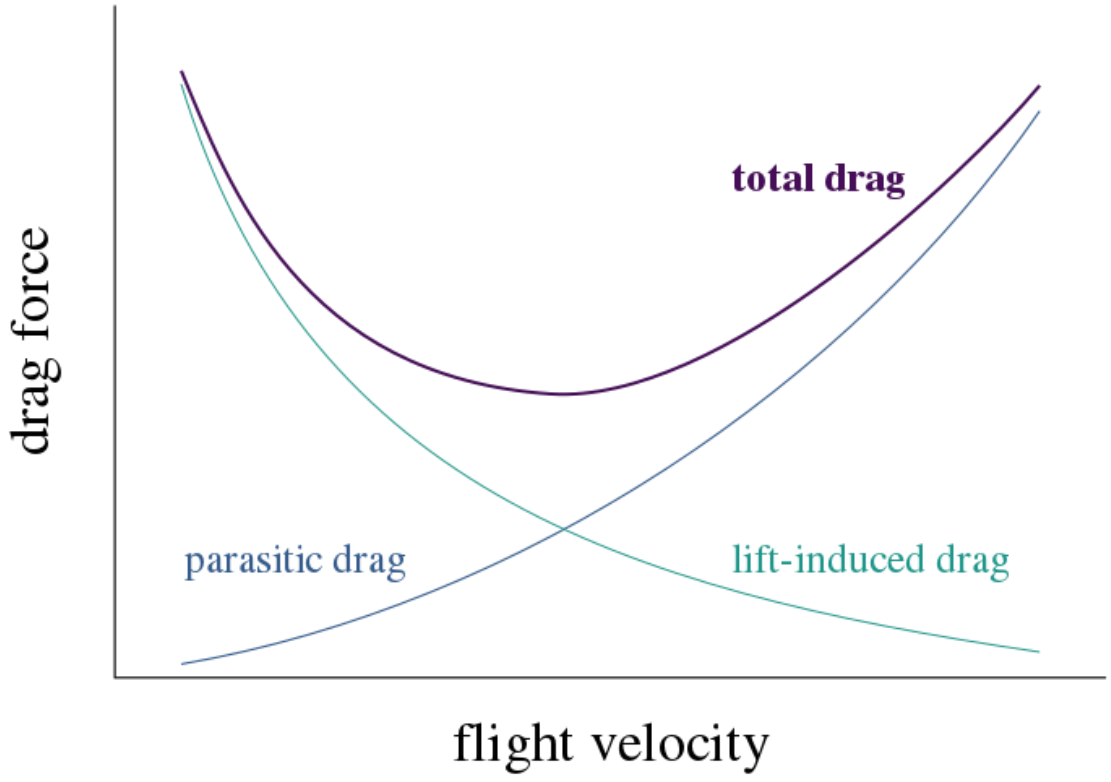

Figure 1: Drag curves for a body in steady flight [1]

As seen in Figure 1, as flight velocity increases, parasite drag becomes dominant in contributing to total drag. Therefore, there is a need for aircraft designers to be able to understand its impact on flight characteristics. One of the significant contributors to parasite drag is skin-friction drag. Skin-friction drag is defined as the shear force caused by viscous airflow over a surface. It is caused by the friction of a fluid against the surface of an object. Due to viscosity, a thin layer of fluid sticks to the surface and resists forward motion. The no-slip condition states that at the surface of a body, the relative velocity between the fluid and the solid surface is zero. This slowly increases until the velocity becomes constant as one move away from the body. This velocity gradient, where the velocity goes from zero to a constant value, is called the boundary layer. The thickness of the boundary layer on a wing is generally small, while the airflow velocity must vary from zero to hundreds of meters per second. Therefore, one can clearly see that there must be shearing forces present in this region. Figure 2 is a visual representation of this phenomenon.

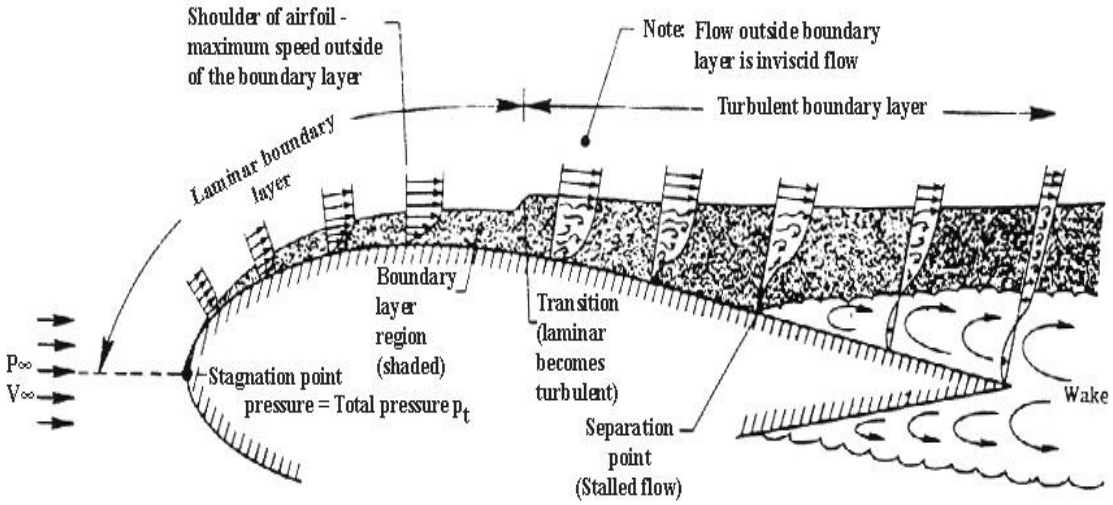

Figure 2: Boundary layers on an airfoil [2]

There exists both laminar and turbulent boundary layer as seen in Figure 2. The turbulent flow, as seen in the aft, creates more friction drag than the laminar flow, as seen in the fore section of Figure 2, due to its greater interaction with the surface of the object. If the surface of the object is rough, it will hasten the transition of the boundary layer from laminar to turbulent. This will lead to an increase in skin-friction drag due to the increase in the thickness of the boundary layer. From this, one can see that skin-friction is a function of the rate of shearing strain as seen in Equation 1.

$$\tau(y) = \mu \frac{\partial u}{\partial y} \tag{1}$$

where τ denotes the shear stress, μ denotes the dynamic viscosity of the fluid, and $\partial u/\partial y$ denotes the velocity gradient. Skin-friction is extracted when y equals zero.

Over the past 50 years, both local and global measurement techniques for skin- friction have been developed. [3-7] These techniques can be broken down into direct and indirect methods, which will be touched on in the next section. Researchers have also tried to create a Computational Fluid Dynamics (CFD) model to extract skin-friction, but it is hard to do so as a turbulent boundary layer is extremely hard to characterize due to its randomness. Anderson [8] stated that for separated flows, i.e., presence of regions of flow separation, the complete numerical Navier-Stokes solution must be used to obtain local skin-friction. It was also stated that the use of CFD to "predict skin-friction in a turbulent flow seems to be no better than about 20 percent accuracy, on the average." [8] Thus, there is a need for researchers to be able to experimentally measure skin-friction for the optimization of aircraft designs.

SKIN-FRICTION MEASUREMENT TECHNIQUES

As discussed earlier, skin-friction measurement techniques have been developed over the past 50 years. These techniques can be broken down into direct and indirect methods. The direct methods do not require any empirical or theoretical correlation, thus allowing skin-friction to be measured experimentally. The most famous example of the direct method is oil-film interferometry. Indirect methods on the other hand require the calibration of instruments before they can be used to extract skin-friction. Examples of the indirect method include the wall hot-wire probe and the wall pulsed-wire probe. The GLOF technique used for this thesis is an example of a direct method, and was developed through the manipulation of the oil-film interferometry technique. This section will focus on oil film techniques as a complete review of methods available have been done in [5].

Oil-film interferometry requires little to no calibration and has the potential to determine the entire skin-friction field if done with great care. This method relies on the change in thickness of a silicon-based oil film applied to a smooth surface, subjected to a shearing flow. The general equation for this method is given in Equation 2.

$$\frac{\partial h}{\partial t} + \frac{\partial}{\partial x}\left(\frac{\tau h^2}{2\mu}\right) = 0 \tag{2}$$

where h is the oil film thickness, τ is skin-friction, and μ is the dynamic viscosity of the oil. A typical oil-film interferometry system uses a light source that is passed through a diffuser. The

light then illuminates the thin oil using a beam splitter. Oil is applied to the smooth surface, usually in lines or dots, and its location noted before the wind tunnel is switched on. Light reflected from the oil and surface is then acquired by a camera, and a set of images are acquired during a run.

Oil-film techniques can be broken down further into different categories. These categories are point measurement techniques such as the Laser Interferometry Skin-Friction (LISF) method, line techniques such as the expanded laser beam interferometry skin-friction method, image based techniques such as the Fringe Imaging Skin-Friction (FISF) method, and global imaging techniques such as Global Imaging Skin-Friction (GISF) method, Surface Imaging Skin-Friction (SISF) method, and Global Luminescent Oil Film (GLOF) method. Equation 2 is the foundation for these methods.

In the LISF method, a He-Ne laser beam is directed to the surface of the object. A thin layer of oil is then applied to this surface. The camera is replaced with a photodetector that acquire the signal of the laser beam as they reflect off the surface. This is done to streamline the data acquisition and analysis process. Since LISF is a point-based method, it is unable to simultaneously measure skin-friction at multiple points. Therefore, measuring the skin-friction over an extended region of the object with this technique will be very expensive and time consuming. Due to the development of image capturing devices, image based techniques have mostly taken over point based techniques due to its ease and accuracy.

The development in LISF led to the use of line techniques with the creation of Charge-Coupled Device (CCD) cameras. These cameras were relatively inexpensive and could capture multiple interferograms thus allowing researchers to collect both spatial and temporal information. The laser beam in the technique above was expanded to illuminate a region of the surface instead

of a single point, thus allowing more information to be acquired in a single experiment. This method allowed for the calculation of skin-friction by determining the change in fringe spacing with respect to time. However, since a line is physically two dimensional, this technique is limited to only two-dimensional flows thus allowing only one shear stress value to be calculated.

As image acquisition devices improved, image based techniques quickly replaced the earlier methods in the extraction of skin-friction. Researchers at NASA Ames [9-10] improved the thin oil-film equation by realizing that it can be integrated at the end of the test, thus allowing researchers to measure the skin-friction over the entire surface instead of a single point or a single line per experiment. This technique was known as the FISF method and has been validated extensively in two and three-dimensional flows. [11-12] The limitation of this approach occurs when there are oil patches next to each other. If the oil from one patch flows into another patch, the fringe pattern will be corrupted. Thus, there needs to be sufficient spacing between patches of oil. Researchers at NASA Ames also developed a technique that is known as SISF. This method uses two-dimensional data acquired from the images to extract skin-friction. Again, this technique has been extensively validated. [13] There are problems that are common among the above oil-film techniques, such as the presence of surface waves in high shear flows, and dust interference on the surface. Since multiple factors such as surface tension, pressure gradients, shear stress gradients, and gravity affect the change in height of the oil during an experiment; the ability to measure these variables simultaneously during an experiment is needed to remove uncertainties. Another limiting factor is the uncertainty of the oil's viscosity. Since the oil's viscosity and density changes with temperature, these tests need to be quick or the temperature of the oil will have to be tracked throughout the experiment as well.

In 1998, Liu and Sullivan [6] created the luminescent oil-film skin-friction meter as a skin-friction measurement technique. Liu and Sullivan [6] have an extensive explanation on how skin-friction is determined through this method, so this will just be a summary on how the method works in general. Unlike the oil-film techniques mentioned above, the luminescent oil-film skin-friction technique tracks the change in luminescent intensity of an oil-film seeded with luminescent probe molecules instead of the change in height of the oil-film. The luminescent oil is then excited with an illumination source with a suitable wavelength and thus emits radiation with a longer wavelength than the source due to the Stokes shift. This method assumes that the thickness of the oil-film is proportional to its luminescent intensity if the oil-film is thin. A CCD camera then acquires the images and these images are then transferred to a computer for data processing. This method removes the need for a polished surface and thus can be applied to various model surfaces in the wind tunnel. Improving on this method, Liu et al. [7] created the Global Luminescent Oil-Film (GLOF) Skin-Friction Meter, which will be explained in the following section, as it is the method used for the experiments performed in this thesis.

GLOBAL LUMINESCENT OIL-FILM SKIN-FRICTION METER

The GLOF method is a global extension of the luminescent oil-film skin-friction meter mentioned above. This method is used to analyze the skin-friction on the delta wings in this thesis. One must note that the theoretical aspect was derived by Liu et al. [7] but will be explained in this section for an understanding of the experimental results. The writer takes no credit for the derivation of the equations used in this section.

The improvement of the luminescent oil-film skin-friction meter was done by measuring the oil-film thickness and projecting the thin oil-film equation onto the image plane. This projection describes the relationship between skin-friction and the temporal and spatial derivatives of the image intensity. A variational formulation, with a regularization term for the smoothness of a skin-friction field, is introduced to solve the projected thin oil-film equation. The resulting functional is then minimized into a set of Euler-Lagrange equations, and then solved numerically by imposing the Neumann condition. The governing equation for this method defines the response of a thin oil film on a surface to an applied three-dimensional flow. This can be seen in Equation 3 below.

$$\frac{\partial h}{\partial t} + \frac{\partial}{\partial X_i}\left[\frac{\tau_i h^2}{2\mu} - \left(\frac{\partial p}{\partial X_i} - \rho g_i\right)\frac{h^3}{3\mu}\right] = 0, \qquad (i = 1,2) \tag{3}$$

where h is the oil-film thickness, τ is the skin-friction vector, p is the pressure, μ is the dynamic

viscosity of the oil, ρ is the oil density, and g is the gravity vector. By applying a thin luminescent oil-film to the surface of the model, its luminescent emission intensity when excited is proportional to the oil-film thickness. This is seen in Equation 4 below.

$$I(X_1, X_2) = aI_{ex}(X_1, X_2)h(X_1, X_2) \tag{4}$$

where I is the luminescent emission intensity under excitation, I_{ex} is the intensity of the excitation light on the surface, and a is a coefficient proportional to the quantum efficiency of seeded luminescent molecules and dye concentration. Substitute Equation 4 into Equation 3, and a new governing equation is derived.

$$\frac{\partial}{\partial t}\left(\frac{I}{I_{ex}}\right) + \frac{\partial}{\partial X_i}\left[\frac{\tau_i}{2\mu a}\left(\frac{I}{I_{ex}}\right)^2 - \left(\frac{\partial p}{\partial X_i} - \rho g_i\right)\frac{1}{3\mu a^2}\left(\frac{I}{I_{ex}}\right)^3\right] = 0, \ (i = 1,2) \tag{5}$$

This equation then allows for a direct mapping between the image plane and the surface. This can be seen in Figure 3 below. When the image plane of the camera is parallel to a flat surface that is being measured, the perspective projection transformation is given as Equation 6.

$$\frac{\partial}{\partial X_i} = \lambda \frac{\partial}{\partial x_i} \tag{6}$$

where λ is a scaling factor, and is constant on a flat surface, X_i refers to the surface coordinates, and x_i refers to the image plane. For a curved surface, like that of the leading edge on a wing or a cylinder, λ will not be a constant, and thus the solution becomes more complicated. A normalized luminescent intensity seen in Equation 7 and the equivalent skin-friction in Equation 8 is then substituted into Equation 5.

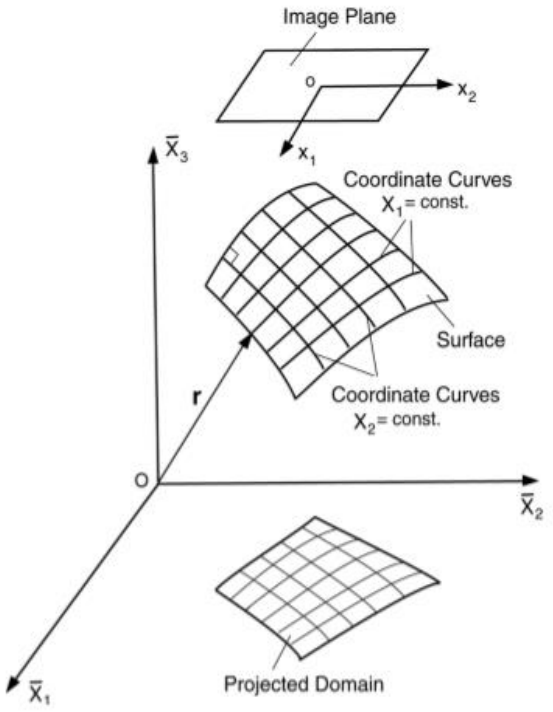

Figure 3: Mapping of the surface to the image plane [34]

$$g = \frac{I}{I_{ex}} \tag{7}$$

$$\bar{\tau} = \tau g\left(\frac{\lambda}{2\mu a}\right) \tag{8}$$

Equation 5 is then written in the image frame coordinates in Equation 9 below,

$$\frac{\partial g}{\partial t} + \nabla(g\bar{\tau}) = f(x_1, x_2, g) \tag{9}$$

where ∇ is the gradient operator in the image plane. This equation describes the projected oil-film for luminescent oil. By introducing the equivalent skin-friction into Equation 9, it now has the same form as the generic projected motion equation for various flow visualizations, and therefore the numerical method to calculate velocity can be used. The relative skin-friction is then the

equivalent skin-friction divided by the normalized luminescent intensity. The effects of the pressure gradient and gravity are then described by Equation 10.

$$f(x_1, x_2, g) = \lambda \frac{\partial}{\partial x_i}\left[\left(\lambda \frac{\partial p}{\partial x_i} - \rho g_i\right)\frac{g^3}{3\mu a^2}\right],\ (i = 1,2) \tag{10}$$

The measured quantity *g*, the normalized luminescent intensity and not the gravity vector, is then mapped onto the image plane. If the radiometric response function of the camera is linear, *g* will then be the normalized gray level in images. If the change in skin-friction is small, then the effects of the pressure gradient and gravity can be neglected. If this holds true, then Equation 9 can be simplified to Equation 11 below.

$$\frac{\partial g}{\partial t} + \bar{\tau} \cdot \nabla g = 0 \tag{11}$$

which has the same form as the optical flow constraint equation derived by Horn and Schunck [14]. Equation 11 provides an initial numerical approximation for Equation 9. However, Equation 9 is not able to determine the equivalent skin-friction field by itself. Therefore, additional constraints in the form of a variational formulation are used to solve for the two skin-friction components. Horn and Schunck [14] derived a regularization term based on the L^2 norm of the skin-friction gradient for computing optical flow. This term ensures that the skin-friction field is continuous in all directions. The assumption is reasonable for a first order approximation. Given *g* and *f*, a functional with the Horn-Schunck regularization term for the skin-friction field in an image domain Ω is then defined as Equation 12 below.

$$J(\bar{\tau}) = \int_{\Omega} \left[\frac{\partial g}{\partial t} + \nabla \cdot (g\bar{\tau}) - f \right]^2 dx_1 dx_2$$

$$+ \alpha \int_{\Omega} (|\nabla \bar{\tau_1}|^2 + |\nabla \bar{\tau_2}|^2)\, dx_1 dx_2 \tag{12}$$

where α is the Lagrange multiplier. The Euler-Lagrange equation for Equation 12 is then

$$g \frac{\partial}{\partial x_1} \left[\frac{\partial g}{\partial t} + \nabla \cdot (g\bar{\tau}) - f \right] + \alpha \nabla^2 \bar{\tau_1} = 0$$

$$g \frac{\partial}{\partial x_2} \left[\frac{\partial g}{\partial t} + \nabla \cdot (g\bar{\tau}) - f \right] + \alpha \nabla^2 \bar{\tau_2} = 0 \tag{13}$$

where the Neumann condition, $\partial\bar{\tau}/\partial n = 0$, is imposed on the domain boundary. Solving Equation 13 for two successive images provides a snapshot solution for the skin-friction field of the two images. To acquire the complete skin-friction field, these skin-friction fields are superimposed for the entire experiment. Liu et al. [7] validated this technique by applying it to a simulated Oseen vortex pair in uniform flow, an oblique impinging jet, a NACA 2412 airfoil and comparing the results with hot-film measurements and CFD simulations.

The GLOF technique has been developed over the years and provides a general and rational foundation for global quantitative skin-friction diagnostics with a high spatial resolution, but also allow for easy and reliable instrumentation based on oil luminescence measurements. Without any calibration, this method can provide a relative or normalized skin-friction field. In the experimental procedure section of this thesis, its application will be discussed.

SKIN-FRICTION TOPOLOGY

To understand the results of the experiments, topological features such as separation lines, reattachment lines, and singular points need to be defined. Flows in three-dimensions are hard to characterize theoretically, and the only understanding of these flows come from observations made from experimental studies that use flow visualization techniques. Lighthill [15] stated that the convergence of skin-friction lines, onto one which originates from a saddle point, is the necessary condition for flow separation.

Singular points in a skin-friction field occur when the skin-friction or the surface vorticity equals zero. Singular points are split into two main types; nodes, and saddle points. Nodes can also be further divided into nodal points and foci. Figure 3 below shows the structure of each type of singular points. A nodal point is a common location to an infinite number of skin-friction lines. At this location, all the skin-friction lines are tangential to a single line as seen Figure 4 (a). At a nodal point of attachment, all the skin-friction lines travel away from the node. Similarly, for a nodal point of separation, all the skin-friction lines travel towards the node. A focus can be distinguished by the lack of a common tangent line as seen in Figure 4 (b). A focus of attachment or separation is defined as the presence of an infinite number of skin-friction lines that spiral away from a single location, or towards it. A special case occurs when the paths of the focus form closed paths around a specific location. The focus will then be called a center. A saddle point is defined as a location that only has two lines passing through it, as seen in Figure 4 (c).

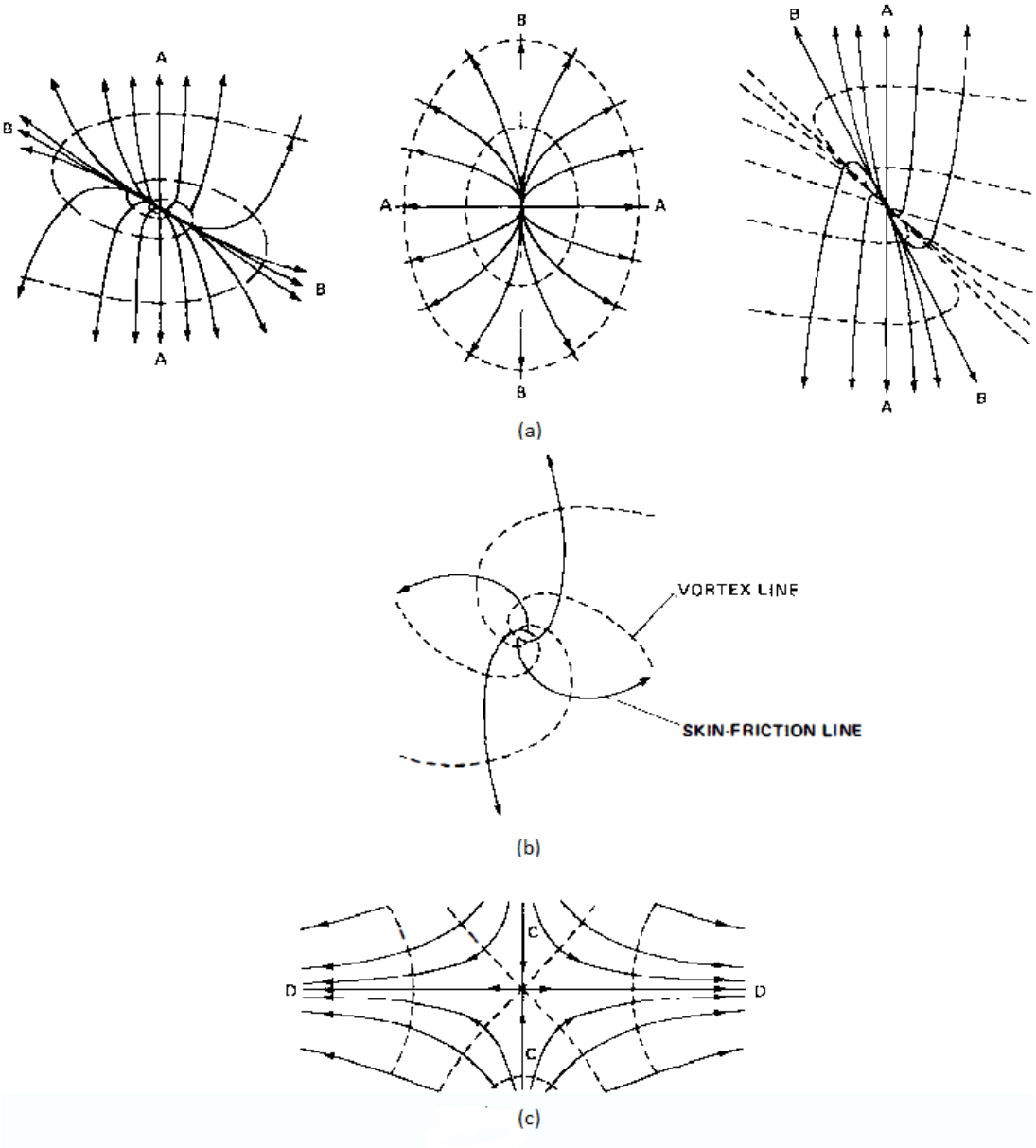

Figure 4: Structures for (a) nodal points, (b) focus, and (c) saddle [16]

The direction of the lines is opposite each other; one being inward and the other outward. The lines act as a barrier in a skin-friction field, not allowing one set of skin-friction lines to touch the other set. From these definitions, it is possible to describe the pattern of a flow near the singular point. For example, a nodal point of attachment is usually a stagnation point on the leading edge of a model, where the flow from upstream attaches itself to the surface of the model. On the other

hand, a nodal point of separation can usually be found on the trailing edge of a model, where the stagnation point acts as a sink.

Tobak and Peake [16] define two generic rules for skin-friction lines on a surface. The first rule is specifically for an isolated closed model, while the second is for a closed three-dimensional model connected to a plane wall. These rules are shown in Equations 14 and 15 respectively.

$$\sum N - \sum S = 2 \tag{14}$$

$$\sum N - \sum S = 0 \tag{15}$$

where *N* is defined by the number of nodal points, and *S* is defined by the number of saddle points. A common practice to examine three-dimensional flow fields is to plot the streamlines of the flow. Since the streamline fields have a topological similarity to the skin-friction fields, topological laws are frequently applied to them. [17] Chapman and Yates [18] identify three different types of flow separation for a three-dimensional flow.

The first, called a type I separation, originates from a saddle point of the skin-friction lines and the fluid surface rolls up to form a vortex. The separation line distinctively separates the surface into different regions, while a nodal point of attachment allows the fluid to move into the different regions.

A type II separation originates from a saddle point of the skin-friction lines, but the difference from a type I separation is the absence of a singular point in the flow. The separation results in vortices that originate at the spiral nodes, and the separation line do not separate the surface into different regions.

The last is called a crossflow separation, and is described as an “open” separation by Wang [19], “local” separation by Tobak and Peake [16] or uneven separation by Lighthill. [15] These laws allow researchers to describe the flow patterns of a complex three-dimensional flow. Foss, Patel and Délery [17,20-21] have published papers extensively comparing the observed vector field of numerous examples with the aforementioned topological laws.

DELTA WING AERODYNAMICS

A delta wing is a type wing with a triangular planform. Some famous aircrafts that use a delta wing configuration are the Concorde, a supersonic civil transport aircraft, and the Lockheed SR-71 Blackbird, a supersonic military long-range reconnaissance aircraft. The advantages of delta wings are its ability to reduce wave drag as well as the ability to operate at high angle of attacks. One of the key characteristic of a flow over a delta wing is the presence of two counter-rotating leading-edge vortices that stay attached to the surface of the wing even at high angles of attack, thus causing a suction effect on the upper surface of the wing, and can be seen in Figure 5 below. A delta wing stalls at a much higher angle of attack compared to a conventional wing, where stall is defined as the complete separation of flow that leads to a loss of lift, due to the characteristic mentioned above. As the flow separates from the leading edge, it forms a shear layer on the surface. A span wise pressure gradient on the upper surface forces the shear layer to move inward and forms what is called a primary vortex on each side of the leading edge. These vortices locally speed up the flow, causing a local suction on the surface of the wing right below the vortices. This suction increases induced drag and vortex lift. Researchers have experimented on delta wings and have found that as the sweep angle increases, the strength of the leading-edge vortices decreases. [22] It was also found that as the angle of attack is increased, the strength of the leading-edge vortices increases as well.

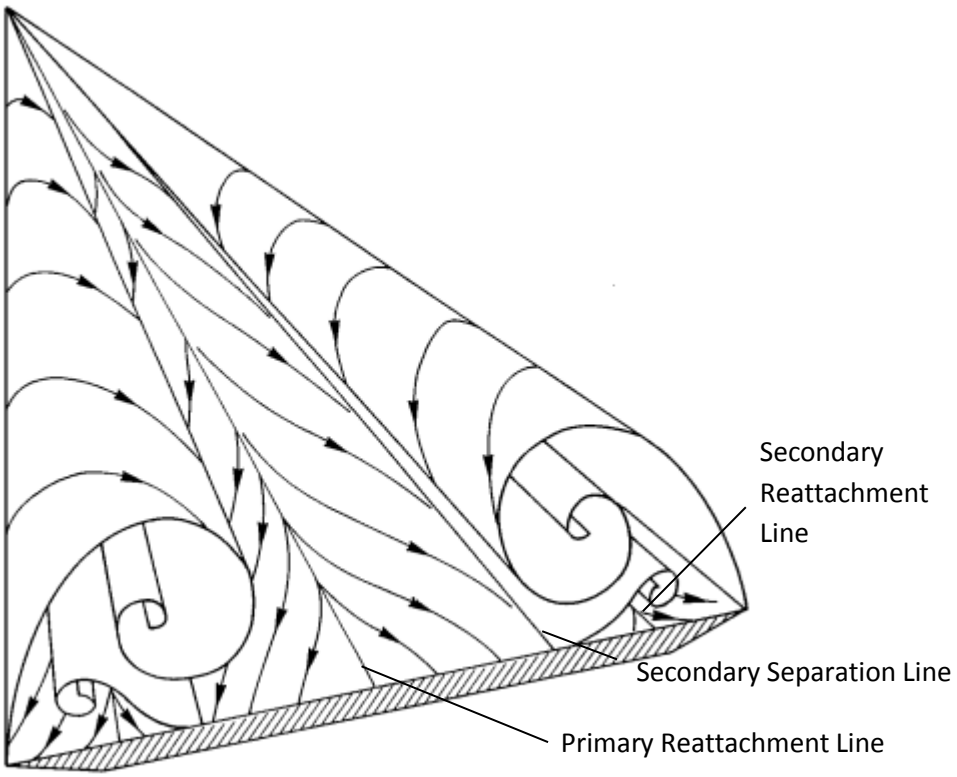

Figure 5: Skin-friction topology on a delta wing [21]

Flow visualization study on the effect of vortex location with respect to angle of attack have also shown that as angle of attack is increased, the primary vortex core tends to move inwards and upwards.

A sharp leading-edge delta wing is usually used in research as the primary separation is fixed. If the leading edge is rounded or blunt, the location of the primary separation will then vary with pressure gradient and boundary layer development, thus making vortex aerodynamics complex. In a sharp leading-edge delta wing, only the angle of attack influences the onset of vortex evolution.

Another key feature of delta wing aerodynamics is the presence of vortex breakdown. As the angle of attack for a delta wing is increased, the strength of the leading-edge vortices increases as well. Due to this, the flow stagnates, and the vortices break down into full-scale turbulence. The location of the vortex breakdown seems to be influenced by both the angle of attack and the sweep angle. As the angle of attack is increased, the location of the vortex breakdown moves towards the sharp tip, and as the sweep angle is increased, the breakdown moves further towards the trailing edge of the wing.

Gursul [23] further distinguished delta wings into slender and non-slender delta wings. Slender delta wings are defined as those with a sweep angle that is equal to or larger than 65°, while non-slender delta wings have a sweep angle that is less than 65°. The leading-edge vortices over slender delta wings tend to have very strong axial flows in the core, and the time-averaged maximum axial velocities can be four or five times the free stream velocity. The magnitude of lift also decreases after the onset of vortex breakdown. Reynolds number, surprisingly, also seem to have negligible effect on the vortices for slender wings. There is a slight difference in the aerodynamics of non-slender delta wings compared to those stated above. The first observation is that the magnitude of lift continues to increase even after the onset of vortex breakdown. The leading-edge vortices also seem to form closer to the surface and the vortex and boundary layer interaction becomes significant at low Reynolds numbers. Compared to the insensitivity of vortices and vortex breakdown with Reynolds number on slender delta wings, an increase of Reynolds number results in an upstream movement in the onset of vortex breakdown for slender wings. Gordnier and Visbal [24] showed that the vortex breakdown on slender delta wings is milder than that of non-slender wings, and that the deceleration of axial velocity is much smaller.

Topology wise, there have been various research done on what the skin-friction lines will look like for delta wings. Délery [21] shows a very clear interpretation of the topology for the flow on the surface, as well as above the surface on a delta wing. For the flow above a delta wing, there is a crossflow separation and a general movement upwards. There are two large foci, one on each side of the wing, which represents the eye of the leading-edge vortices. There are also two smaller foci under the primary vortices, and these correspond to secondary vortices that form due to the separation of the fluid on the wing's surface. On the surface, there is a primary attachment line, secondary separation lines, and secondary attachment lines. The primary attachment line usually splits the flow symmetrically down the center, as seen in Figure 5. However, the symmetry of this line depends on the turbulence of the flow and the strength of the leading-edge vortices. The secondary separation line is typically caused by the primary vortex, while the secondary attachment line is caused by the interaction of the primary and secondary vortices.

EXPERIMENTAL TECHNIQUE

With the background information on GLOF and delta wing aerodynamics defined, this section will focus on the experimental setup, procedure, and equipment used. Experiments were conducted at the Applied Aerodynamics Laboratory at Western Michigan University. All tests were done in the Small Wind Tunnel (SWT) facility that has a low-speed wind tunnel with a test section of 16 by 16 inches. The freestream velocity was set at 20 meters per second, and the corresponding Reynolds number for all test cases was calculated to be around 250,000.

Equipment

The basis of the GLOF method is the luminescent oil. The luminescent oil is prepared by mixing silicone oil with an oil-based ultraviolet tracer. Silicone oil of varying viscosities from Sigma Aldrich were used as it has a few desirable characteristics like the fluid being clear, colorless, odorless, and non-toxic. A few of the key parameters are listed in the table below.

Melting/freezing point	-55 °C
Boiling point	140 °C
Flash point	316 °C
Auto-ignition temperature	400 °C
Decomposition temperature	200 °C

Table 1: Key parameters for the silicone oil

The parameters in table 1 are identical in all the silicone oil used; the only parameter that changes with viscosity is the relative density, where relative density is defined as the ratio of densities between the silicone oil and water. The more viscous the oil, the higher its relative density. As seen in table 1, the low melting point, and the high boiling point of this silicone oil is ideal, as the oil will be stored at temperatures between 10 and 25 degrees Celsius. The experiments are also conducted at room temperature, and the low freestream velocity allows for the assumption that temperature of the oil remained constant throughout the experiment, thus eliminating the error caused by temperature effects. For this thesis, oil viscosities of 50, 100, 200, 350, 500, and 1000 centistokes (cSt) were used to study the effect of viscosity on the skin-friction fields.

The silicone oil is then mixed with a small amount of oil-based ultraviolet tracer. The tracer used is the DFSB-K175 fluorescent oil-based ultraviolet tracer dye made by Risk Reactor, and can be obtained commercially. One batch of luminescent oil is then made by mixing the tracer and silicone oil at a ratio of 0.5 ml to 100 ml respectively. This luminescent oil then emits radiation at a longer wavelength when excited by the UV LED array due to the Stokes shift.

Delta wings of various sweep angles, namely 50, 55, 60, 65, and 70 degrees, were machined by hand. The chord length was kept constant at 18.9 cm, while the span was changed accordingly to achieve the aforementioned sweep angles. These wings can be seen in Figure 6 below. The bottom surface was chamfered at a 45-degree angle to keep the tip sharp, and an attachment welded at the center of gravity for each of them. This attachment allowed the wing to be secured to the force balance in the wind tunnel. The upper surface of the wings was also covered with a 0.075mm white Mylar adhesive sheet to enhance the luminescent emission of the luminescent oil, as well as allow for repeatability as it is easily replaced.

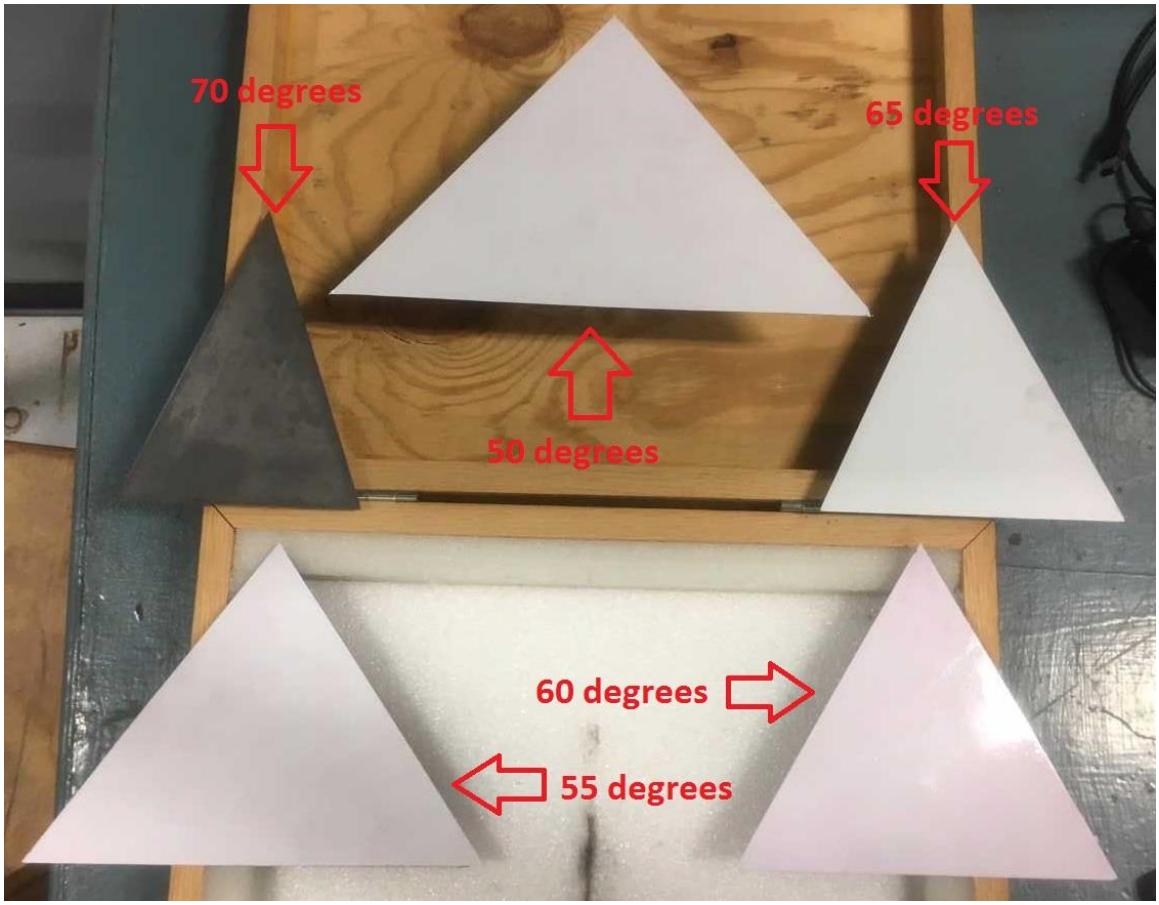

Figure 3: Delta wings configuration

These wings were then attached to the force balance in the small wind tunnel, which can measure the lift, drag, and pitching moment of the model. The balance uses a strain gage design where an increase in force will result in a change of voltage. The balance was calibrated using a pulley system and attaching known weights to it. This allowed for a relation between voltage and force to be made with a linear curve of best fit. Figure 7 below shows how the model was attached to the balance. The front rod controls the angle of attack, while the back rod is attached to the strain gages. The model attachment is secured to the force balance using pins.

Figure 4: Force balance and model attachment

Woodiga [25] did an analysis of the wavelength emitted with the use of different excitation sources and found that the UV LED array made by Chauvet Lightning is the most suitable. This UV LED array, also known as LED Shadow, consists of 192 LEDs at 0.25 Watts each, and emits a wavelength of 405 nm. The LED Shadow can be bought commercially, and is very easy to use. For this experiment, two LED arrays were used and placed on both sides of the wind tunnel to ensure a uniform illumination of the model surface. The equipment and the setup can be seen in Figure 8.

The camera, a Basler Aviator camera (model number: ava1000-100gm) was used to acquire the images. The camera can capture up to 101 frames per second at 1MP resolution. A 500 nm

long-pass filter was attached to the lens thus allowing only the emission of the luminescent oil, which was found to be around 530nm, to be detected by the camera. Although the experiments were conducted in a dark room environment, it is impossible to completely block out all light sources. This filter prevents any light from the environment to be detected by the camera, thus reducing noise in the results. The camera is placed above the test section of the wind tunnel, where a glass window allows optical access into the test section, and calibrated to be parallel to the model surface. Basler's open-source software, Pylon Viewer, works well with the camera and was used to acquire the images. Acquired images were then processed using a Matlab code to obtain skin-friction lines and vectors for each test.

Lastly, a foam brush was used to apply the oil to the model surface. A uniform oil-film is ideal as it allows for the extraction of high quality skin-friction fields. Since the surface area was relatively small, a foam brush was deemed sufficient.

Experimental Setup

The experimental setup can be seen in Figures 8 and 9 below. Each equipment has been labelled appropriately. Figure 8 shows the setup with the overhead lights switched on. Figure 9 shows the setup with the UV lights switched on in a darkroom setting. Figure 10 shows an initial image for a 65° delta wing at 0° Angle of Attack (AoA). The camera is attached to a three-axis camera stand, and is suspended by two steel tubes. The LED Shadows were set at the same angle, and the same distance away from the wind tunnel on each side to provide an illumination field that is as uniform as possible.

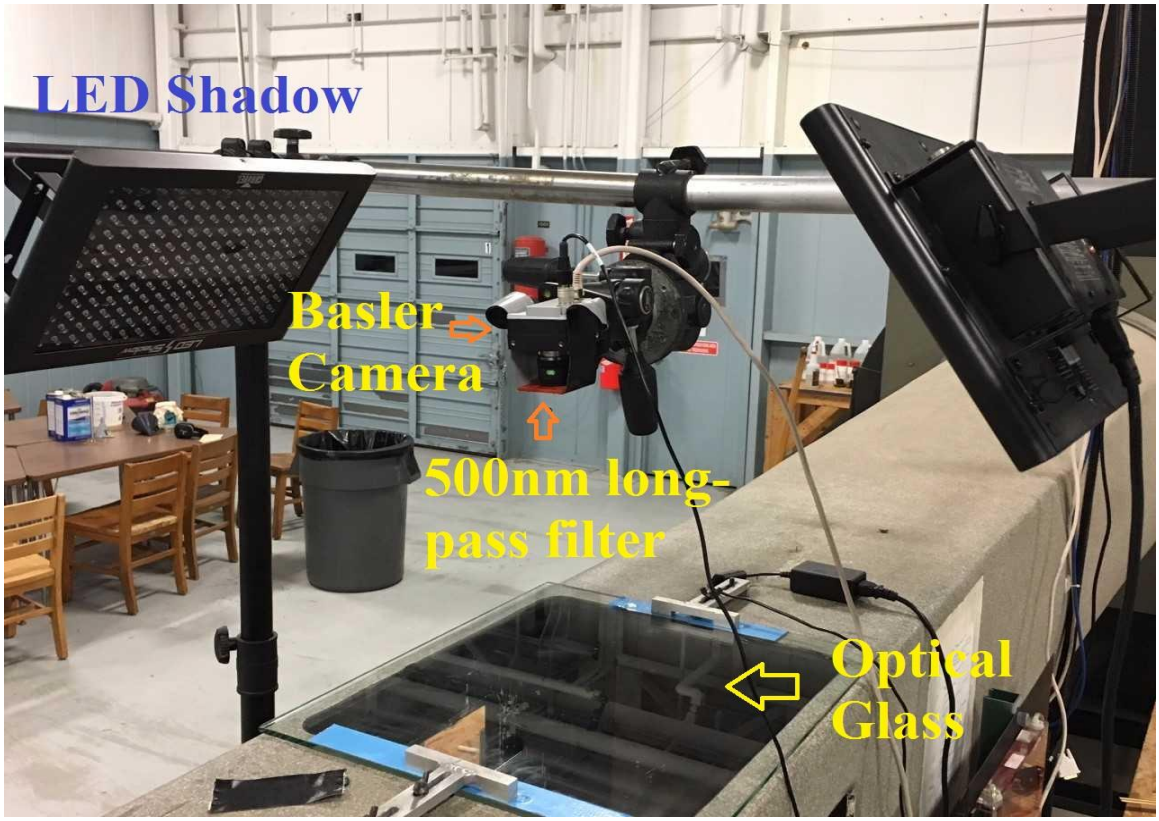

Figure 5: Experimental setup with overhead lights

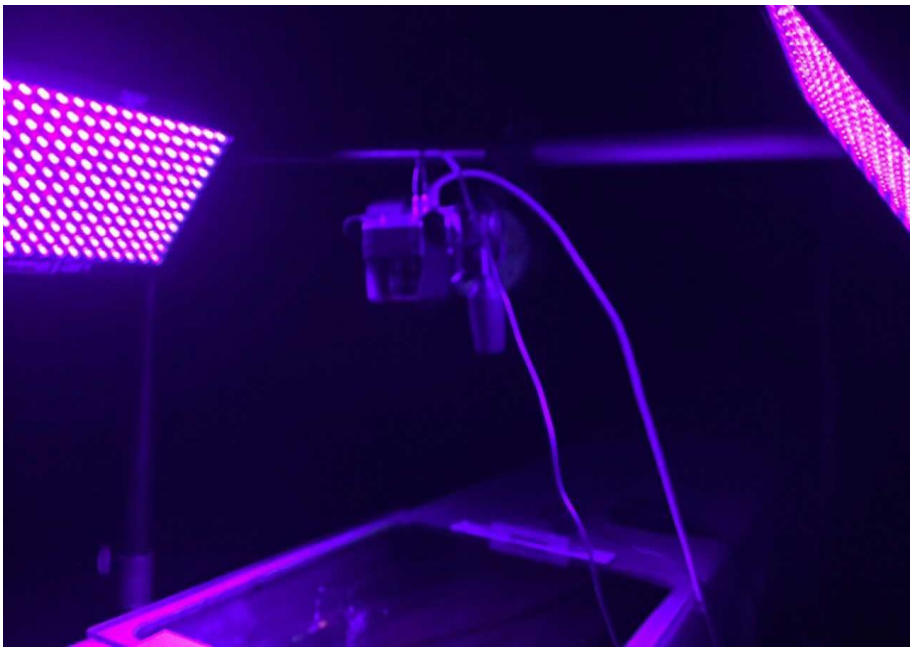

Figure 6: Experimental setup with UV lights

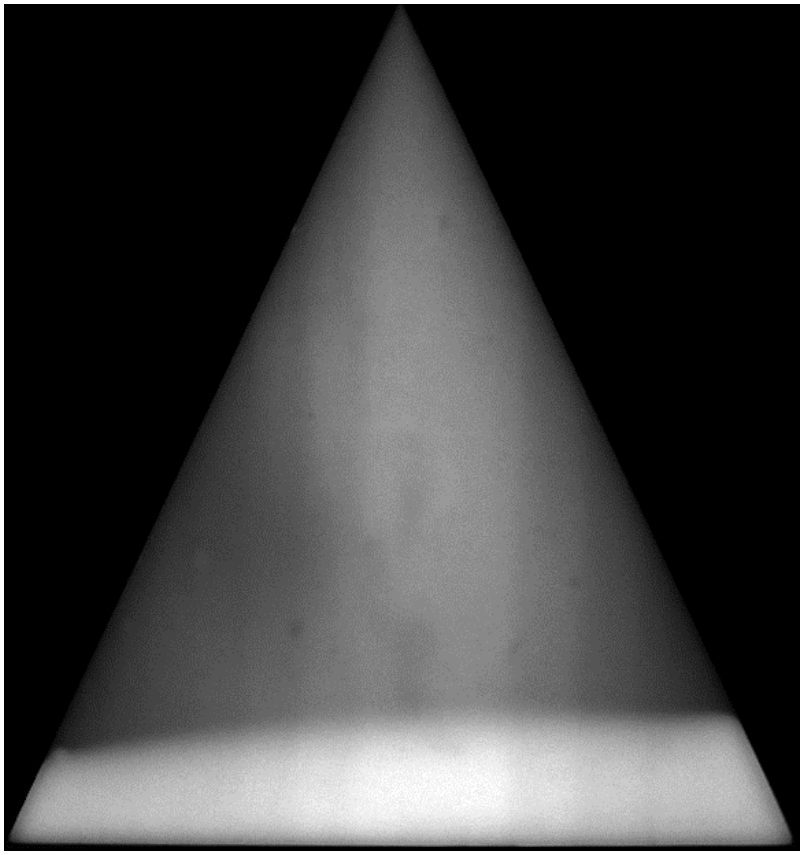

Figure 10: Actual image seen by camera for a 65° delta wing at 0°AoA

Experimental Procedure

Variables such as time step, viscosity, and number of superpositions were studied to see their effect on the skin-friction fields of a delta wing. All experiments were conducted at five frames per second totaling 1500 images each. The standard 65° delta wing at 13° AoA was used for these experiments due to the accessibility of publications to compare with the experimental results.

The first experiment conducted was to determine the optimum step size in the analysis. The optimum step size ensures that there is sufficient change of the oil-film between images. A step size that allows for too much or too little of a change will result in an inaccurate skin-friction field.

In this experiment, the number of superpositions and oil viscosity were fixed at 20 and 200 cSt respectively, while the time step was changed between 5 and 25 with an increment of five per run.

The second experiment conducted was to determine the optimum number of superpositions using the optimum step size acquired from the first experiment. This parameter is important as too little or too large a number will equate to an under-developed or an over-developed oil-film respectively (i.e., the oil-film is still changing if too little, and the oil-film has stopped changing if too large). In this experiment, the optimum step size was used for all runs, which was found to be a step size of five, and the oil viscosity was set at 200 cSt. The number of superpositions was then changed between 5 and 30, with an increment of five per run.

The third experiment conducted was to determine the optimum oil viscosity. Using the optimum step size and the number of superpositions, oil viscosities of 50, 100, 200, 350, 500, and 1000 cSt were used.

With the optimum step size, number of superpositions, and oil viscosity found in the above experiments, these were then applied to each of the delta wings as the AoA is changed between -5 to 25 degrees, at an increment of 5° per run. Force measurement were also conducted on the 65 and 70 degrees delta wings and compared to published data.

PARAMETRIC RESULTS

Parametric study to find the optimum variables listed in the previous section is necessary to ensure that the extracted skin-friction fields make sense. All experiments in this section were done on a 65° delta wing at an AoA of 13°, with a freestream velocity of 20 meters per second and a corresponding Reynolds number of 250,000. Reynolds number is defined as the ratio between inertial and viscous forces. It is dimensionless and is used to predict flow patterns. In the first experiment, the number of superpositions and oil viscosity were fixed at 20 and 200 cSt respectively while the time step was changed between 5 and 25, at an increment of five per run. In the second experiment, the number of step size and oil viscosity were fixed at 5 and 200 cSt respectively while the number of superpositions were changed between 5 and 30, at an increment of 5 per run. An optimum number of superpositions will track the change of the oil-film until it is completely developed. The last experiment explores the effect of oil viscosity on the skin-friction fields. The step size and number of superpositions were fixed at 5 and 20 respectively, while oil viscosities of 50, 100, 200, 350, 500, 1000 cSt were applied to the model surface. The results for these experiments are shown below, and observations for each study are presented at the end.

Figures 11 (a), (b), (c), and (d) are the initial luminescent oil image, the final luminescent oil image, the skin-friction line plot, and the skin-friction vector plot respectively for the case of a 65° delta wing at 13° AoA and a step size of 5.

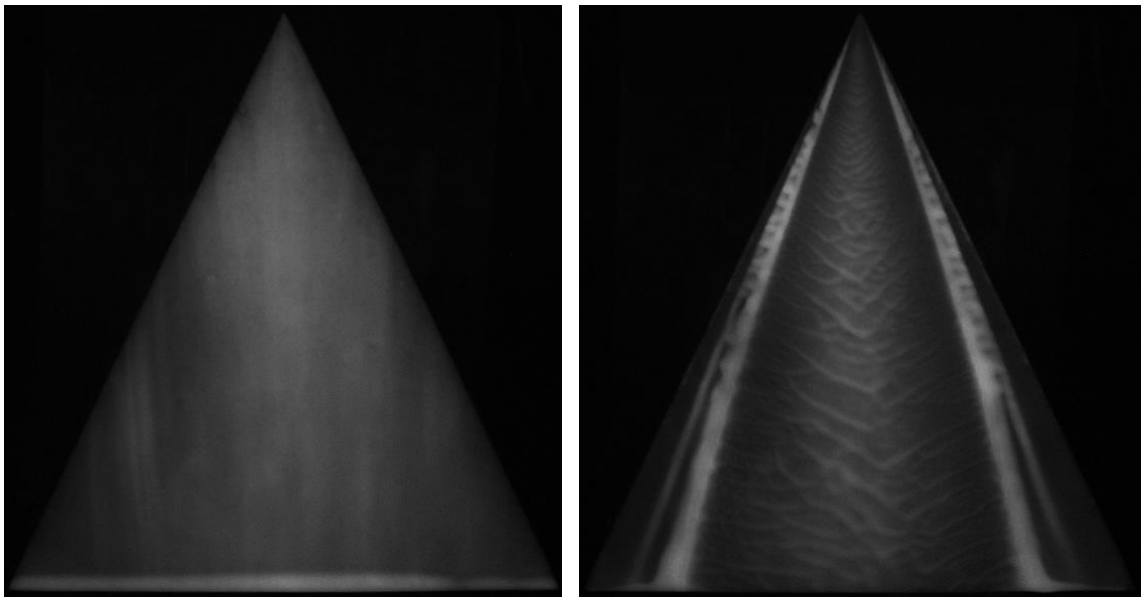

(a) (b)

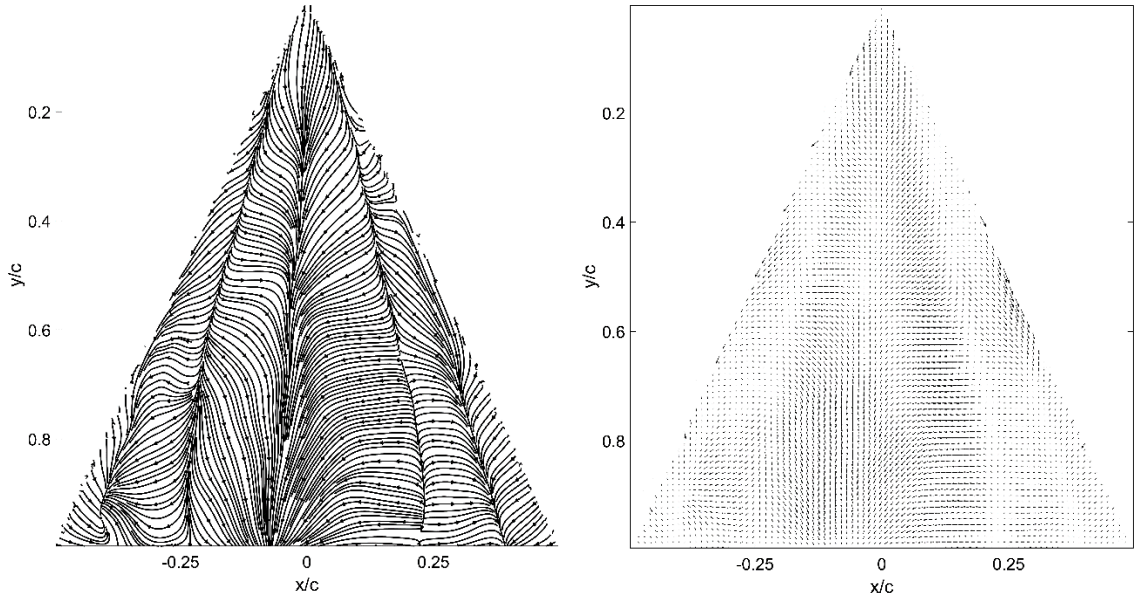

(c) (d)

Figure 11: (a) initial image, (b) final image, (c) skin-friction lines, and (d) skin-friction vectors for step size of 5, 200 cSt oil and 20 superpositions

Figures 12 (a), (b), (c), and (d) are the initial luminescent oil image, the final luminescent oil image, the skin-friction line plot, and the skin-friction vector plot respectively for the case of a 65° delta wing at 13° AoA and a step size of 10.

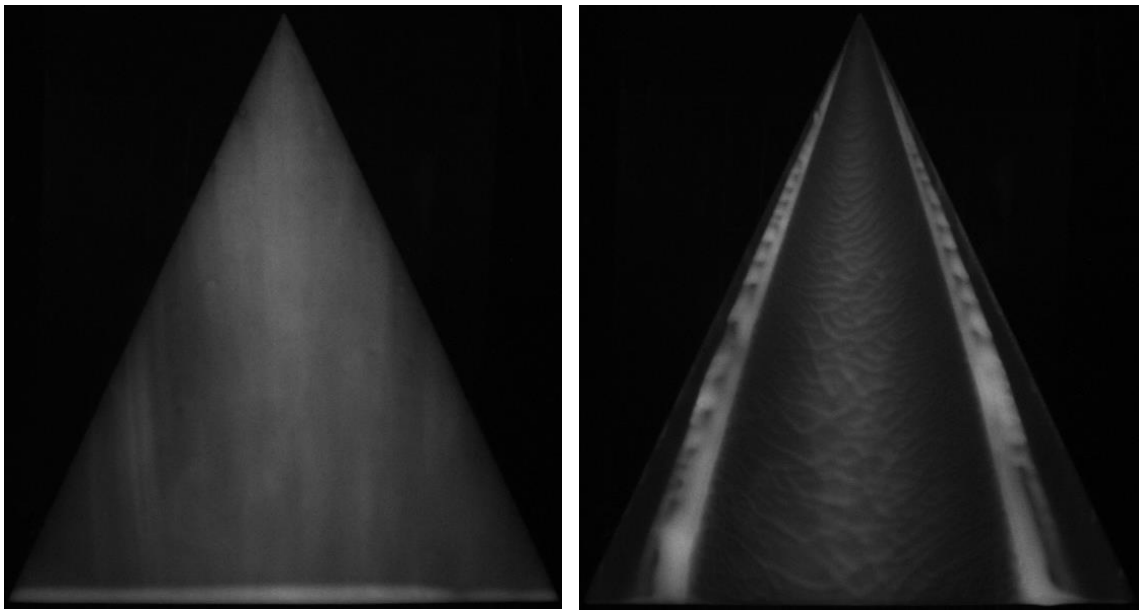

(a) (b)

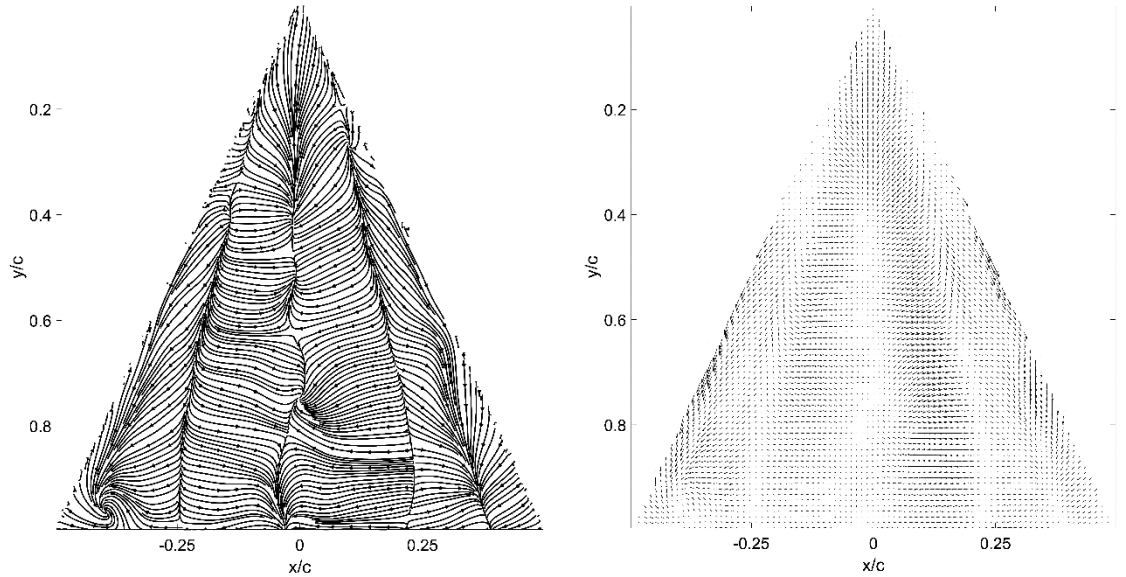

(c) (d)

Figure 12: (a) initial image, (b) final image, (c) skin-friction lines, and (d) skin-friction vectors for step size of 10, 200 cSt oil and 20 superpositions

Figures 13 (a), (b), (c), and (d) are the initial luminescent oil image, the final luminescent oil image, the skin-friction line plot, and the skin-friction vector plot respectively for the case of a 65° delta wing at 13° AoA and a step size of 15.

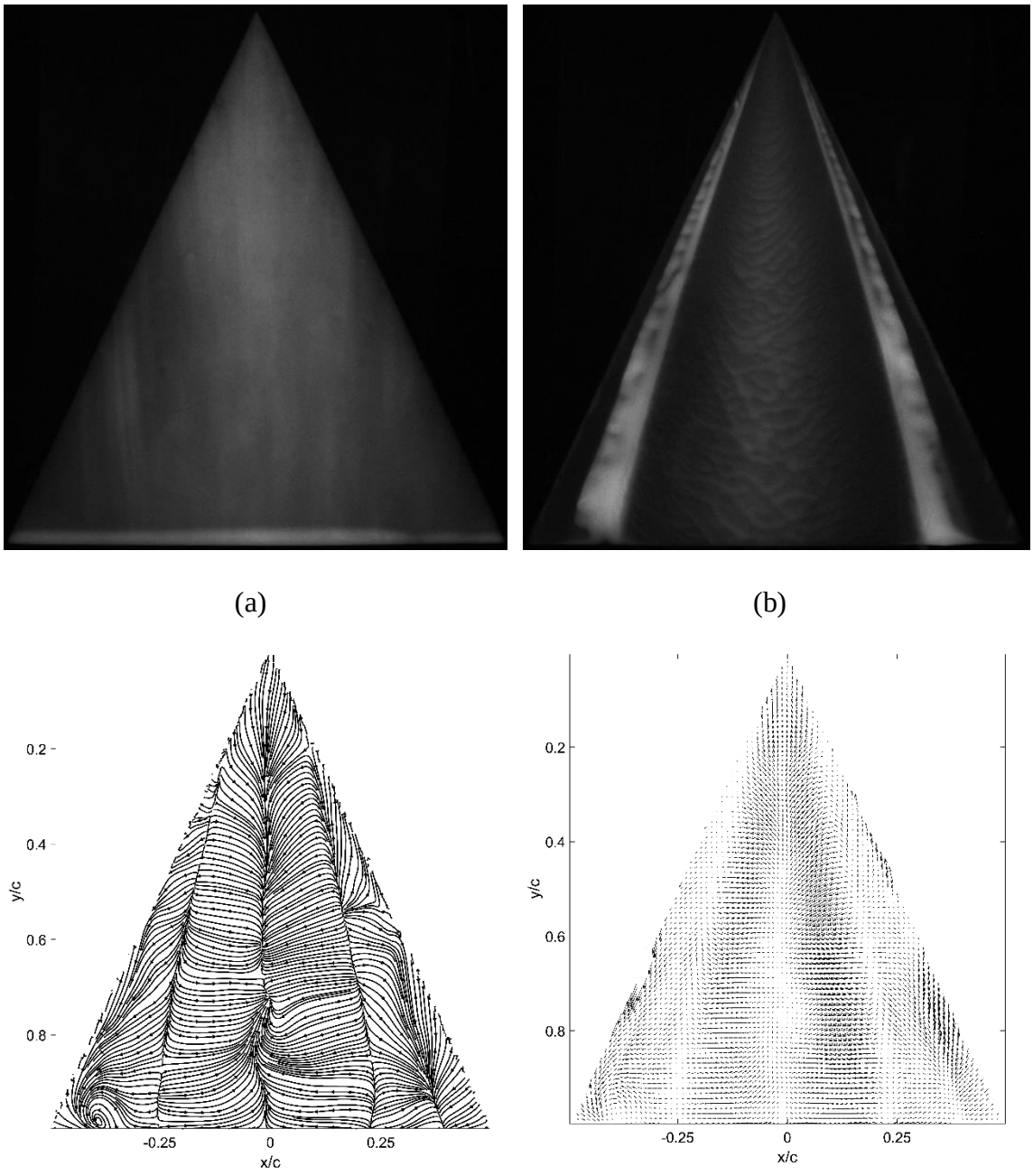

Figure 13: (a) initial image, (b) final image, (c) skin-friction lines, and (d) skin-friction vectors for step size of 15, 200 cSt oil and 20 superpositions

Figures 14 (a), (b), (c), and (d) are the initial luminescent oil image, the final luminescent oil image, the skin-friction line plot, and the skin-friction vector plot respectively for the case of a 65° delta wing at 13° AoA and a step size of 20.

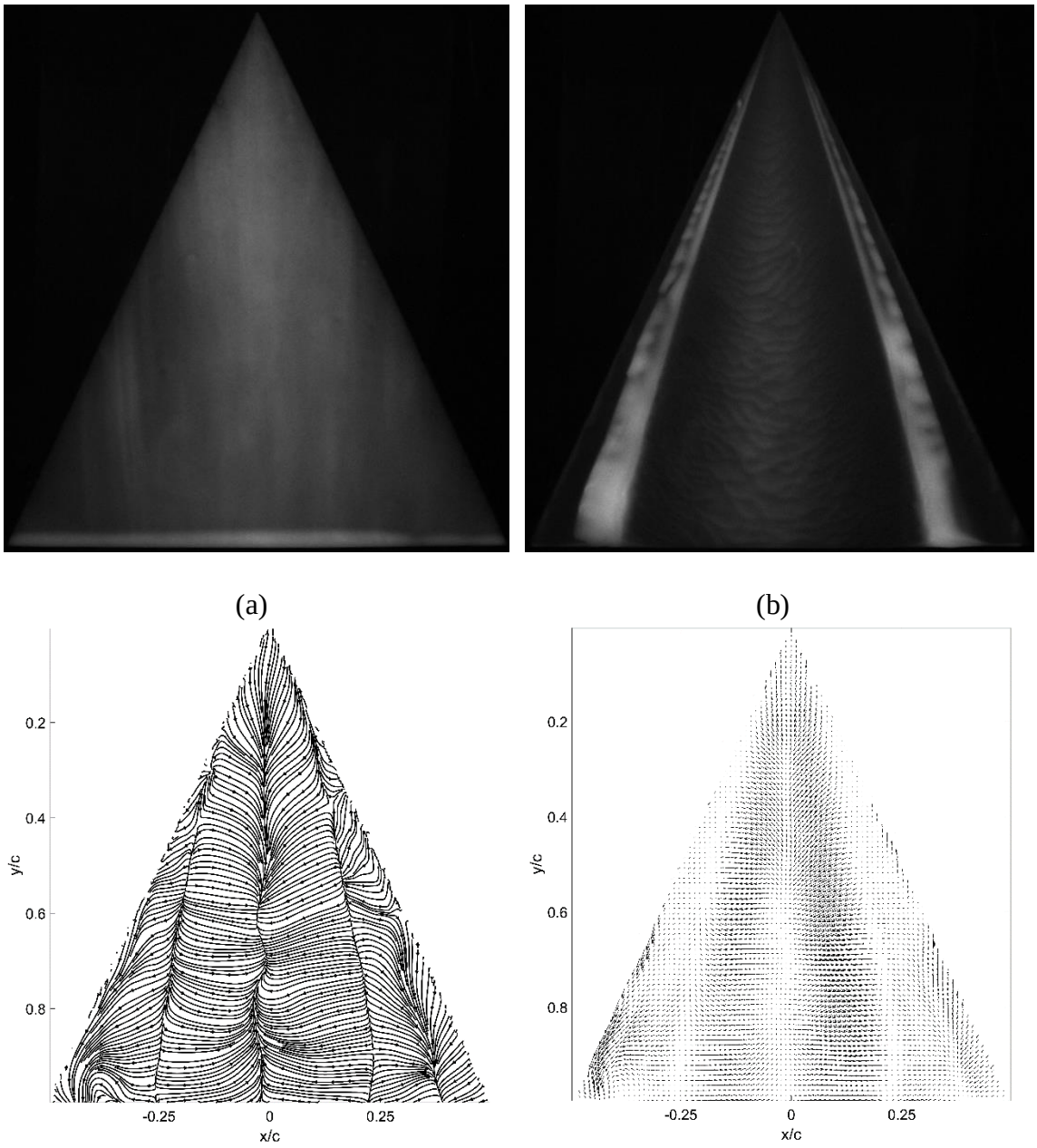

Figure 14: (a) initial image, (b) final image, (c) skin-friction lines, and (d) skin-friction vectors for step size of 20, 200 cSt oil and 20 superpositions

Figures 15 (a), (b), (c), and (d) are the initial luminescent oil image, the final luminescent oil image, the skin-friction line plot, and the skin-friction vector plot respectively for the case of a 65° delta wing at 13° AoA and a step size of 25.

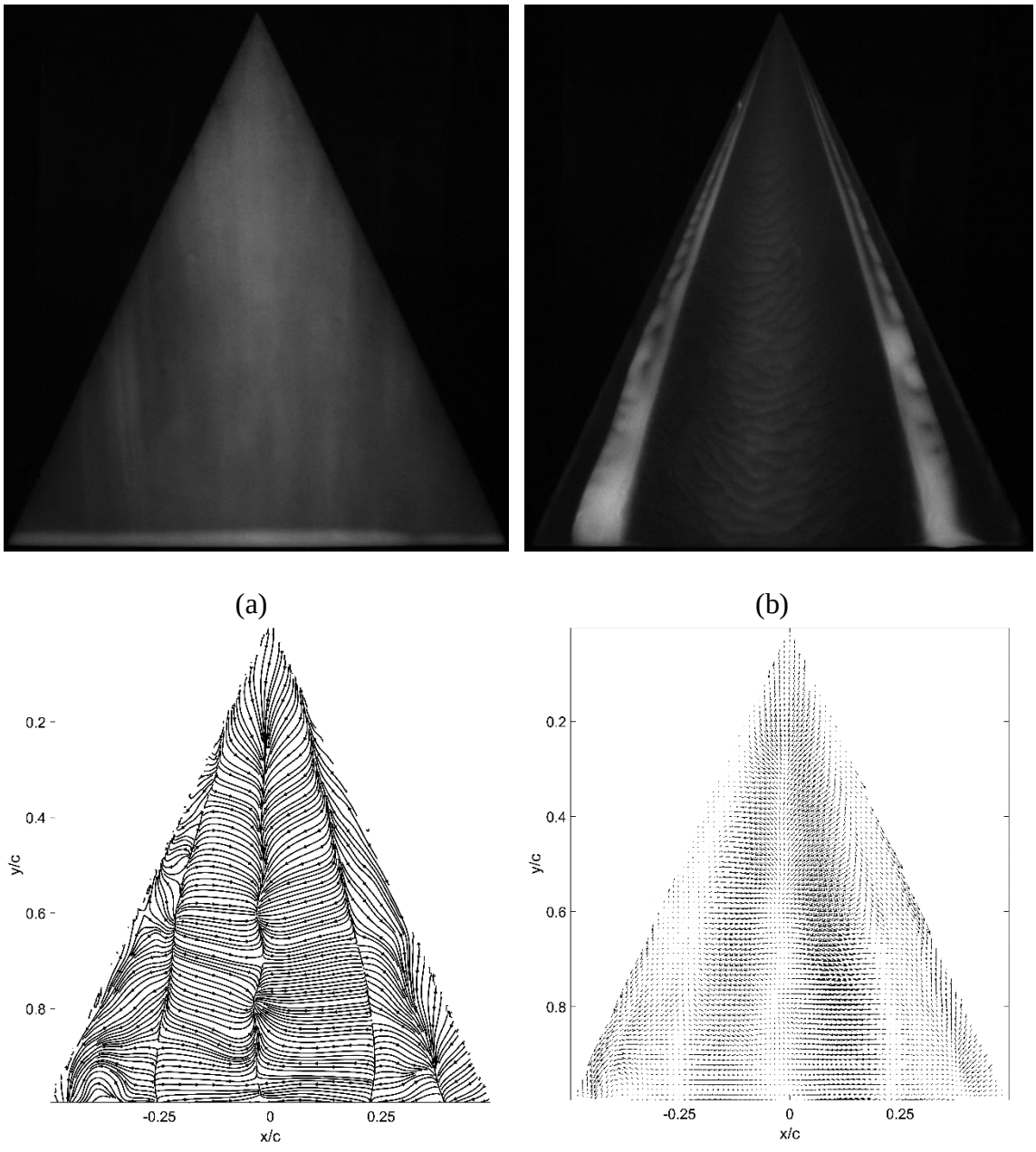

Figure 15: (a) initial image, (b) final image, (c) skin-friction lines, and (d) skin-friction vectors for step size of 25, 200 cSt oil and 20 superpositions

The initial image in Figures 11 to 15 is the same, as this image was taken before the wind tunnel is switched on. The main difference in the final image of Figures 11 to 15 is that as the step size is increased, there is an accumulation of oil near the trailing edge of the wing which distorts the extracted skin-friction fields. This increase in accumulation can be explained by an increase in the total time taken as the step size is increased. For example, a step size of 5 and 20 superpositions will require 100 images. At five frames per second, these parameters correlate to a total time of 20 seconds for the experiment. At a step size of 25 and 20 superpositions, the analysis will require 500 images. This will correlate to a total time of 100 seconds for the experiment, thus allowing the oil to continue moving towards the trailing edge due to a combination of the shearing force applied by the incoming flow and the tip vortices created by the delta wing geometry.

This distortion of the extracted skin-friction fields can be seen clearly in the skin-friction lines of Figures 11 to 15. The primary separation line (down the middle) is still relatively straight in Figure 11(c), which should be the case as the delta wing has a symmetry down the middle. The secondary reattachment line is also relatively straight until around $y/c = 0.65$, where a vortex breakdown occurs as expected with the characteristic of delta wing aerodynamics. The secondary separation line at $x/c = 0.4$ and -0.45 are still relatively clear, which should be the case theoretically as seen in Figure 4. Comparing these results with that of Figure 15(c), the secondary separation line on the left is completely gone, while the one on the right is not as clear as the one in Figure 11(c). Therefore, it can be concluded that the optimum step size for this test is five as the extracted skin-friction lines somewhat resemble the theoretical topology seen in Figure 4.

Comparing the experimental results with Woodiga and Liu [26], the difference is evident when a comparison was made between the secondary separation lines. This difference can be

attributed to the fact that the Reynolds number for the paper was set at 440,000. Since the Reynolds numbers do not match, both experiments are not dynamically similar and thus, experiences different flow regimes. The unsymmetrical skin-friction lines can also be attributed to a few reasons. Firstly, since the delta wings were machined by hand, it is not as accurate as one machined by a CNC machine. Uneven heating, especially near the edges during machining, may affect the tip of the delta wing by warping the thin metal. This small warping may influence the incoming flow a small amount, but it is then exacerbated by the low-speed condition set for the experiments. The solution for this source of error would be to increase the incoming flow velocity, thus reducing the effect of a slightly asymmetric model on the flow in general. Secondly, while the SWT has a turbulence intensity of 0.2%, there is no way to tell if the flow over the model is symmetric. Even a small yaw angle of 0.5° for the model with respect to the incoming flow would result in an asymmetric flow over the model. Similarly, increasing the incoming flow velocity will reduce this source of error.

In the next set of experiments, the number of step size and oil viscosity were fixed at 5 and 200 cSt respectively while the number of superpositions were changed between 5 and 30, at an increment of 5 per run. Theoretically, a higher number of superpositions will result in a more accurate data. However, if the oil-film has completely developed, then there is no reason to continue to superimpose the skin-friction fields as there will no longer be a change of luminescent intensity in the images. The number of superpositions will be referred to as the sample size in the discussion below.

Figures 16 (a), (b), (c), and (d) are the initial luminescent oil image, the final luminescent oil image, the skin-friction line plot, and the skin-friction vector plot respectively for the case of a 65° delta wing at 13° AoA and a sample size of 5.

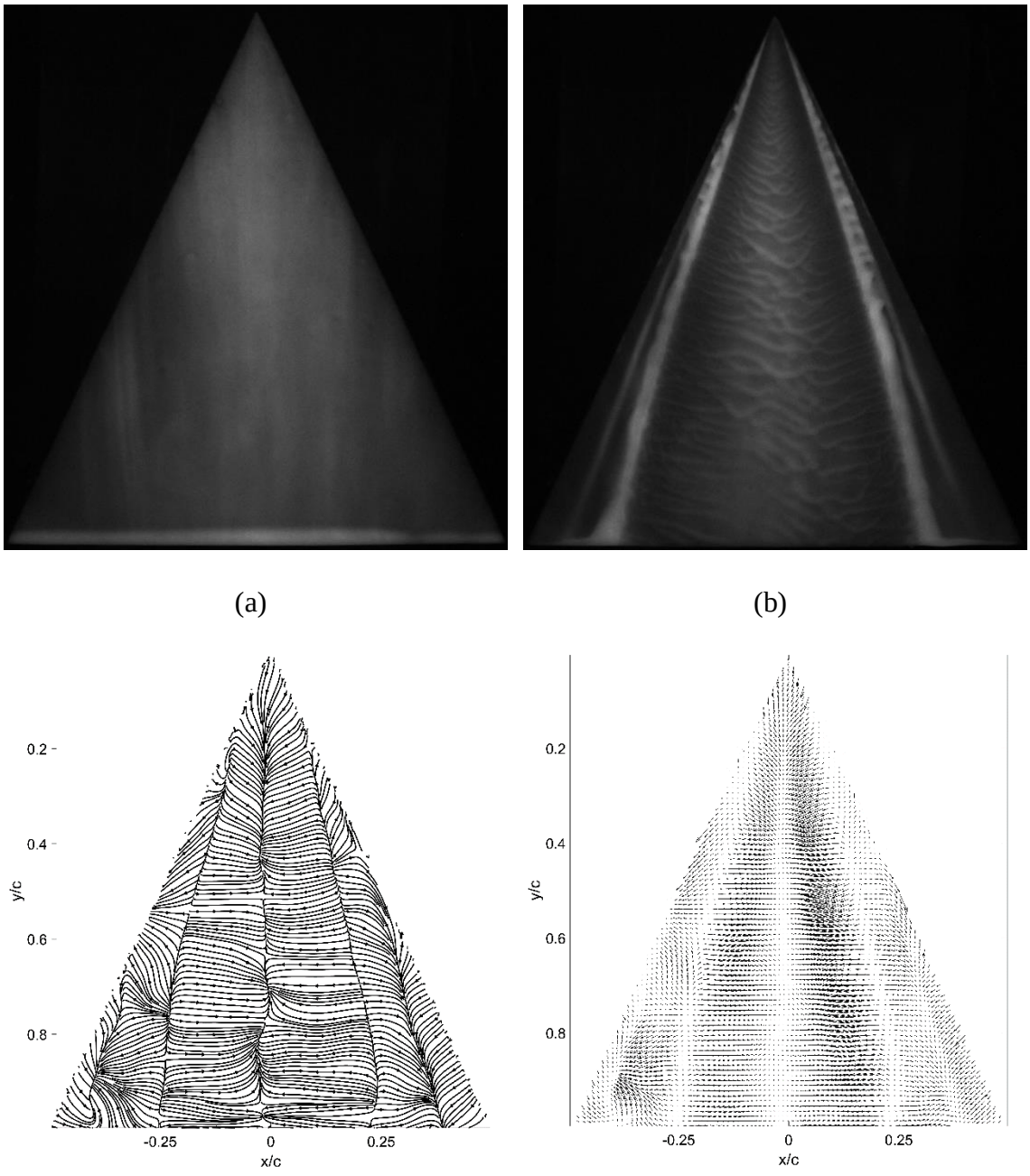

Figure 16: (a) initial image, (b) final image, (c) skin-friction lines, and (d) skin-friction vectors for step size of 5, 200 cSt oil and 5 superpositions

Figures 17 (a), (b), (c), and (d) are the initial luminescent oil image, the final luminescent oil image, the skin-friction line plot, and the skin-friction vector plot respectively for the case of a 65° delta wing at 13° AoA and a sample size of 10.

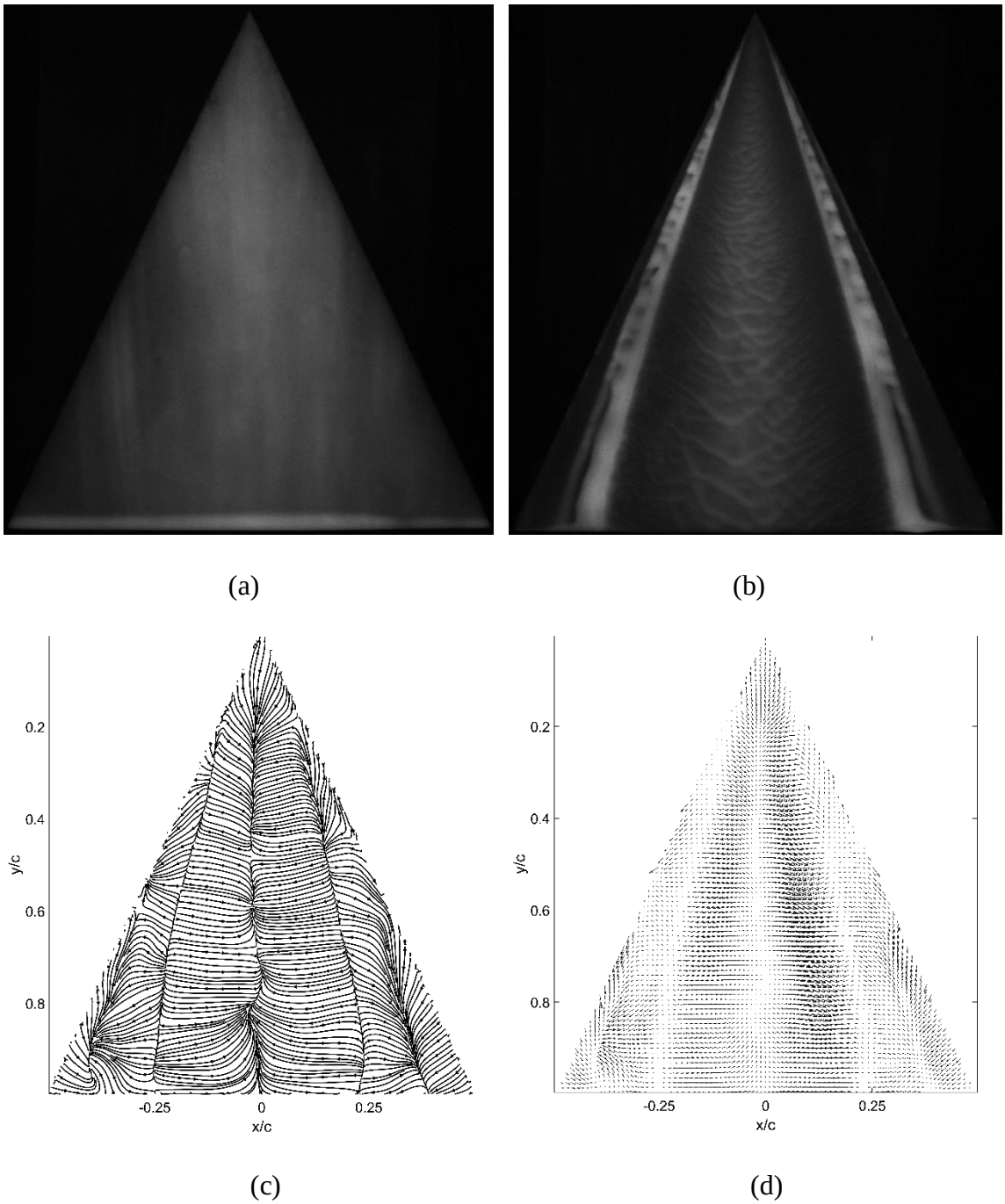

Figure 17: (a) initial image, (b) final image, (c) skin-friction lines, and (d) skin-friction vectors for step size of 5, 200 cSt oil and 10 superpositions

Figures 18 (a), (b), (c), and (d) are the initial luminescent oil image, the final luminescent oil image, the skin-friction line plot, and the skin-friction vector plot respectively for the case of a 65° delta wing at 13° AoA and a sample size of 15.

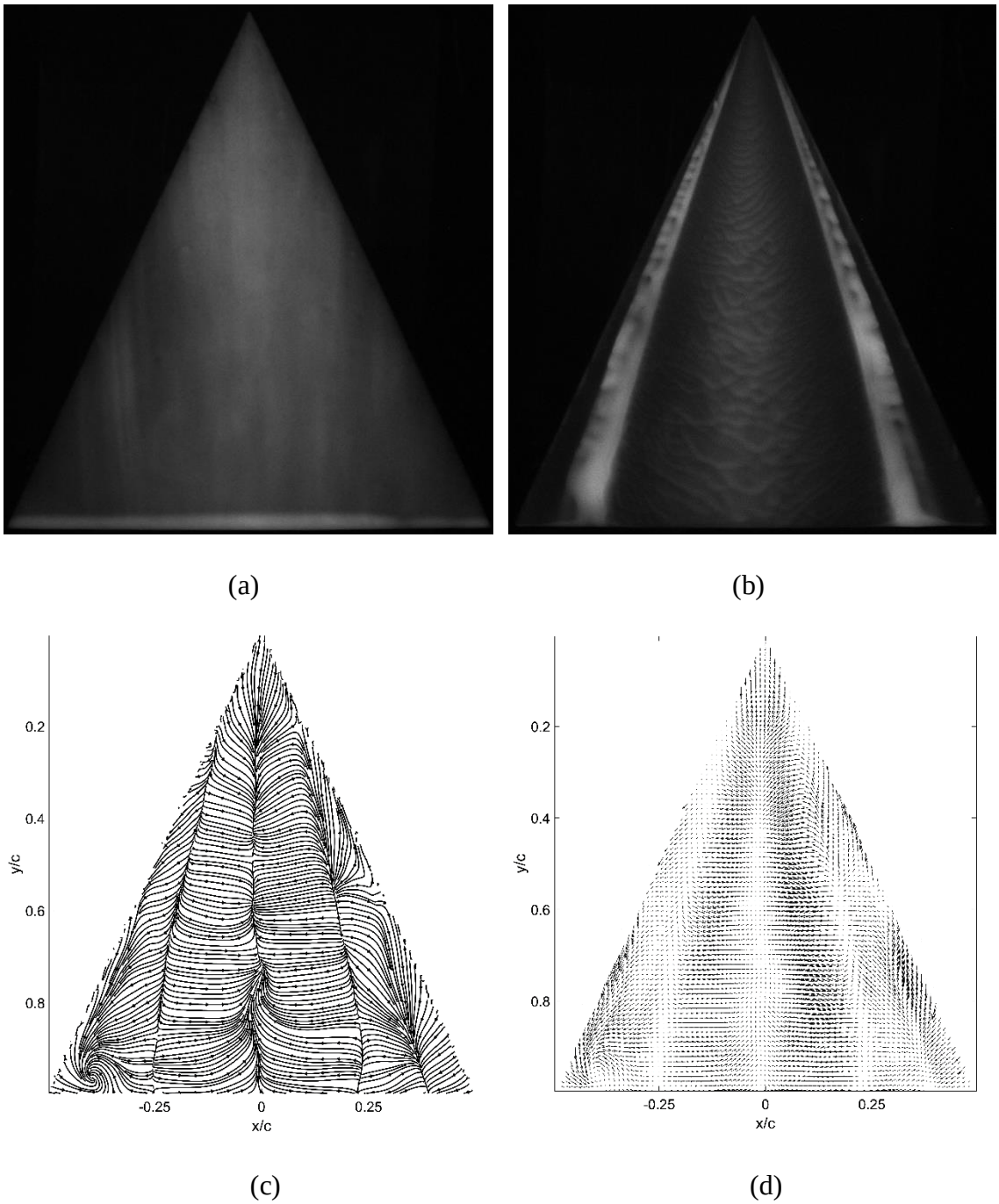

Figure 18: (a) initial image, (b) final image, (c) skin-friction lines, and (d) skin-friction vectors for step size of 5, 200 cSt oil and 15 superpositions

Figures 19 (a), (b), (c), and (d) are the initial luminescent oil image, the final luminescent oil image, the skin-friction line plot, and the skin-friction vector plot respectively for the case of a 65° delta wing at 13° AoA and a sample size of 20.

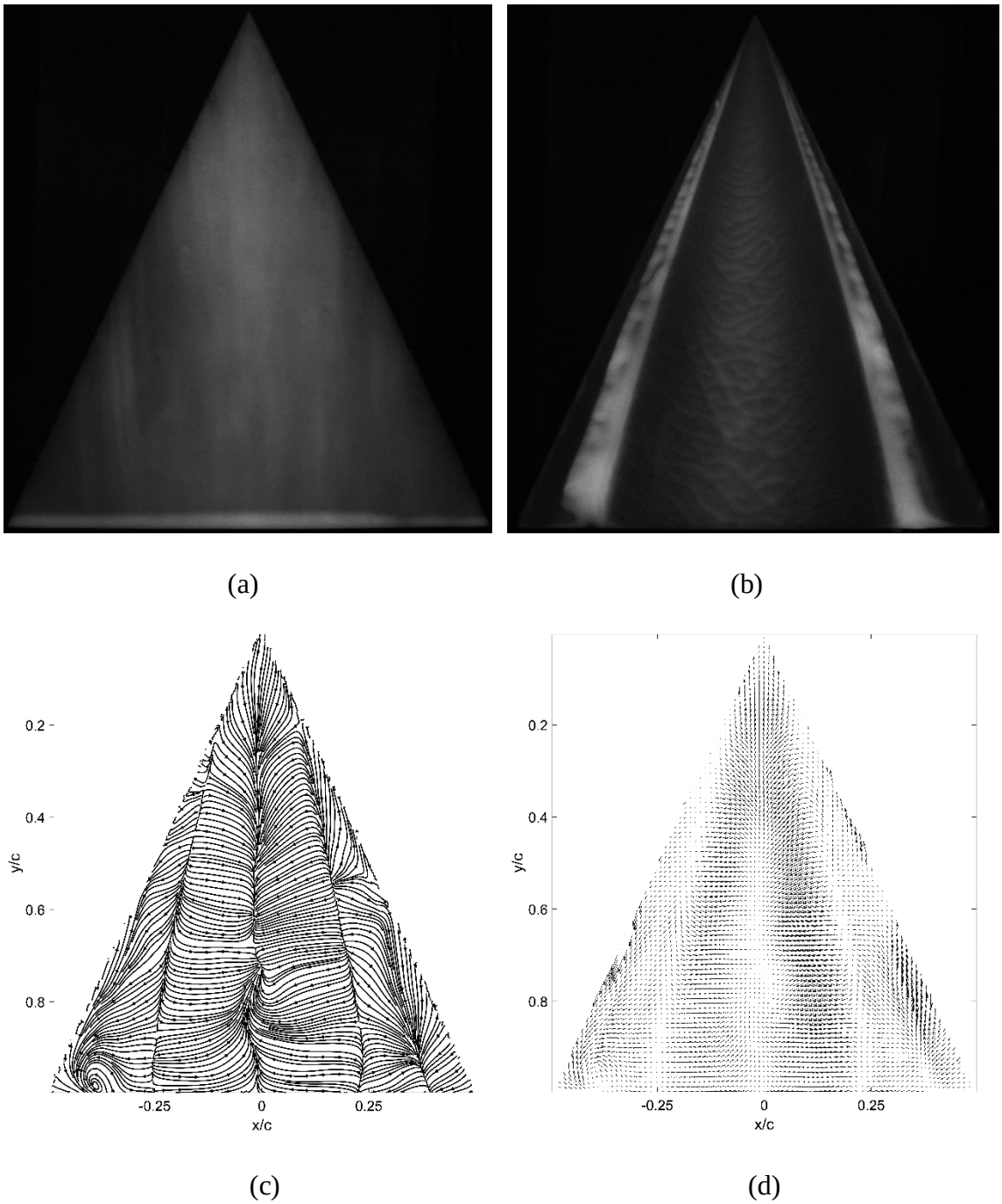

Figure 19: (a) initial image, (b) final image, (c) skin-friction lines, and (d) skin-friction vectors for step size of 5, 200 cSt oil and 20 superpositions

Figures 20 (a), (b), (c), and (d) are the initial luminescent oil image, the final luminescent oil image, the skin-friction line plot, and the skin-friction vector plot respectively for the case of a 65° delta wing at 13° AoA and a sample size of 25.

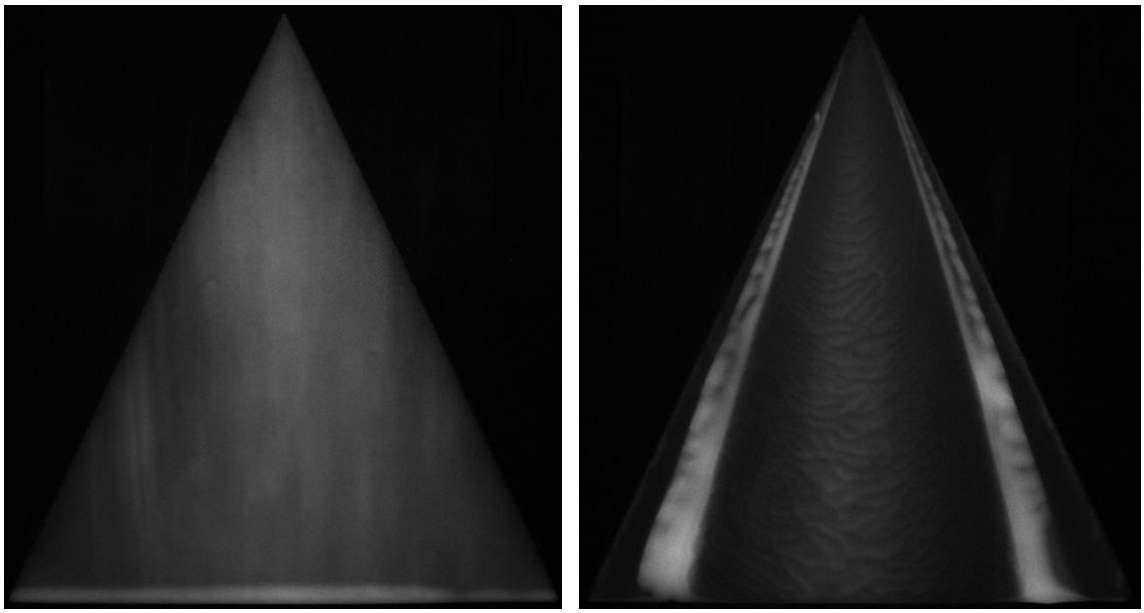

(a) (b)

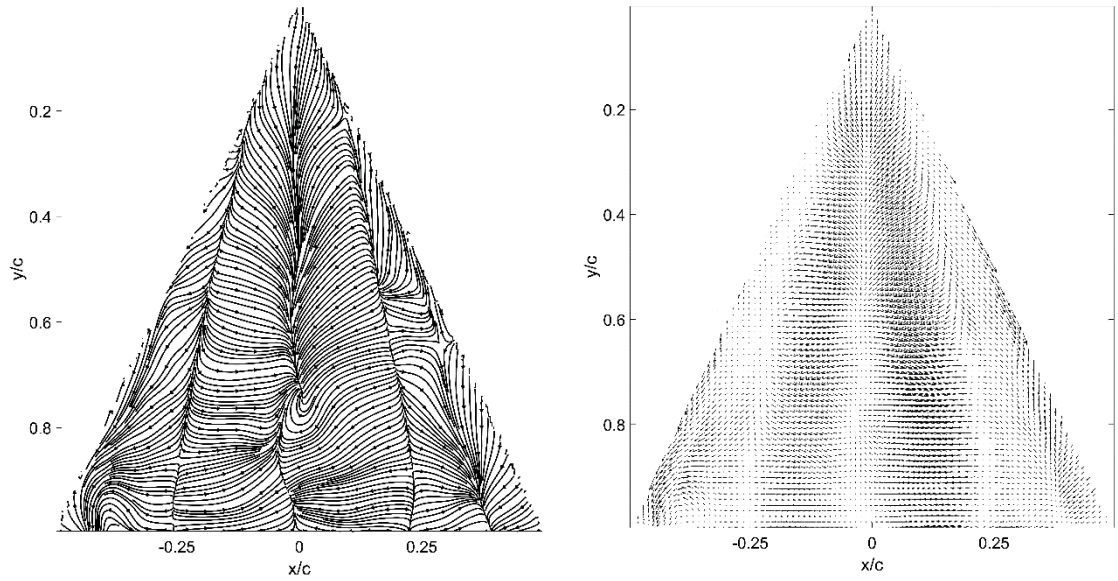

(c) (d)

Figure 20: (a) initial image, (b) final image, (c) skin-friction lines, and (d) skin-friction vectors for step size of 5, 200 cSt oil and 25 superpositions

Figures 21 (a), (b), (c), and (d) are the initial luminescent oil image, the final luminescent oil image, the skin-friction line plot, and the skin-friction vector plot respectively for the case of a 65° delta wing at 13° AoA and a sample size of 30.

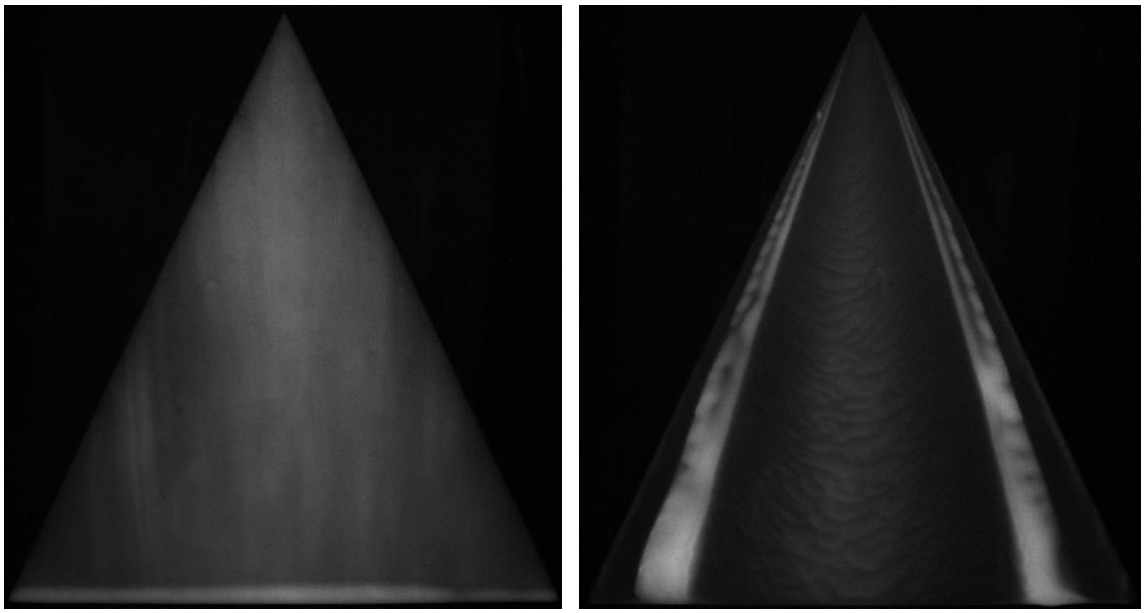

(a) (b)

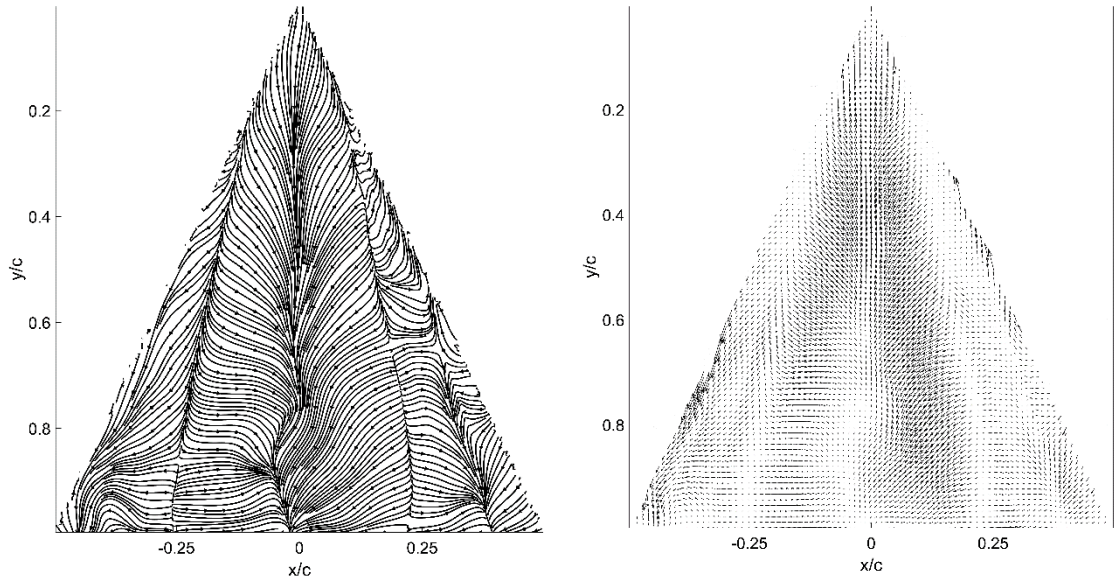

(c) (d)

Figure 21: (a) initial image, (b) final image, (c) skin-friction lines, and (d) skin-friction vectors for step size of 5, 200 cSt oil and 30 superpositions

Looking at Figures 16(b) to 21(b), the minimum sample size will be 20. This is because there is still a large change of the oil-film (y/c = 0.2) between a sample size of 5 to 20, as can be seen in the movement of the oil at x/c = -0.4 and 0.4. In the sample size of 20, 25, and 30, the movement of the oil relatively smaller (y/c = 0.02) and thus, it can be assumed that the oil-film has completely developed. Comparing Figures 19(c) to 21(c), the primary separation line (down the middle) disintegrates at around y/c = 0.75 and is more evident as the sample size was increased. Just by looking at this feature, a sample size of 20 resembles the theoretical topology seen in Figure 4 the most. As for the secondary features, a tip vortex can be seen at x/c = -0.4 in Figure 19(c) whereby it is not clearly seen with a sample size of 25 and 30. It is unclear if this feature is the result of the tip vortex, or if it just noise that is extracted. This feature is not seen in any of the skin-friction diagnostic publications, but one must note that all known publications were done at a much higher Reynolds and Mach numbers. This feature might be unique to low-speed flow over a delta wing. Considering the aforementioned observations, the optimum sample size was found to be 20.

The last experiment explores the effect of oil viscosity on the extracted skin-friction fields. Silicone oil of 50, 100, 200, 350, 500, and 1000 cSt were used while the step size and sample size were set at 5 and 20 respectively. A more viscous oil will require a higher freestream velocity for the oil-film to move the same amount as a less viscous oil. However, the freestream velocity for this experiment was not changed to limit the number of variables that can affect the skin-friction fields. The range for oil viscosities were selected after reviewing previous work done with the GLOF technique.

Figures 22 (a), (b), (c), and (d) are the initial luminescent oil image, the final luminescent oil image, the skin-friction line plot, and the skin-friction vector plot respectively for the case of a 65° delta wing at 13° AoA and an oil viscosity of 50 cSt.

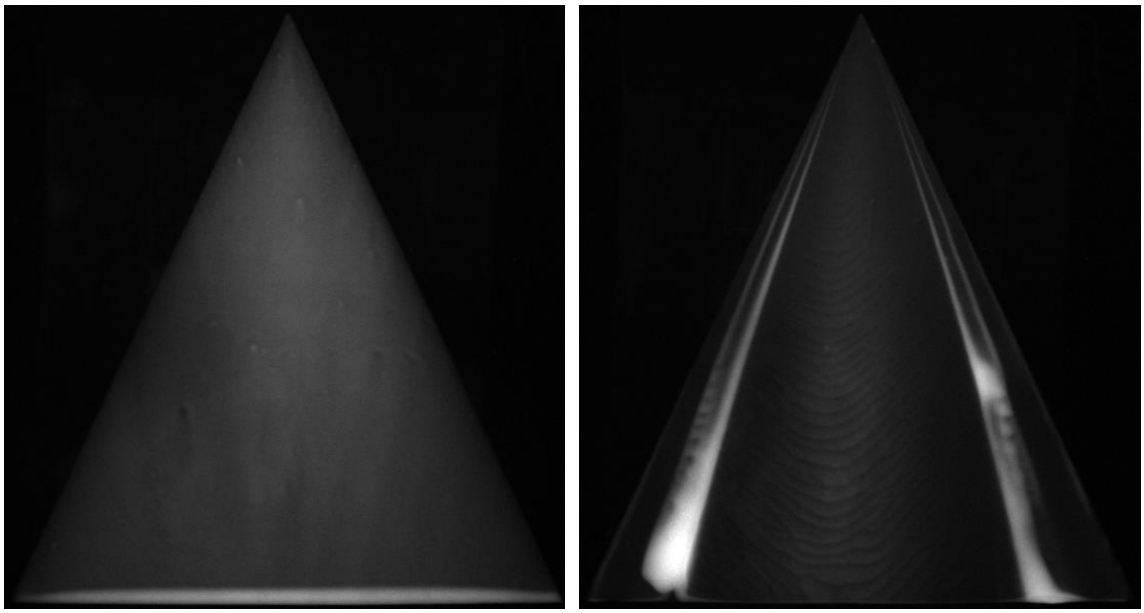

(a) (b)

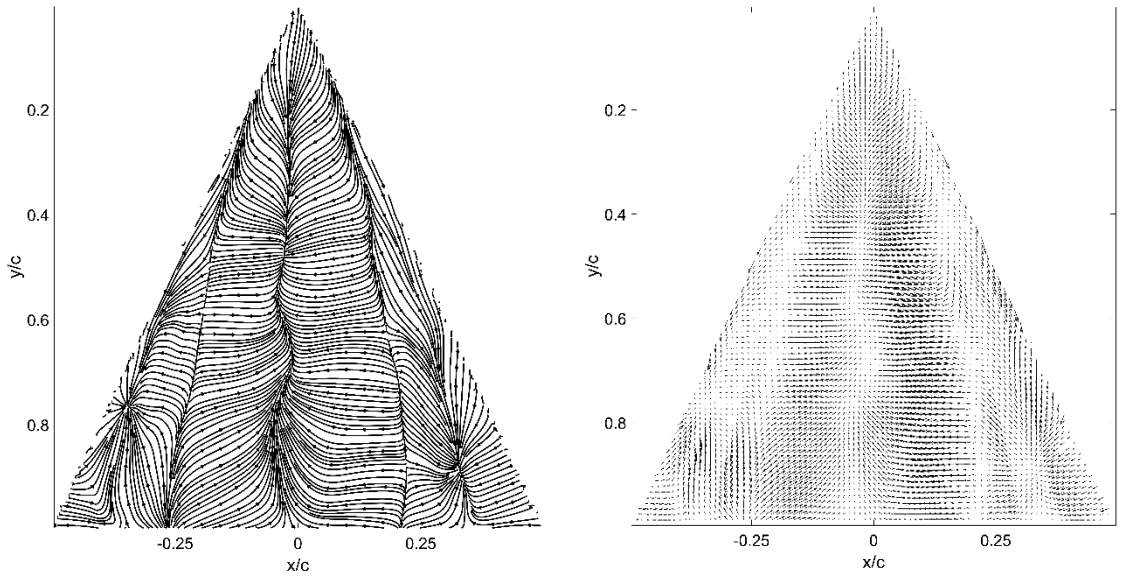

(c) (d)

Figure 22: (a) initial image, (b) final image, (c) skin-friction lines, and (d) skin-friction vectors for step size of 5, 50 cSt oil and 20 superpositions

Figures 23 (a), (b), (c), and (d) are the initial luminescent oil image, the final luminescent oil image, the skin-friction line plot, and the skin-friction vector plot respectively for the case of a 65° delta wing at 13° AoA and an oil viscosity of 100 cSt.

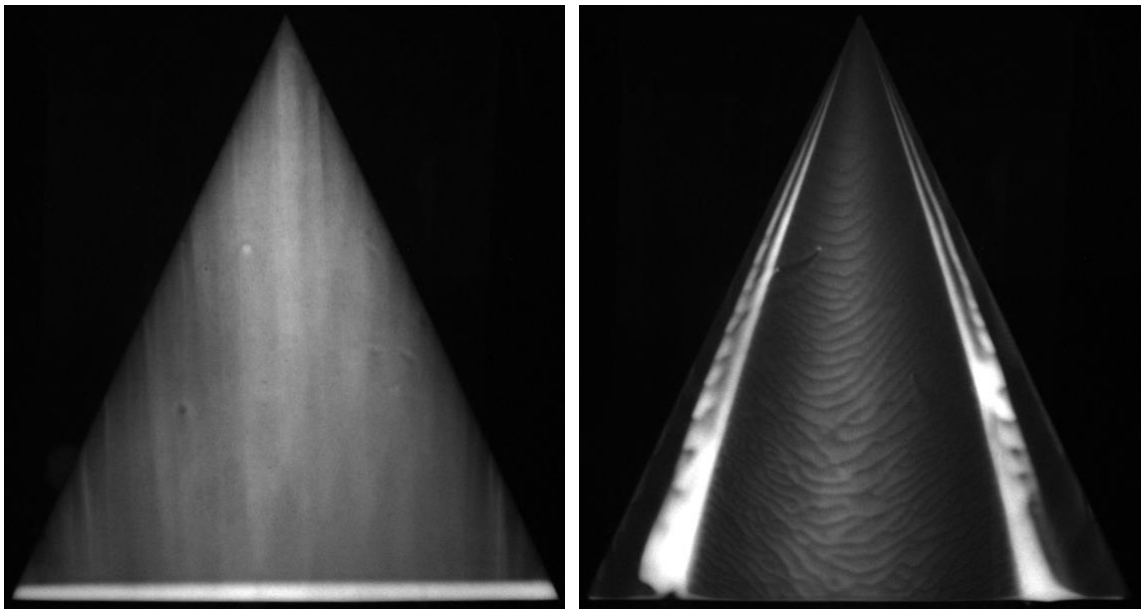

(a) (b)

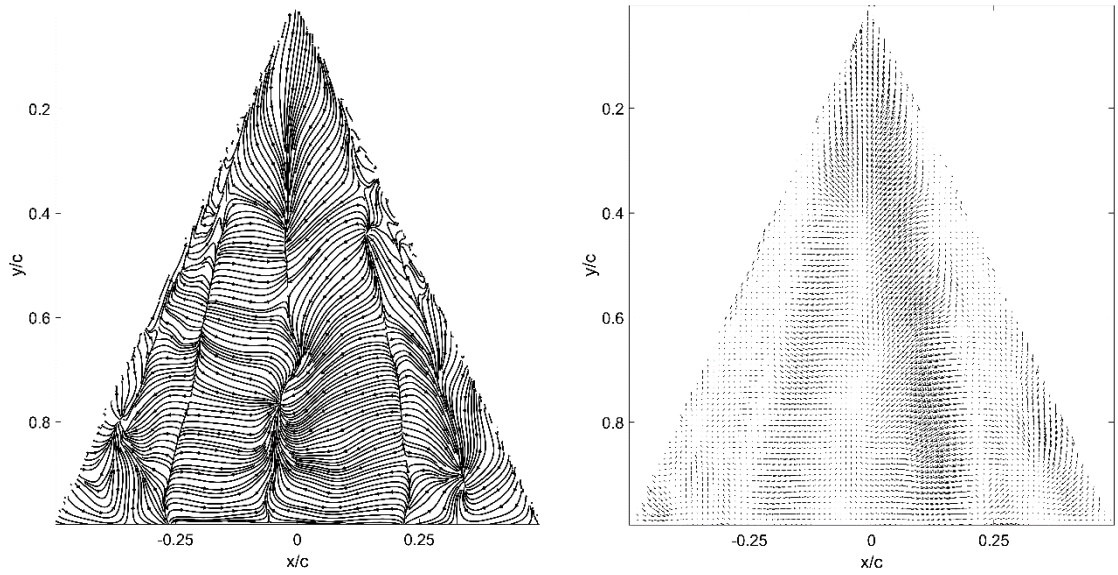

(c) (d)

Figure 23: (a) initial image, (b) final image, (c) skin-friction lines, and (d) skin-friction vectors for step size of 5, 100 cSt oil and 20 superpositions

Figures 24 (a), (b), (c), and (d) are the initial luminescent oil image, the final luminescent oil image, the skin-friction line plot, and the skin-friction vector plot respectively for the case of a 65° delta wing at 13° AoA and an oil viscosity of 200 cSt.

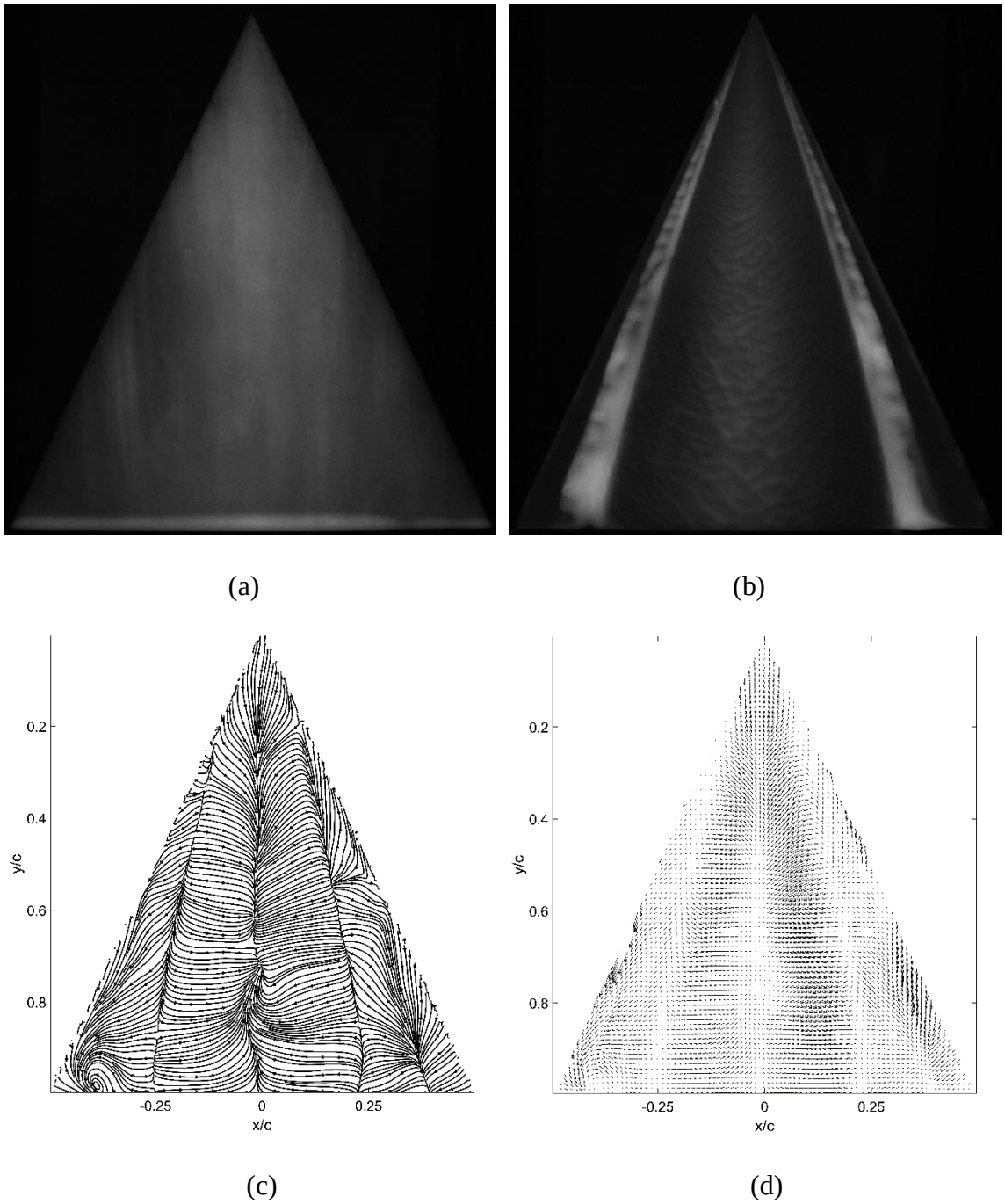

Figure 24: (a) initial image, (b) final image, (c) skin-friction lines, and (d) skin-friction vectors for step size of 5, 200 cSt oil and 20 superpositions

Figures 25 (a), (b), (c), and (d) are the initial luminescent oil image, the final luminescent oil image, the skin-friction line plot, and the skin-friction vector plot respectively for the case of a 65° delta wing at 13° AoA and an oil viscosity of 350 cSt.

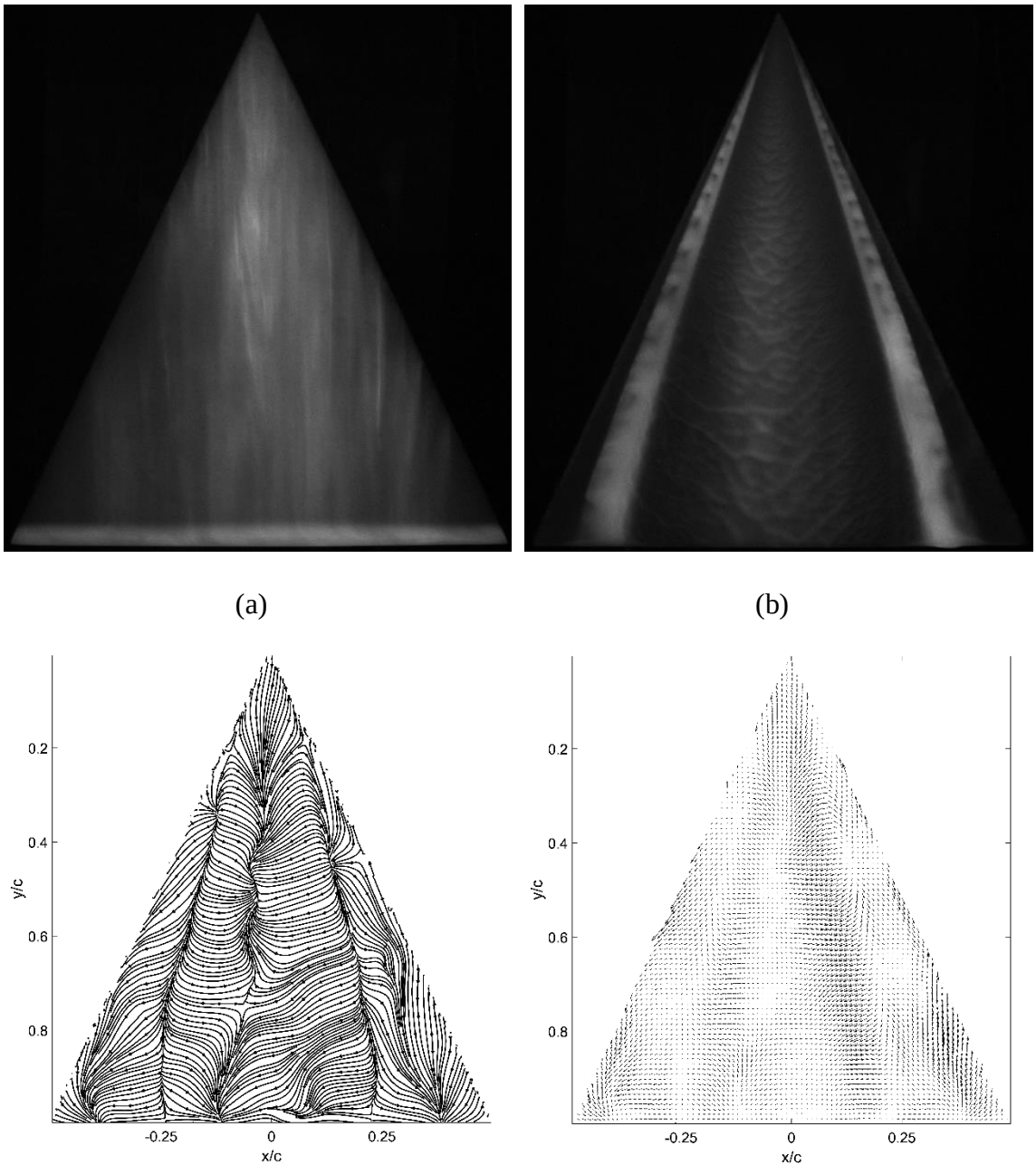

Figure 25: (a) initial image, (b) final image, (c) skin-friction lines, and (d) skin-friction vectors for step size of 5, 350 cSt oil and 20 superpositions

Figures 26 (a), (b), (c), and (d) are the initial luminescent oil image, the final luminescent oil image, the skin-friction line plot, and the skin-friction vector plot respectively for the case of a 65° delta wing at 13° AoA and an oil viscosity of 500 cSt.

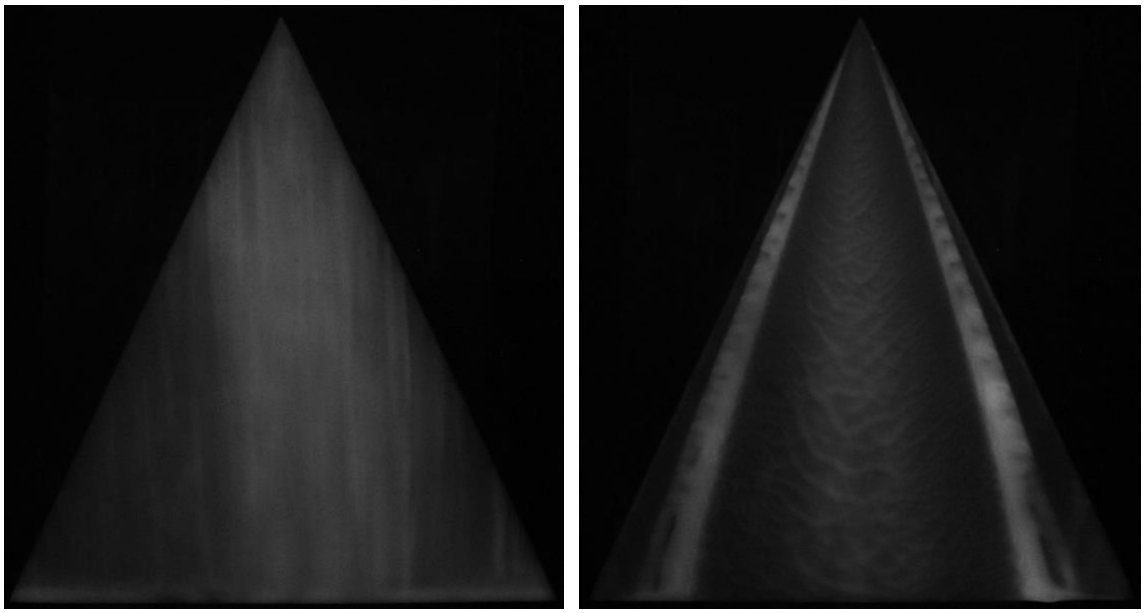

(a) (b)

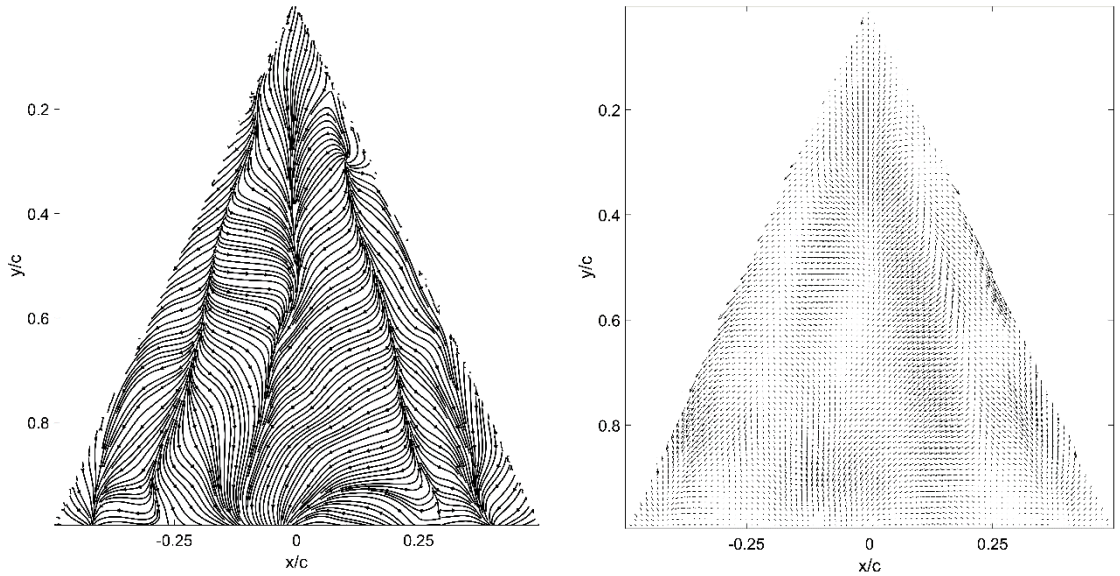

(c) (d)

Figure 26: (a) initial image, (b) final image, (c) skin-friction lines, and (d) skin-friction vectors for step size of 5, 500 cSt oil and 20 superpositions

Figures 27 (a), (b), (c), and (d) are the initial luminescent oil image, the final luminescent oil image, the skin-friction line plot, and the skin-friction vector plot respectively for the case of a 65° delta wing at 13° AoA and an oil viscosity of 1000 cSt.

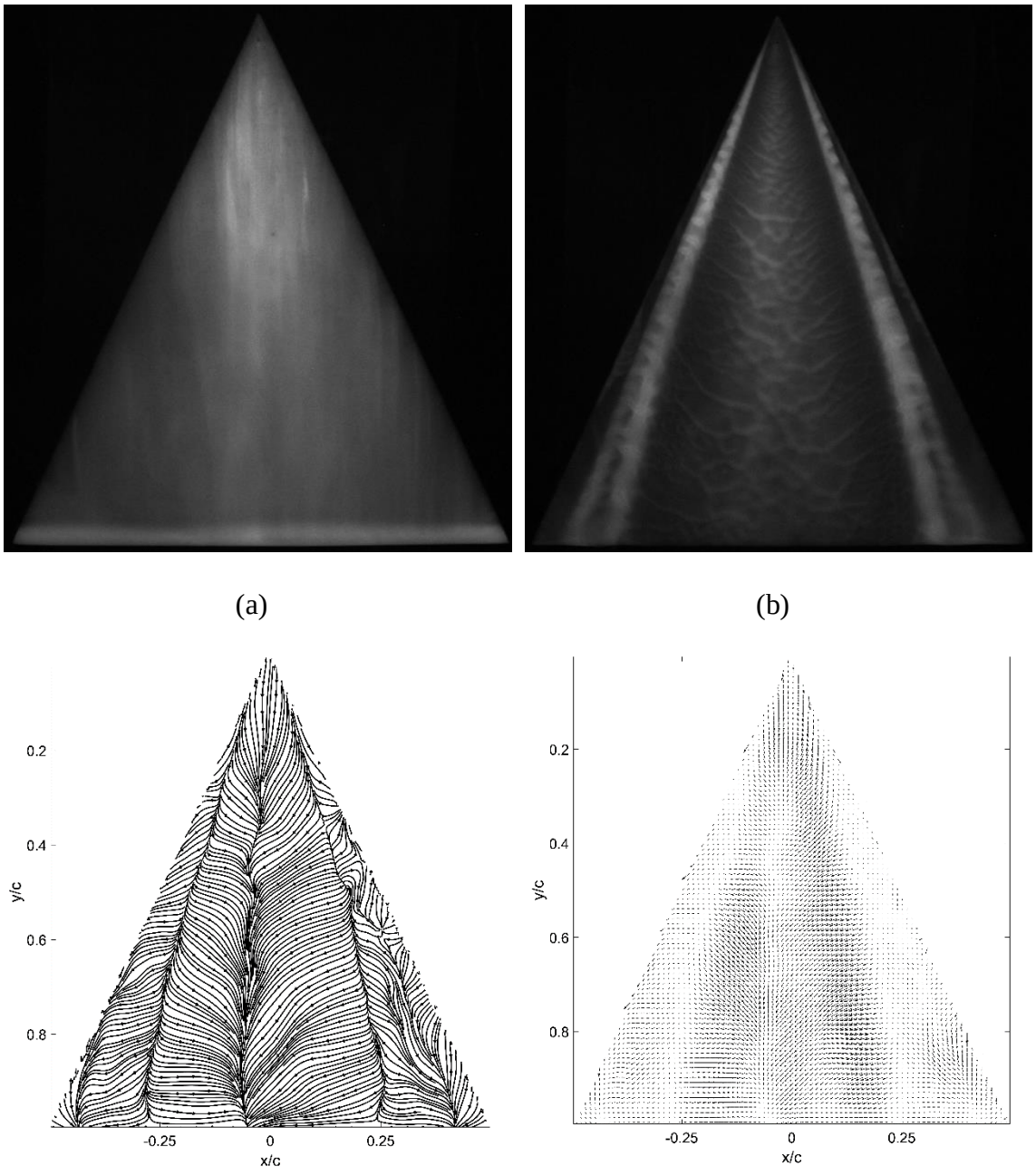

Figure 27: (a) initial image, (b) final image, (c) skin-friction lines, and (d) skin-friction vectors for step size of 5, 1000 cSt oil and 20 superpositions

Looking at Figures 22(b) and 23(b), it is evident that the oil-film did not develop symmetrically for oil at 50 and 100 cSt, thus eliminating these viscosities for the experiments conducted at a Reynolds number of 250,000. With a viscosity of 350, 500, and 1000 cSt, the primary reattachment line is largely asymmetric as seen in Figures 25(c), 26(c), and 27(c) respectively. The skin-friction topology and characteristics for the 200 cSt silicone oil has been mentioned earlier in the step size and sample size comparison.

Based on the findings above, the optimum step size, sample size, and oil viscosity is 5, 20, and 200 cSt respectively. These findings are based solely on observations, and shows that both step and sample sizes affect the extracted skin-friction fields. Therefore, these values should be chosen carefully for each unique experiment. In the following tests performed on the different delta wings, the Reynolds number is kept constant and therefore these variables were kept constant as well. This experimental study has also shown how the GLOF technique is able to extract skin-friction fields from a series of images, thus allowing researchers to better understand the interaction of flow over a surface.

DELTA WING RESULTS

Delta wings have a triangular planform and are most famously used in the Concorde, and the SR71 military aircraft. A tip vortex forms over the upper surface of the wing, thus enhancing lift. As the AoA is increased, the strength of the tip vortex also increases, which in turn energizes the flow over the surface and delaying flow separation. The delta wing is favorable in military aircrafts as it has a relatively high stall angle compared to conventional airfoils. The delta wing is also favorable for supersonic flight, as the wing's leading edge remains behind the shock cone.

For this thesis, delta wings with sweep angles of 50°, 55°, 60°, 65°, and 70° were machined by hand and placed in the wind tunnel. The GLOF technique was then applied and skin-friction fields were extracted from the images. The freestream velocity and Reynolds number were fixed at 20 meters per second and 250,000 respectively. The step size, sample size, and oil viscosity used for all experiments were also fixed at 5, 20, and 200 cSt as found in the parametric study. Each delta wing is then exposed to the flow at -5° AoA to 25° AoA, at an increment of 5° per run.

50° Delta Wing

The 50° delta wing has a chord length of 189mm and a span of 317mm. The 50° delta wing is considered a non-slender delta wing, and due to its size, generates a significant amount of drag at high angles of attack. The results are presented below.

Figures 28 (a), (b), (c), and (d) are the initial luminescent oil image, the final luminescent oil image, the skin-friction line plot, and the skin-friction vector plot respectively for the case of a 50° delta wing at -5° AoA.

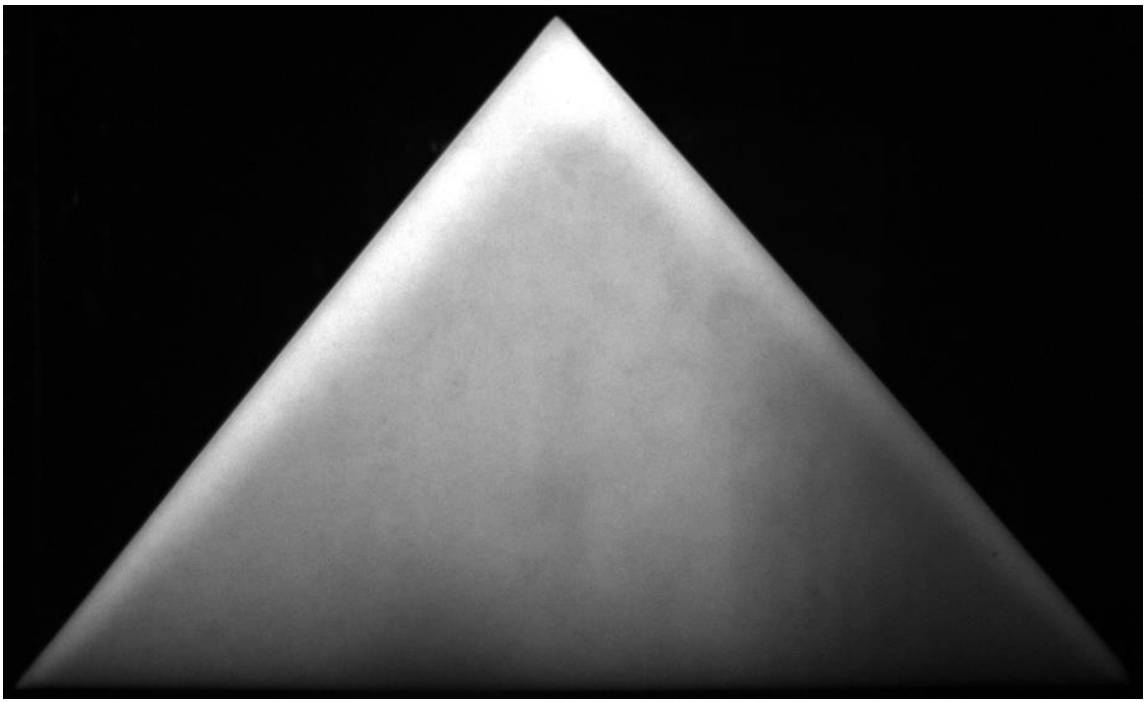

(a)

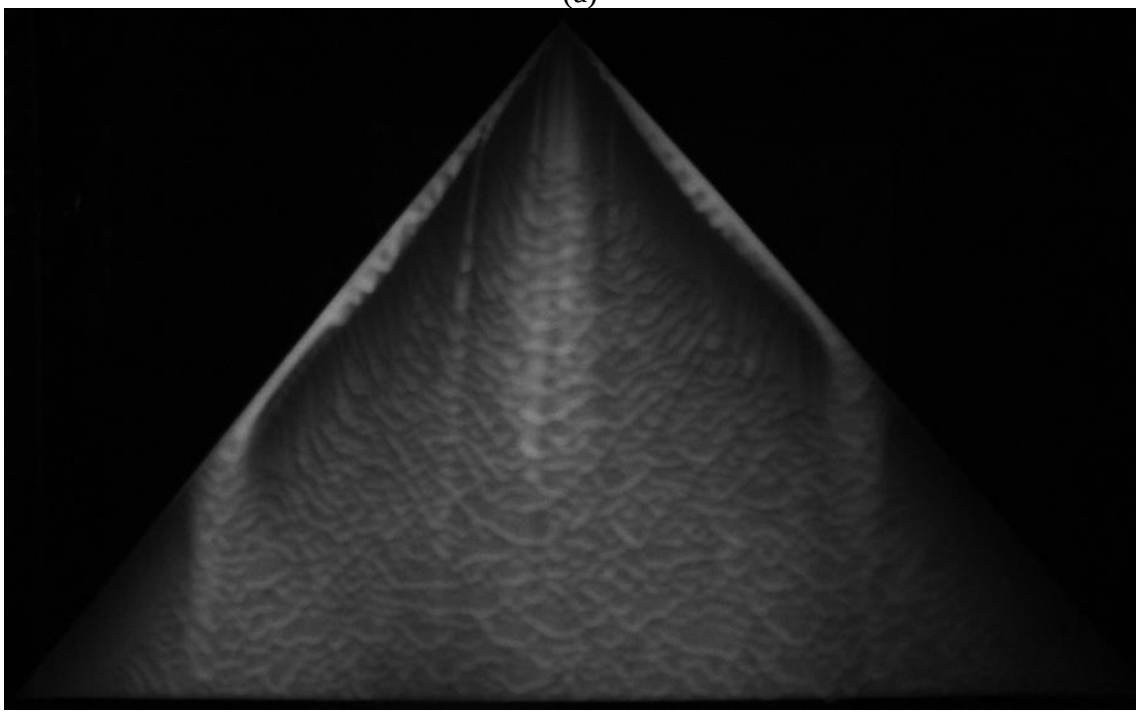

(b)

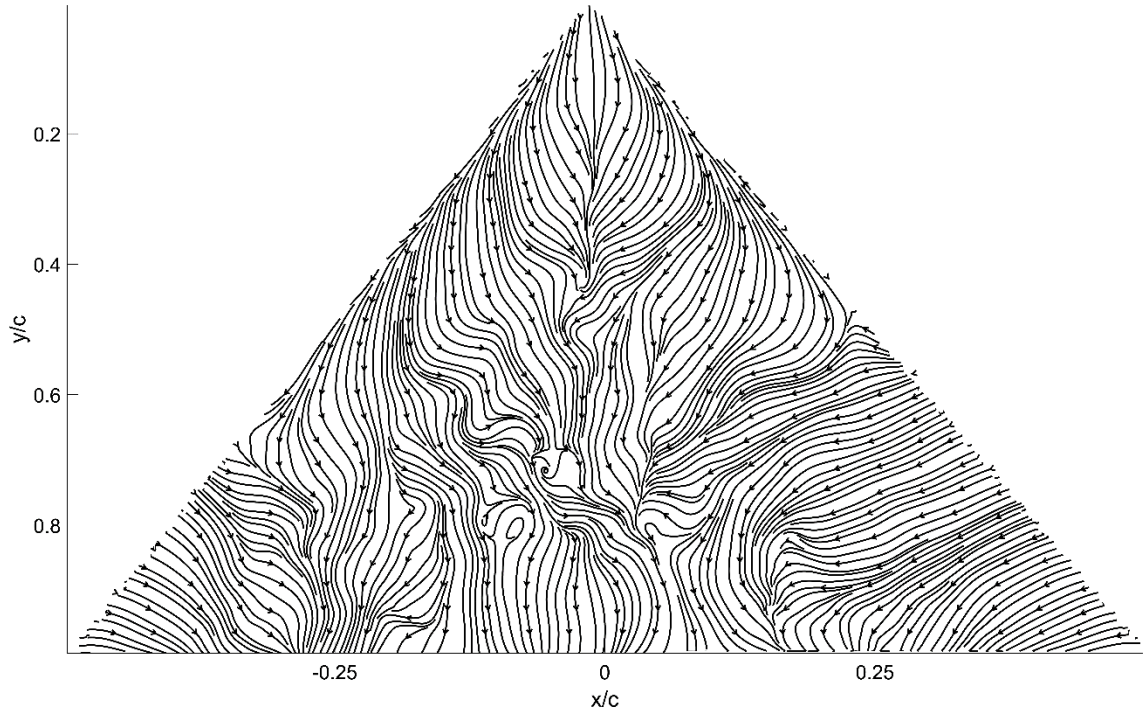

(c)

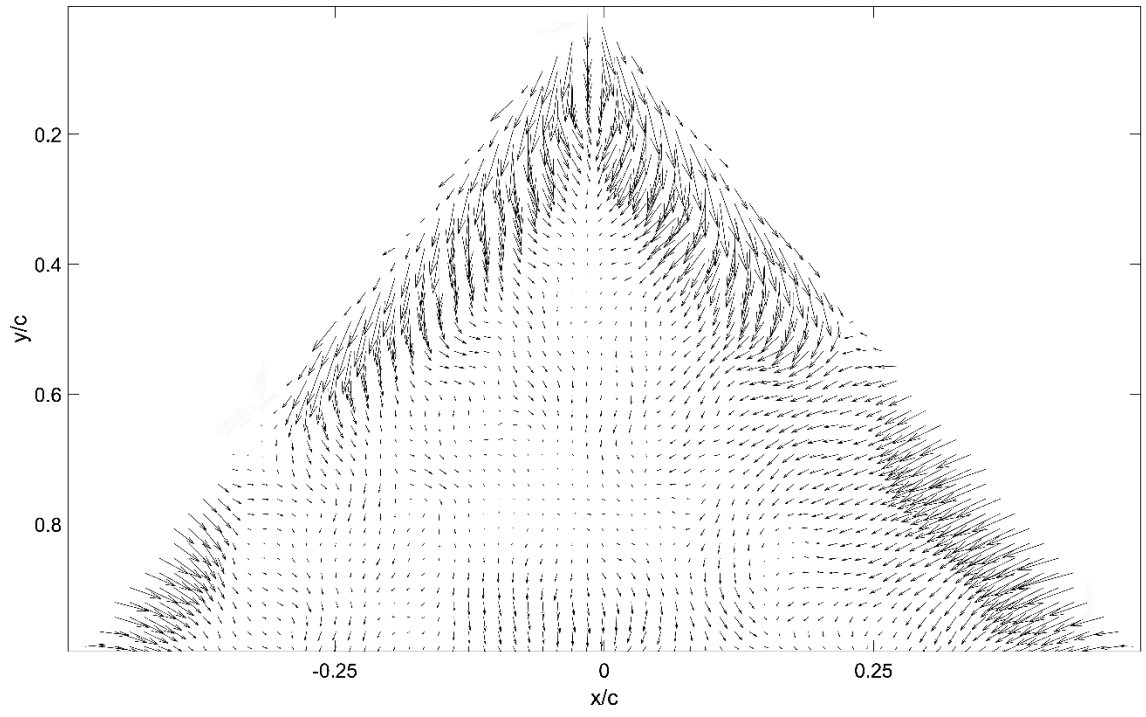

(d)

Figure 28: (a) initial image, (b) final image, (c) skin-friction lines, and (d) skin-friction vectors for 50° delta wing at -5° AoA

Figures 29 (a), (b), (c), and (d) are the initial luminescent oil image, the final luminescent oil image, the skin-friction line plot, and the skin-friction vector plot respectively for the case of a 50° delta wing at 0° AoA.

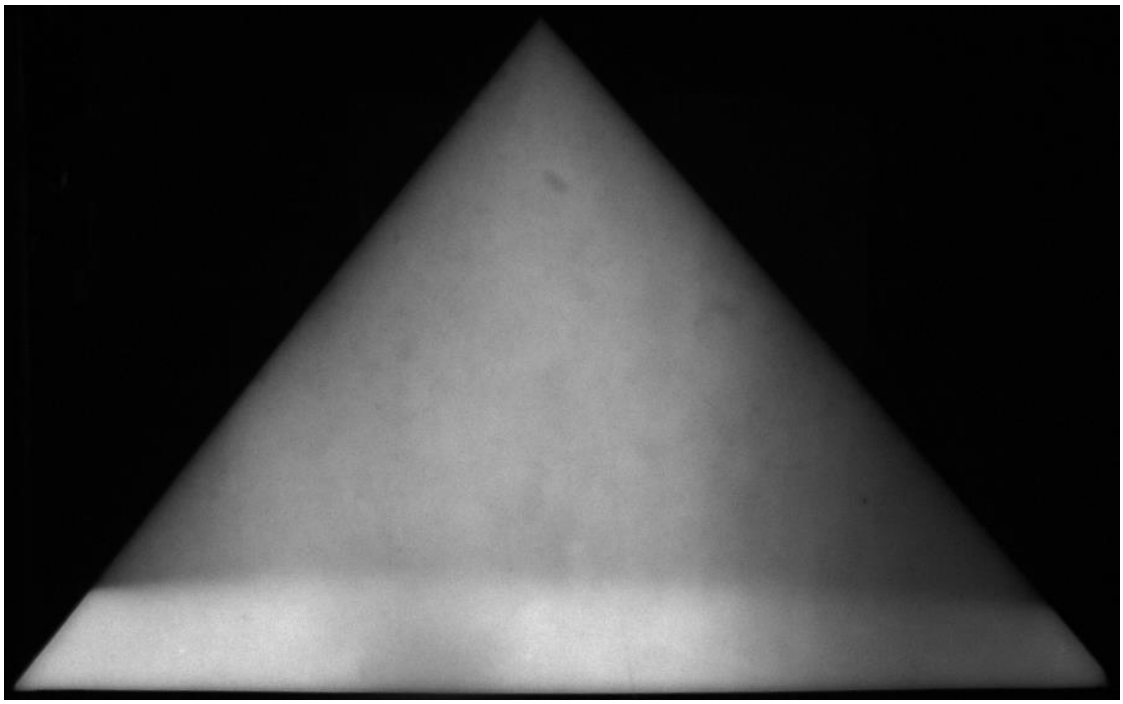

(a)

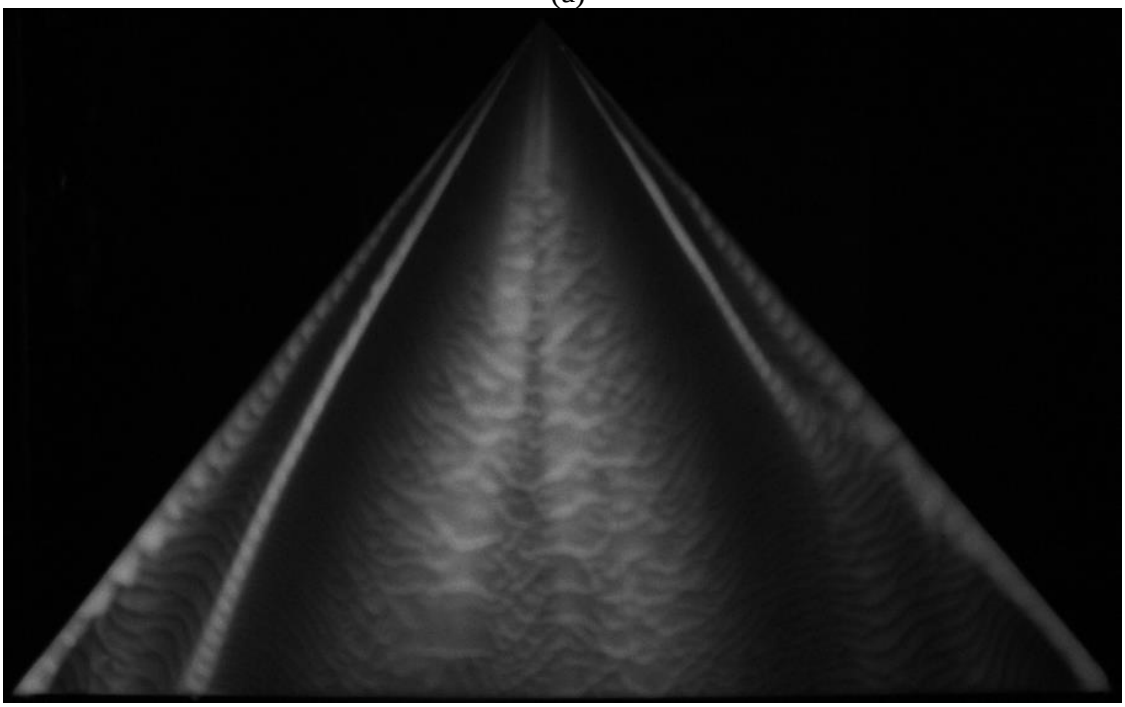

(b)

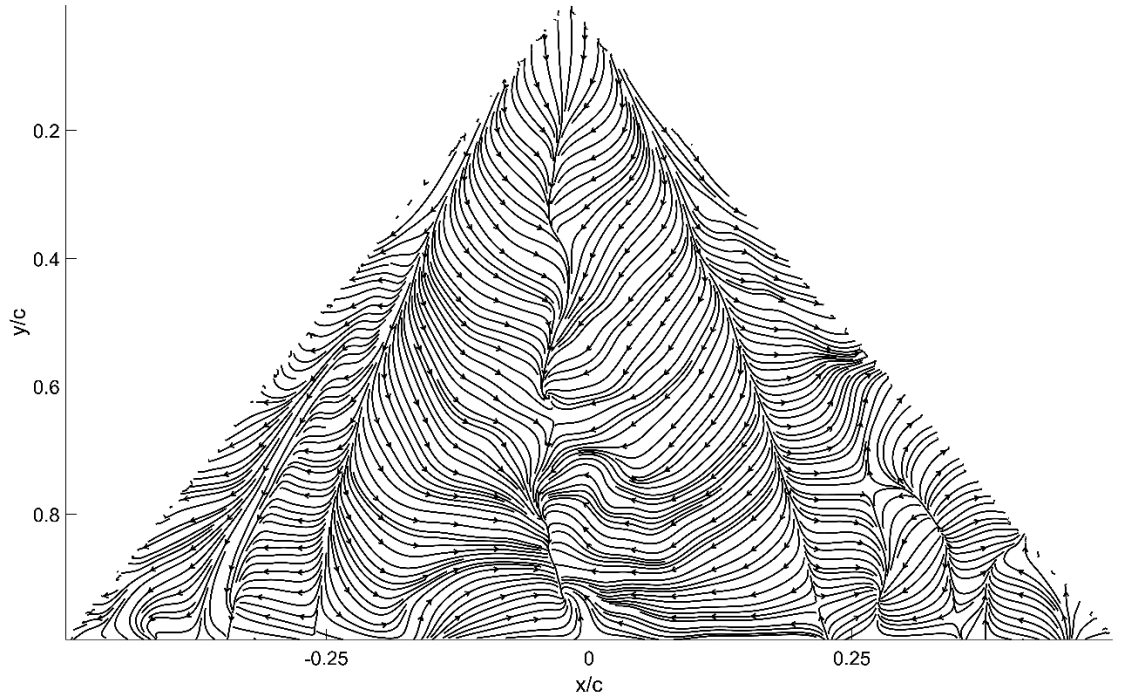

(c)

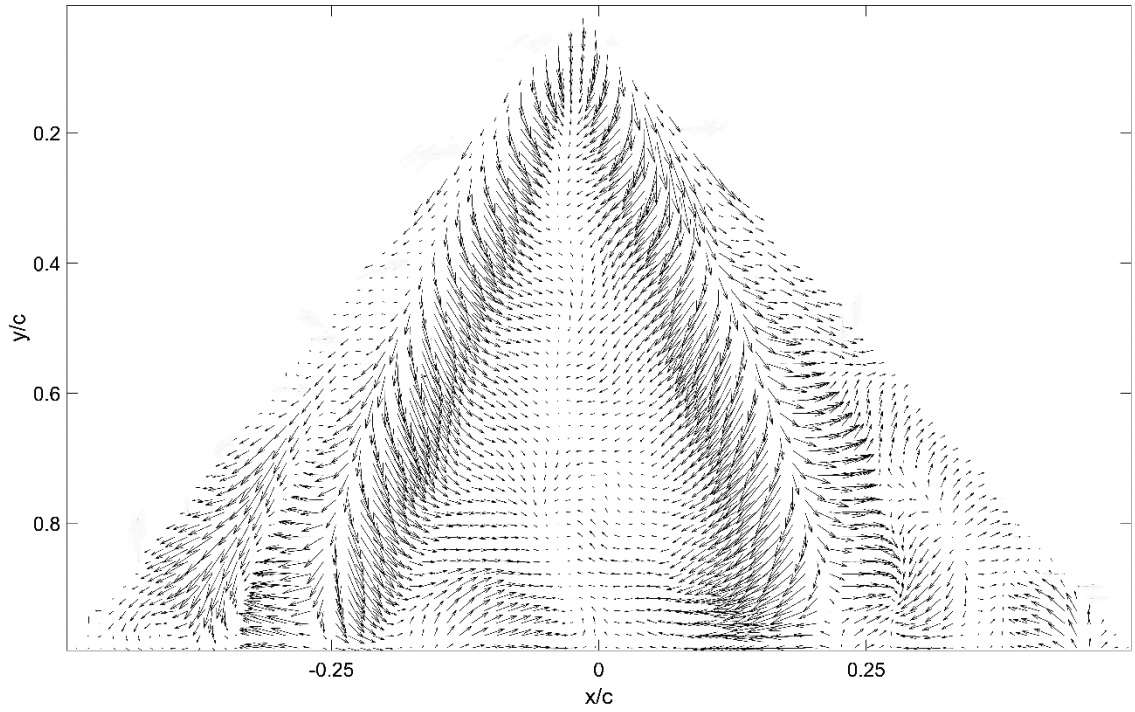

(d)

Figure 29: (a) initial image, (b) final image, (c) skin-friction lines, and (d) skin-friction vectors for 50° delta wing at 0° AoA

Figures 30 (a), (b), (c), and (d) are the initial luminescent oil image, the final luminescent oil image, the skin-friction line plot, and the skin-friction vector plot respectively for the case of a 50° delta wing at 5° AoA.

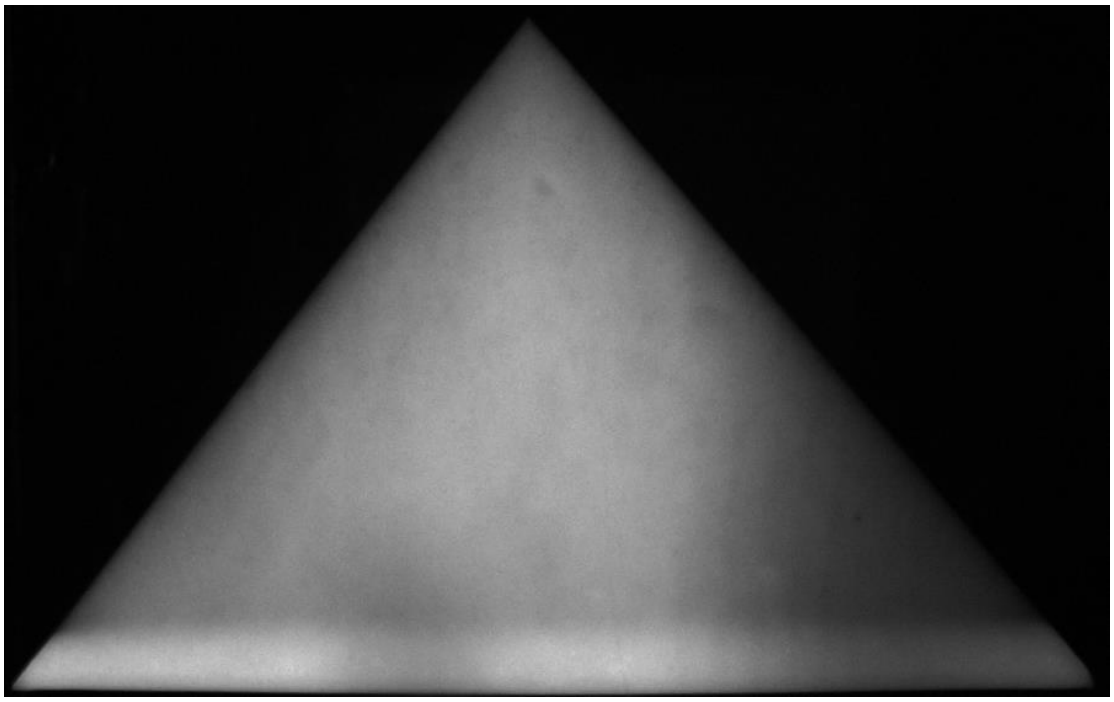

(a)

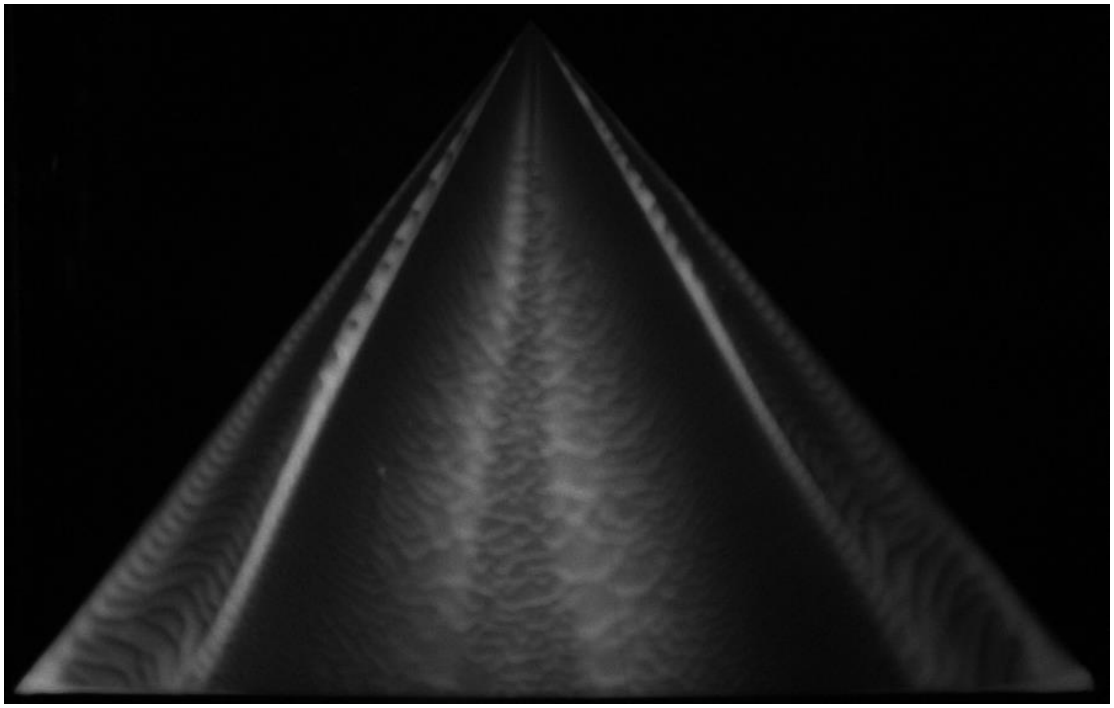

(b)

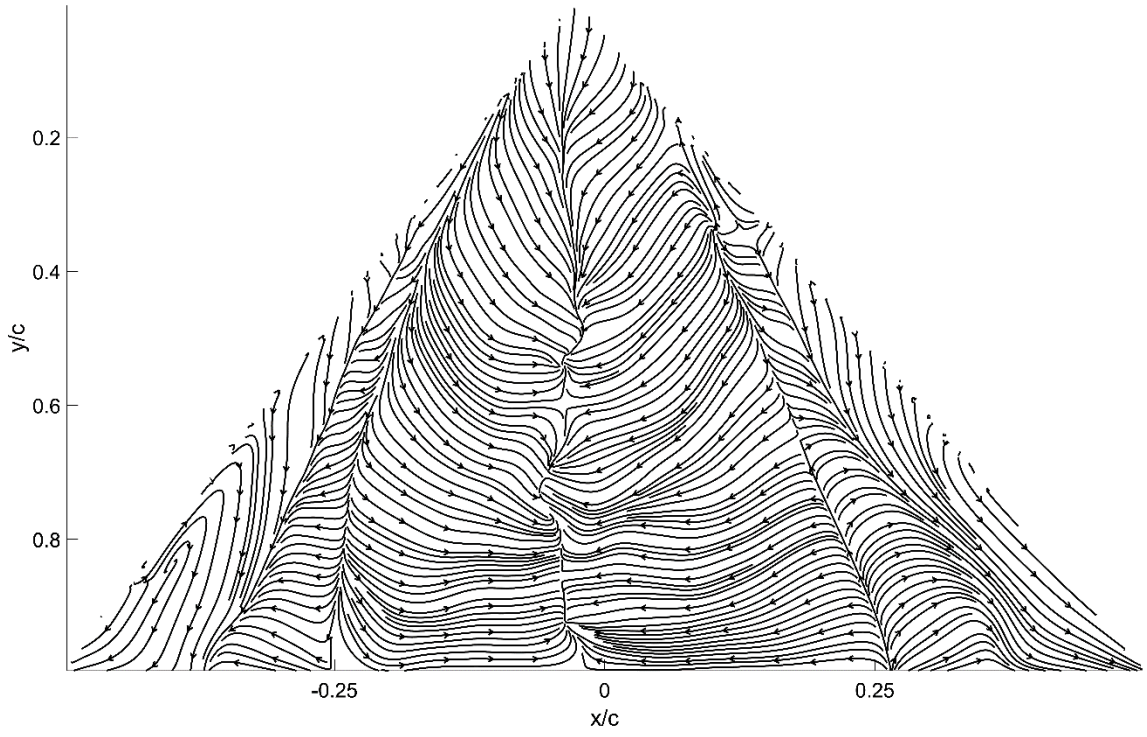

(c)

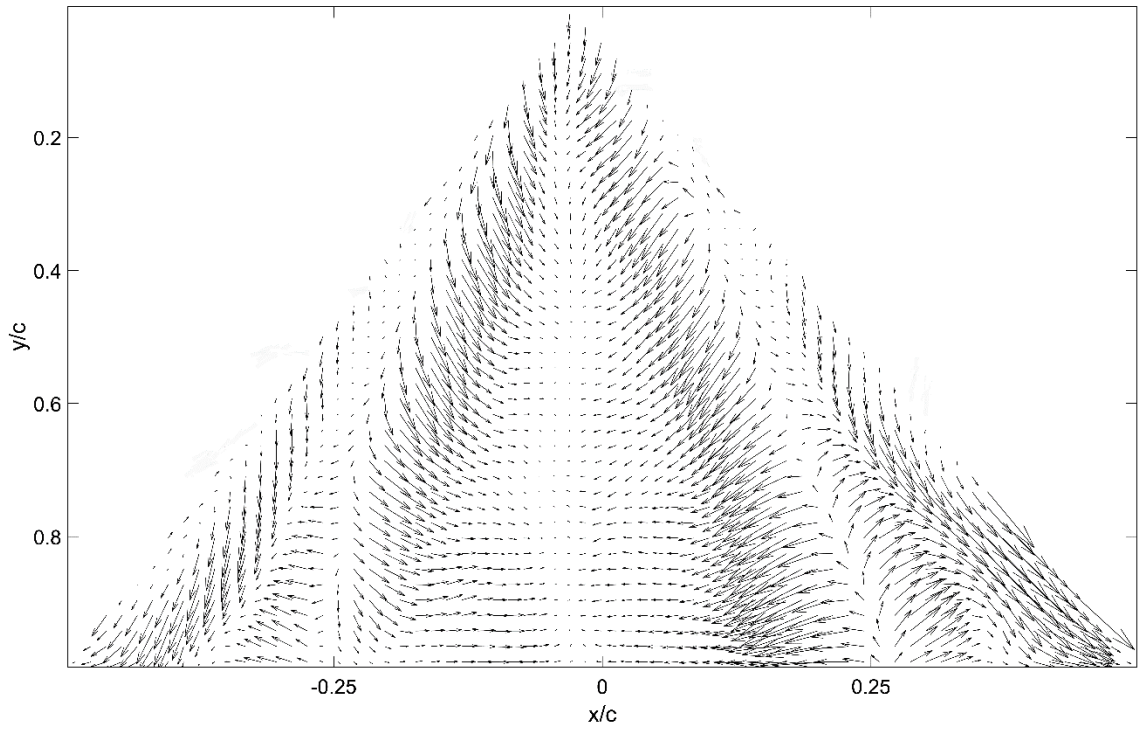

(d)

Figure 30: (a) initial image, (b) final image, (c) skin-friction lines, and (d) skin-friction vectors for 50° delta wing at 5° AoA

Figures 31 (a), (b), (c), and (d) are the initial luminescent oil image, the final luminescent oil image, the skin-friction line plot, and the skin-friction vector plot respectively for the case of a 50° delta wing at 10° AoA.

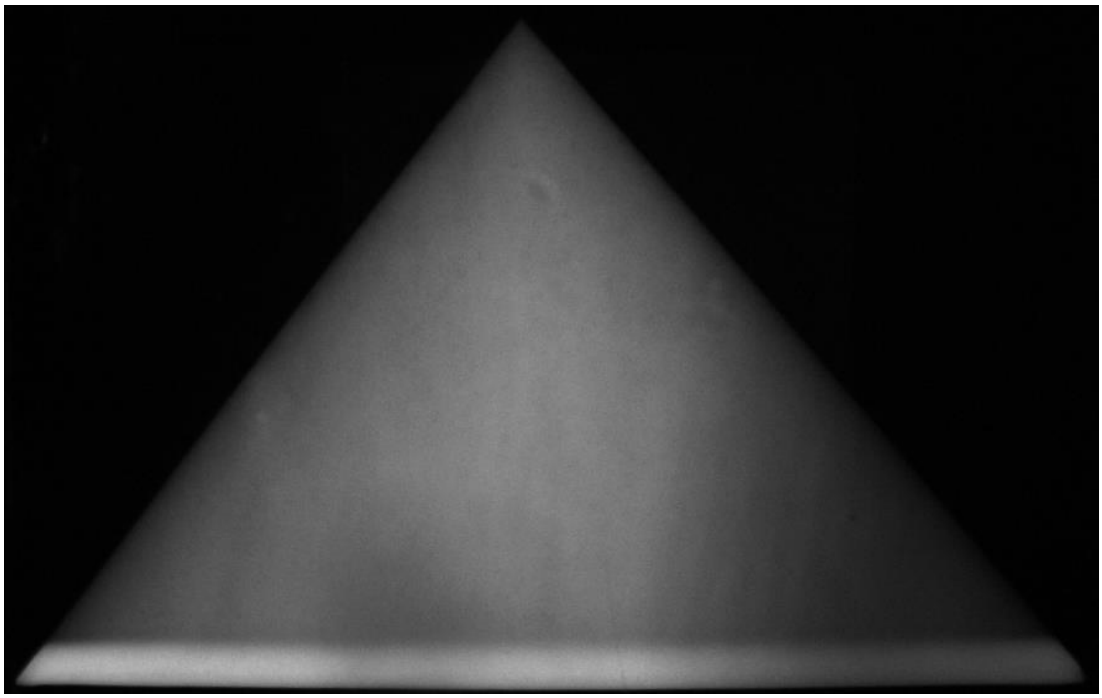

(a)

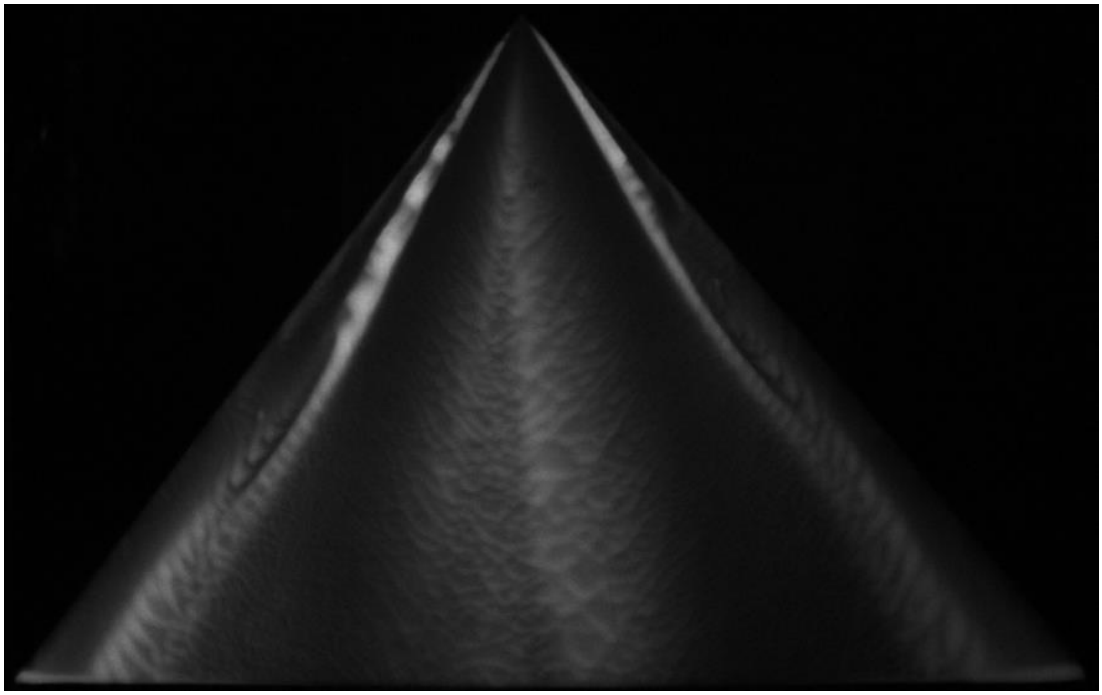

(b)

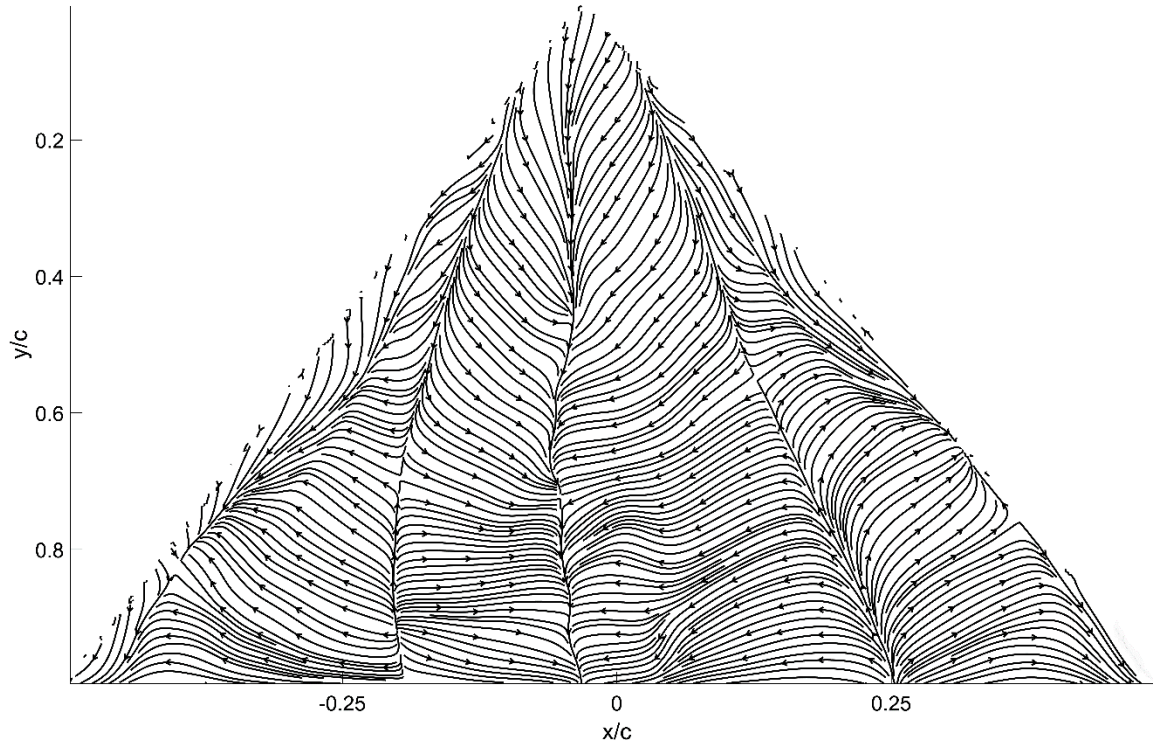

(c)

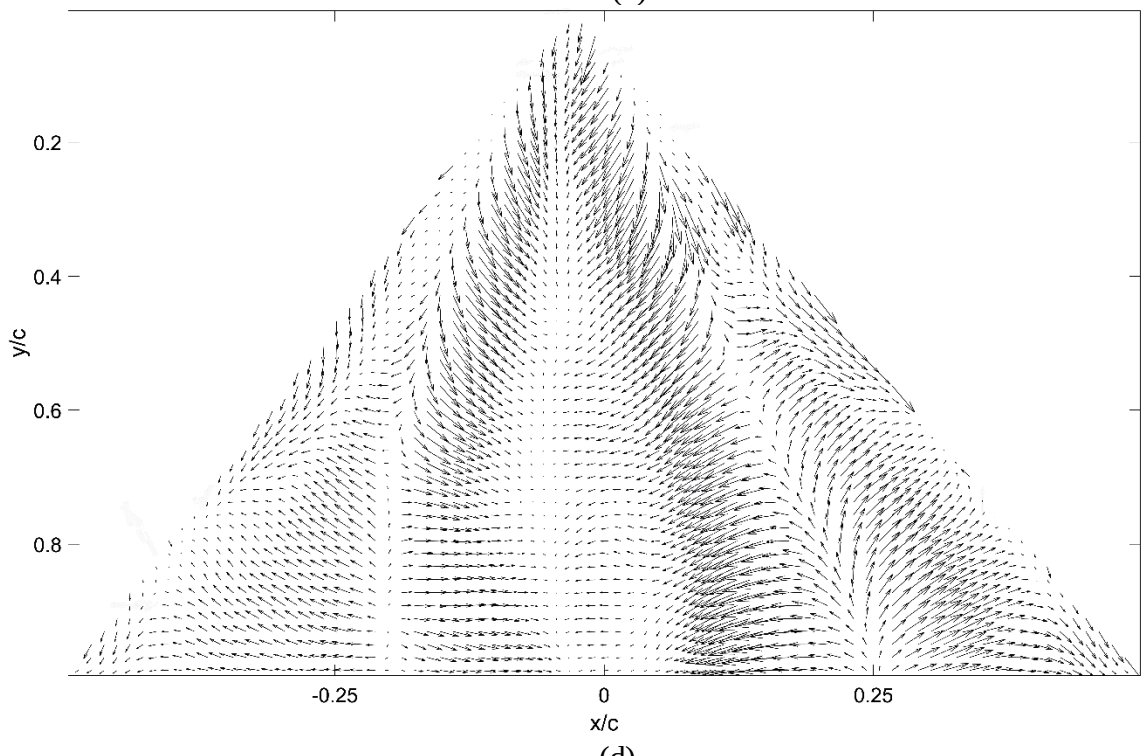

(d)

Figure 31: (a) initial image, (b) final image, (c) skin-friction lines, and (d) skin-friction vectors for 50° delta wing at 10° AoA

Figures 32 (a), (b), (c), and (d) are the initial luminescent oil image, the final luminescent oil image, the skin-friction line plot, and the skin-friction vector plot respectively for the case of a 50° delta wing at 15° AoA.

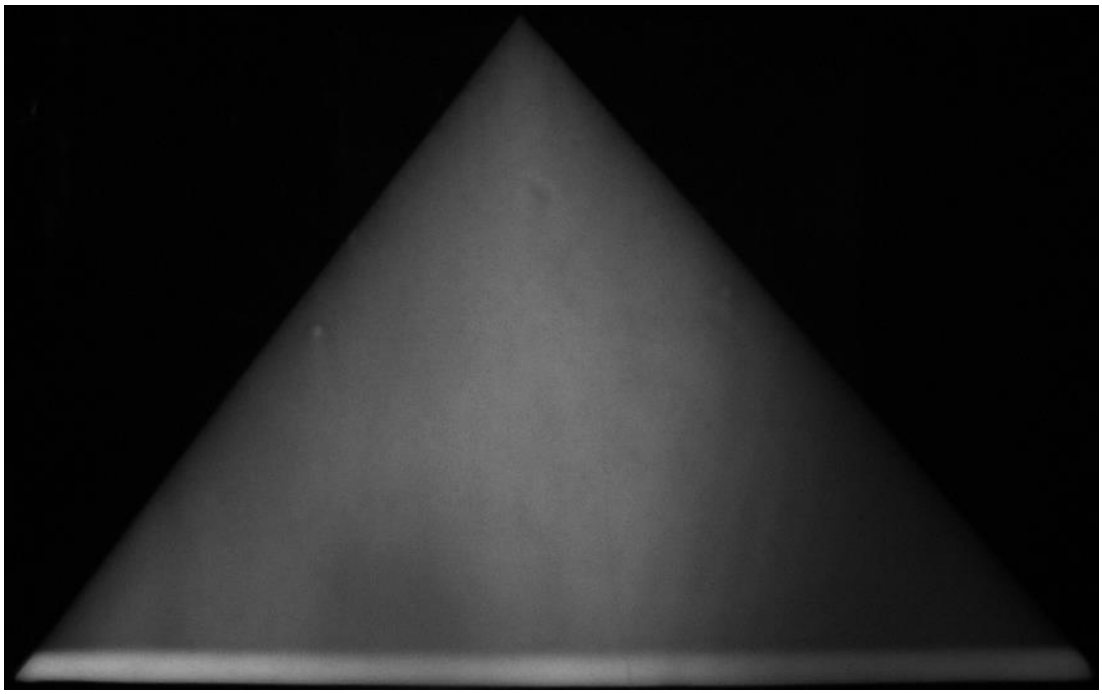

(a)

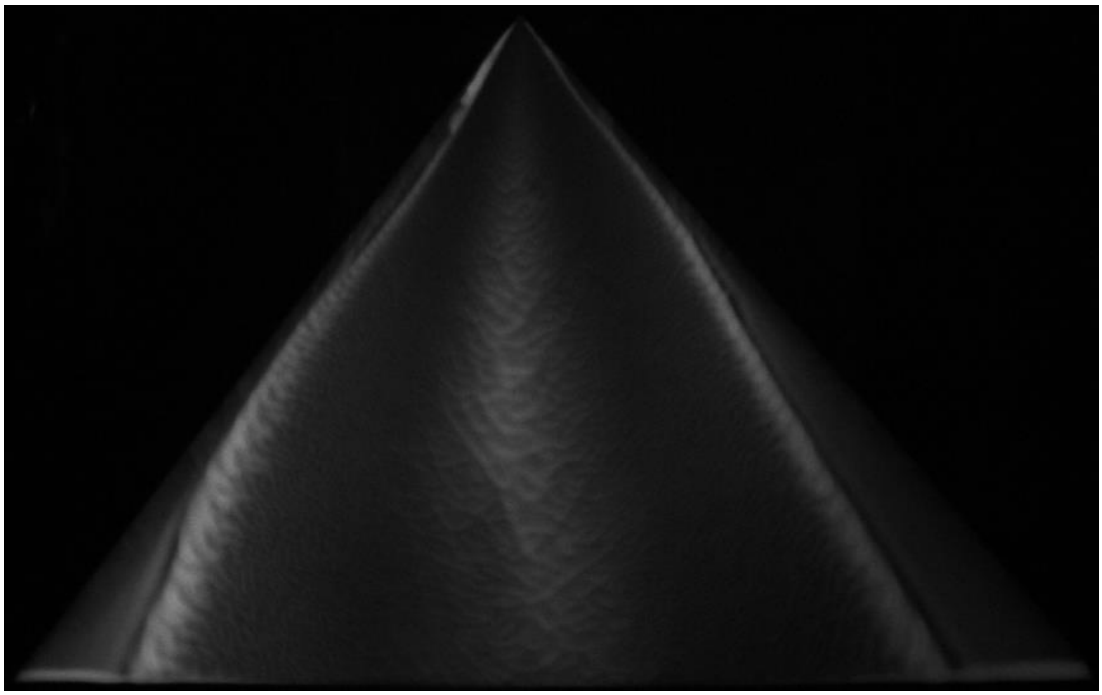

(b)

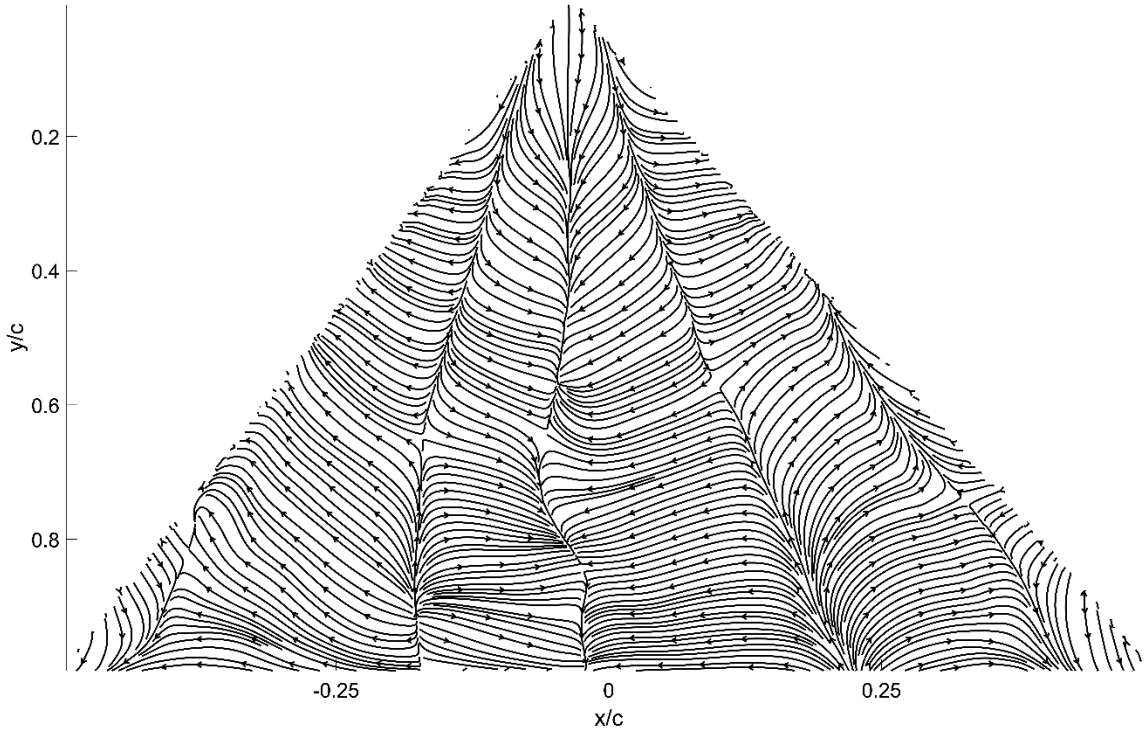

(c)

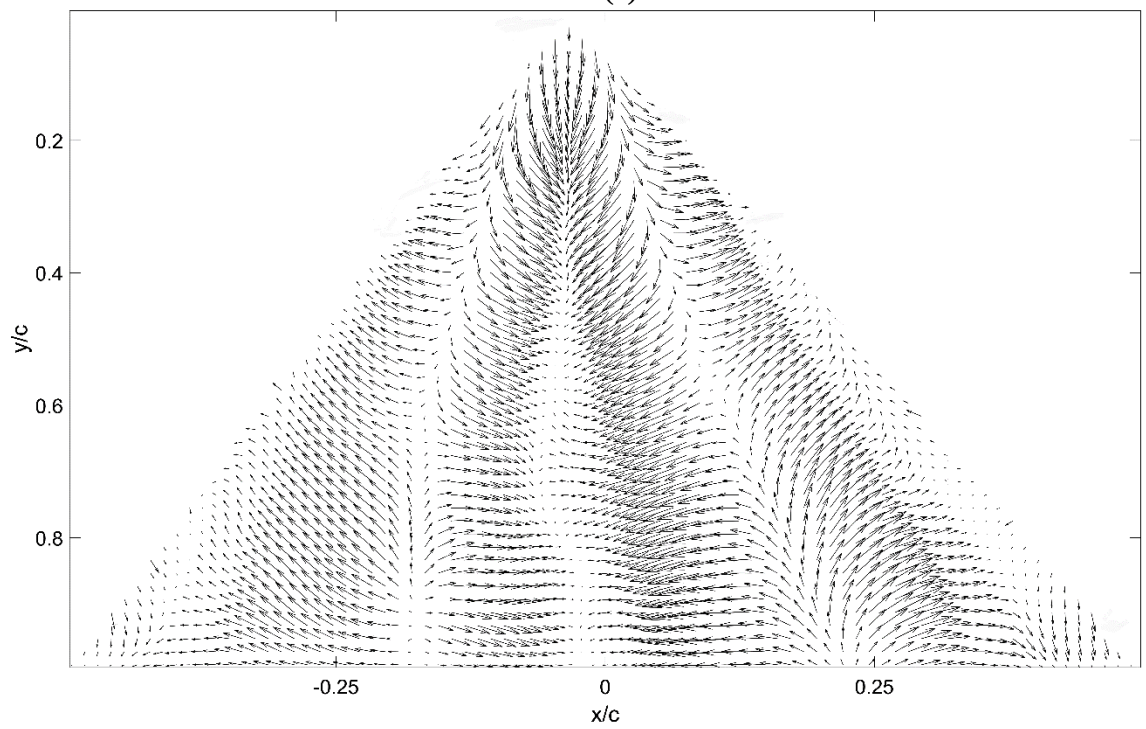

(d)

Figure 32: (a) initial image, (b) final image, (c) skin-friction lines, and (d) skin-friction vectors for 50° delta wing at 15° AoA

Figures 33 (a), (b), (c), and (d) are the initial luminescent oil image, the final luminescent oil image, the skin-friction line plot, and the skin-friction vector plot respectively for the case of a 50° delta wing at 20° AoA.

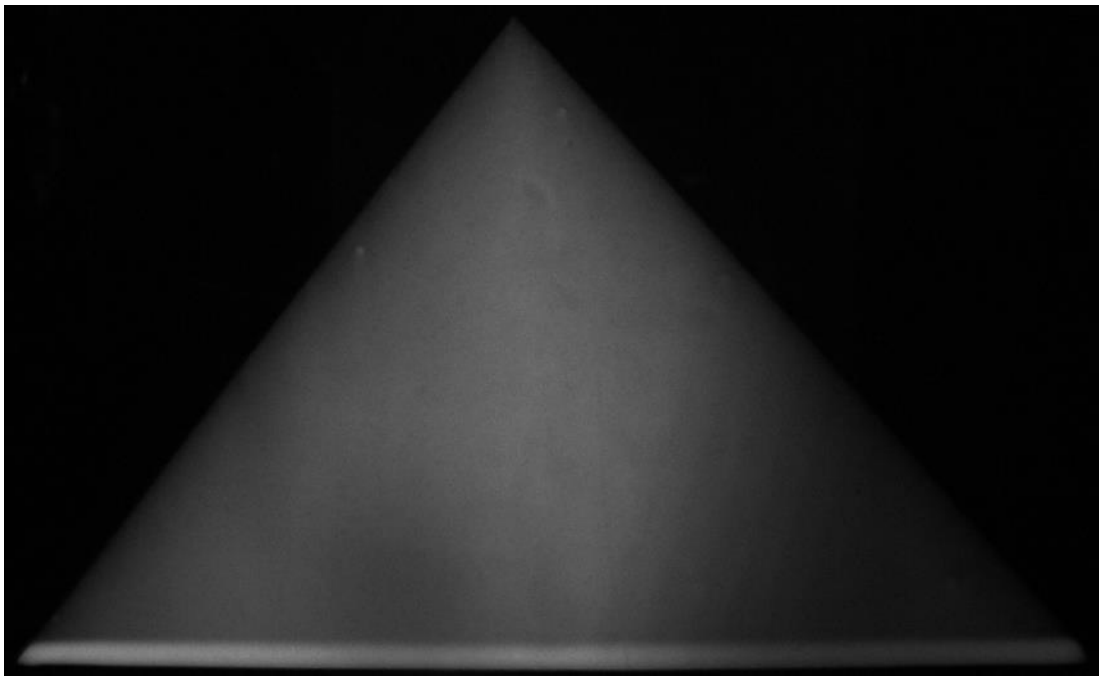

(a)

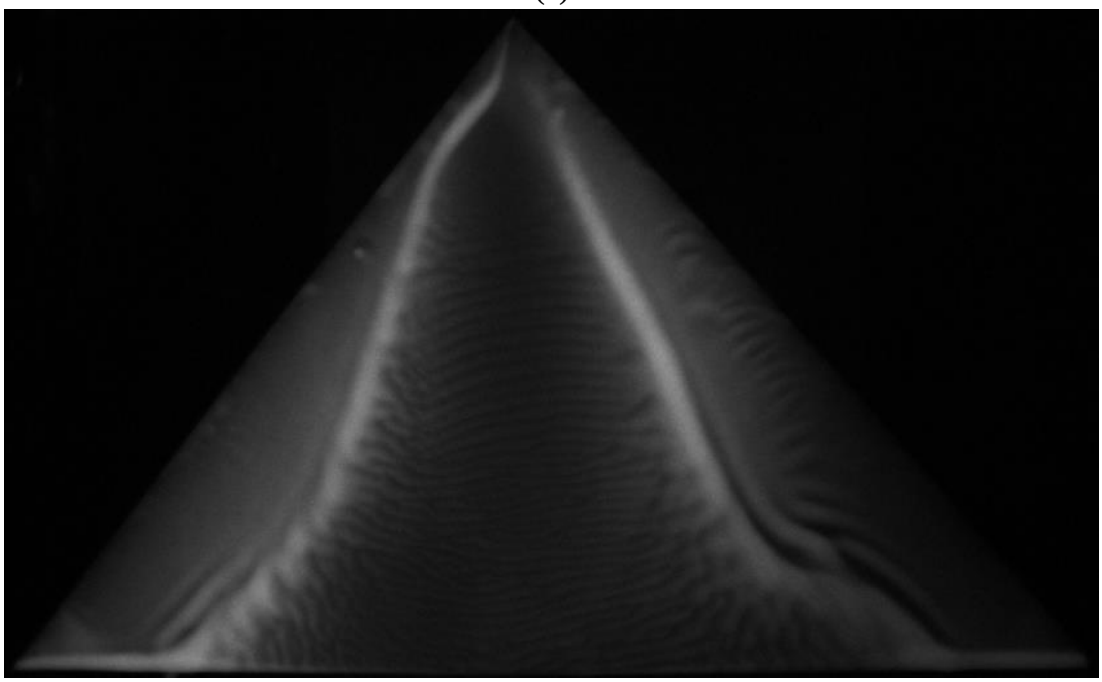

(b)

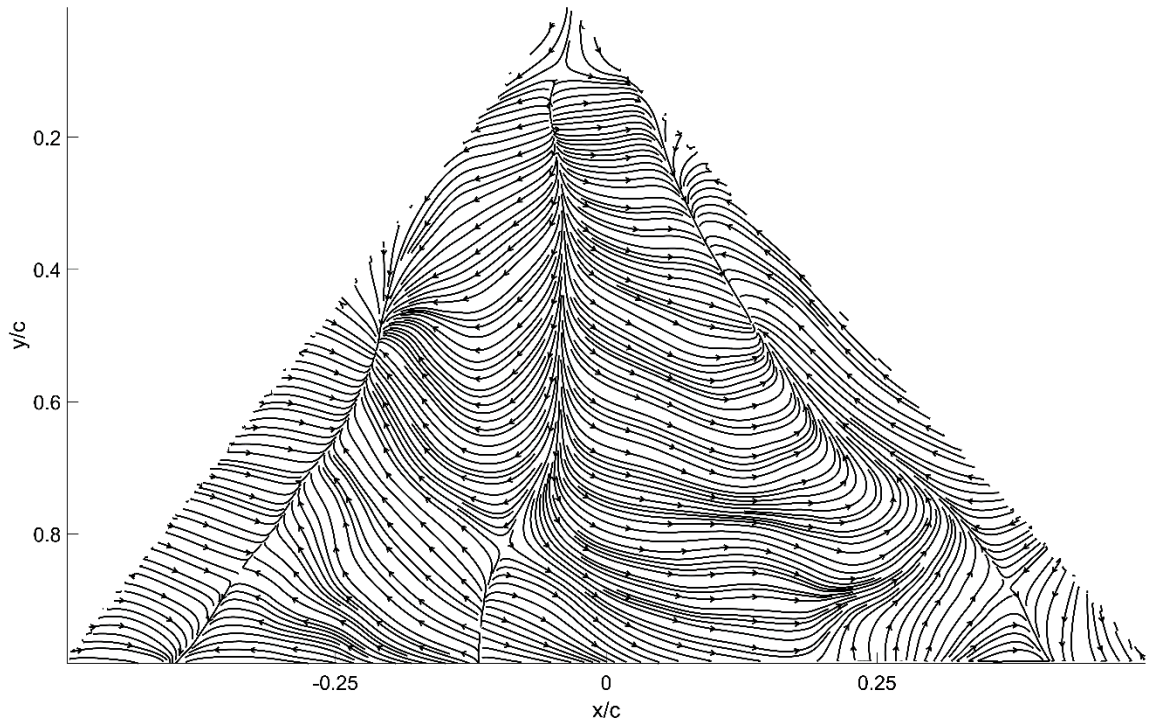

(c)

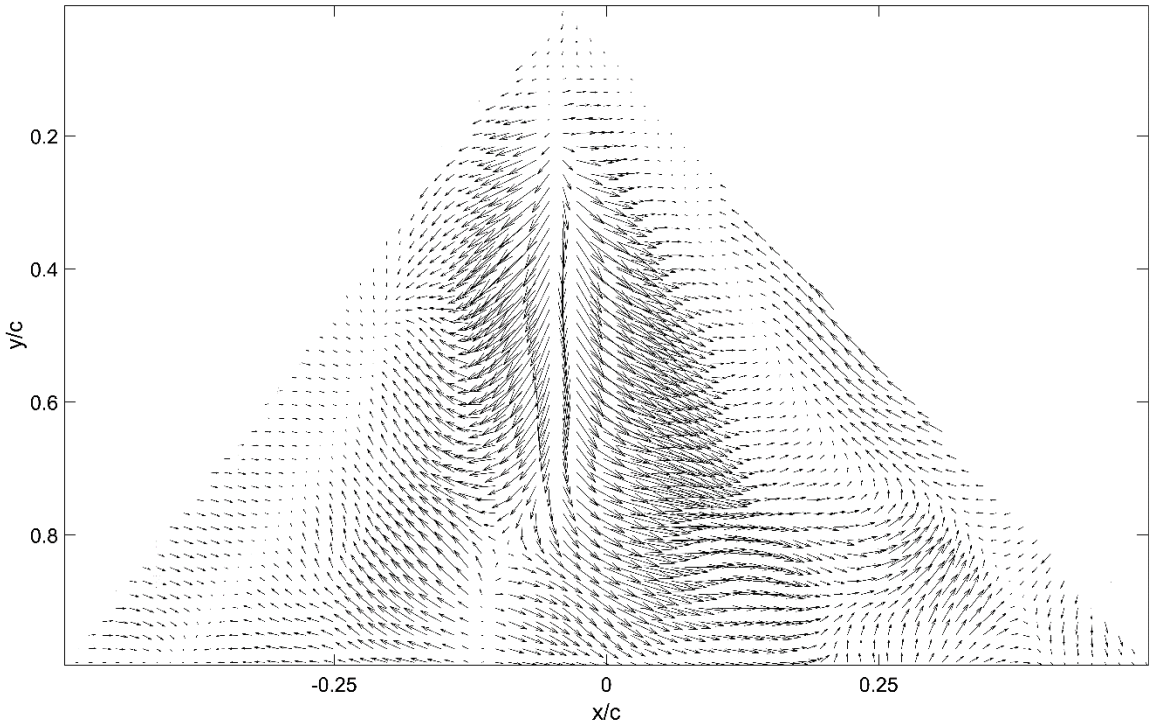

(d)

Figure 33: (a) initial image, (b) final image, (c) skin-friction lines, and (d) skin-friction vectors for 50° delta wing at 20° AoA

Figures 34 (a), (b), (c), and (d) are the initial luminescent oil image, the final luminescent oil image, the skin-friction line plot, and the skin-friction vector plot respectively for the case of a 50° delta wing at 25° AoA.

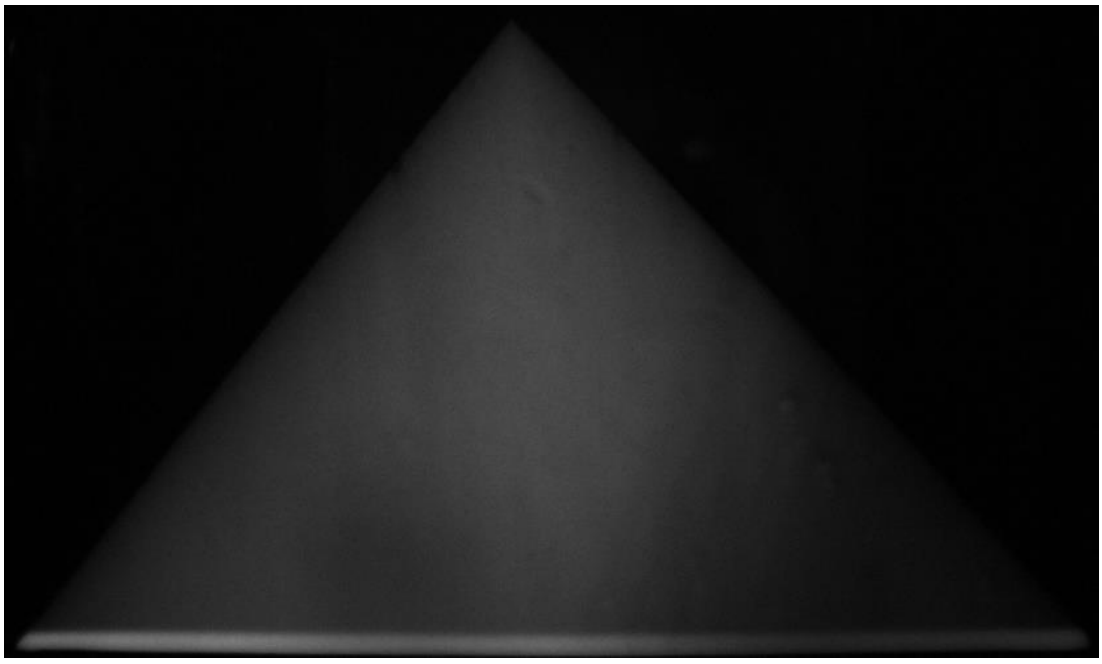

(a)

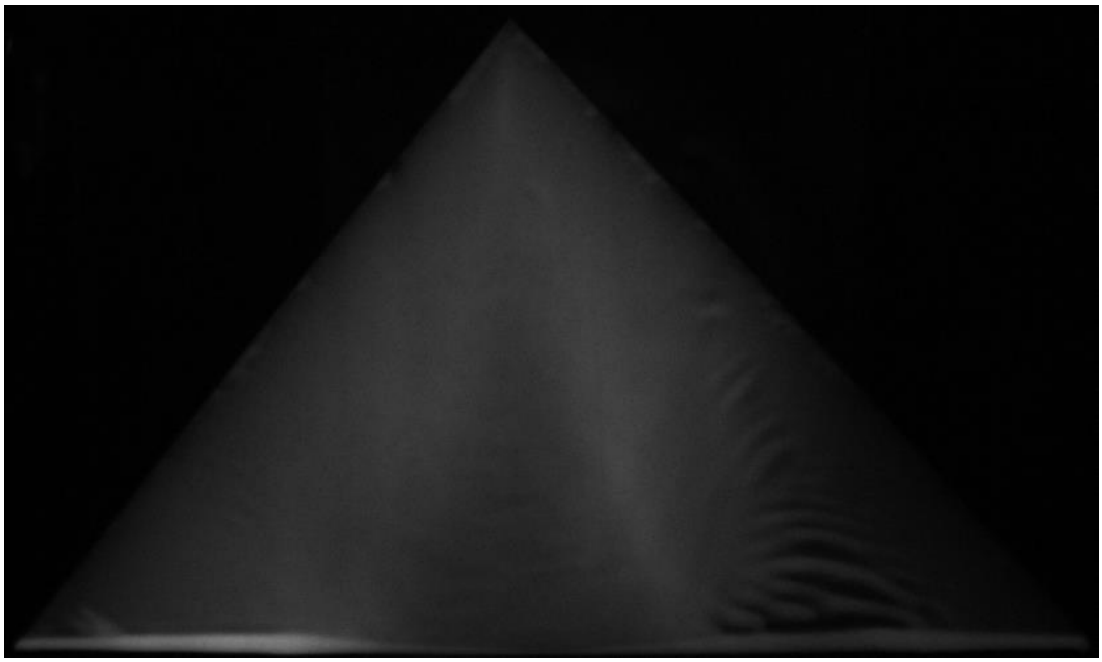

(b)

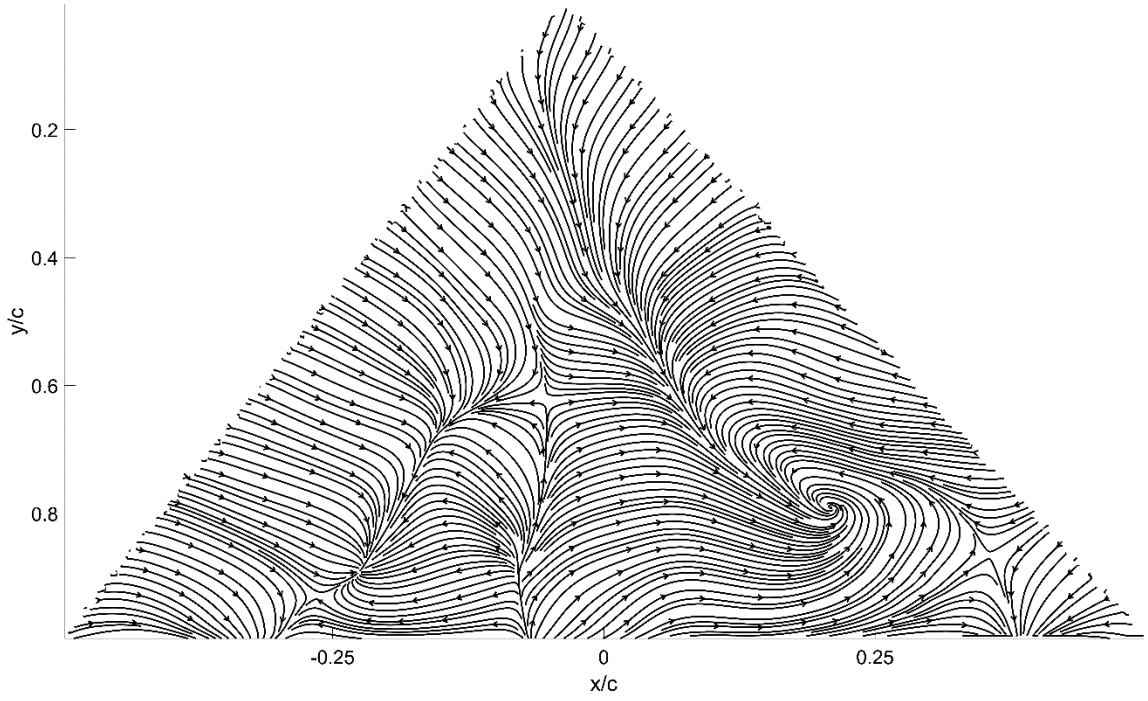

(c)

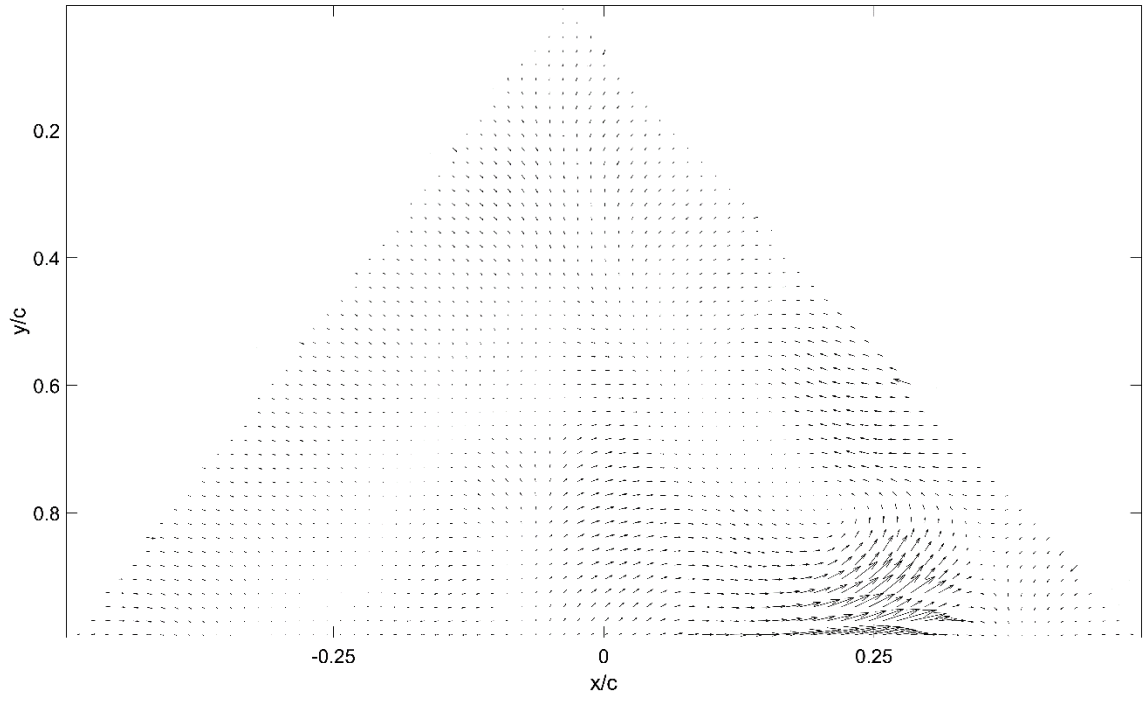

(d)

Figure 34: (a) initial image, (b) final image, (c) skin-friction lines, and (d) skin-friction vectors for 50° delta wing at 25° AoA

As expected for the negative AoA, there is a lack of pattern in the skin-friction lines due to the lack of a tip vortex, which is critical in delta wing aerodynamics. The lines in Figure 28 (c) are generally random and Figure 28 (d) shows that there is little interaction between the flow and the oil at the center of the surface. Likewise, with the 0° AoA, there is a weak tip vortex as seen in Figure 29 (c). The absence of a clear and relatively straight primary reattachment line supports this observation. Two saddle points are formed at y/c = 0.65 and x/c = -0.05 for the first one, and y/c = 0.75 and x/c = 0.3 for the second one. The secondary separation line can be seen clearly at around x/c = -0.25 and 0.25 as the weak tip vortex still induces wing-tip vortices, thus making the oil move in opposite directions. For the case of 5° AoA in Figure 30 (c), the two saddle points moved upwards due to a stronger tip vortex, and their location are at y/c = 0.6, x/c = -0.05 and at y/c = 0.4, x/c = 0.18. A stronger tip vortex also induces stronger wing-tip vortices, and can be substantiated with the presence of clear primary reattachment, secondary separation, and secondary reattachment lines. In the case of the 10° AoA in Figure 31 (c), the secondary reattachment lines disappear from the topology, but one can clearly see the location of the vortex breakdown by the presence of saddle points on the secondary separation lines. These are found at y/c = 0.7, x/c = -0.2, and at y/c = 0.6, x/c = 0.2. Chen and Wang [27] performed a numerical simulation for a 50° delta wing at a Reynolds number of 274,000 and an 8° AoA, and found that the vortex core is located at y/c = 0.65 on the left, and at y/c = 0.63 on the right. This roughly coincides with what was observed for the 10° case, and the variance can be attributed to the difference in Reynolds number.

For the 15° case in Figure 32 (c), an interesting observation made is the presence of the secondary separation very near the edge, at x/c = -0.45 and x/c = 0.45. In addition, the number of saddle points increased to a total of five, one each at the primary separation, secondary

reattachment, and secondary separation lines. These are located at y/c = 0.85, 0.65, 0.65, 0.6, 0.75 and x/c = -0.45, -0.2, -0.09, 0.15, 0.35 respectively. At 20° and 25° AoA, the line down the center of the delta wing becomes a primary reattachment line instead of a primary separation line in the previous cases. Intuitively this makes sense as at these high AoA, flow separation occurs. For the 20° AoA in Figure 33 (c), the number of saddle points reduces to 4 and these occur at y/c = 0.85, 0.8, 0.9, and x/c = -0.35, -0.1, 0.35 respectively. One special saddle point is found at y/c = 0.1 right down the middle, and this could indicate the location of the tip vortex. Non-slender delta wing aerodynamics has stated that the primary vortex forms closer to the surface thus creating a stronger interaction between the vortices and the boundary layer of the wing. At 25°, the flow is completely separated and can be seen in the lack of change between Figures 34 (a) and (b). An interesting vortex can be seen in Figure 34 (c) due to the flow separation, and the primary reattachment and secondary separation lines cannot be seen all the way through, from the leading edge to the trailing edge.

55° Delta Wing

The 55° delta wing has a chord length of 189mm and a span of 265mm. Unfortunately, there have been no research or publications done on this specific sweep angle. Therefore, the results will be derived purely from observations and compared to the results for the 50° delta wing.

Figures 35 (a), (b), (c), and (d) are the initial luminescent oil image, the final luminescent oil image, the skin-friction line plot, and the skin-friction vector plot respectively for the case of a 55° delta wing at -5° AoA.

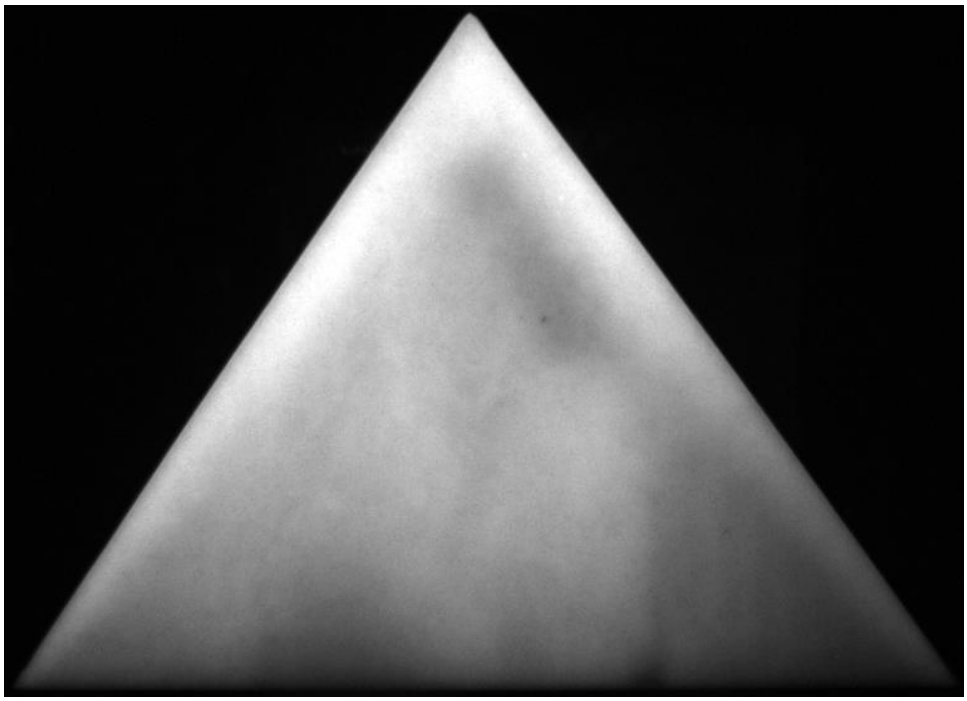

(a)

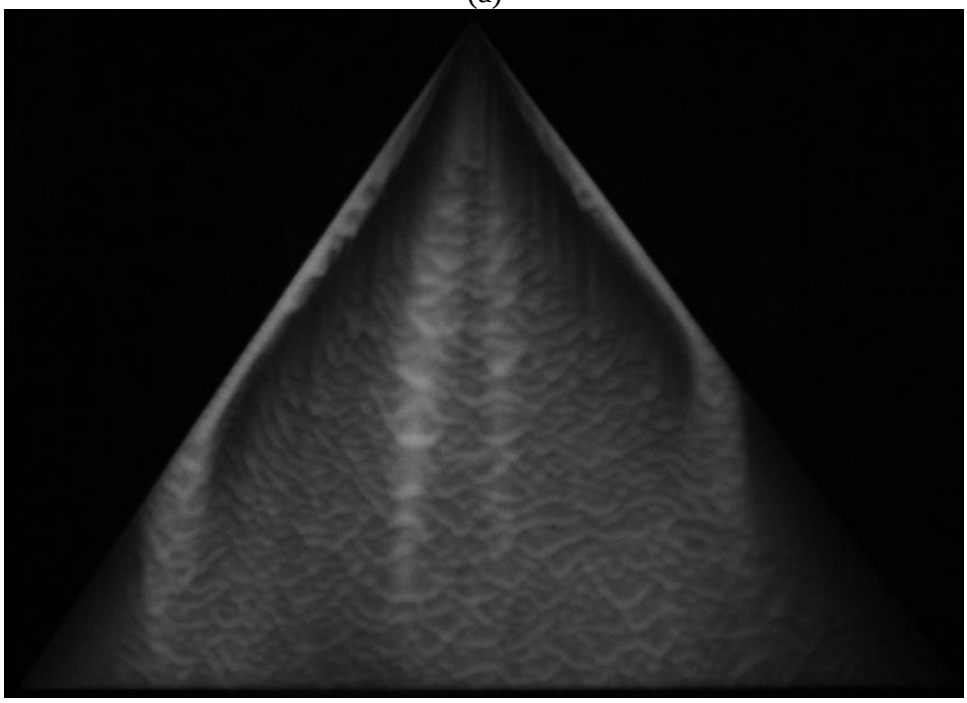

(b)

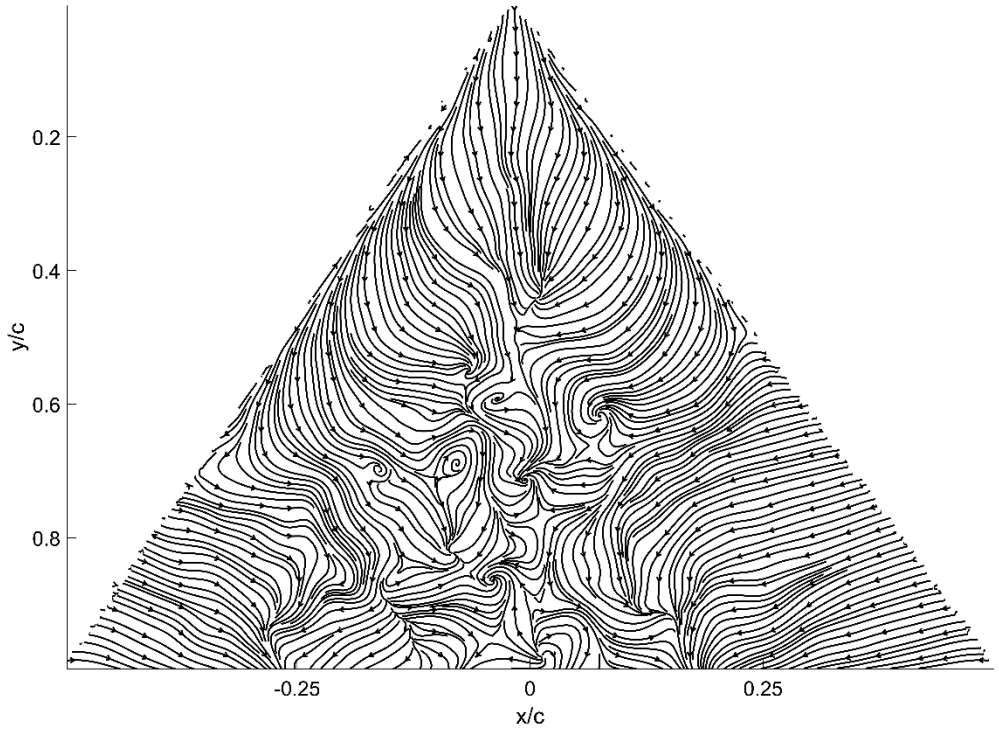

(c)

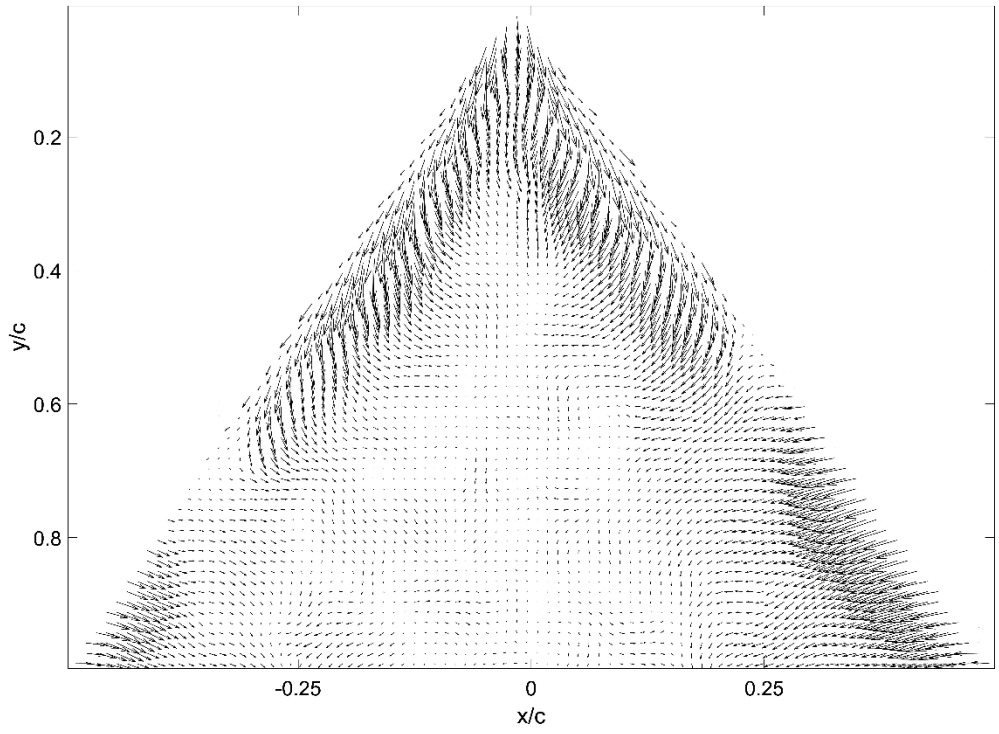

(d)

Figure 35: (a) initial image, (b) final image, (c) skin-friction lines, and (d) skin-friction vectors for 55° delta wing at -5° AoA

Figures 36 (a), (b), (c), and (d) are the initial luminescent oil image, the final luminescent oil image, the skin-friction line plot, and the skin-friction vector plot respectively for the case of a 55° delta wing at 0° AoA.

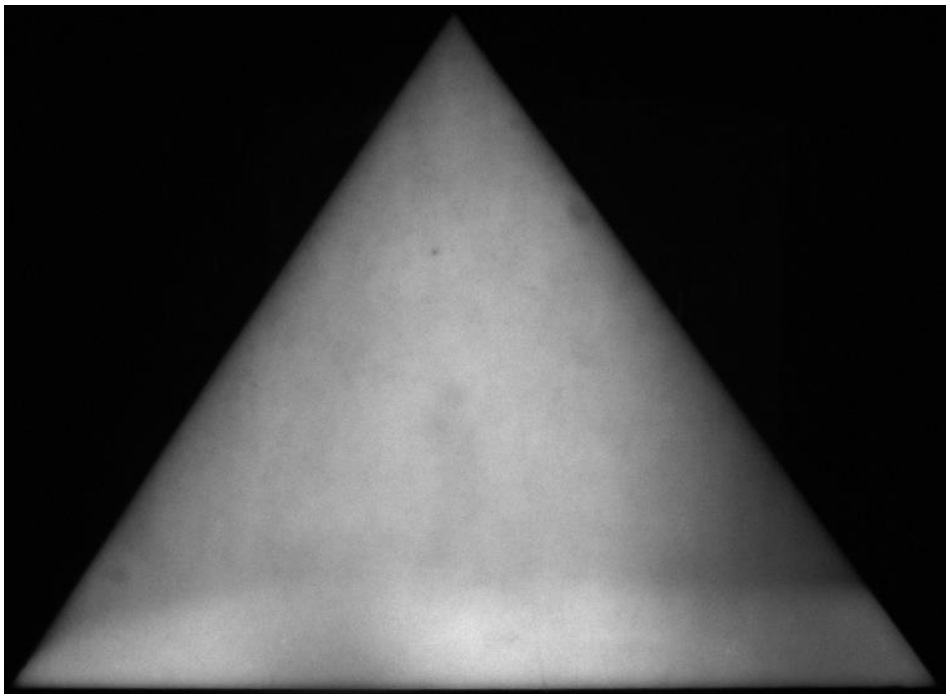

(a)

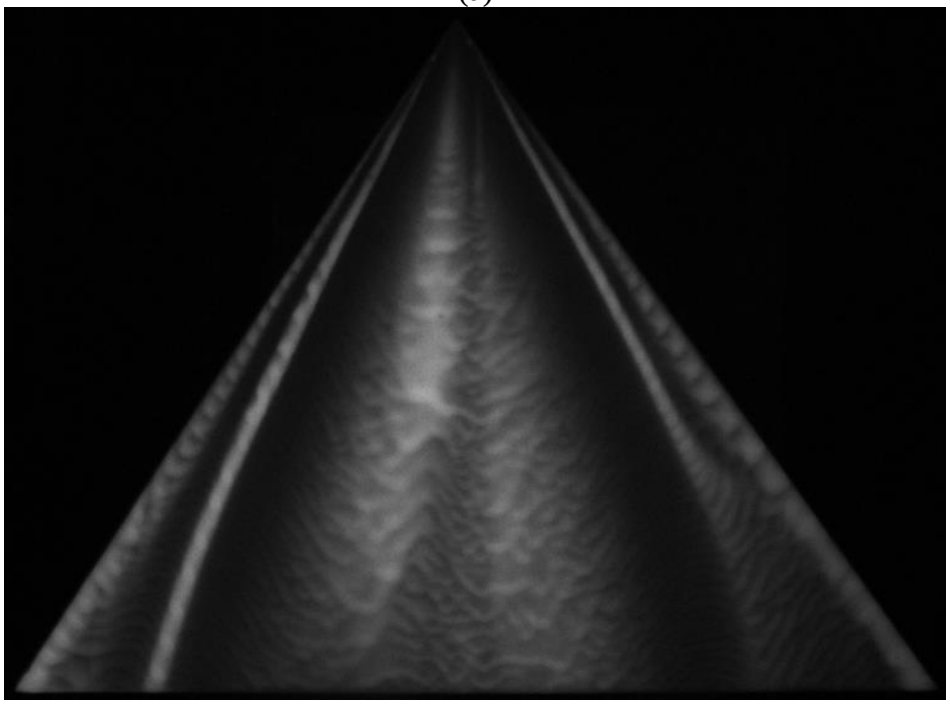

(b)

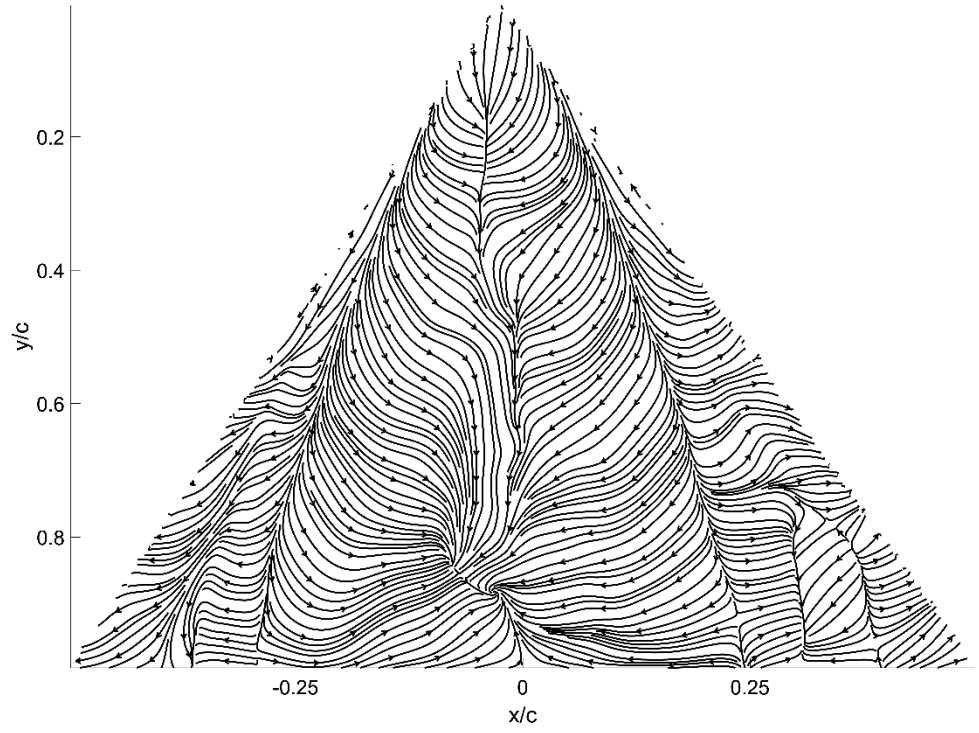

(c)

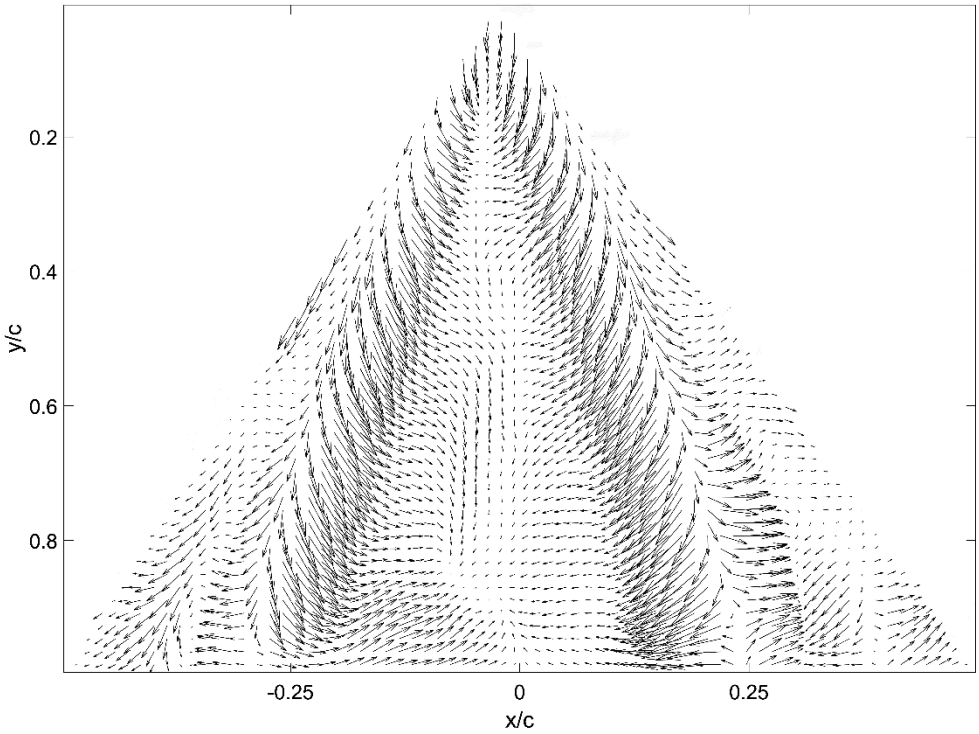

(d)

Figure 36: (a) initial image, (b) final image, (c) skin-friction lines, and (d) skin-friction vectors for 55° delta wing at 0° AoA

Figures 37 (a), (b), (c), and (d) are the initial luminescent oil image, the final luminescent oil image, the skin-friction line plot, and the skin-friction vector plot respectively for the case of a 55° delta wing at 5° AoA.

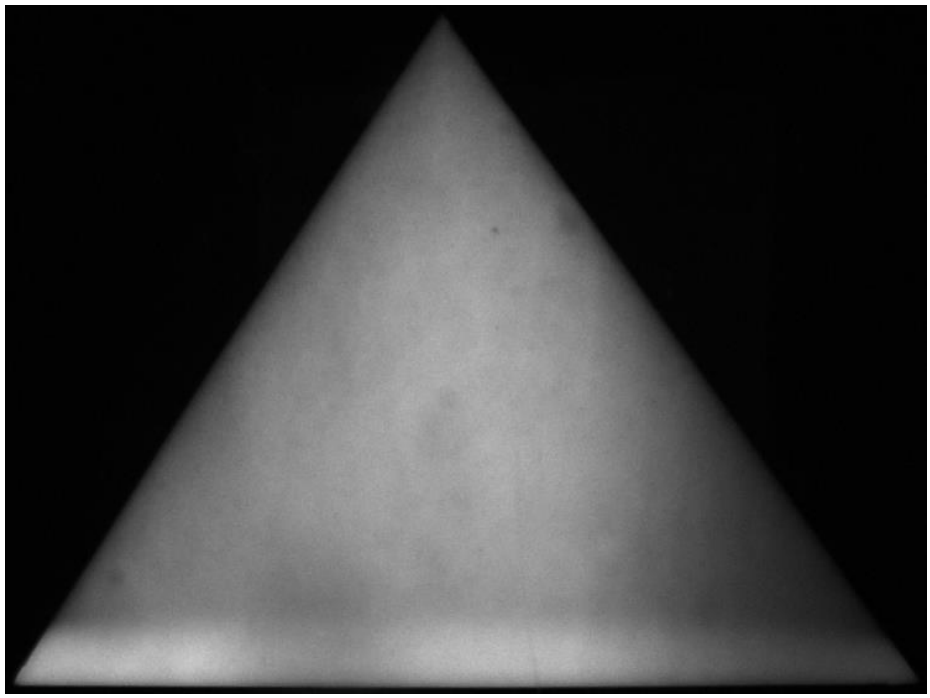

(a)

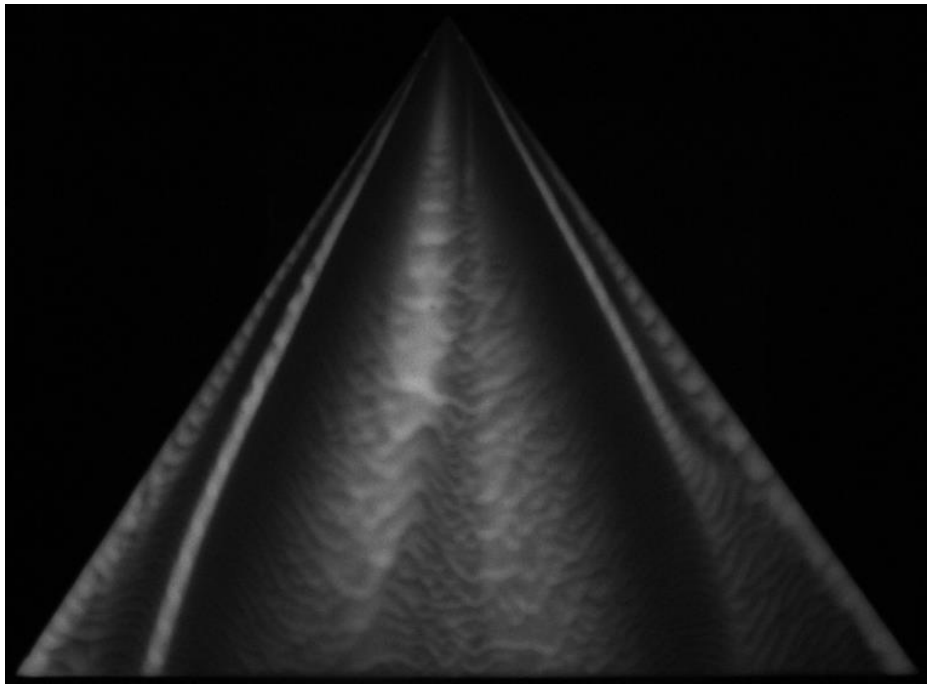

(b)

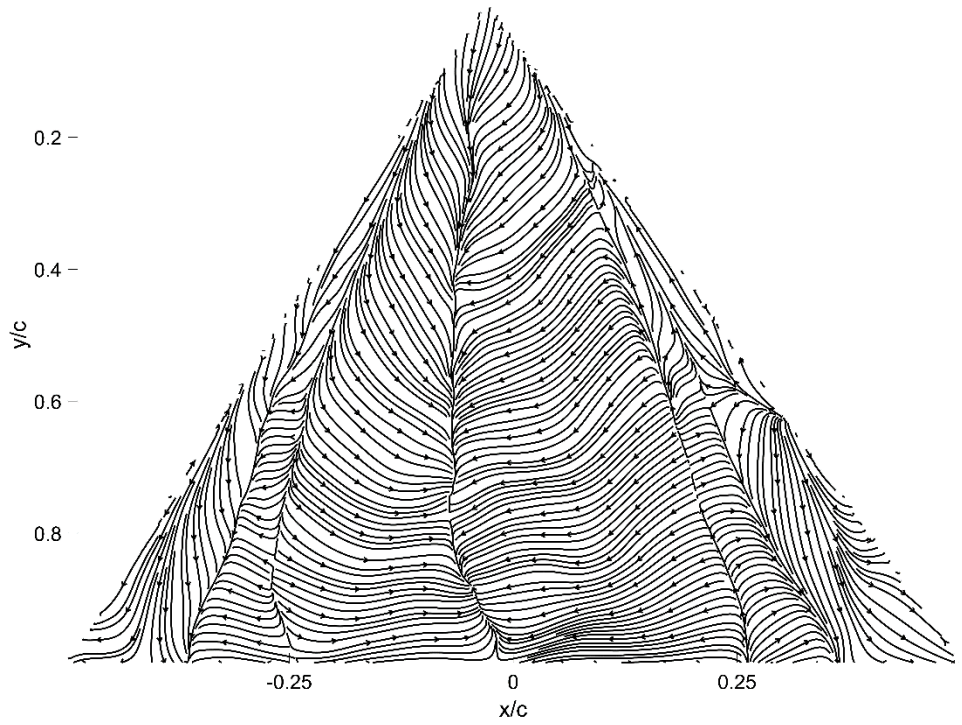

(c)

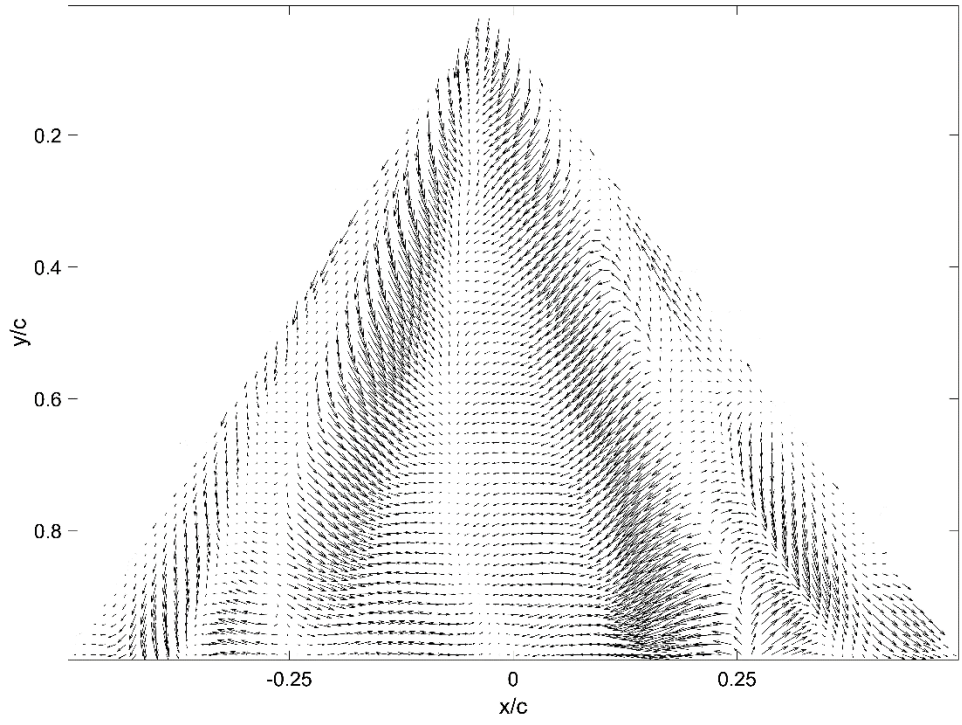

(d)

Figure 37: (a) initial image, (b) final image, (c) skin-friction lines, and (d) skin-friction vectors for 55° delta wing at 5° AoA

Figures 38 (a), (b), (c), and (d) are the initial luminescent oil image, the final luminescent oil image, the skin-friction line plot, and the skin-friction vector plot respectively for the case of a 55° delta wing at 10° AoA.

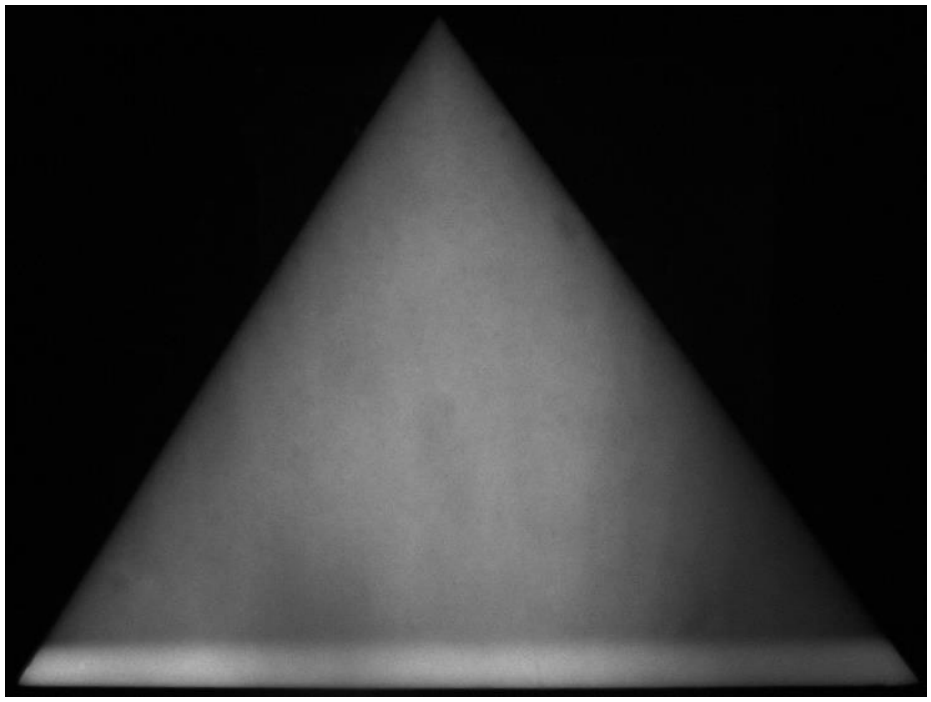

(a)

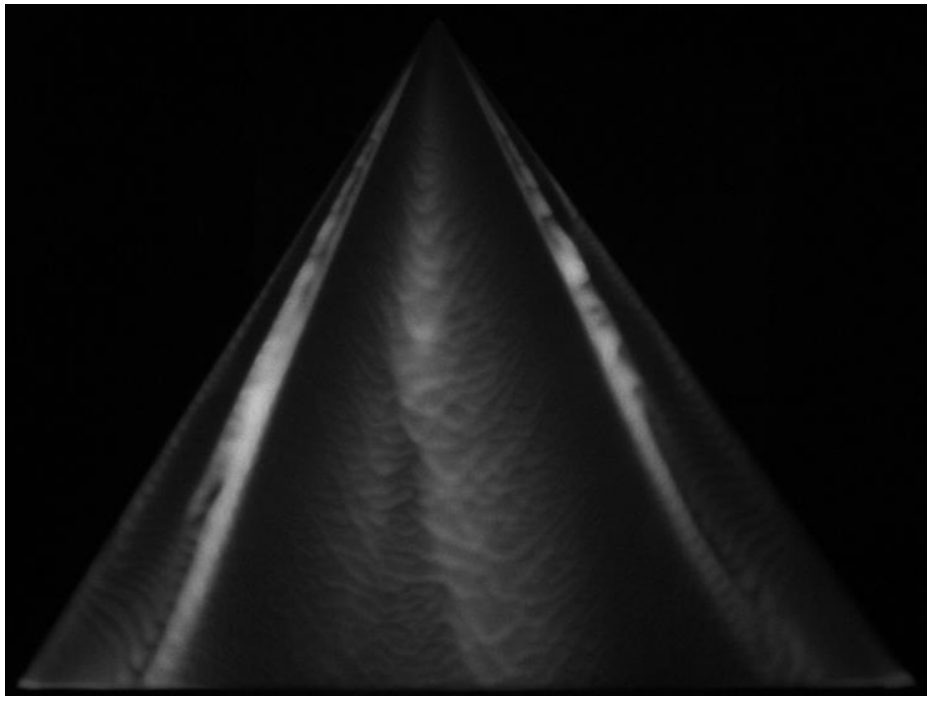

(b)

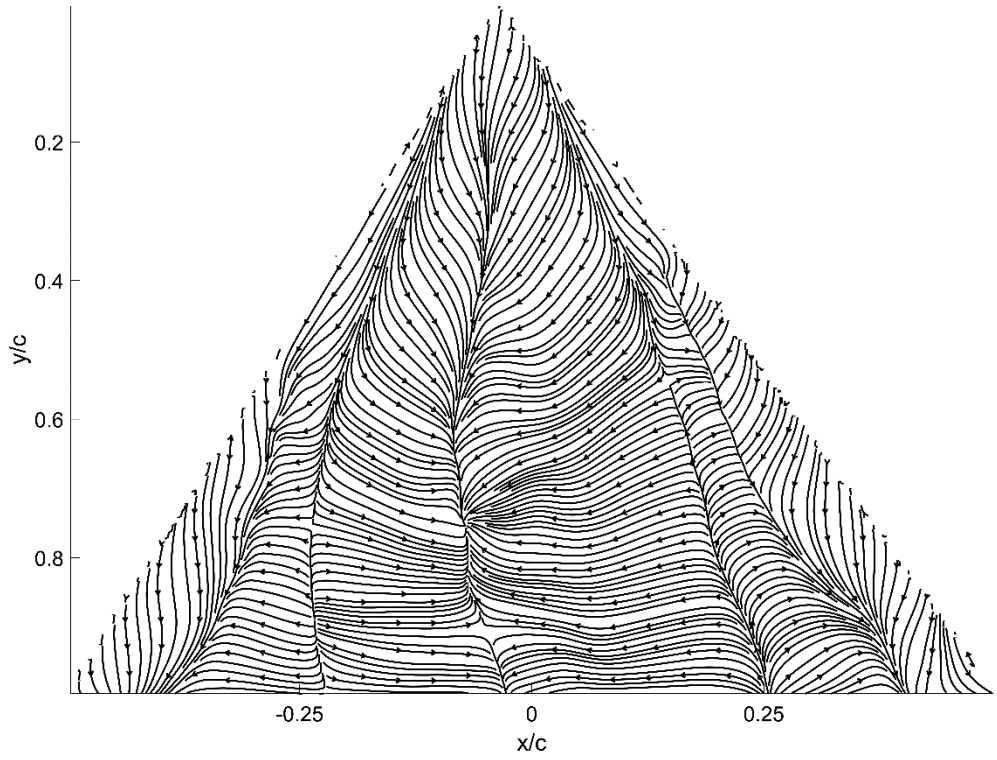

(c)

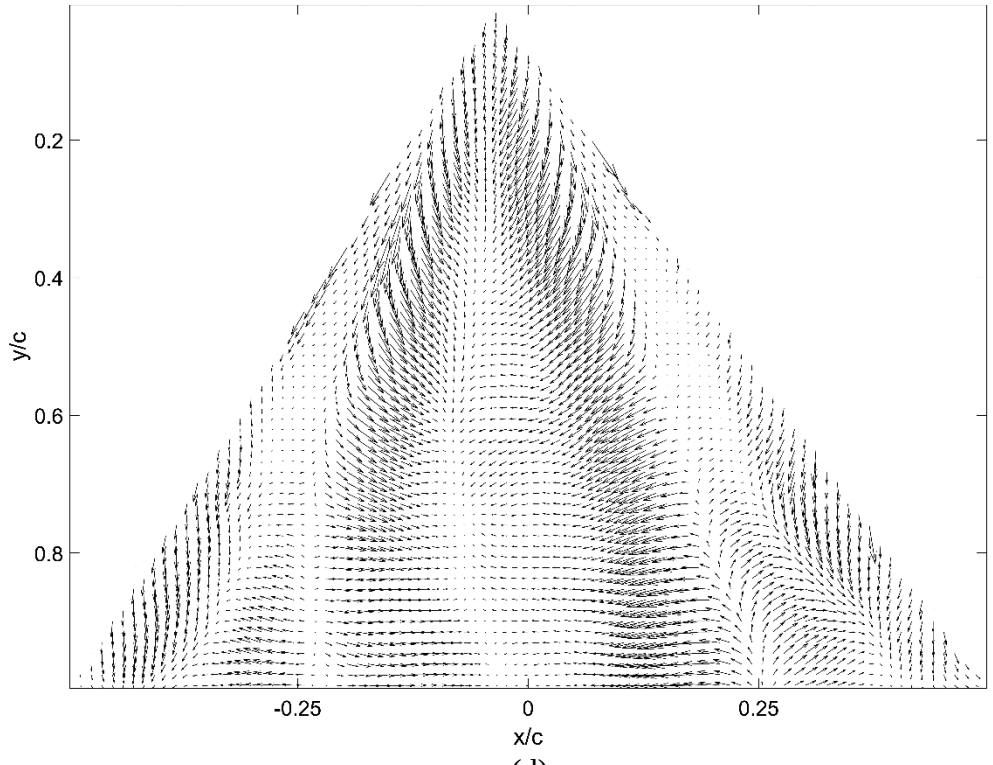

(d)

Figure 38: (a) initial image, (b) final image, (c) skin-friction lines, and (d) skin-friction vectors for 55° delta wing at 10° AoA

Figures 39 (a), (b), (c), and (d) are the initial luminescent oil image, the final luminescent oil image, the skin-friction line plot, and the skin-friction vector plot respectively for the case of a 55° delta wing at 15° AoA.

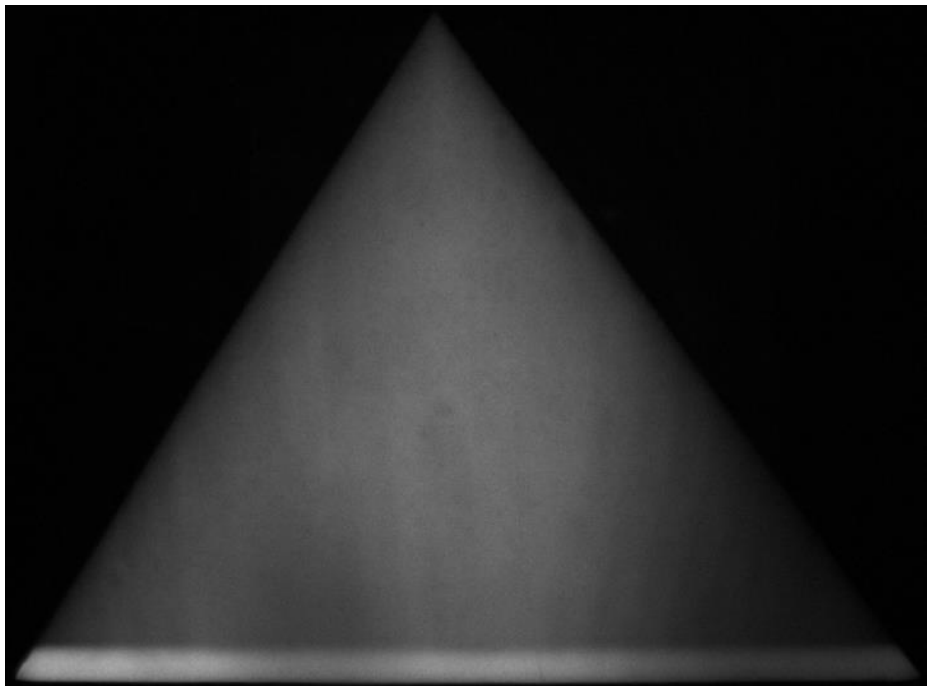

(a)

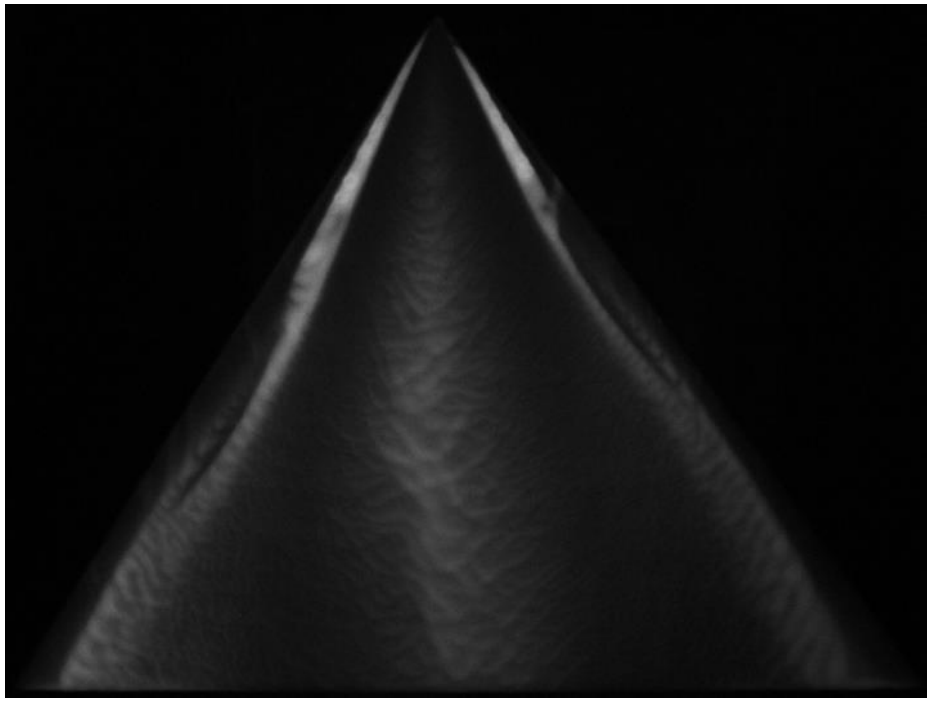

(b)

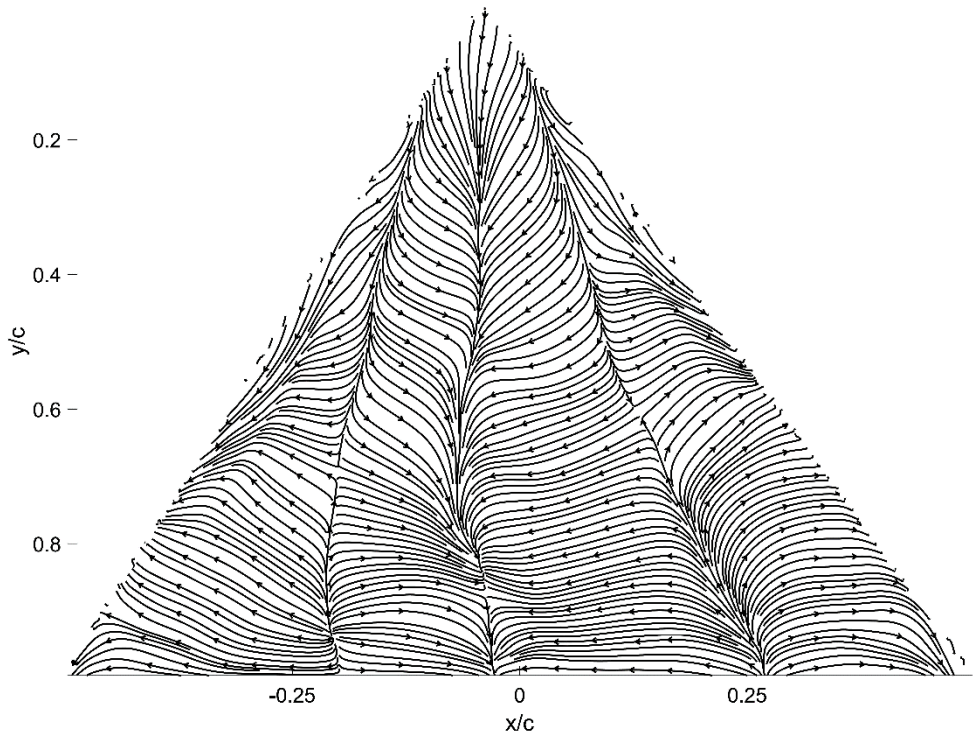

(c)

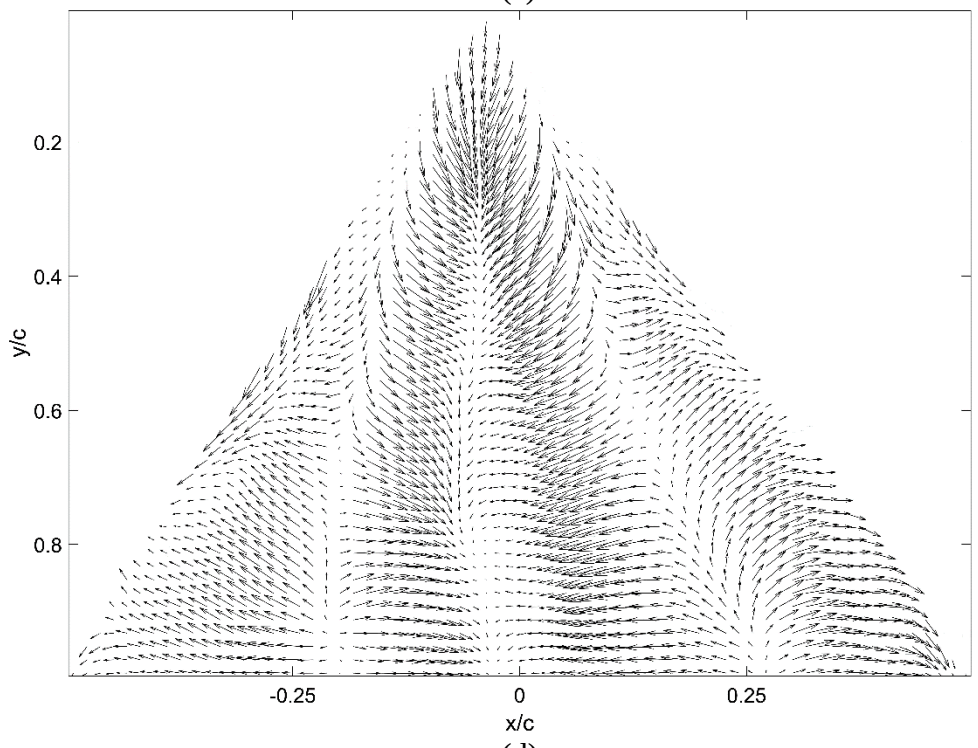

(d)

Figure 39: (a) initial image, (b) final image, (c) skin-friction lines, and (d) skin-friction vectors for 55° delta wing at 15° AoA

Figures 40 (a), (b), (c), and (d) are the initial luminescent oil image, the final luminescent oil image, the skin-friction line plot, and the skin-friction vector plot respectively for the case of a 55° delta wing at 20° AoA.

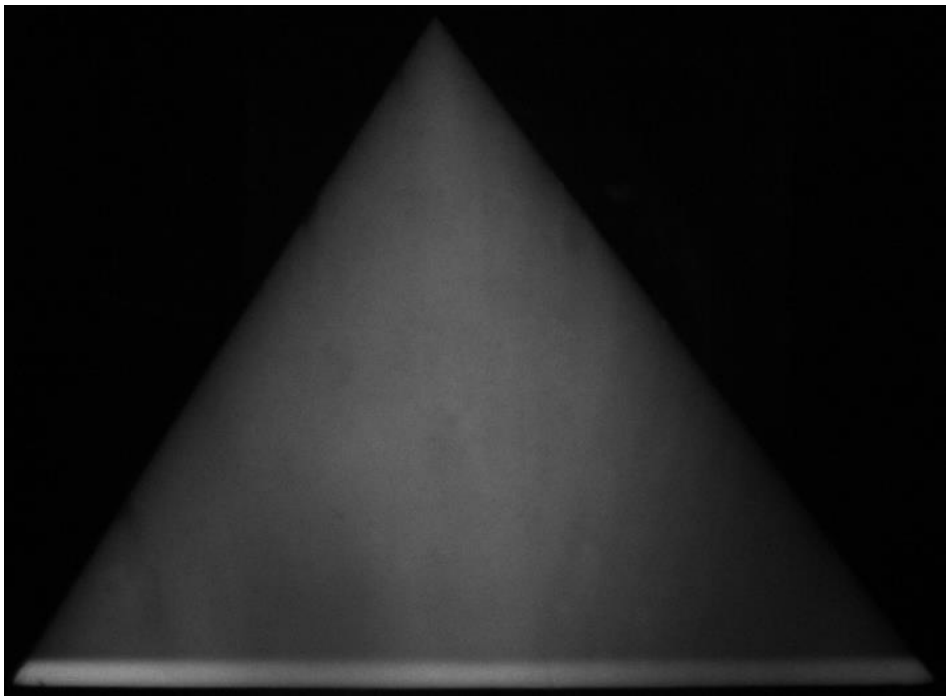

(a)

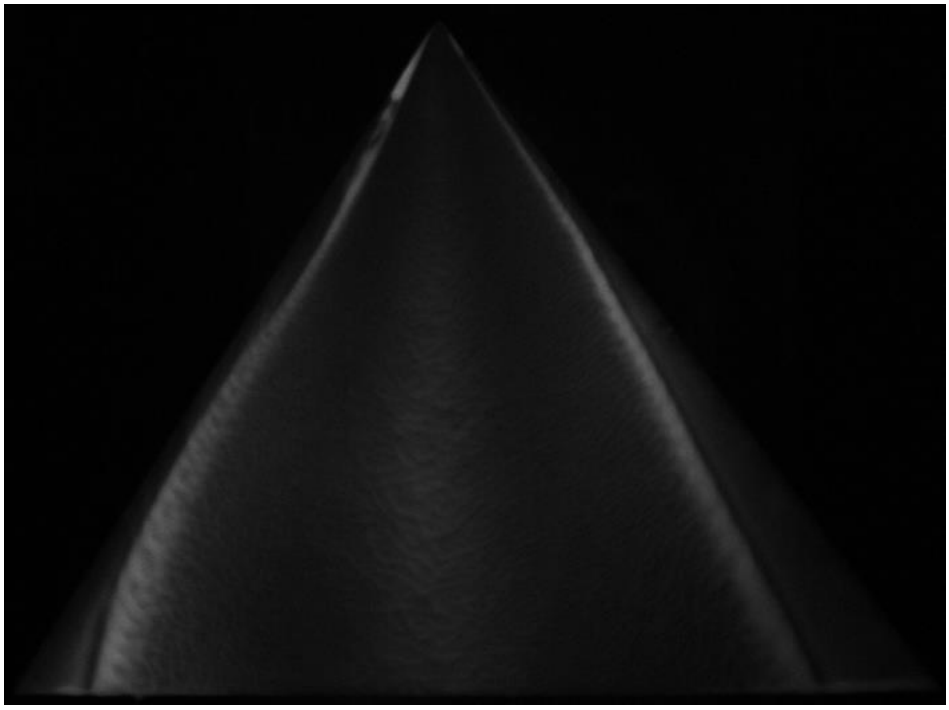

(b)

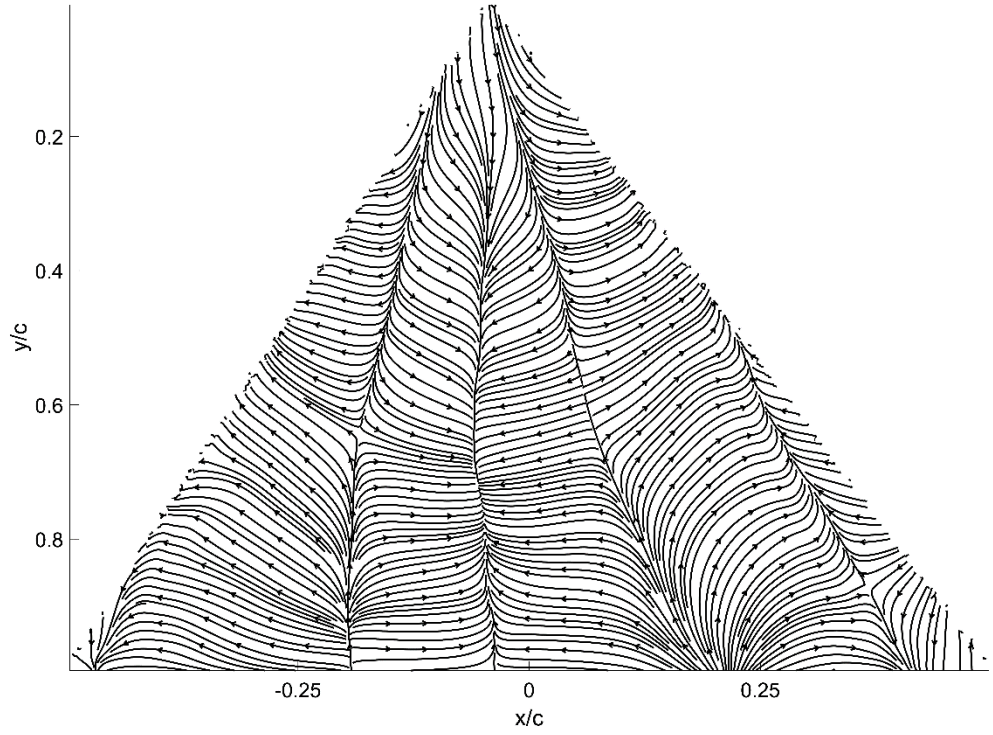

(c)

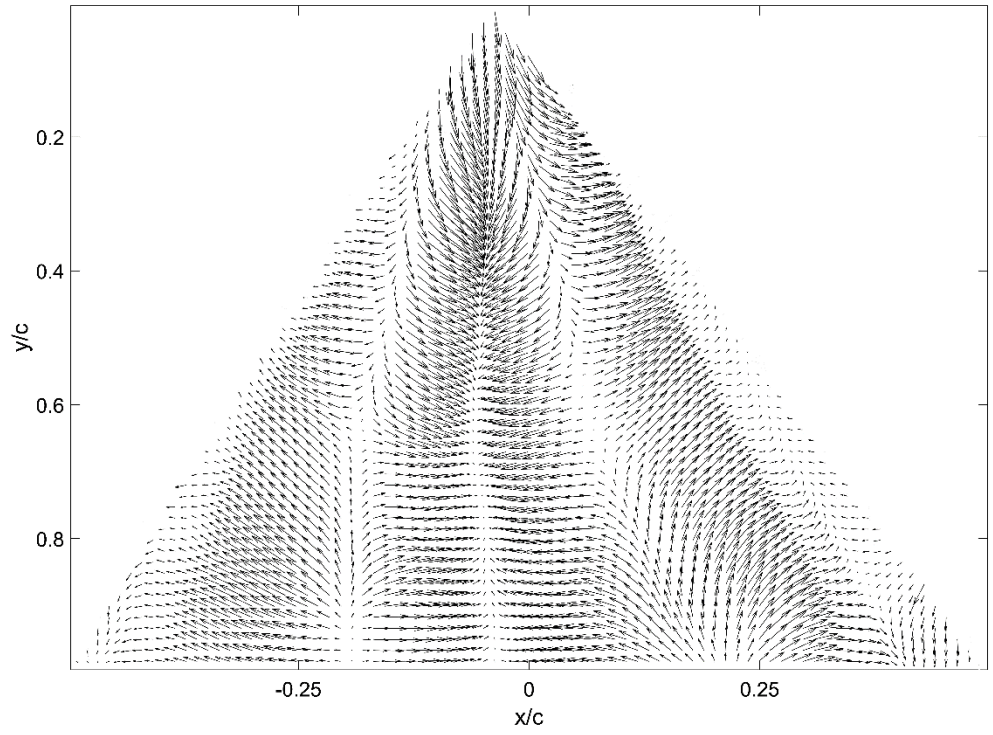

(d)

Figure 40: (a) initial image, (b) final image, (c) skin-friction lines, and (d) skin-friction vectors for 55° delta wing at 20° AoA

Figures 41 (a), (b), (c), and (d) are the initial luminescent oil image, the final luminescent oil image, the skin-friction line plot, and the skin-friction vector plot respectively for the case of a 55° delta wing at 25° AoA.

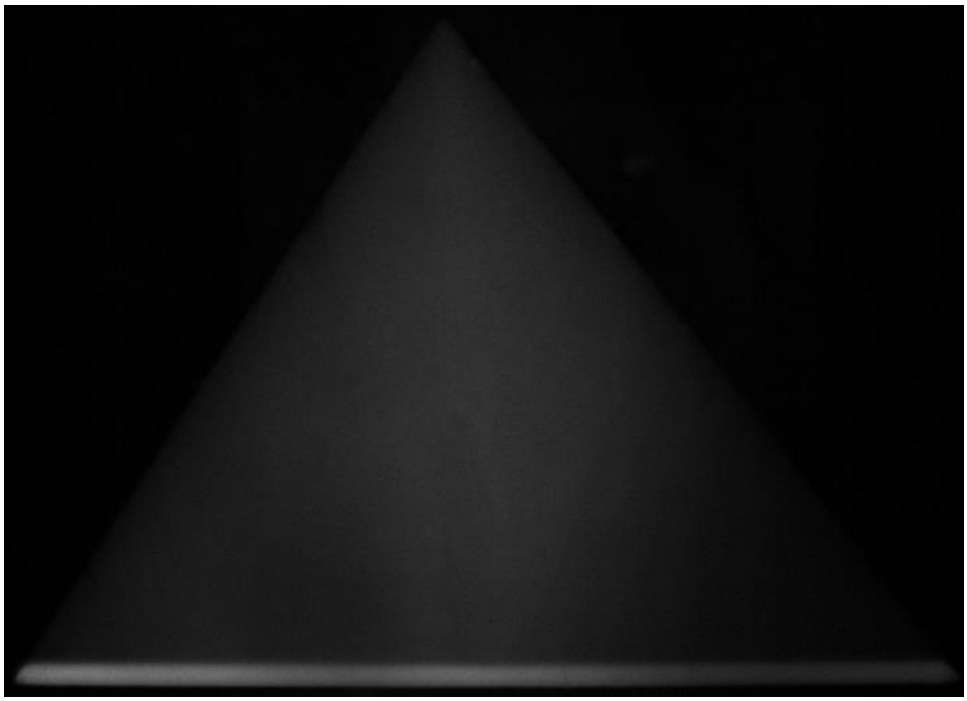

(a)

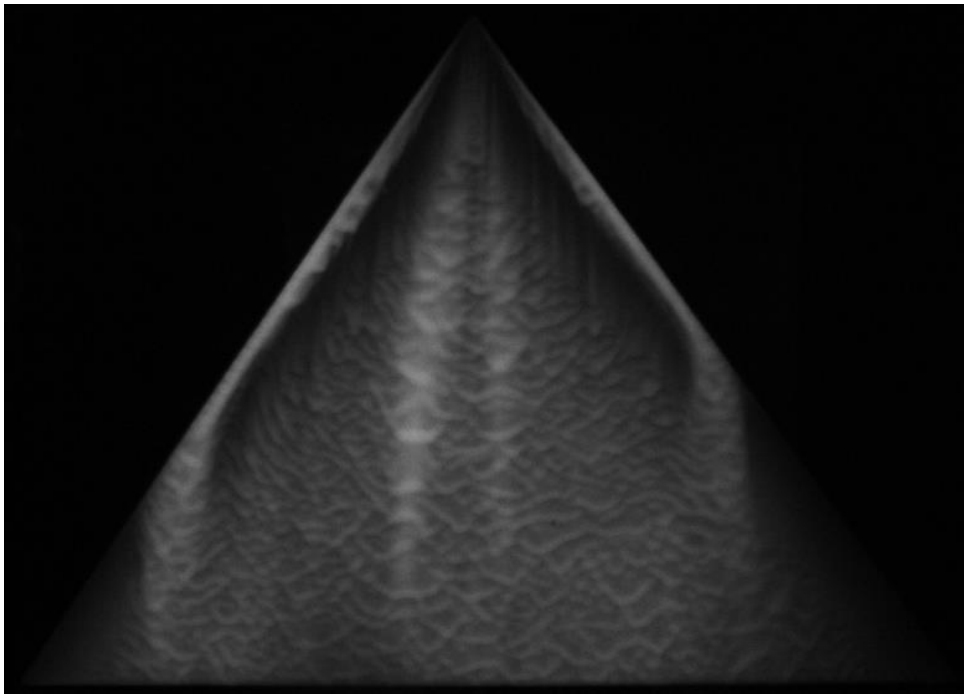

(b)

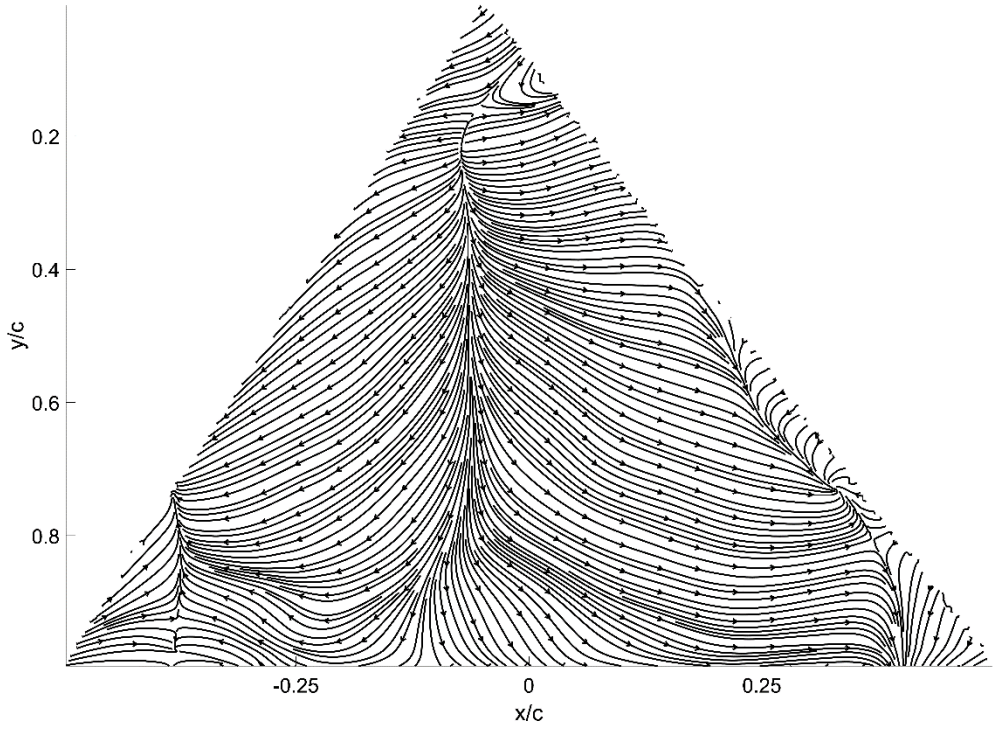

(c)

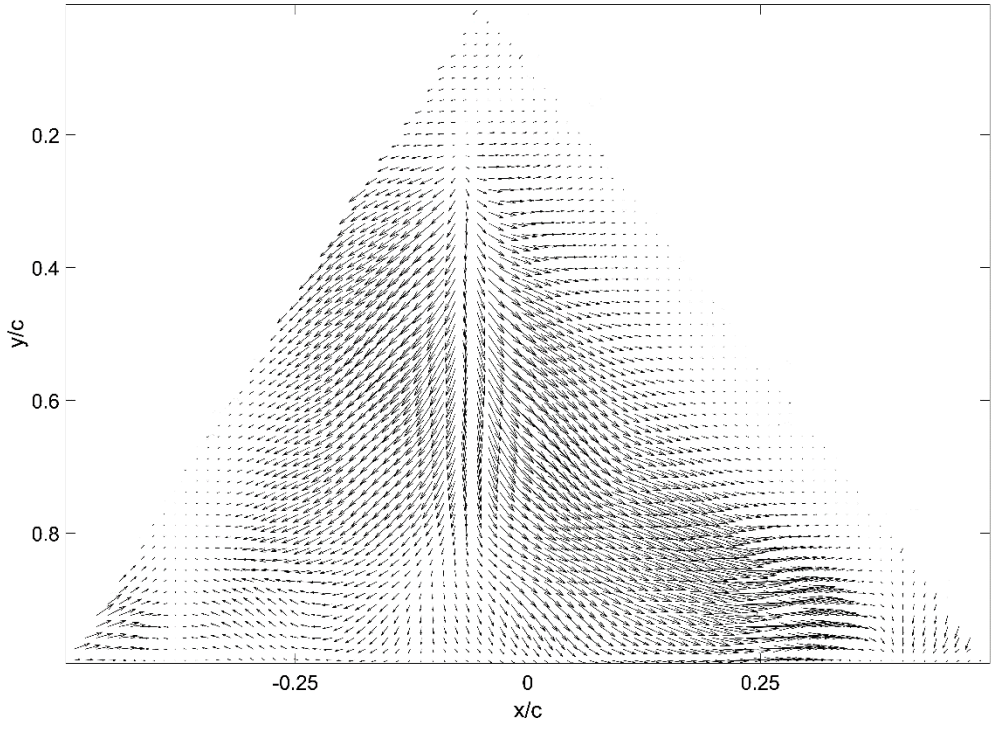

(d)

Figure 41: (a) initial image, (b) final image, (c) skin-friction lines, and (d) skin-friction vectors for 55° delta wing at 25° AoA

Like the 50° delta wing, the skin-friction lines for the -5° AoA case shows a lack of pattern in the skin-friction lines due to the lack of a tip vortex. For the 0° AoA, the presence of a weak tip vortex is apparent in the broken primary separation line. The secondary reattachment line also moved outward to x/c = -0.3 and 0.25, compared to the 50° delta wing. A focus is also formed at x/c = -0.05 and y/c = 0.9, which is not apparent in the 50° delta wing. A saddle point is also formed at x/c = 0.25 and y/c = 0.92, which is closer to the trailing edge compared to the 50° case, thus implying that the vortex core is further back. The secondary separation lines are also broken, compared to that of the 50° case. An explanation for this is since there is a higher sweep angle, the primary vortex forms further from the surface, thus there is less interaction between the vortices and boundary layer of the wing when compared to the 50° case.

In the 5° AoA, the number of saddle points increased from 2 to 4. Their locations are y/c = 0.8, 0.8, 0.8, 0.6 and x/c = -0.05, -0.25, 0.2, 0.25 respectively. The primary separation, secondary reattachment, and secondary separation lines can be seen clearly and are relatively symmetric. The secondary reattachment lines end at x/c = -0.25 and 0.25, while the secondary separation lines end at x/c = -0.35 and 0.35. One thing to note that at the same Reynolds number, freestream velocity, and AoA, the location of the saddle points moved downwards, thus reinforcing the idea that the primary vortex acts further away from the surface compared to the 50° delta wing. For the 10° case, the secondary separation lines moved outwards, and are now at x/c = -0.4 and 0.4 respectively. There are now three saddle points located at y/c = 0.9, 0.55, 0.75 and x/c = -0.05, 0.2, -0.22 respectively. The saddle points in the secondary separation lines can no longer be seen, and are no longer straight compared to that of the 5° AoA. This can be interpreted as a wing-tip vortex that moves outwards and upwards as angle of attack is increased. This observation coincides with known delta wing aerodynamics. For the 15° AoA, the absence of the secondary separation

lines coincides with the observation that the wing-tip vortices are moving outwards as AoA is increased. The location of the saddle points remained relatively the same as that of the 10° case. The main difference between the 50° and 55° delta wings at 20° AoA is that the line down the center of the wing for the 55° delta wing is still a primary separation line. This phenomenon only changes to a primary reattachment line at 25° AoA for the 55° delta wing. Another observation made is that the secondary reattachment line moved closer to the center of the wing for the 20° AoA case. They are now located at x/c = -0.2 and 0.2 instead of -0.25 and 0.25 at 15° AoA. Lastly, for the 25° AoA, there is a clear impression of the vortex breakdown in Figure 41 (b). The line down the middle also becomes a primary reattachment line, ending at y/c = 0.8 instead of going all the way to the trailing edge. This shows that the flow has separated. The findings from this case is consistent with non-slender delta wing aerodynamics in that due to a higher sweep angle, the primary vortex forms further away to the surface compared to that of the 50° delta wing.

60° Delta Wing

The 60° delta wing has a chord length of 189mm and a span of 218mm. Research done for this specific sweep angle have mainly been for transonic and supersonic flows. Therefore, like the 55° delta wing, the results for this section will be derived purely from observations and compared to the results of the other delta wings.

Figures 42 (a), (b), (c), and (d) are the initial luminescent oil image, the final luminescent oil image, the skin-friction line plot, and the skin-friction vector plot respectively for the case of a 60° delta wing at -5° AoA.

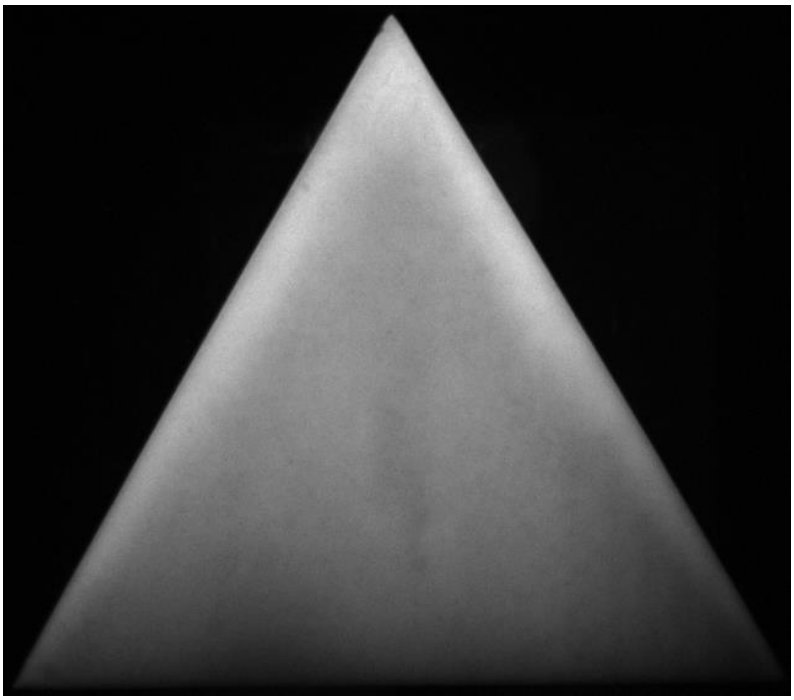

(a)

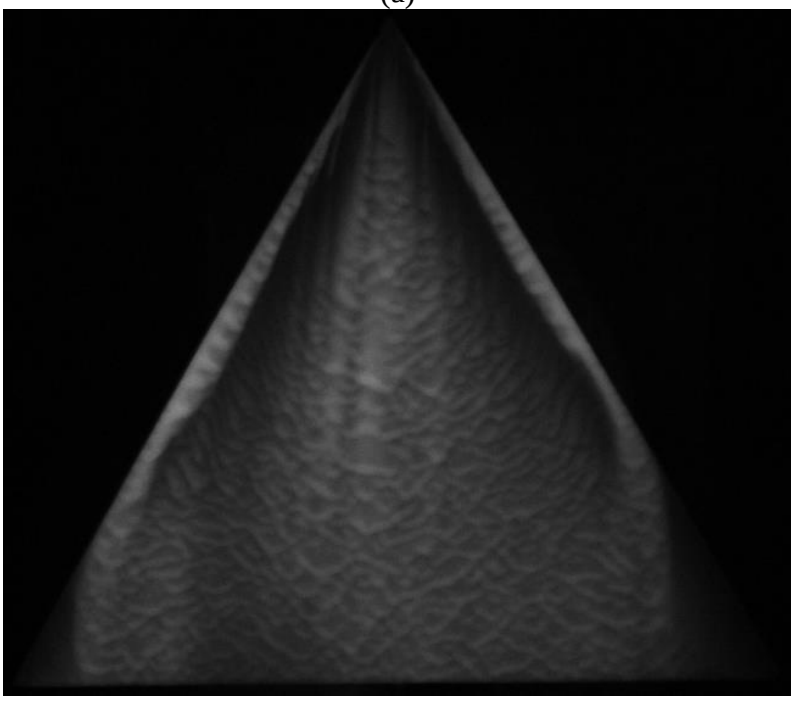

(b)

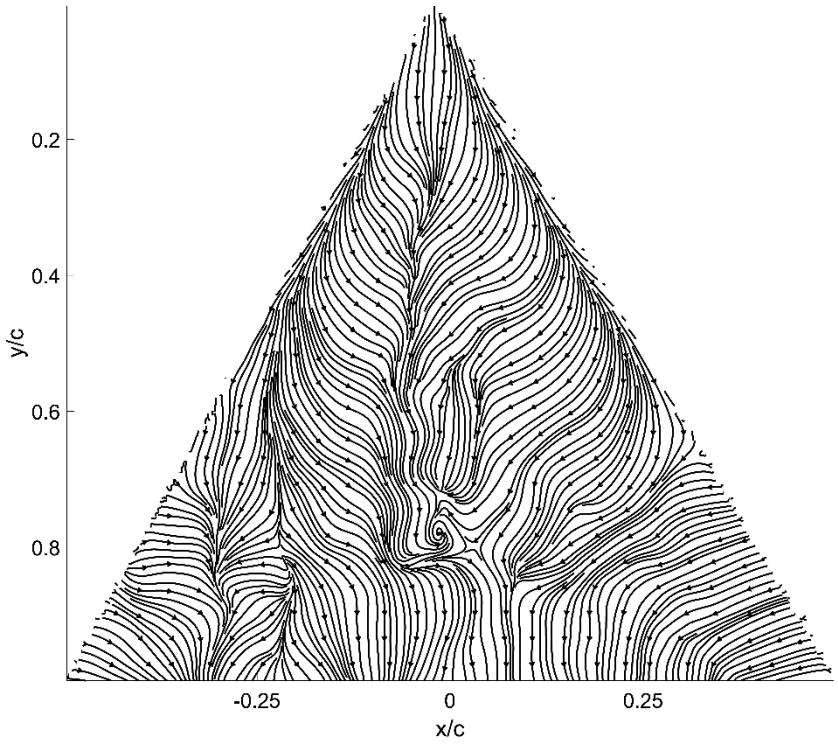

(c)

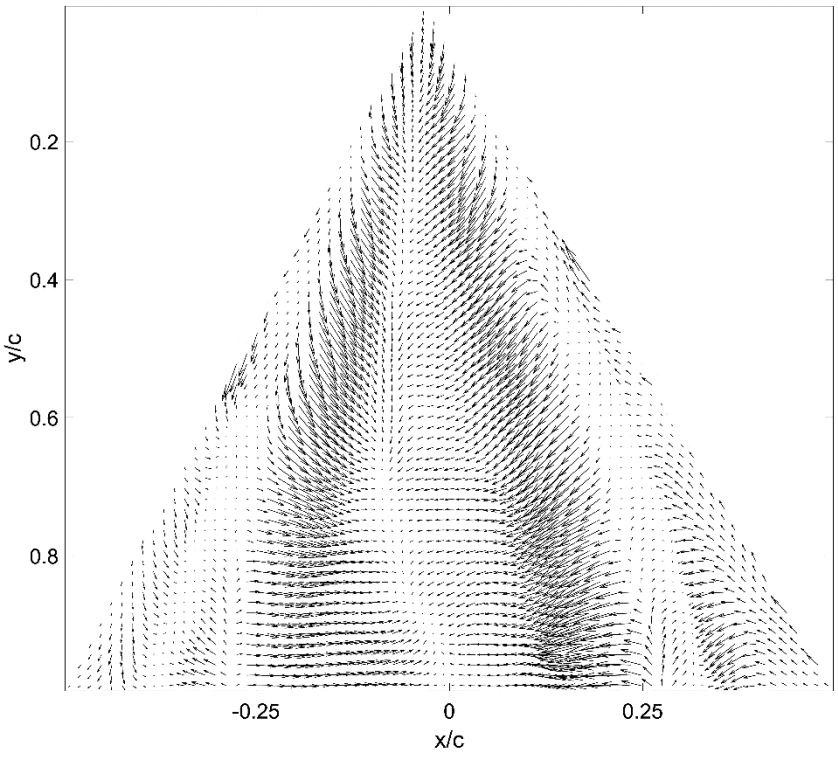

(d)

Figure 42: (a) initial image, (b) final image, (c) skin-friction lines, and (d) skin-friction vectors for 60° delta wing at -5° AoA

Figures 43 (a), (b), (c), and (d) are the initial luminescent oil image, the final luminescent oil image, the skin-friction line plot, and the skin-friction vector plot respectively for the case of a 60° delta wing at 0° AoA.

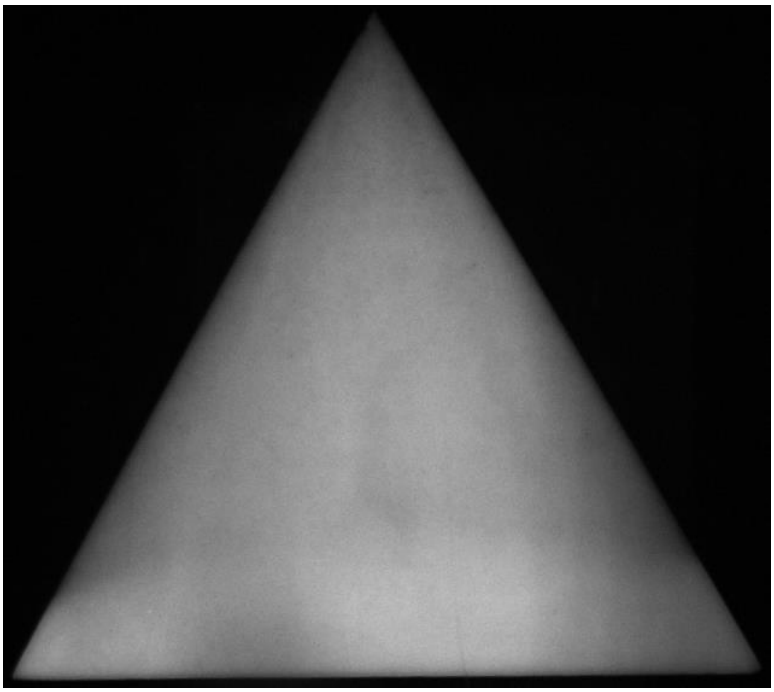

(a)

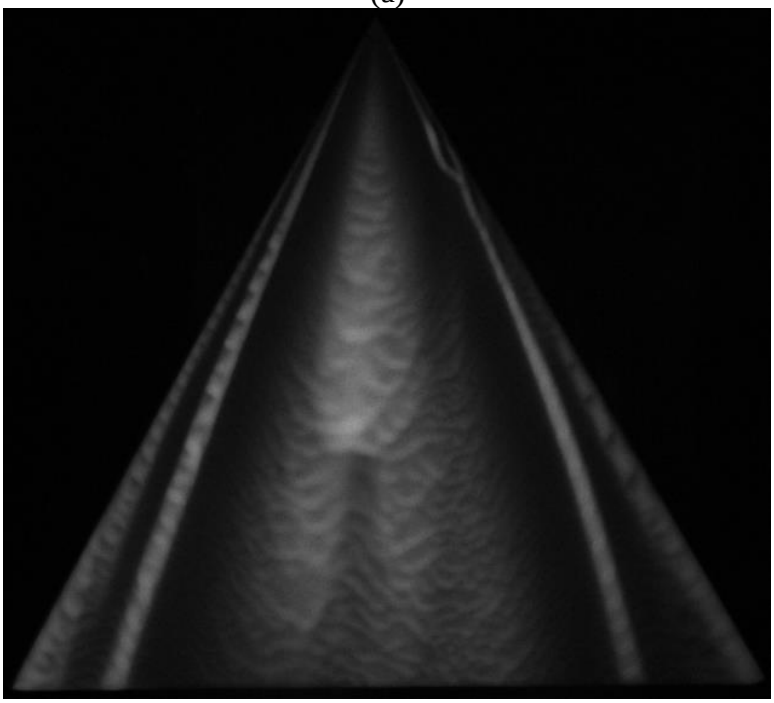

(b)

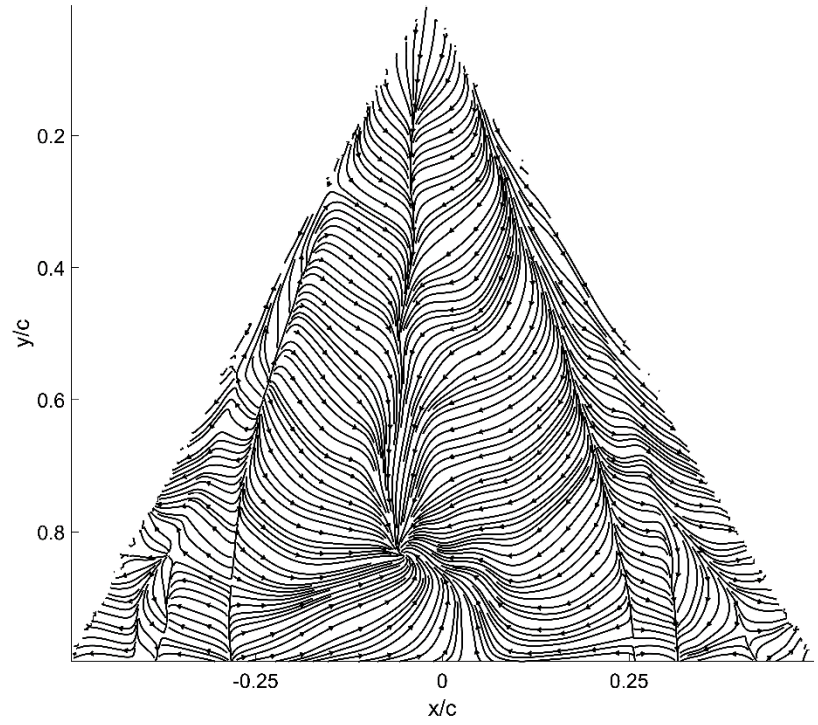

(c)

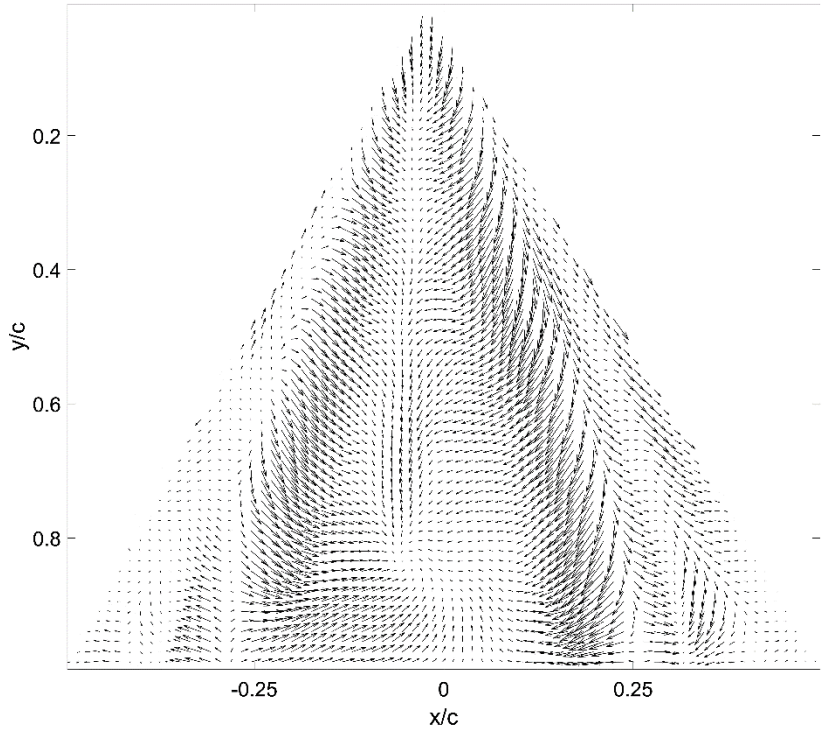

(d)

Figure 43: (a) initial image, (b) final image, (c) skin-friction lines, and (d) skin-friction vectors for 60° delta wing at 0° AoA

Figures 44 (a), (b), (c), and (d) are the initial luminescent oil image, the final luminescent oil image, the skin-friction line plot, and the skin-friction vector plot respectively for the case of a 60° delta wing at 5° AoA.

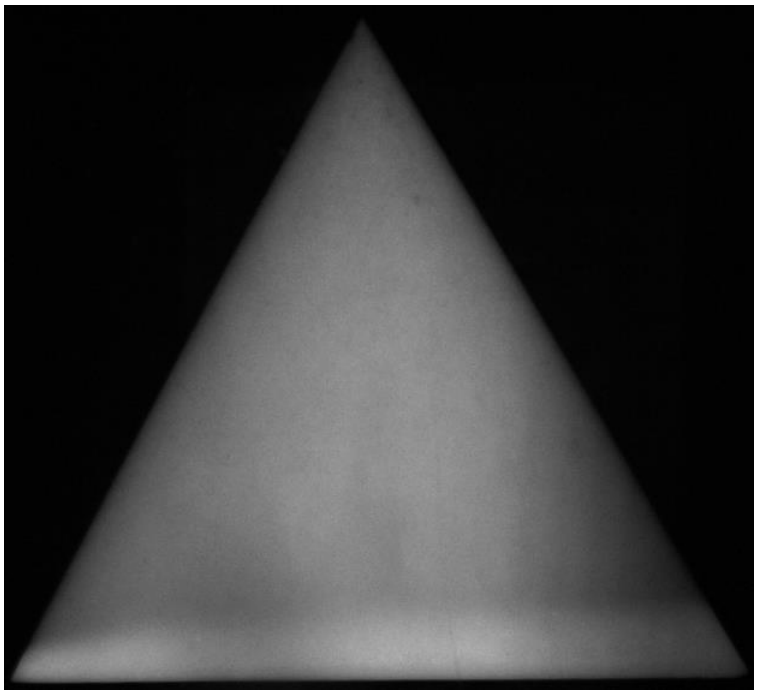

(a)

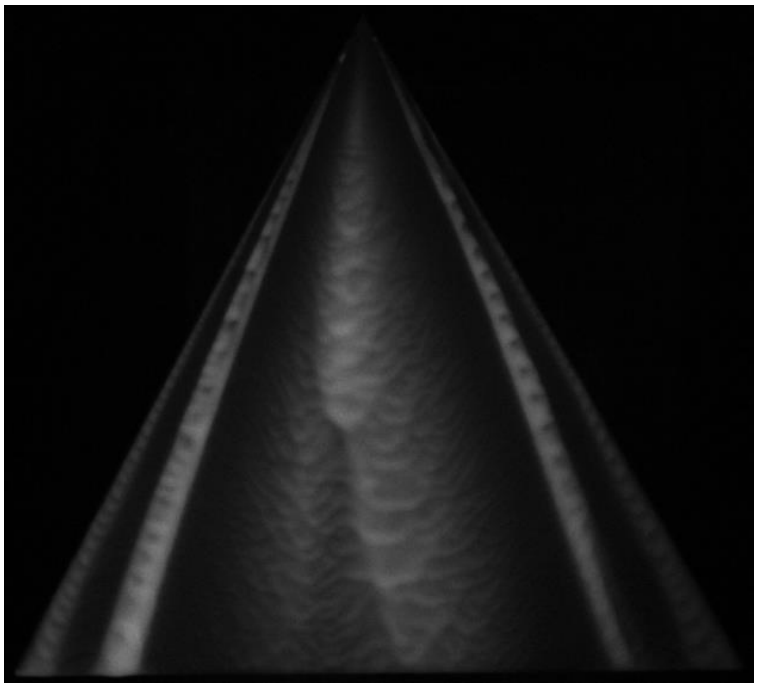

(b)

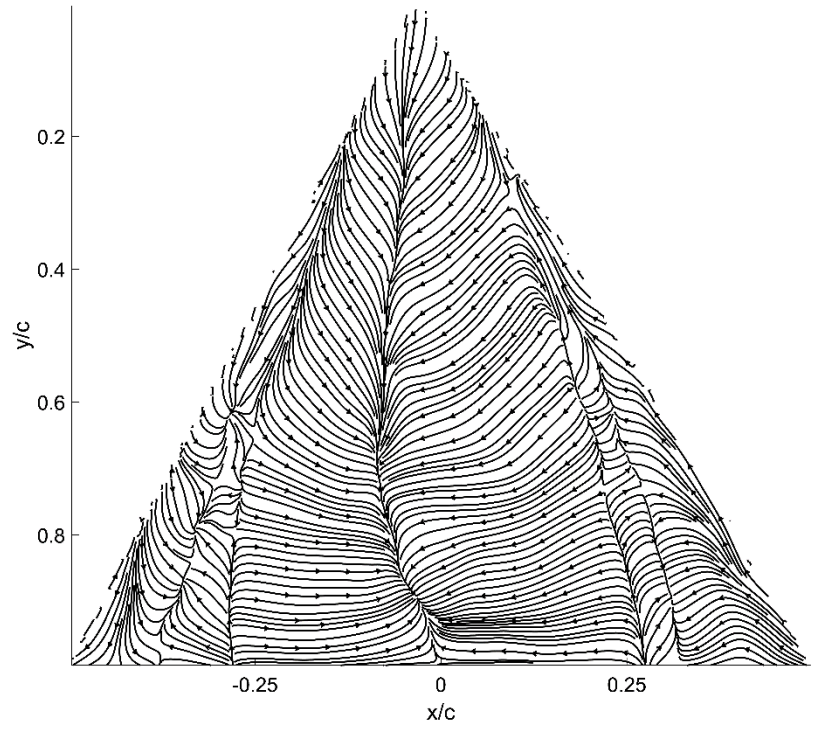

(c)

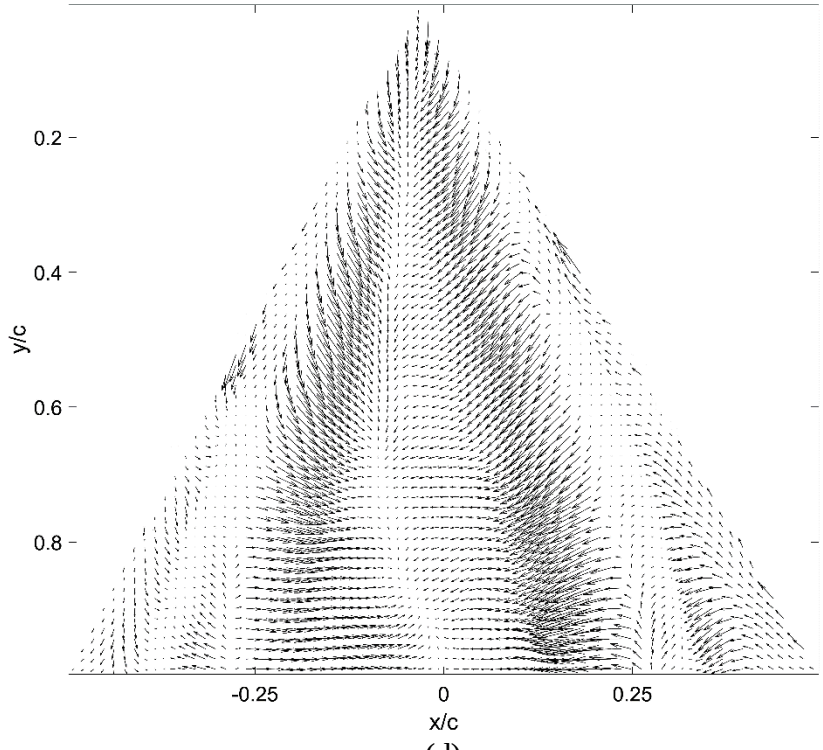

(d)

Figure 44: (a) initial image, (b) final image, (c) skin-friction lines, and (d) skin-friction vectors for 60° delta wing at 5° AoA

Figures 45 (a), (b), (c), and (d) are the initial luminescent oil image, the final luminescent oil image, the skin-friction line plot, and the skin-friction vector plot respectively for the case of a 60° delta wing at 10° AoA.

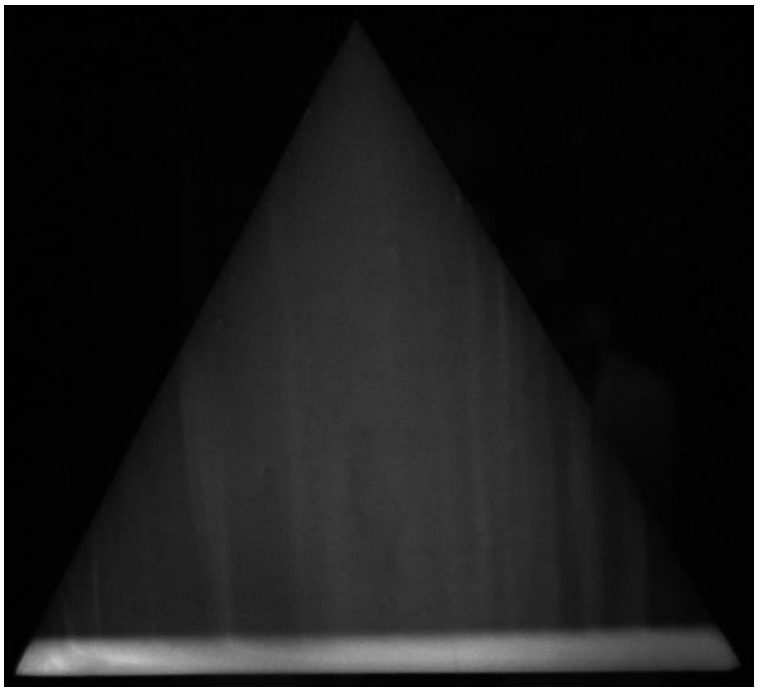

(a)

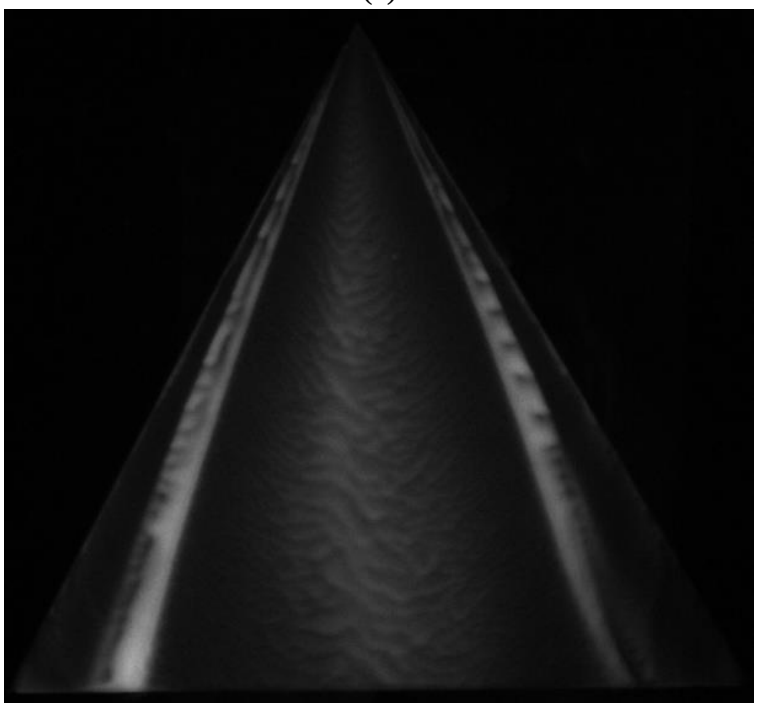

(b)

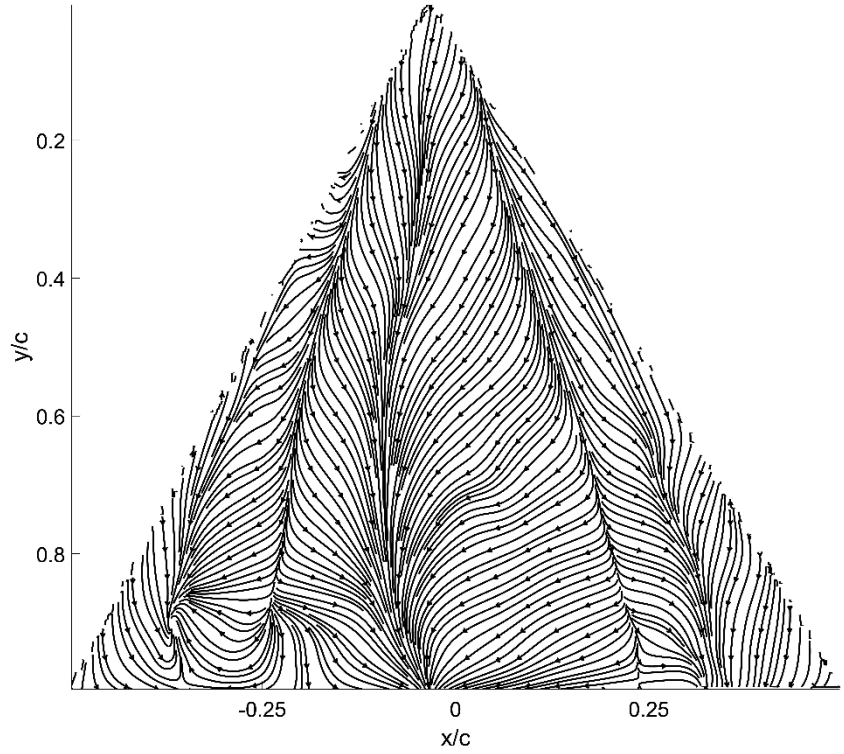

(c)

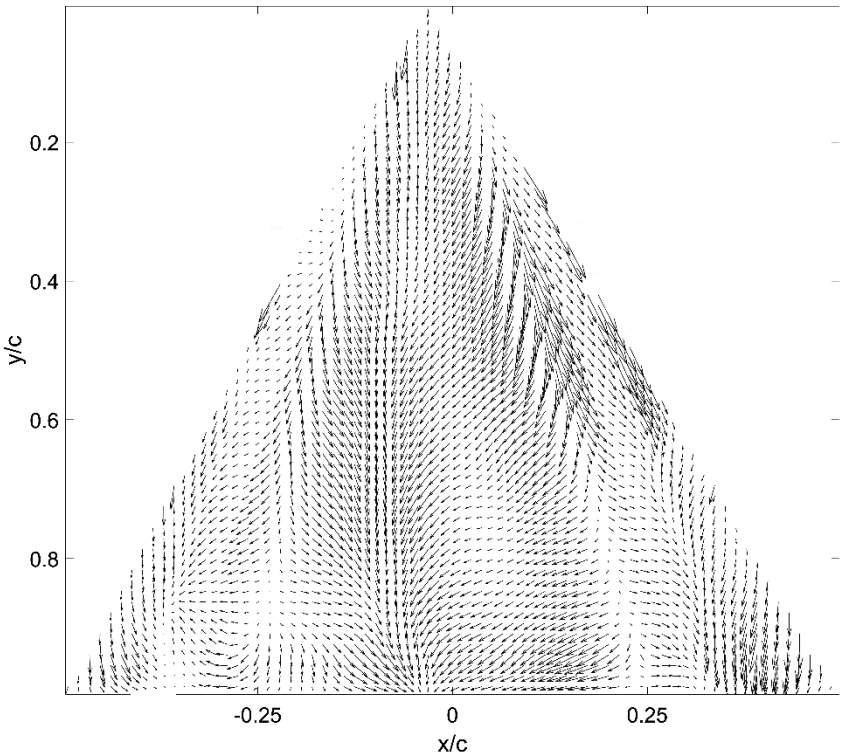

(d)

Figure 45: (a) initial image, (b) final image, (c) skin-friction lines, and (d) skin-friction vectors for 60° delta wing at 10° AoA

Figures 46 (a), (b), (c), and (d) are the initial luminescent oil image, the final luminescent oil image, the skin-friction line plot, and the skin-friction vector plot respectively for the case of a 60° delta wing at 15° AoA.

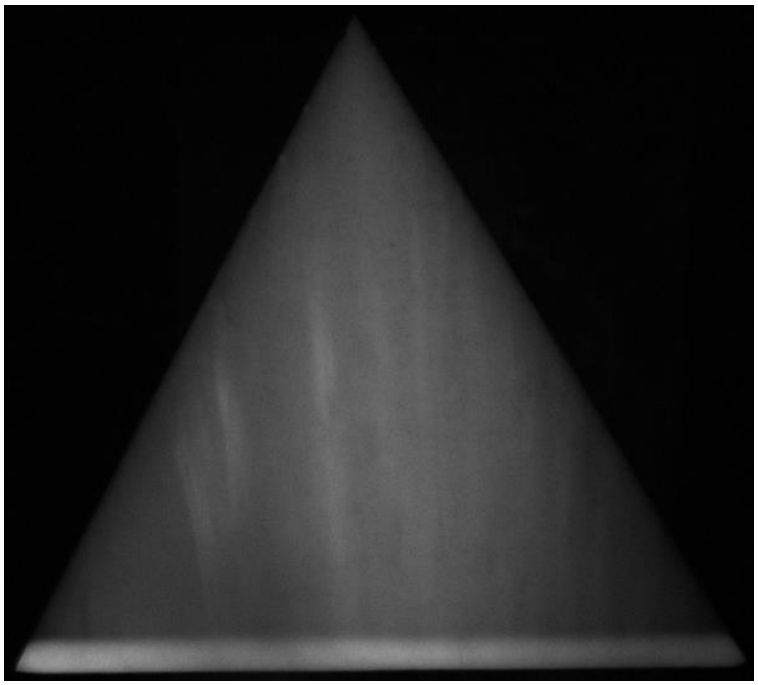

(a)

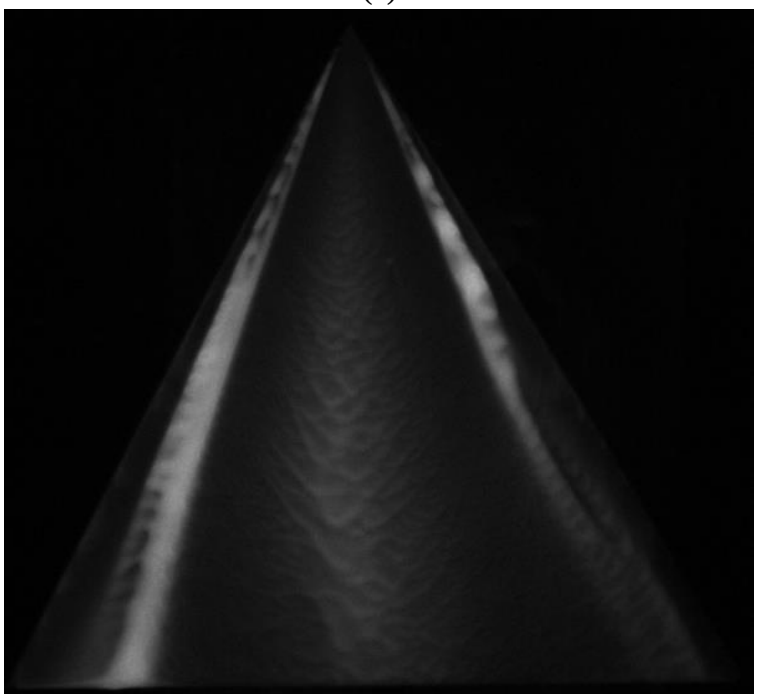

(b)

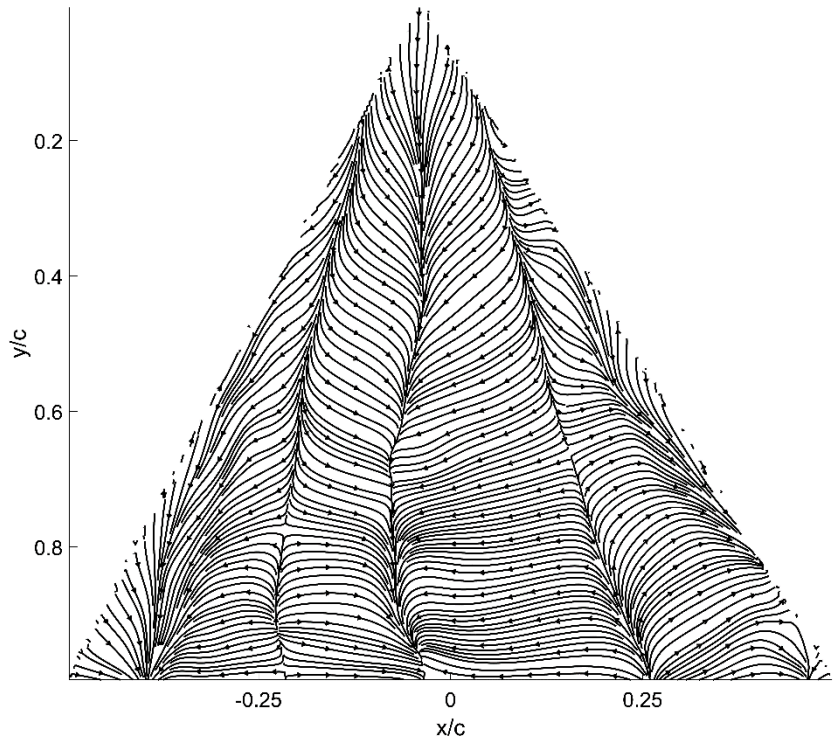

(c)

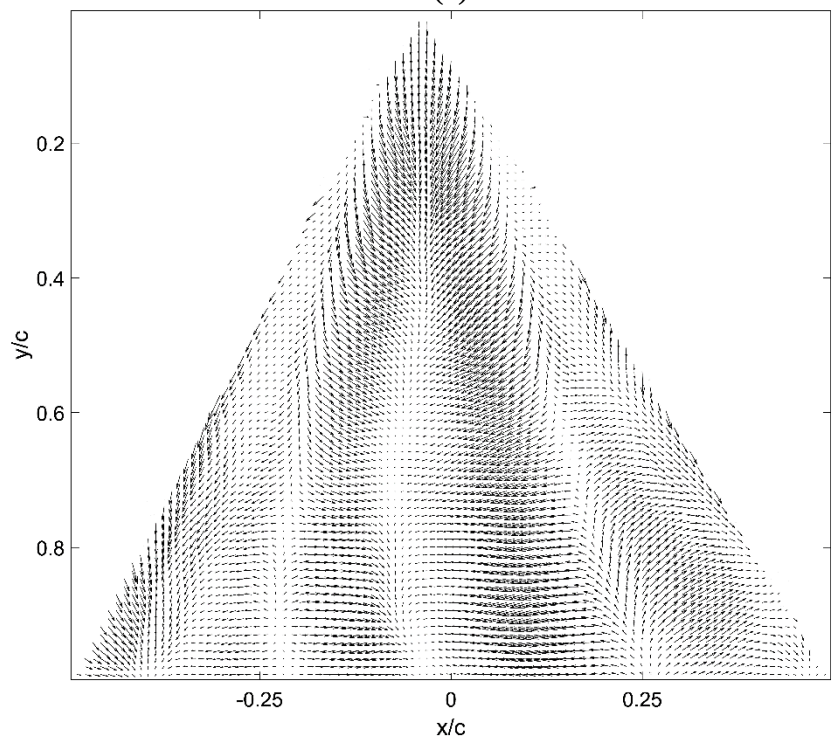

(d)

Figure 46: (a) initial image, (b) final image, (c) skin-friction lines, and (d) skin-friction vectors for 60° delta wing at 15° AoA

Figures 47 (a), (b), (c), and (d) are the initial luminescent oil image, the final luminescent oil image, the skin-friction line plot, and the skin-friction vector plot respectively for the case of a 60° delta wing at 20° AoA.

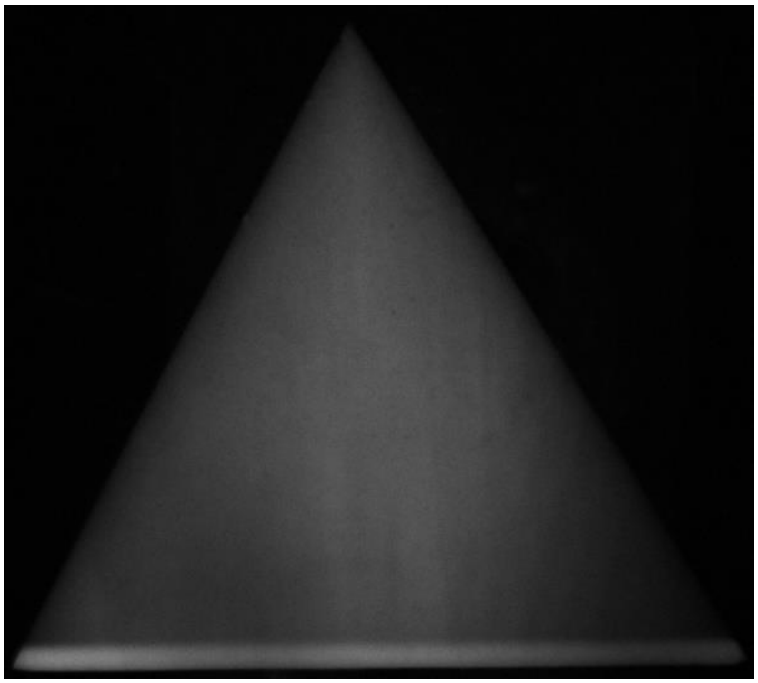

(a)

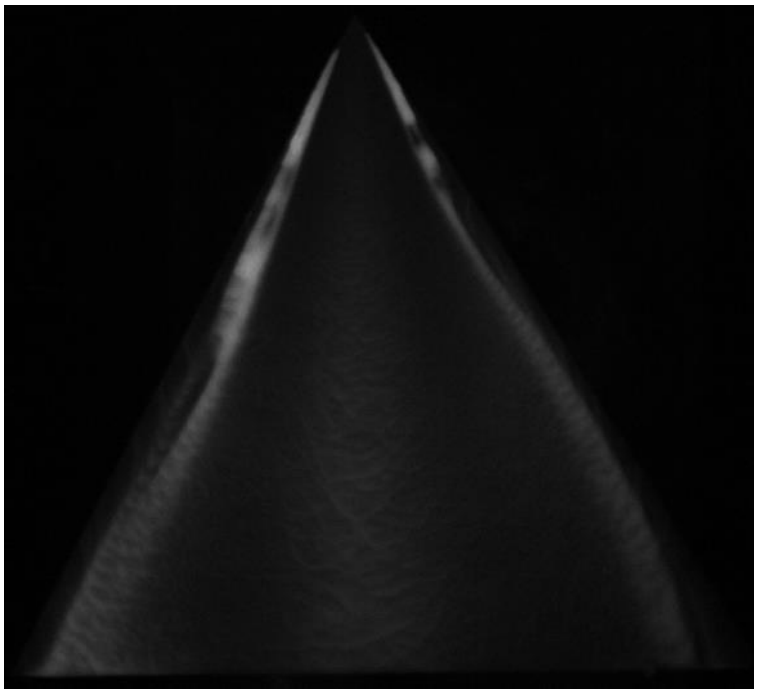

(b)

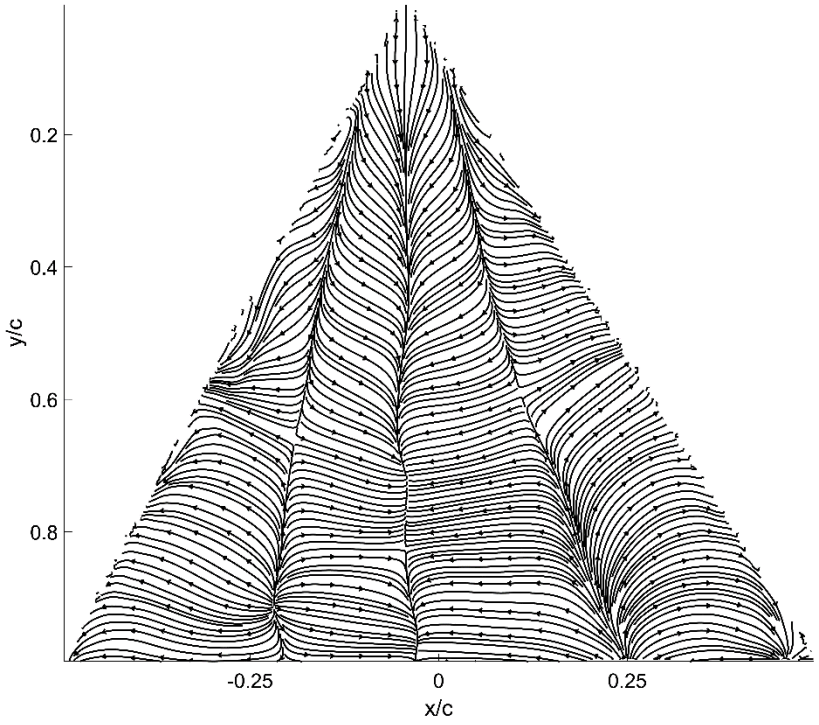

(c)

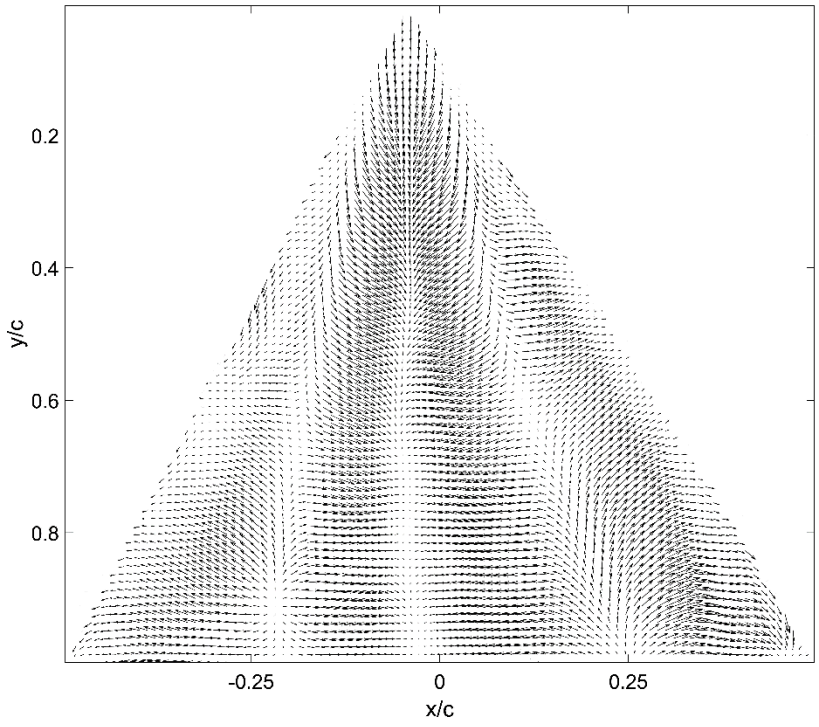

(d)

Figure 47: (a) initial image, (b) final image, (c) skin-friction lines, and (d) skin-friction vectors for 60° delta wing at 20° AoA

Figures 48 (a), (b), (c), and (d) are the initial luminescent oil image, the final luminescent oil image, the skin-friction line plot, and the skin-friction vector plot respectively for the case of a 60° delta wing at 25° AoA.

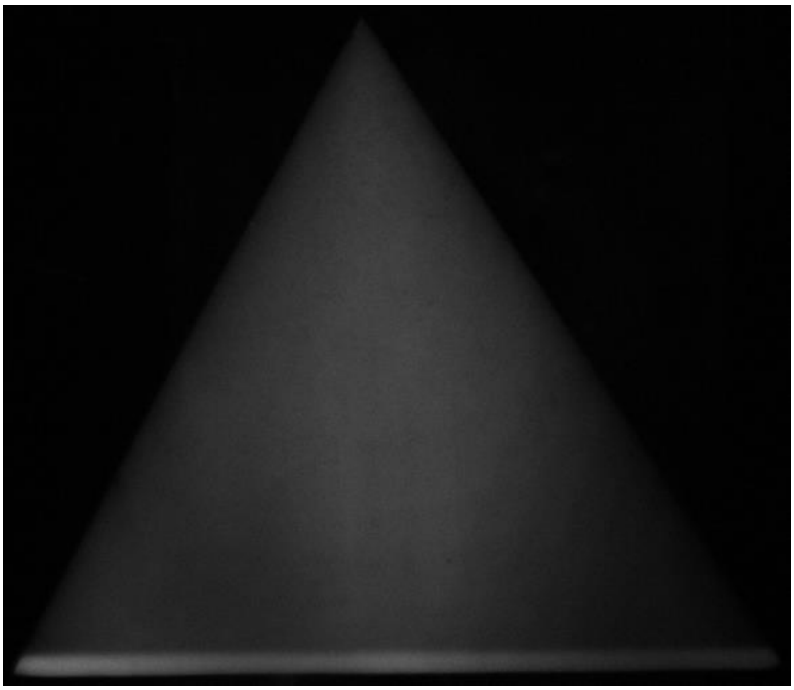

(a)

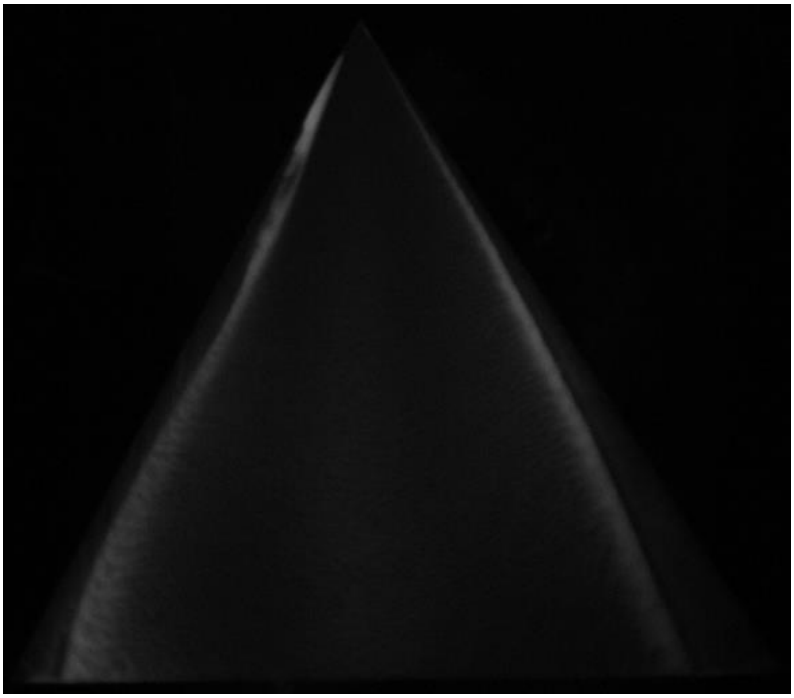

(b)

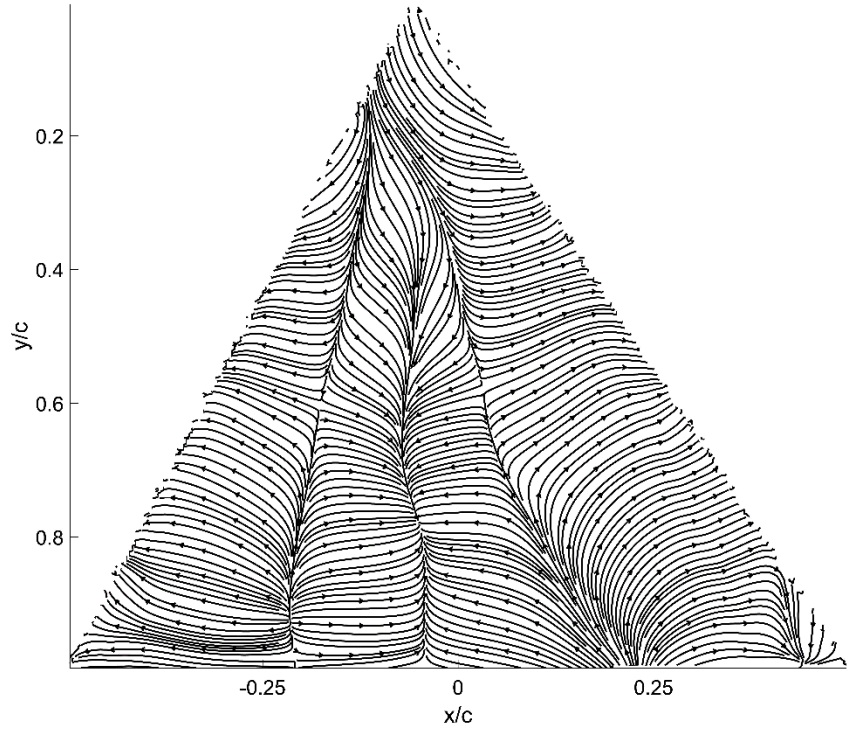

(c)

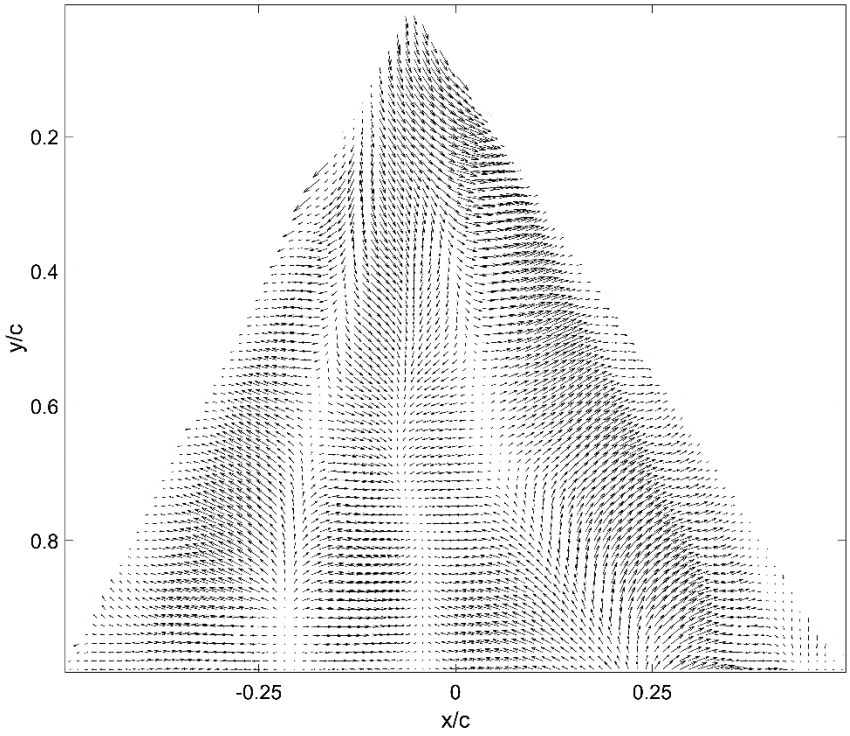

(d)

Figure 48: (a) initial image, (b) final image, (c) skin-friction lines, and (d) skin-friction vectors for 60° delta wing at 25° AoA

As expected, no discernible pattern can be seen for the skin-friction lines at -5° AoA. At 0° AoA, there is a clear primary separation line down the middle, until about y/c = 0.8. The secondary separation lines are also weak, which is the case for the 55° delta wing as well. There are now three saddle points, compared to 1 for the 55° delta wing at the same AoA. Their locations are y/c = 0.3, 0.87, 0.98 and x/c = -0.15, -0.3, 0.25 respectively. For the 5° AoA, the location of the secondary separation lines is relatively closer to the center compared to the other delta wings mentioned above. These can be found at x/c = 0.3 and -0.35. The location of the saddle points is relatively similar to that of the 55° delta wing. There are 4 saddle points located at y/c = 0.85, 0.8, 0.72, 0.75 and x/c = -0.35, -0.27, 0.25, 0.3 respectively. For the 10° case, there is a lack of clear secondary separation lines. A focus has formed instead of saddle points at y/c = 0.9 and x/c = -0.375. An interesting observation is the lack of discernible saddle points unlike that of the 50° and 55° delta wings.

For the 15° AoA, there is also an absence of the secondary separation lines, which is similar to that seen in the 55° delta wing case. One important observation seen in Figure 46 (b) is that there seems to be an asymmetric oil movement. The oil-film on the right side of the wing moved less than the left, and a vortex breakdown occurs around y/c = 0.4 on the right. A number of variables might have contributed to this. The first being the presence of a small yaw angle. While the experiment was set to be as centered in the wind tunnel as possible, the effect of a small angle is exacerbated by the low-speed condition chosen for the experiments. The second, which is less likely, is that the flow in the wind tunnel might be unsteady. Theoretically, the flow should be steady and symmetric since the delta wing is symmetric. However, in an experiment setting, many factors like viscosity and imperfect model may affect the flow over the wing. When compounded together, these unforeseen variables may or may not influence how the flow interacts with the

boundary layer of the wing. Similarly, for the 20° AoA case, there seems to be vortex breakdowns at y/c = 0.2 on the right of the centerline, and at y/c = 0.5 on the left of the centerline. There are now three saddle points when there was none at 15° AoA. They are located at y/c = 0.65, 0.6, 0.82 and x/c = -0.2, 0.15, -0.05. Lastly, the 25° AoA condition shows that the tip vortex induced wing tip vortices that are very near the edges as seen in Figure 48 (b). The presence of a primary separation line down the middle, instead of a primary reattachment line at 25° AoA, is the main difference for the 60° delta wing compared to the 50° and 55° wings. All the lines are asymmetric, and the primary separation line does not start at the tip unlike the other wings. to a higher sweep angle, the primary vortex forms further away to the surface compared to that of the 50° delta wing.

65° Delta Wing

The 65° delta wing has a chord length of 189mm and a span of 176mm. This specific delta wing is considered a slender delta wing, and research done on a 65° delta wing includes numerical simulation and many experiments performed over the past 50 years. Therefore, this configuration is better known as the “classical” delta wing. The tip vortices on slender delta wings are also not as heavily dependent on Reynolds number compared to non-slender delta wings.

Figures 49 (a), (b), (c), and (d) are the initial luminescent oil image, the final luminescent oil image, the skin-friction line plot, and the skin-friction vector plot respectively for the case of a 65° delta wing at -5° AoA.

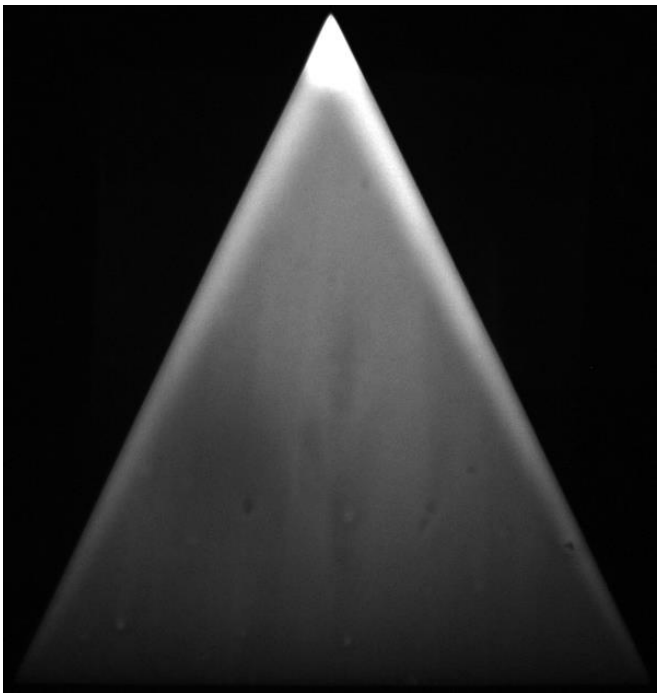

(a)

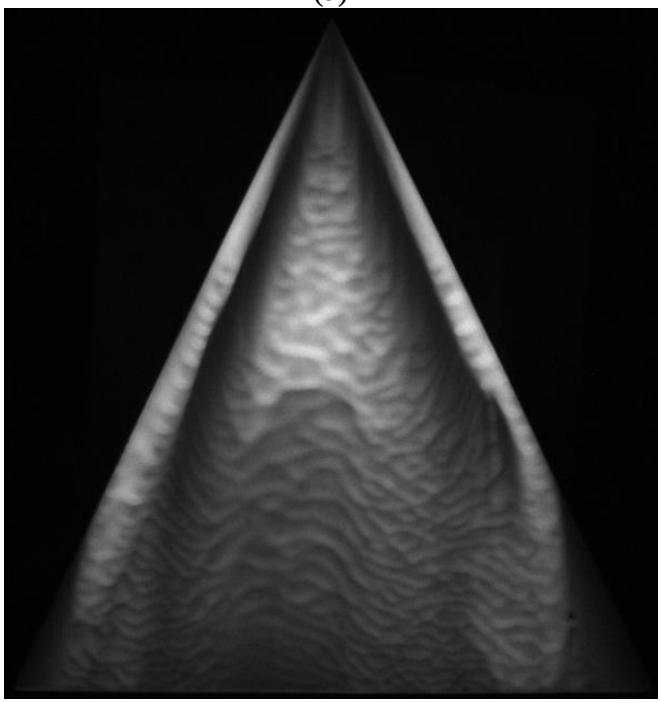

(b)

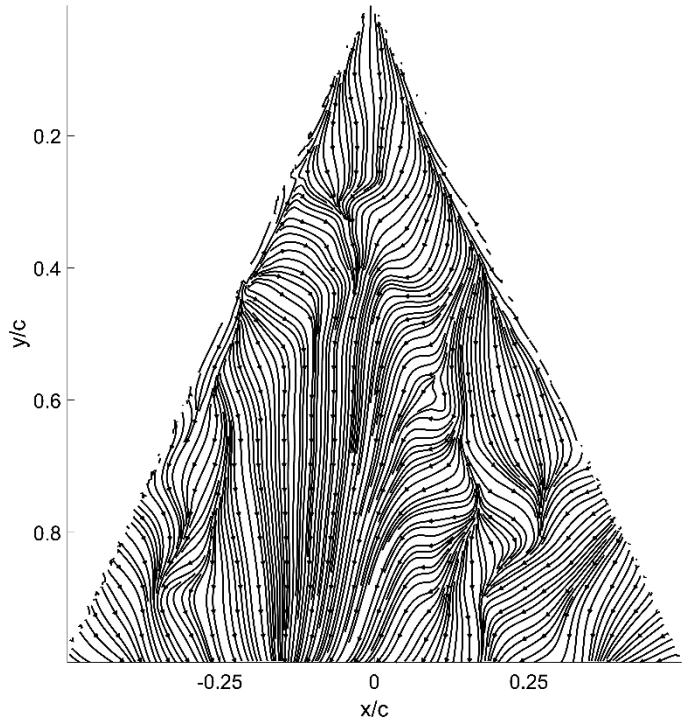

(c)

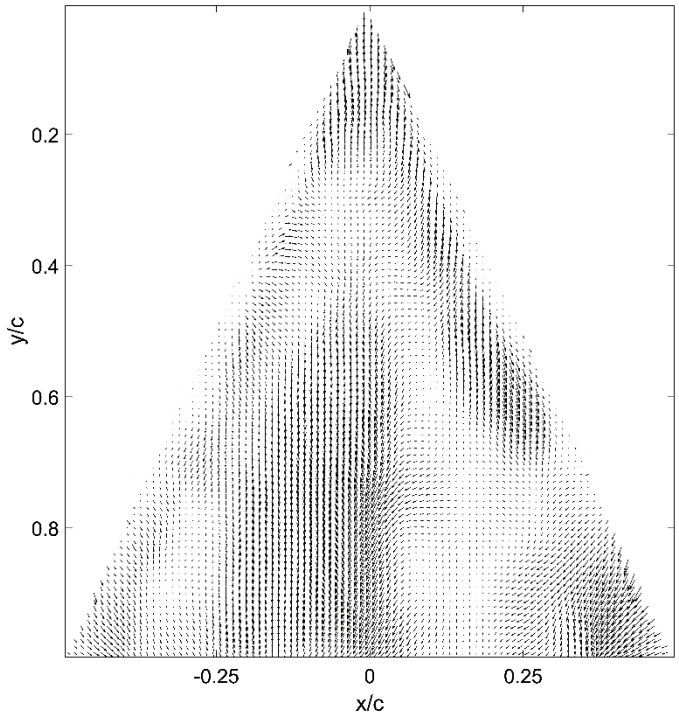

(d)

Figure 49: (a) initial image, (b) final image, (c) skin-friction lines, and (d) skin-friction vectors for 65° delta wing at -5° AoA

Figures 50 (a), (b), (c), and (d) are the initial luminescent oil image, the final luminescent oil image, the skin-friction line plot, and the skin-friction vector plot respectively for the case of a 65° delta wing at 0° AoA.

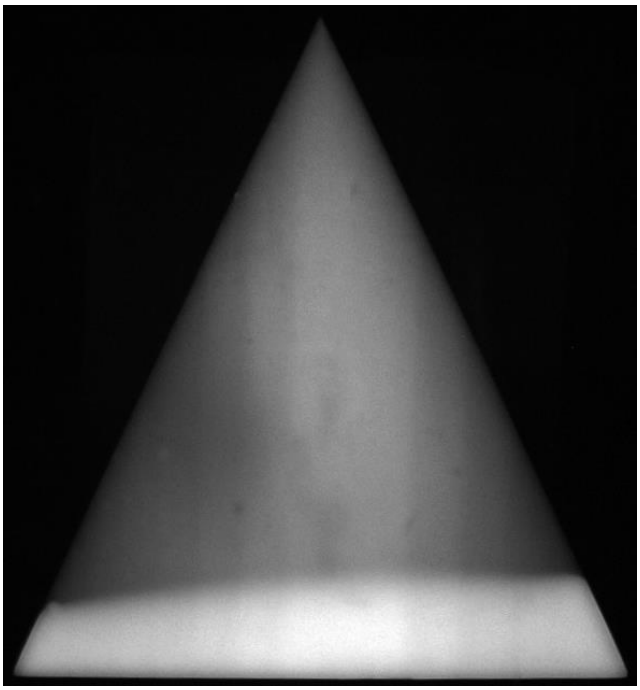

(a)

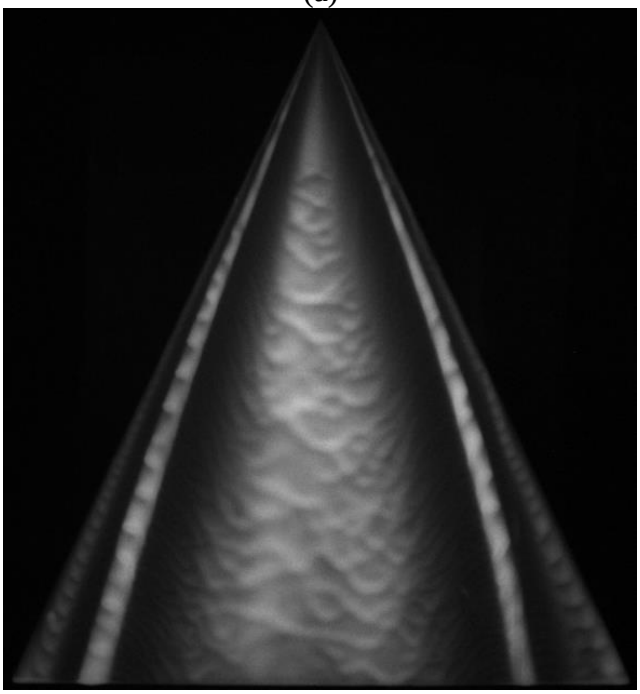

(b)

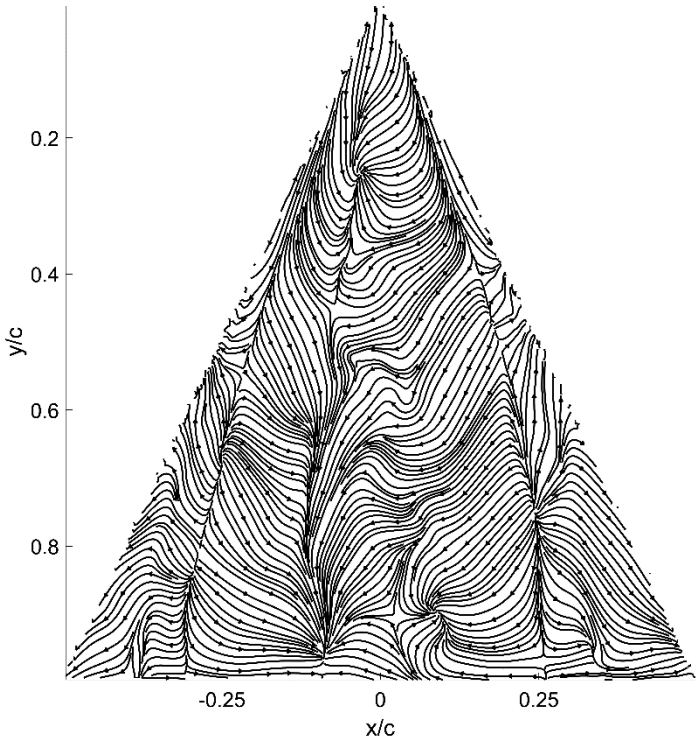

(c)

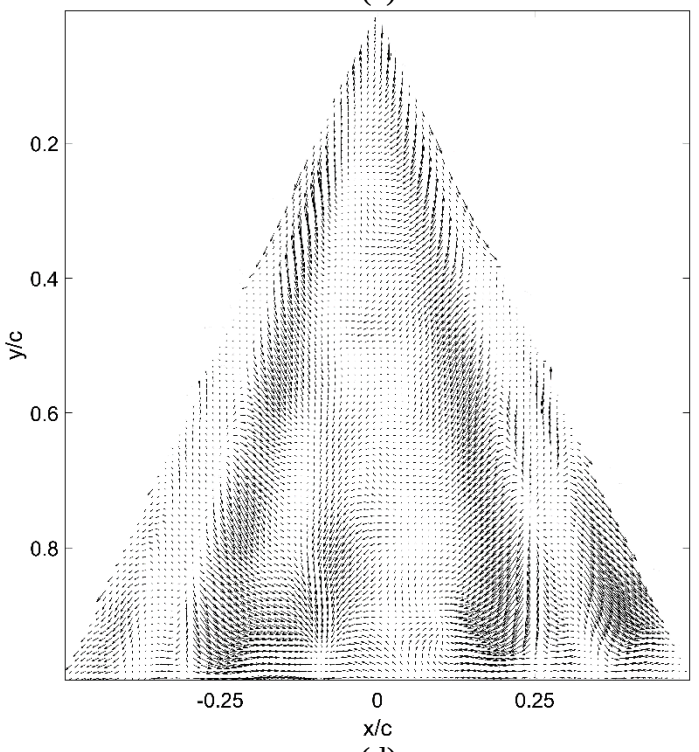

(d)

Figure 50: (a) initial image, (b) final image, (c) skin-friction lines, and (d) skin-friction vectors for 65° delta wing at 0° AoA

Figures 51 (a), (b), (c), and (d) are the initial luminescent oil image, the final luminescent oil image, the skin-friction line plot, and the skin-friction vector plot respectively for the case of a 65° delta wing at 5° AoA.

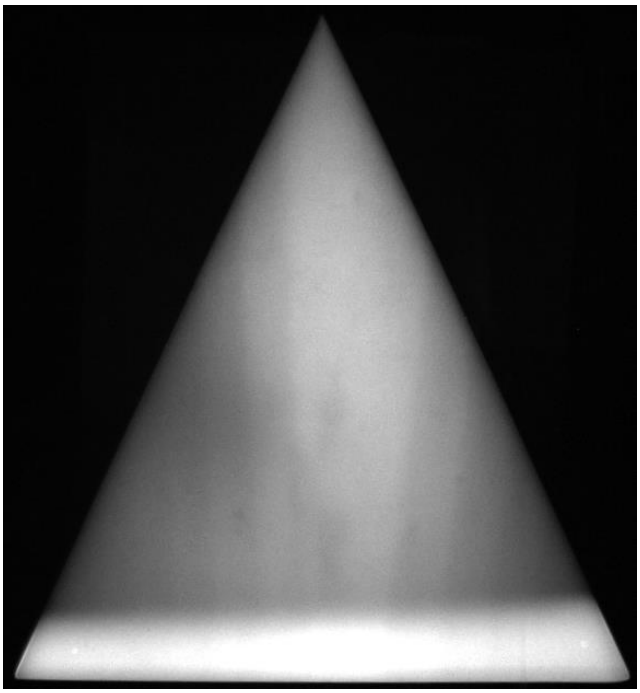

(a)

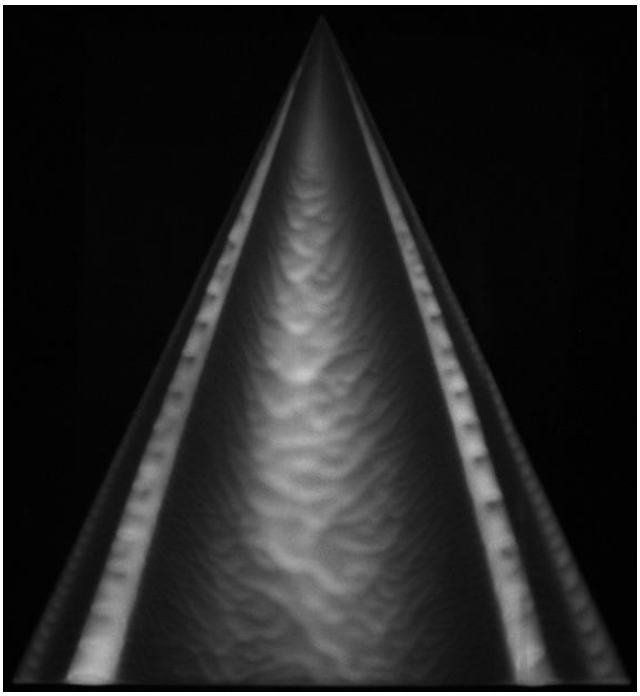

(b)

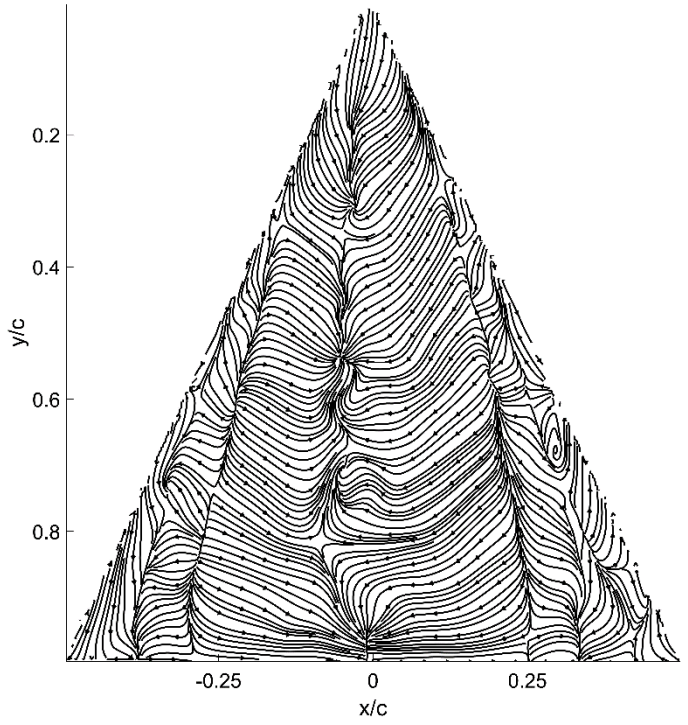

(c)

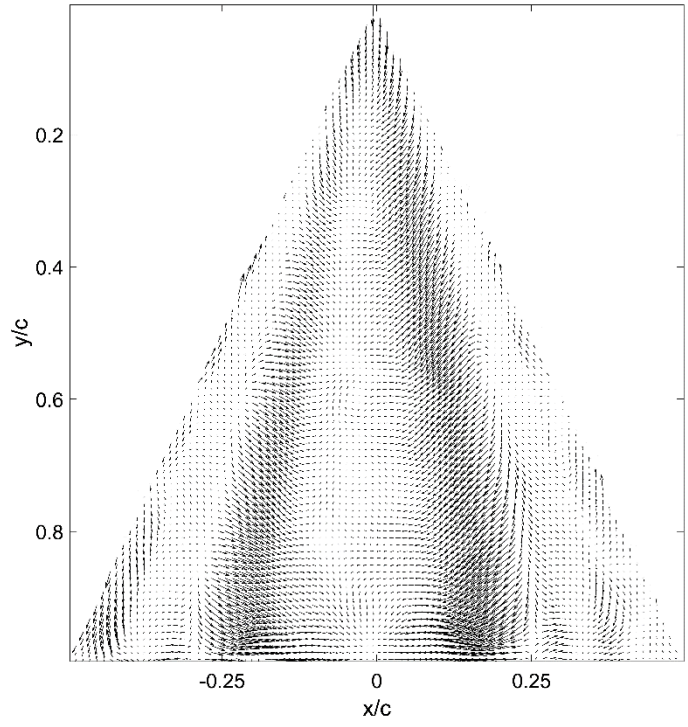

(d)

Figure 51: (a) initial image, (b) final image, (c) skin-friction lines, and (d) skin-friction vectors for 65° delta wing at 5° AoA

Figures 52 (a), (b), (c), and (d) are the initial luminescent oil image, the final luminescent oil image, the skin-friction line plot, and the skin-friction vector plot respectively for the case of a 65° delta wing at 10° AoA.

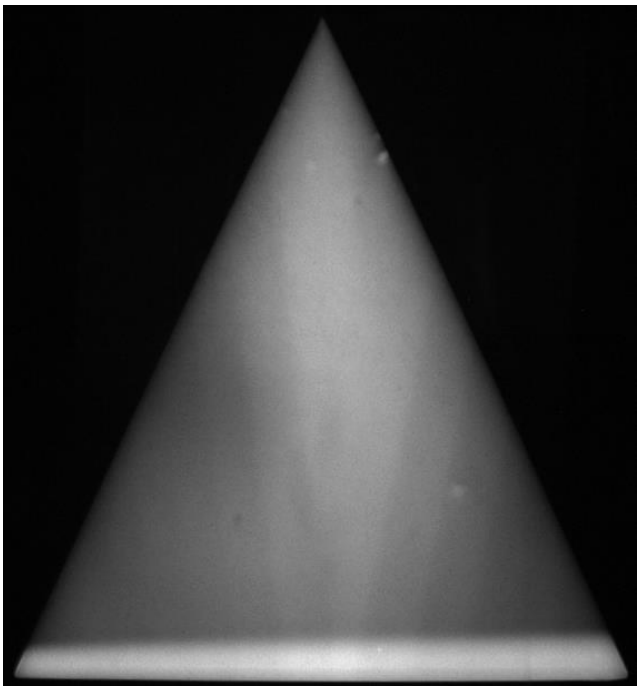

(a)

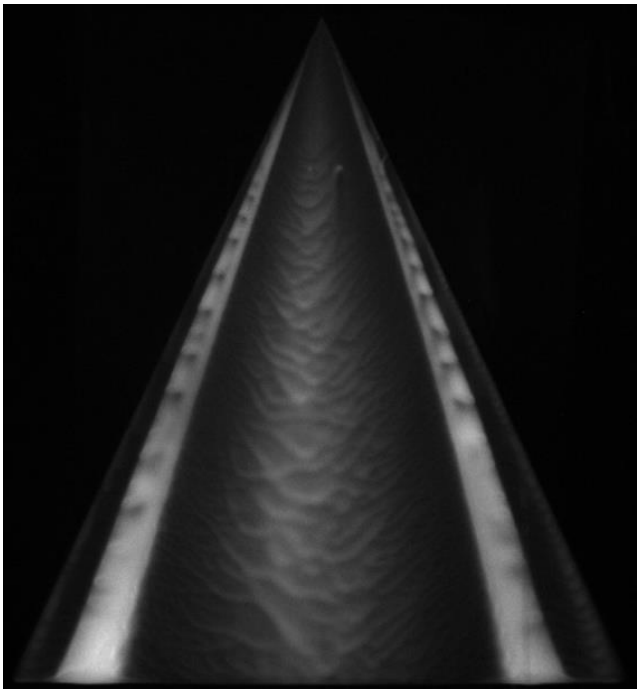

(b)

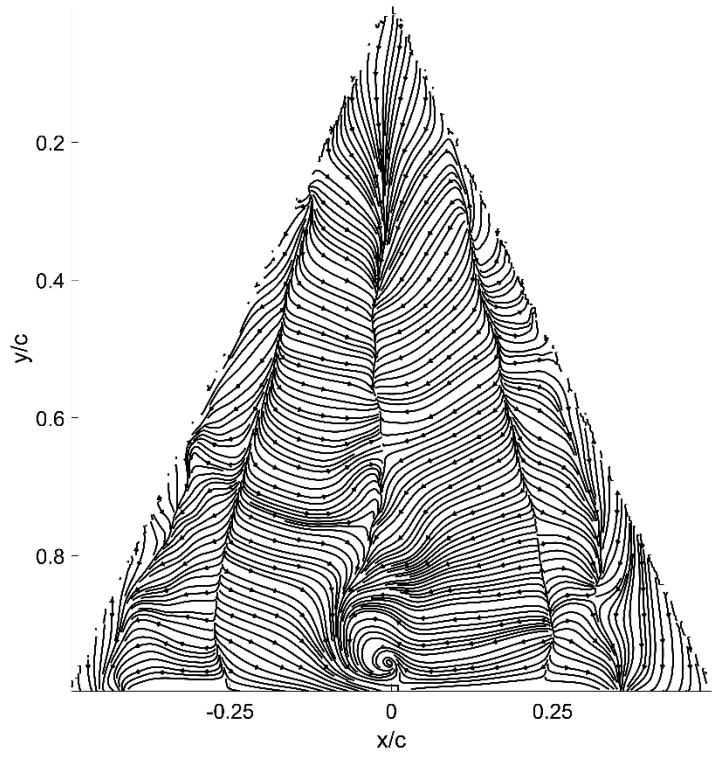

(c)

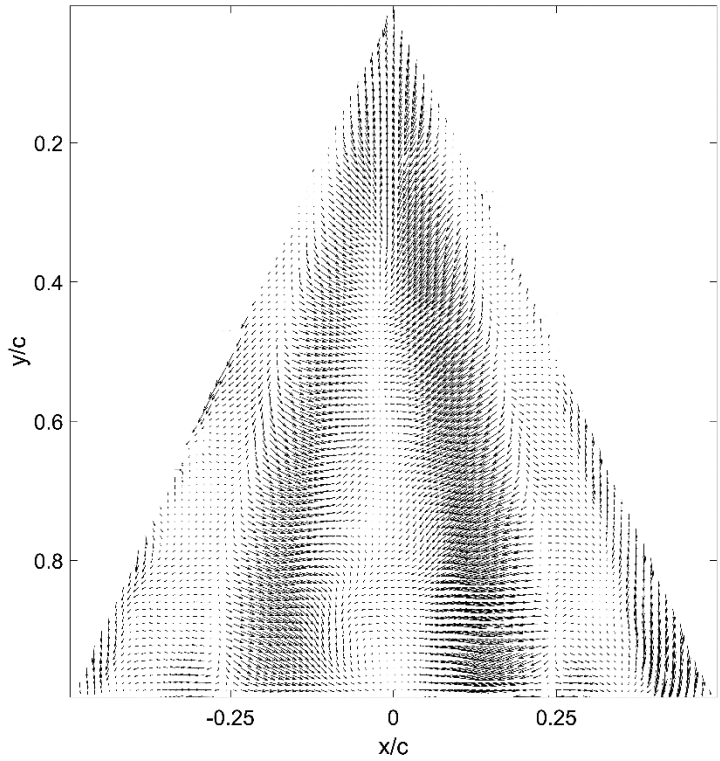

(d)

Figure 52: (a) initial image, (b) final image, (c) skin-friction lines, and (d) skin-friction vectors for 65° delta wing at 10° AoA

Figures 53 (a), (b), (c), and (d) are the initial luminescent oil image, the final luminescent oil image, the skin-friction line plot, and the skin-friction vector plot respectively for the case of a 65° delta wing at 15° AoA.

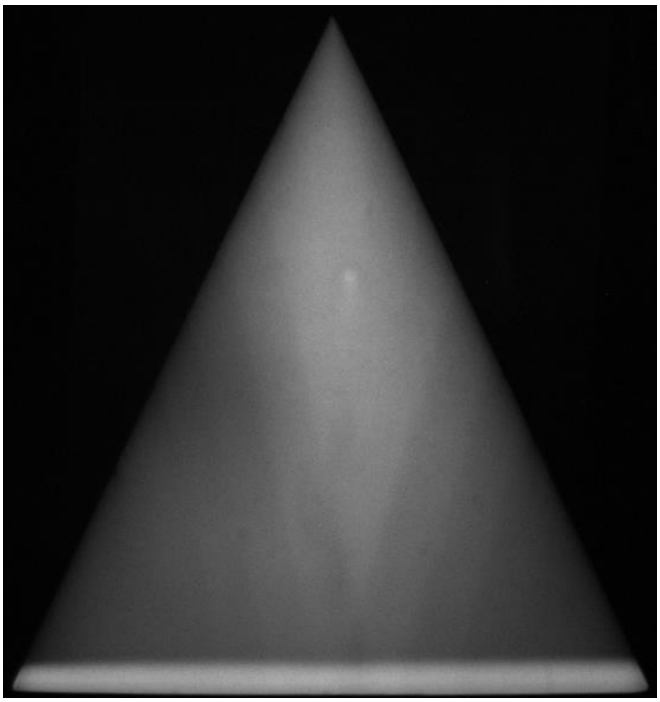

(a)

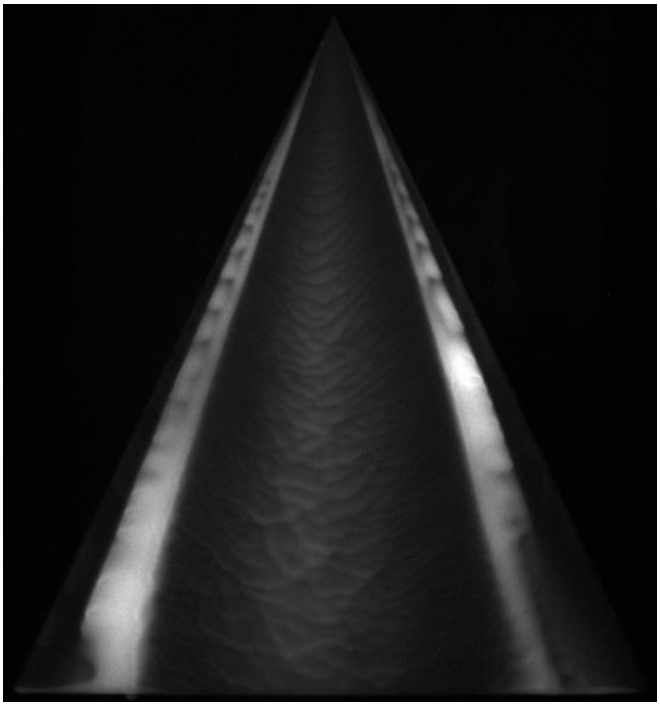

(b)

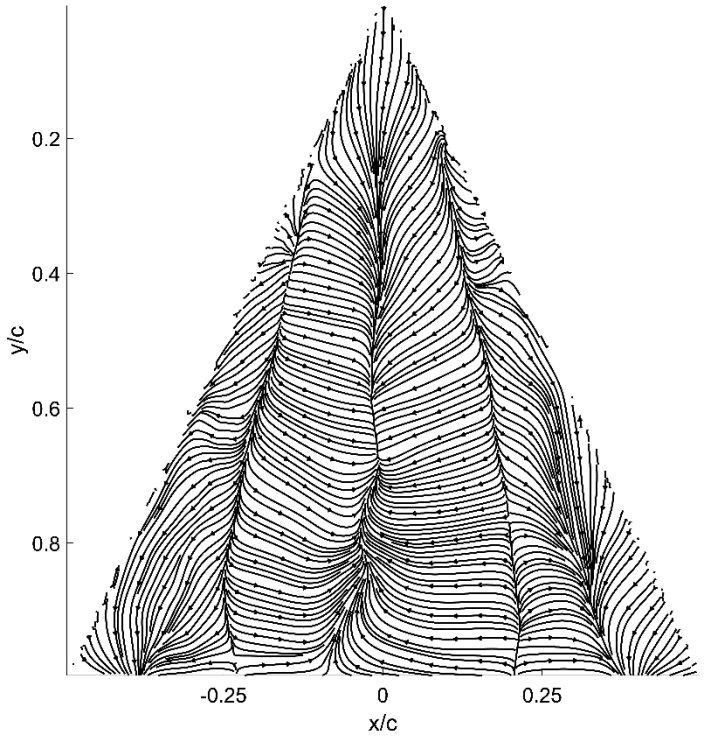

(c)

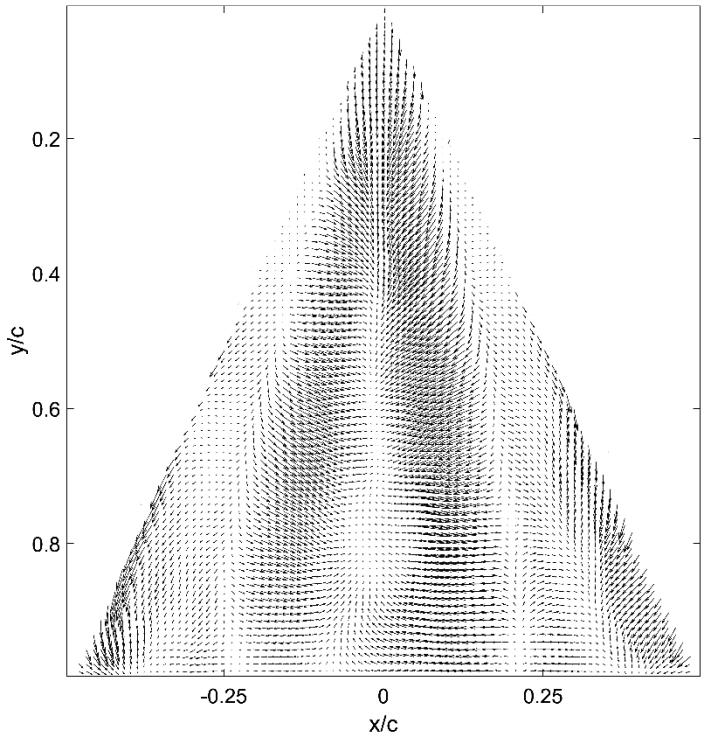

(d)

Figure 53: (a) initial image, (b) final image, (c) skin-friction lines, and (d) skin-friction vectors for 65° delta wing at 15° AoA

Figures 54 (a), (b), (c), and (d) are the initial luminescent oil image, the final luminescent oil image, the skin-friction line plot, and the skin-friction vector plot respectively for the case of a 65° delta wing at 20° AoA.

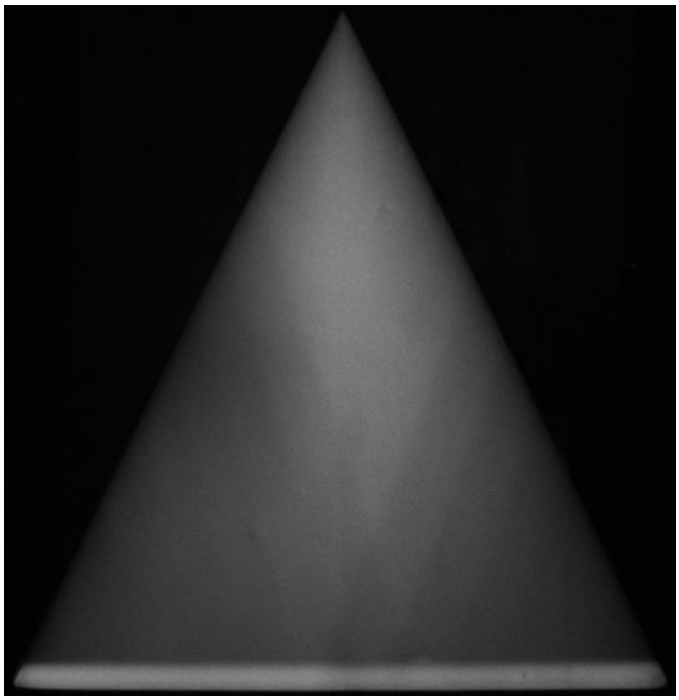

(a)

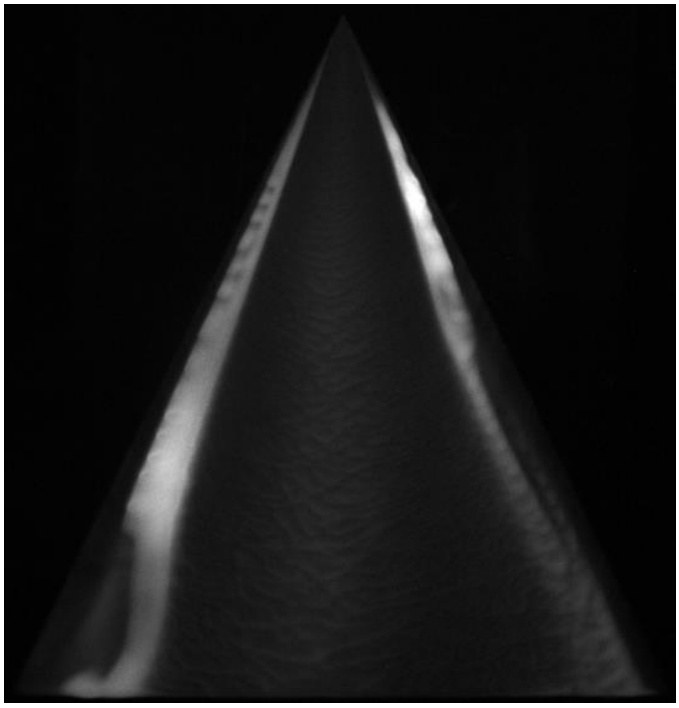

(b)

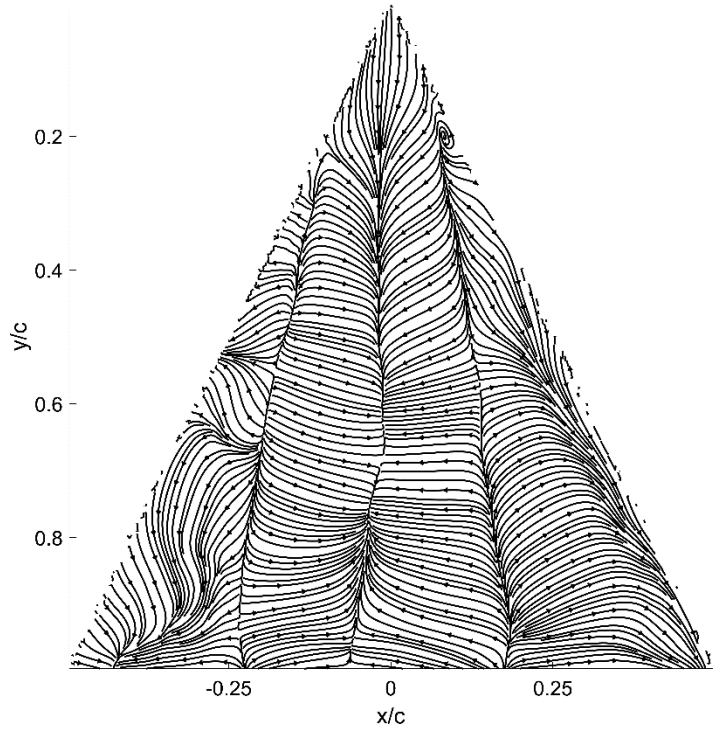

(c)

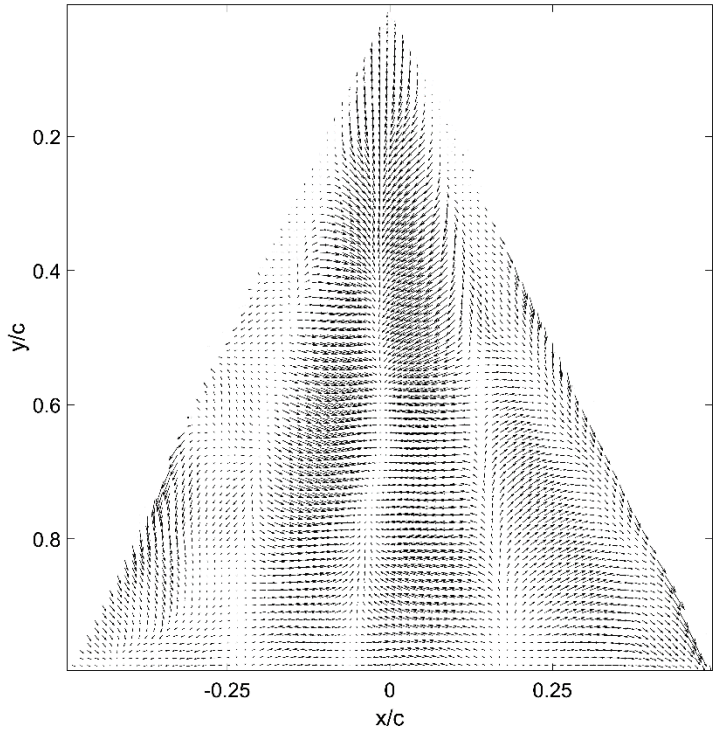

(d)

Figure 54: (a) initial image, (b) final image, (c) skin-friction lines, and (d) skin-friction vectors for 65° delta wing at 20° AoA

Figures 55 (a), (b), (c), and (d) are the initial luminescent oil image, the final luminescent oil image, the skin-friction line plot, and the skin-friction vector plot respectively for the case of a 65° delta wing at 25° AoA.

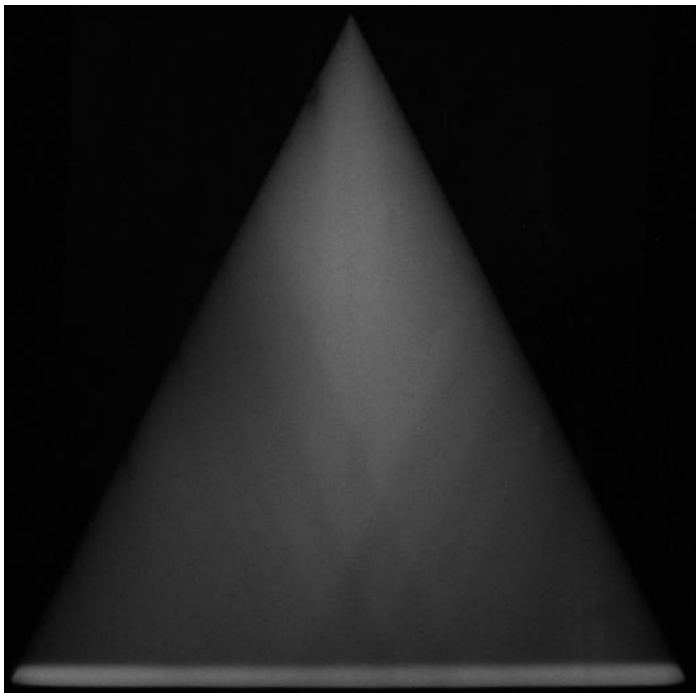

(a)

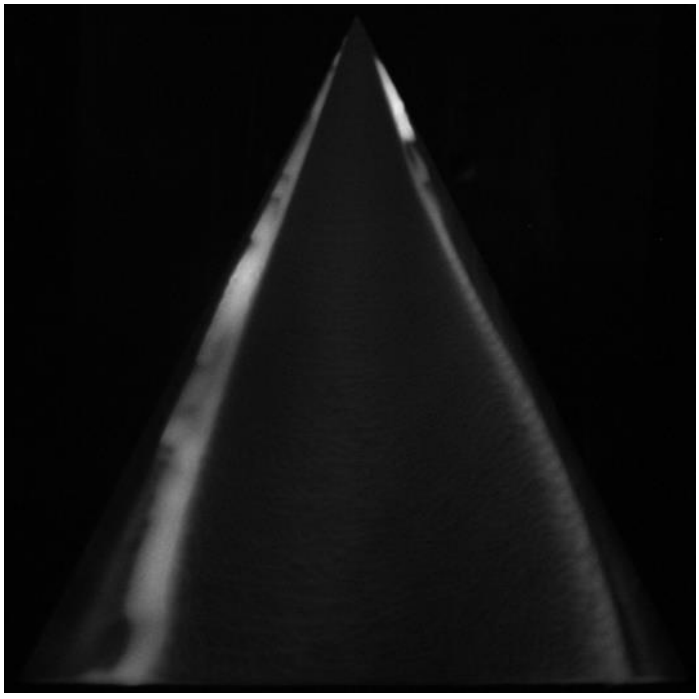

(b)

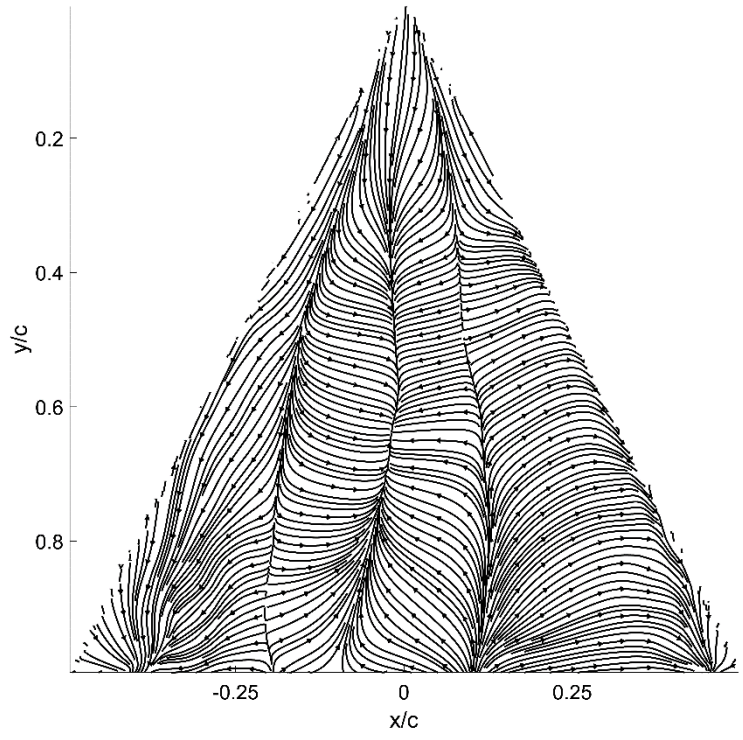

(c)

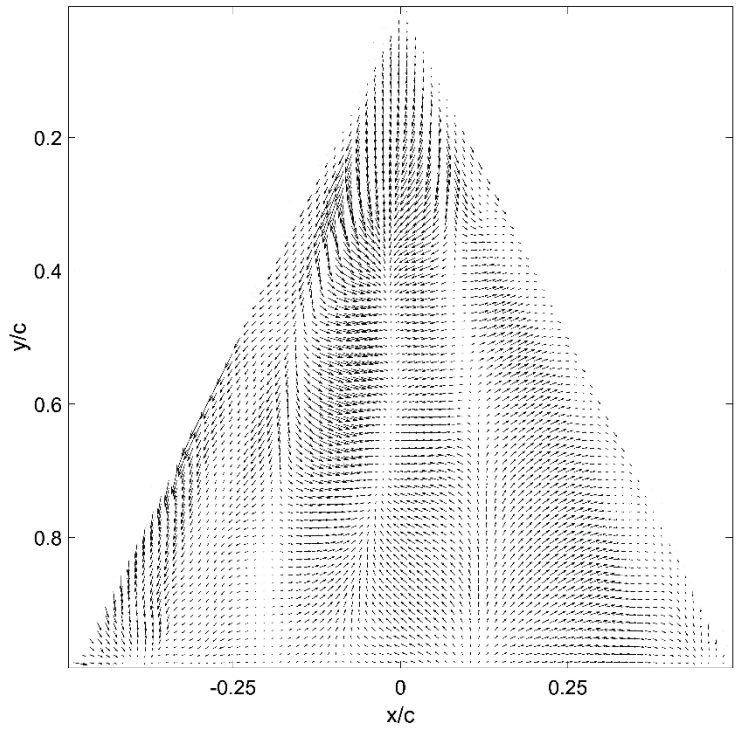

(d)

Figure 55: (a) initial image, (b) final image, (c) skin-friction lines, and (d) skin-friction vectors for 65° delta wing at 25° AoA

Some observations are made before comparisons are done with published work. Like all the other delta wings, there is no discernible pattern at a -5° AoA in the skin-friction lines. At 0° AoA, a weak primary separation line suggests a weak tip vortex, as supported by it being highly asymmetric. At a 5° AoA, there seems to be 10 saddle points, which does not correlate with delta wings of lower sweep angles. The multiple saddle points may purely be the result of noise. The experiment should be repeated to see if this is the actual flow characteristic of a 65° delta wing at 5° AoA, or if an error occurred during image acquisition. In the case of the 10° AoA, there is a very stable primary separation line down the middle until it reaches y/c = 0.7. From this location, the lines converge to form a single vortex near the trailing edge at y/c = 0.95. There are also no secondary separation lines. At 15° AoA, there is still a stable primary separation until y/c = 0.7. Figure 53 (b) also shows that there is an uneven oil movement, which is consistent with the images taken for the other delta wings. The absence of secondary separation lines persists, and there does not seem to be any saddle points that are easily observed. At 20° and 25° AoA, the key difference is that the primary separation and secondary reattachment lines are still relatively clear and symmetric, unlike those for the non-slender delta wings. Again, Figures 54 and 55 (b) shows an uneven oil movement over the surface. Hypothetical reasons for this were discussed earlier.

Woodiga and Liu [26] performed tests on a 65° delta wing at 5°, 10°, 15°, and 20° AoA, with a Reynolds number of 440,000, and there are very distinct differences between the skin-friction lines. For the 5° AoA, the multiple saddle points that were observed are not present in the published data. The only similarity between the two experiments is the presence of a weak primary separation line. As stated earlier, there is a high suspicion that either the data collected was corrupted, or that noise was not efficiently filtered out during the analysis. For the 10° AoA, the main difference is the presence of a very clear secondary separation line on both sides. This feature

is not evident after analysis of the experimental data. Some likely reasons for the difference include different Reynolds Number, different step size, and different sample size. The experiment was done at 25 frames per second, with a step size of 10, and a sample size of 150. A different Reynolds number for both experiments will mean that it experiences different flows. A study was done by Woodiga [25] and showed that the step and sample sizes were sensitive variables that must be chosen carefully. The optimal step and sample sizes chosen for the experiments in this thesis were largely experimental and chosen by observation. A method to track the luminescent intensity of different points in the image became tricky, as oil on the leading edge moved at a greater speed compared to oil near the trailing edge. A quantifiable approach on optimizing step and sample sizes for the GLOF method will be beneficial for future work. For the 15° AoA, the same difference occurs with the presence of a distinct secondary separation line, while the analysis performed above did not show this feature. Another difference is that the primary separation line is only stable until y/c = 0.5 compared to y/c = 0.7 above, before smoothening out. At 20° AoA, the only similarity between the two is the absence of secondary separation lines, and the secondary reattachment lines disappear at y/c = 0.7 for the published work due to vortex bursting, which is not evident above.

Another set of experiments performed for the 65° delta wing is the measurement of aerodynamic forces, such as Coefficient of Drag (C_D) and Coefficient of Lift (C_L) since the wings were already placed on the balance for GLOF. Calibration was done by attaching a pulley system to the balance and attaching known weights onto a bucket. This calibration allowed for the conversion of voltage into force. The results are shown below.

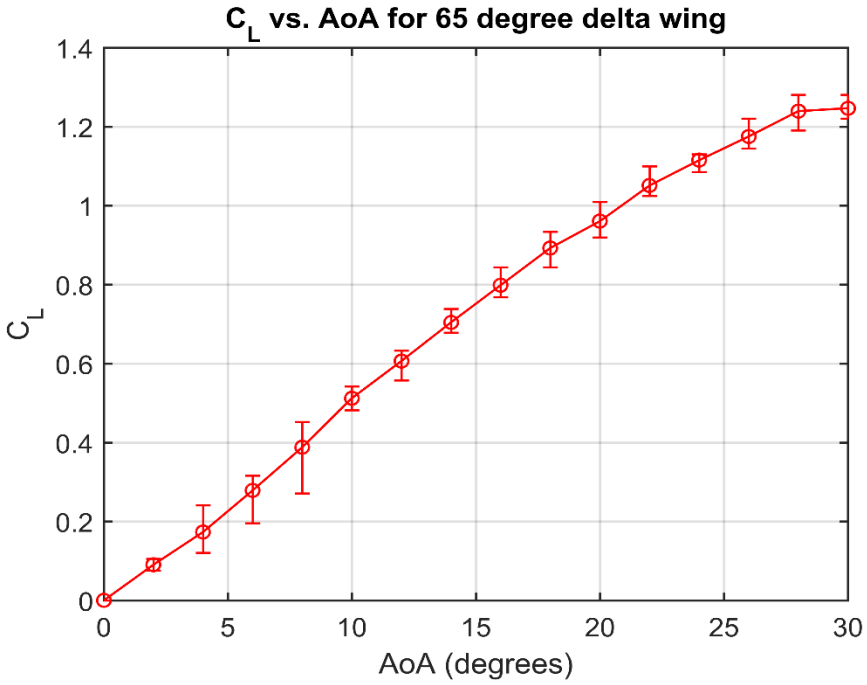

Figure 56: C_L vs. Alpha graph for 65° delta wing

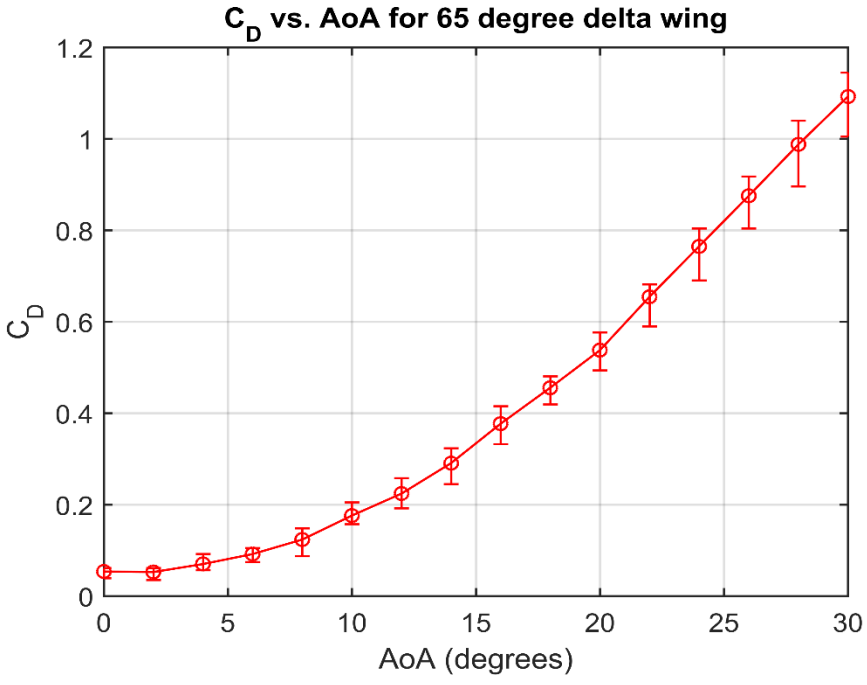

Figure 57: C_D vs. Alpha graph for 65° delta wing

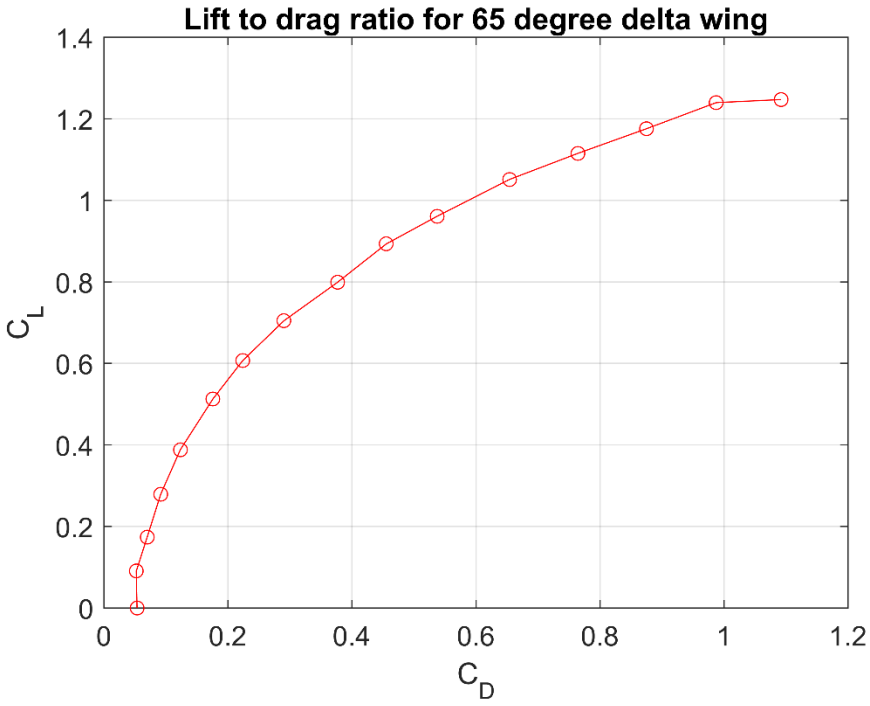

Figure 58: C_L vs. C_D graph for 65° delta wing

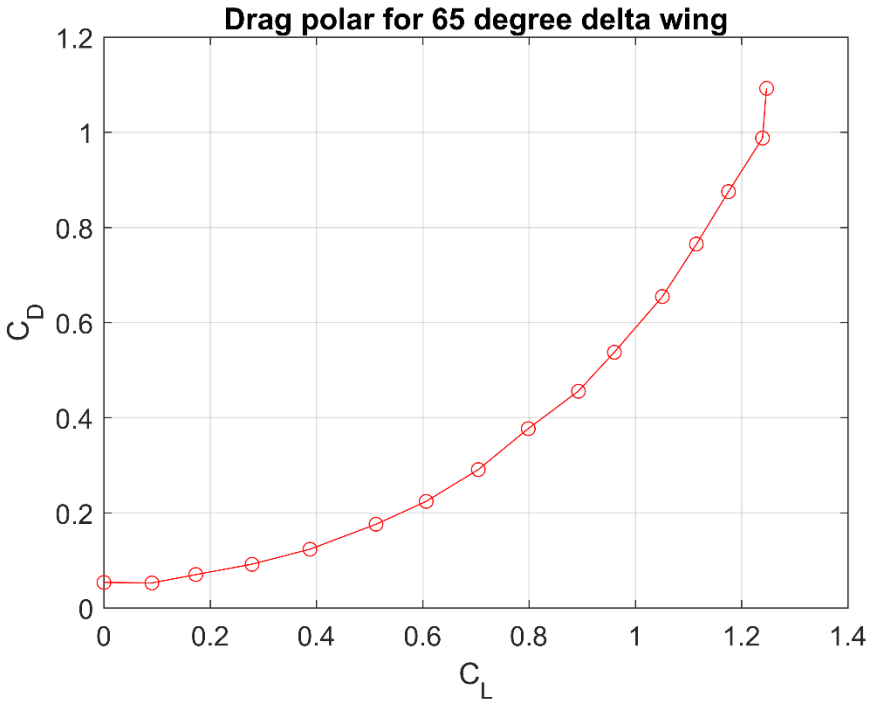

Figure 59: C_D vs. C_L graph for 65° delta wing

The trend for the C_L vs. Alpha curve in Figure 56 is the same when compared to Traub et al [28] and Roy et al [29]. The published reports show a linear trend until around 40° AoA when the wing stalls. The magnitude for the coefficient of lift will not be the same due to different Reynolds number and model dimensions. However, the values are relatively close, and C_L peaks at around 1.3 for a 65° delta wing.

The trend for the C_D vs. Alpha curve in Figure 57 is relatively similar as well. Theoretically, the exponential increase in C_D as AoA is increased can be boiled down to a larger exposed surface area at higher AoA.

70° Delta Wing

The 70° delta wing has a chord length of 189mm and a span of 138mm. This configuration has also been widely studied as seen in the discussion below. With a chord length of 189mm, this configuration is the maximum sweep angle possible for the SWT facility. This is because a 19mm thick attachment had to be welded on the bottom of the wings, and this material's thickness is fixed to ensure structural integrity. These attachments are located at the wing's center of gravity and allow the wings to be fixed onto the balance. With a span of 138mm, a 19mm thick attachment is equal to 14% of the wing's span. If the sweep angle was increased to 75° for example and if the chord length was kept the same, the attachment would affect the flow significantly.

Figures 60 (a), (b), (c), and (d) are the initial luminescent oil image, the final luminescent oil image, the skin-friction line plot, and the skin-friction vector plot respectively for the case of a 70° delta wing at -5° AoA.

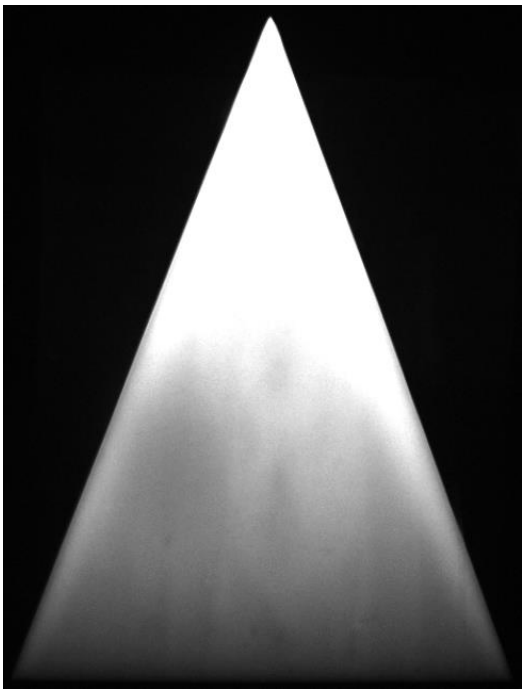

(a)

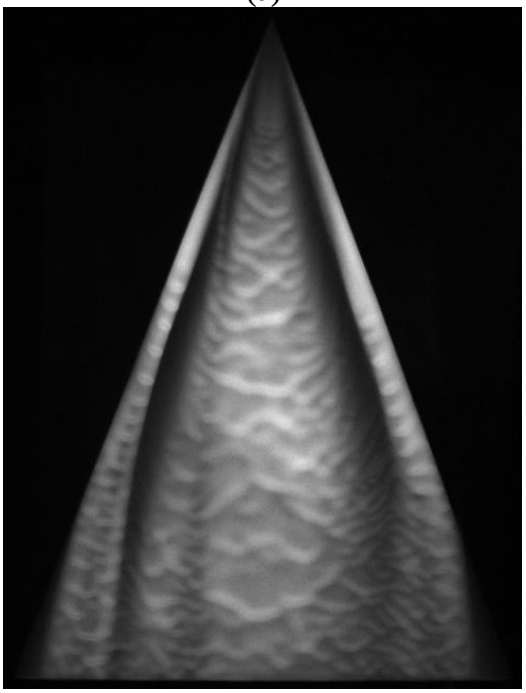

(b)

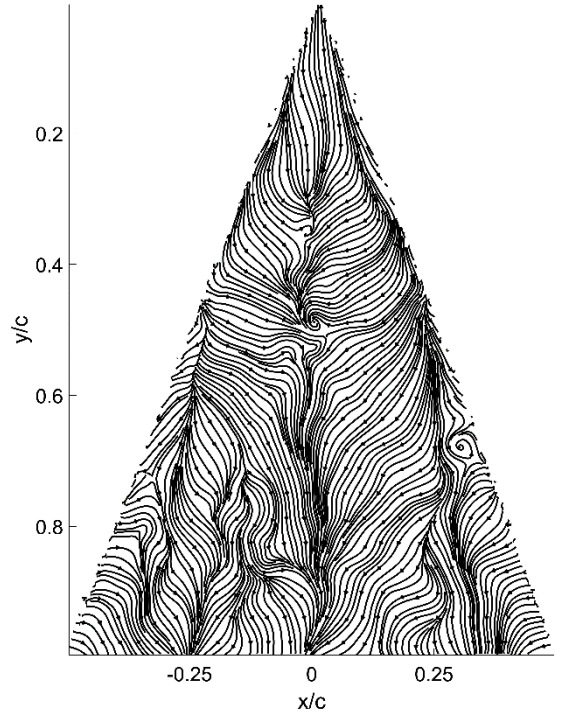

(c)

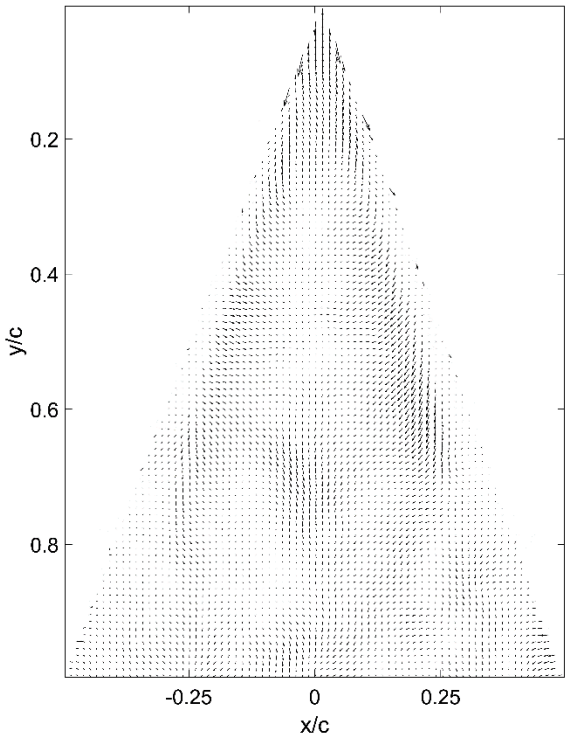

(d)

Figure 60: (a) initial image, (b) final image, (c) skin-friction lines, and (d) skin-friction vectors for 70° delta wing at -5° AoA

Figures 61 (a), (b), (c), and (d) are the initial luminescent oil image, the final luminescent oil image, the skin-friction line plot, and the skin-friction vector plot respectively for the case of a 70° delta wing at 0° AoA.

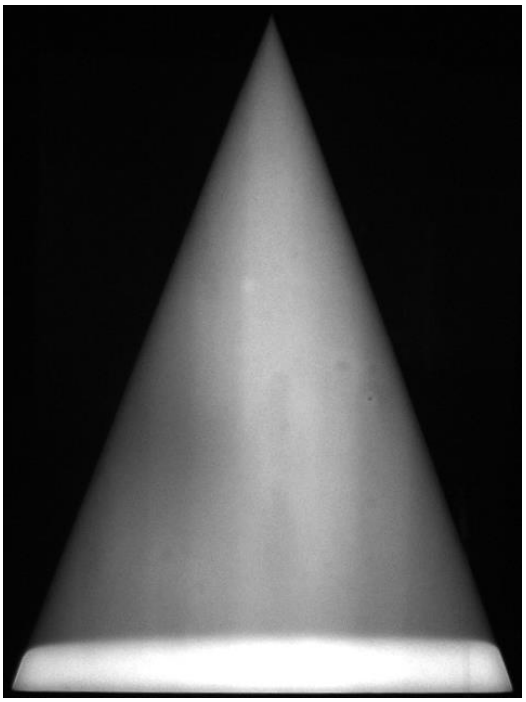

(a)

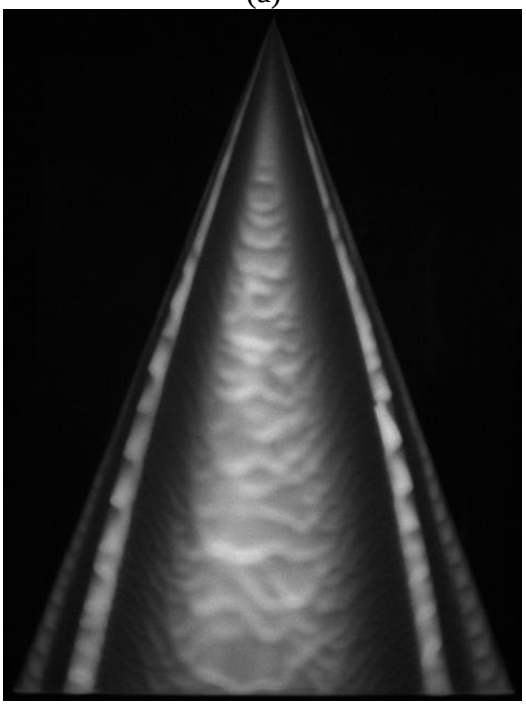

(b)

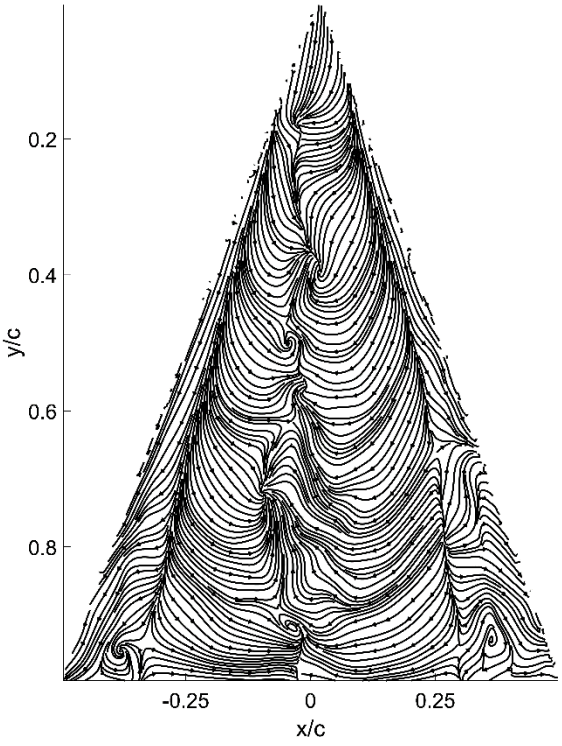

(c)

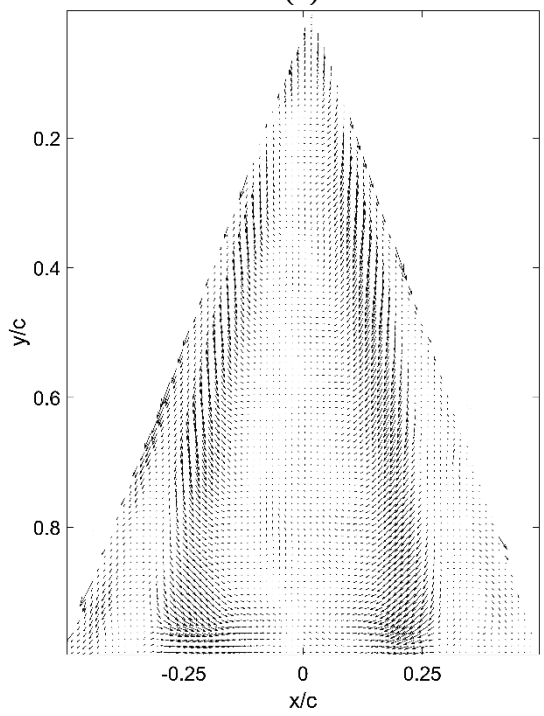

(d)

Figure 61: (a) initial image, (b) final image, (c) skin-friction lines, and (d) skin-friction vectors for 70° delta wing at 0° AoA

Figures 62 (a), (b), (c), and (d) are the initial luminescent oil image, the final luminescent oil image, the skin-friction line plot, and the skin-friction vector plot respectively for the case of a 70° delta wing at 5° AoA.

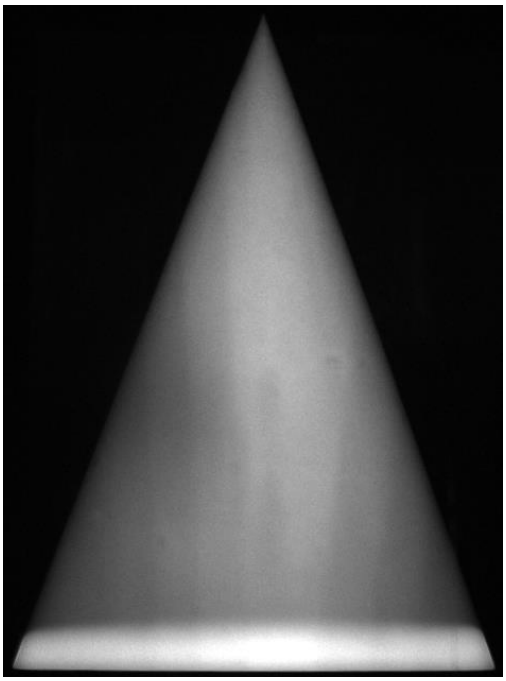

(a)

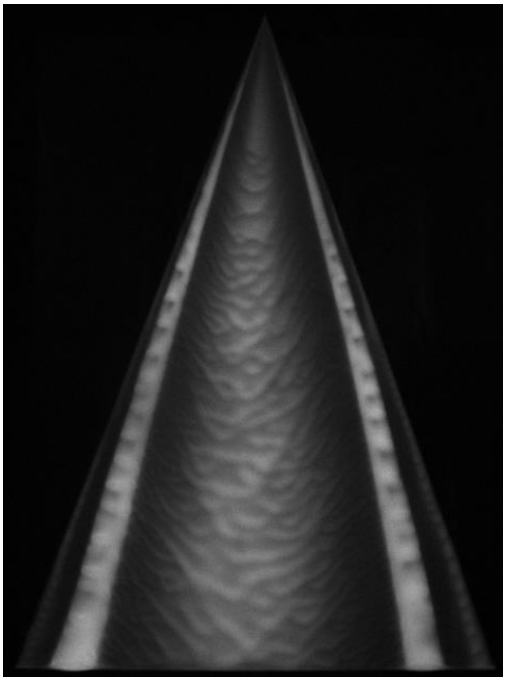

(b)

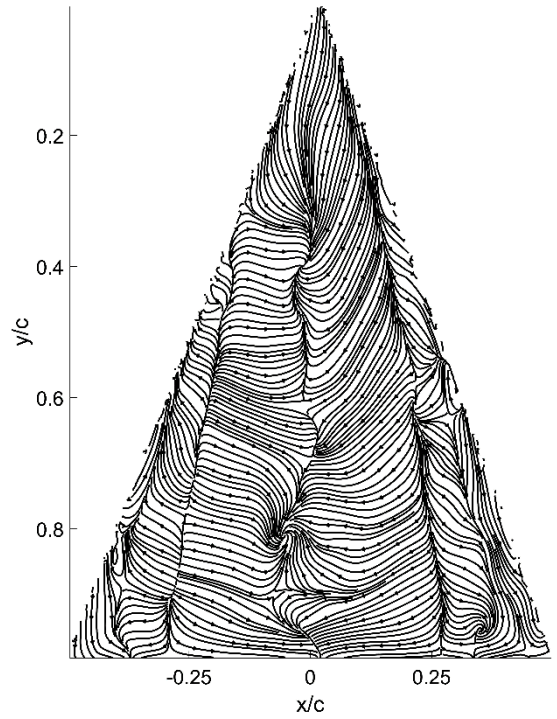

(c)

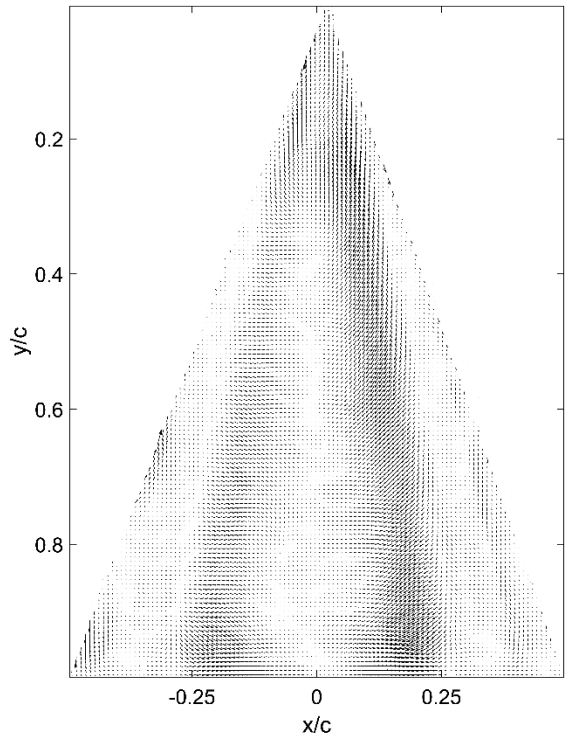

(d)

Figure 62: (a) initial image, (b) final image, (c) skin-friction lines, and (d) skin-friction vectors for 70° delta wing at 5° AoA

Figures 63 (a), (b), (c), and (d) are the initial luminescent oil image, the final luminescent oil image, the skin-friction line plot, and the skin-friction vector plot respectively for the case of a 70° delta wing at 10° AoA.

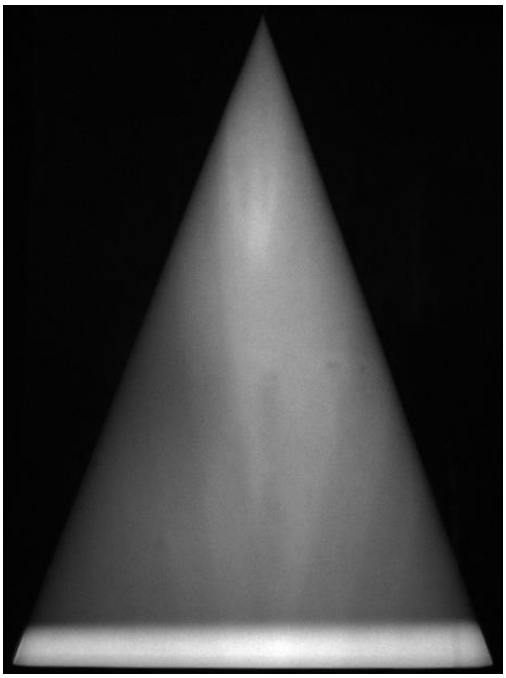

(a)

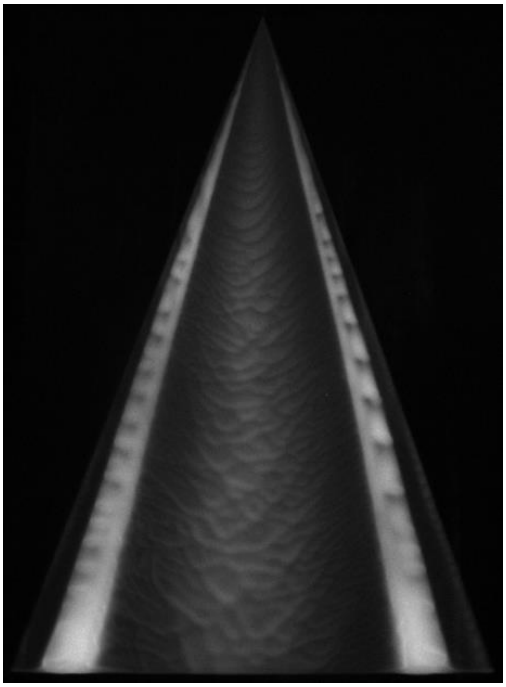

(b)

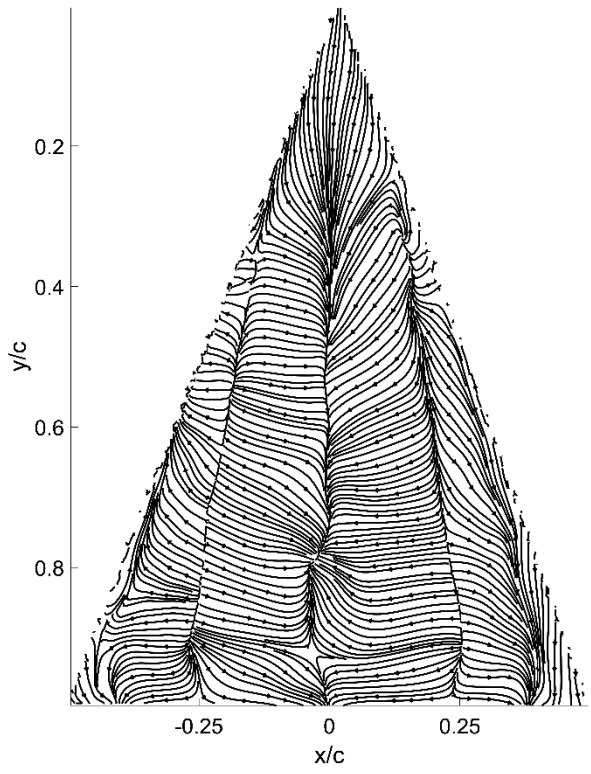

(c)

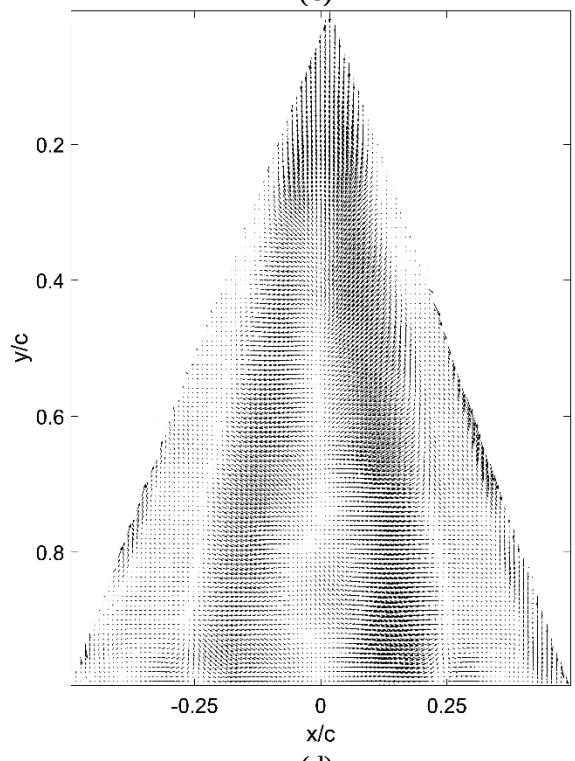

(d)

Figure 63: (a) initial image, (b) final image, (c) skin-friction lines, and (d) skin-friction vectors for 70° delta wing at 10° AoA

Figures 64 (a), (b), (c), and (d) are the initial luminescent oil image, the final luminescent oil image, the skin-friction line plot, and the skin-friction vector plot respectively for the case of a 70° delta wing at 15° AoA.

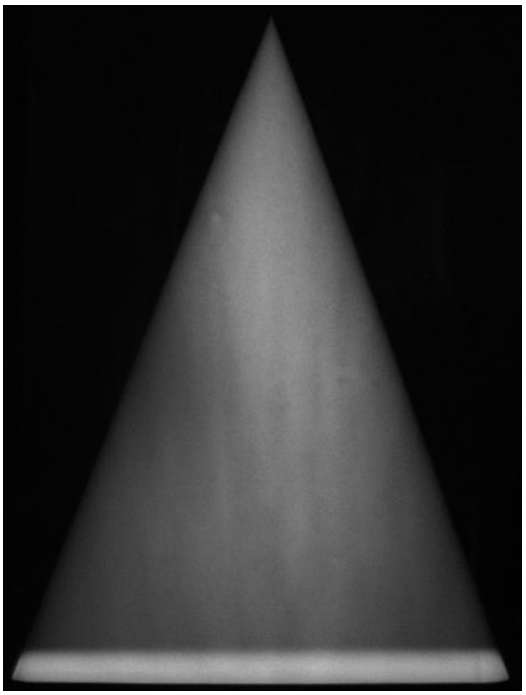

(a)

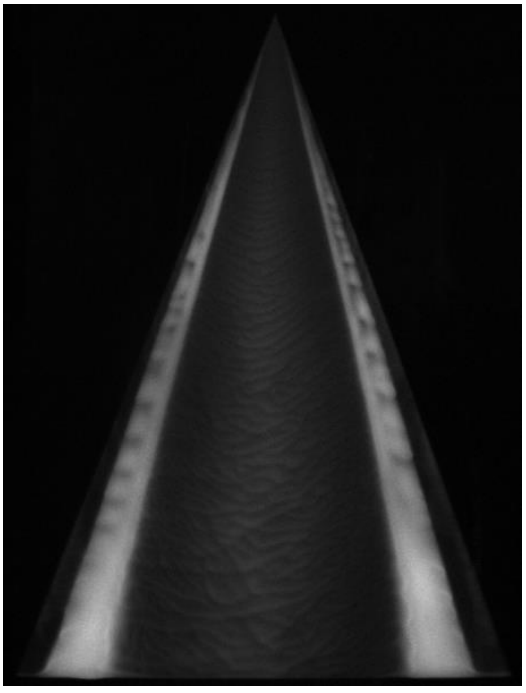

(b)

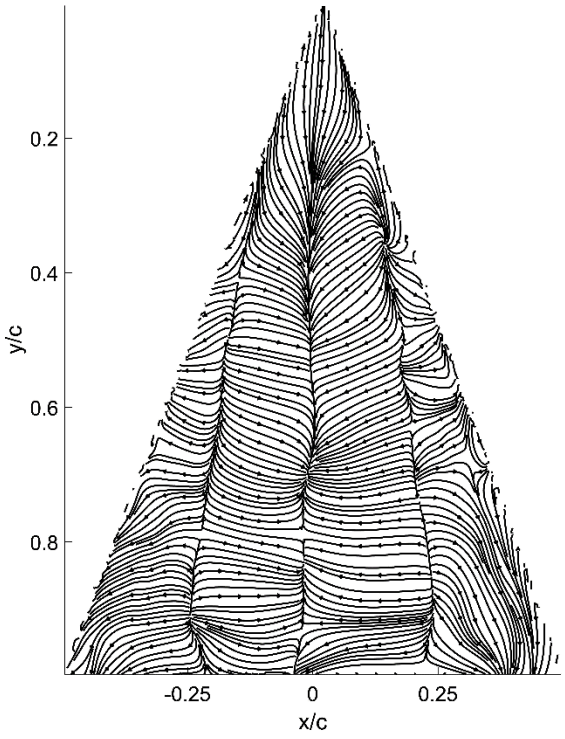

(c)

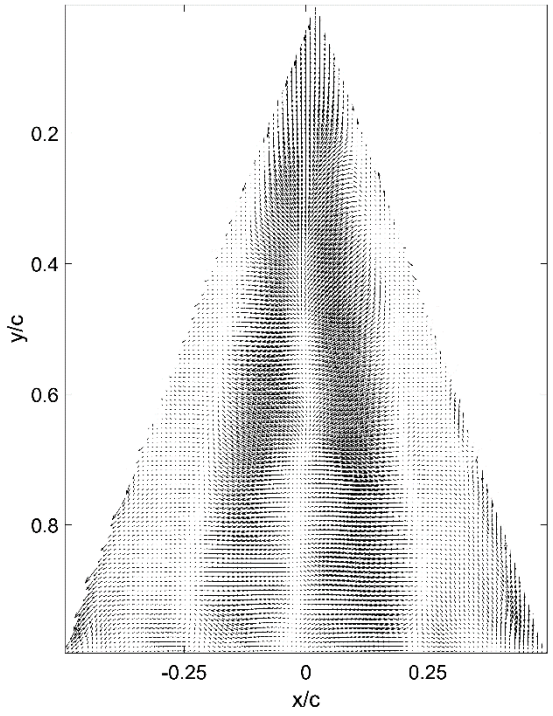

(d)

Figure 64: (a) initial image, (b) final image, (c) skin-friction lines, and (d) skin-friction vectors for 70° delta wing at 15° AoA

Figures 65 (a), (b), (c), and (d) are the initial luminescent oil image, the final luminescent oil image, the skin-friction line plot, and the skin-friction vector plot respectively for the case of a 70° delta wing at 20° AoA.

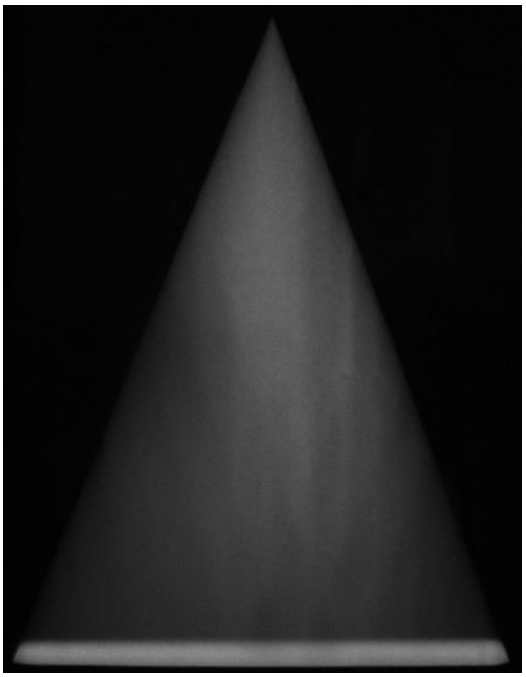

(a)

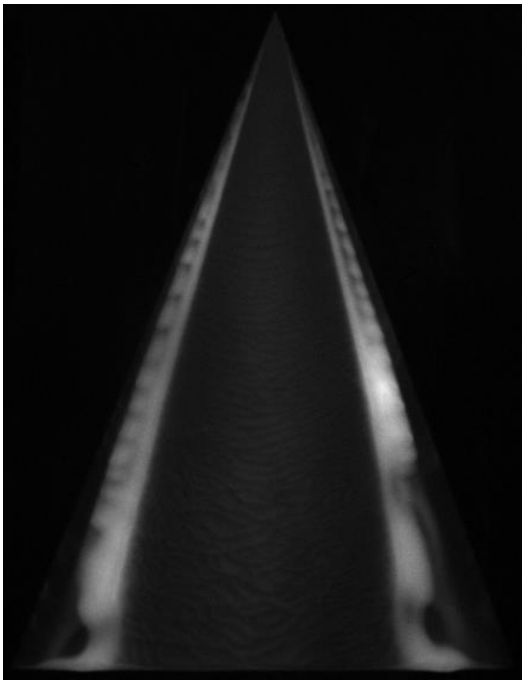

(b)

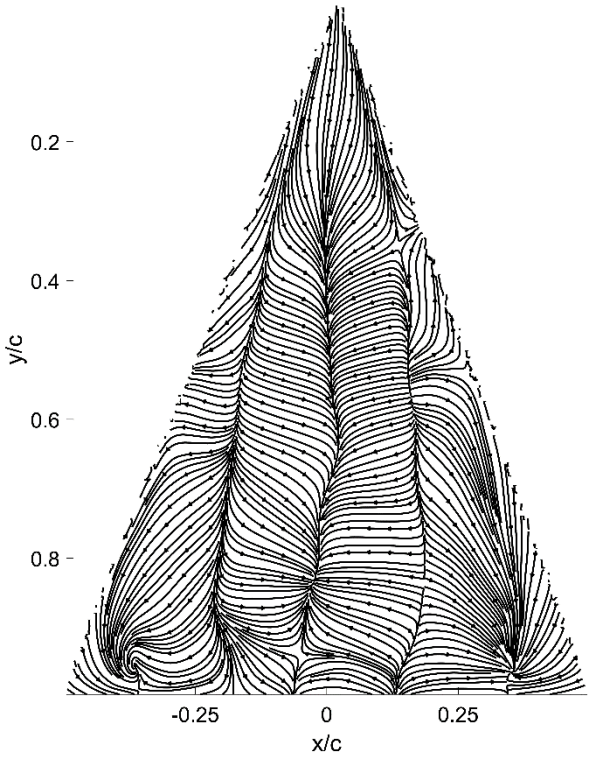

(c)

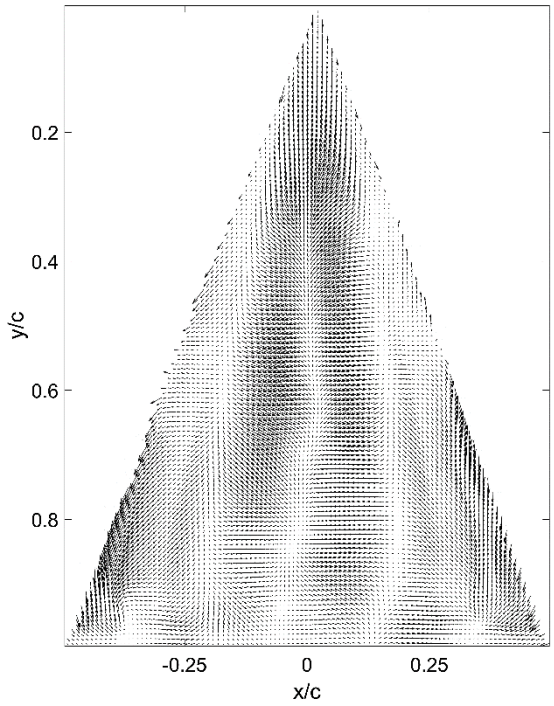

(d)

Figure 65: (a) initial image, (b) final image, (c) skin-friction lines, and (d) skin-friction vectors for 70° delta wing at 20° AoA

Figures 66 (a), (b), (c), and (d) are the initial luminescent oil image, the final luminescent oil image, the skin-friction line plot, and the skin-friction vector plot respectively for the case of a 70° delta wing at 25° AoA.

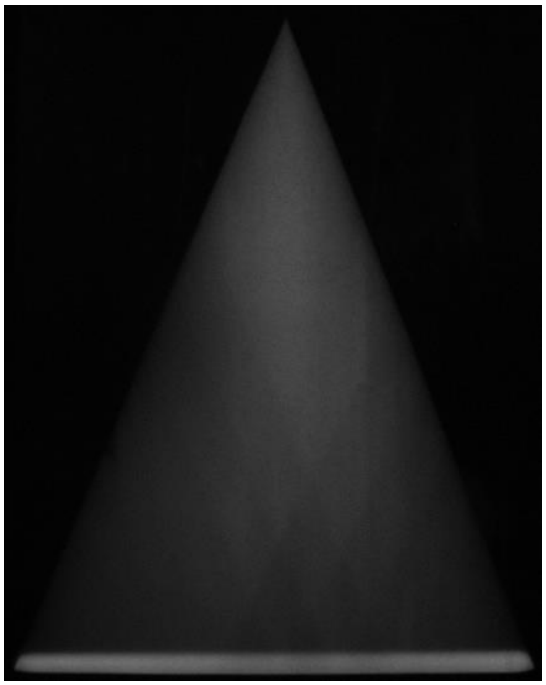

(a)

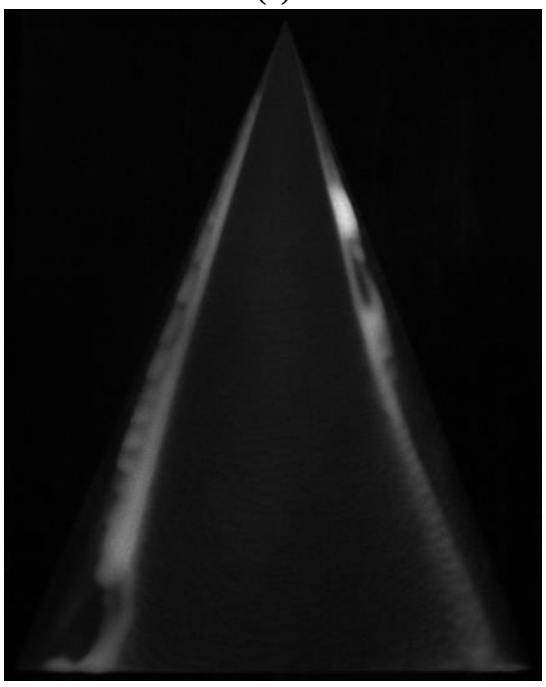

(b)

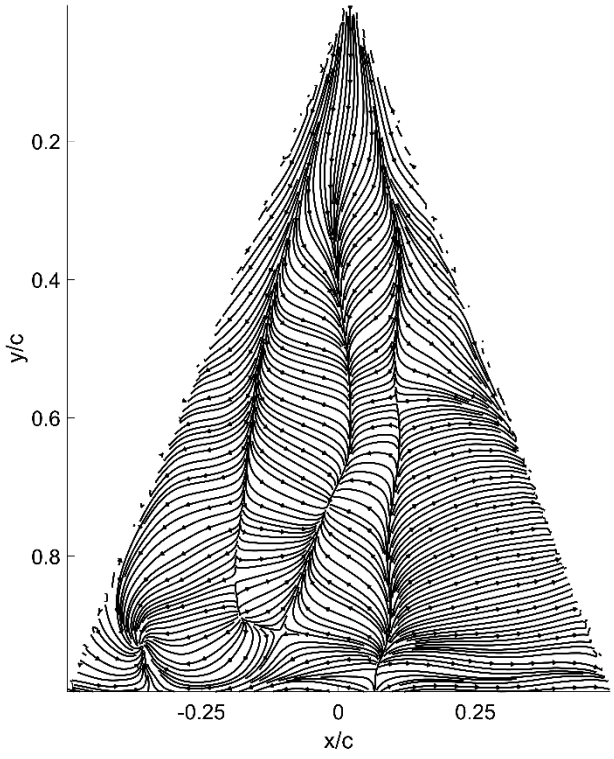

(c)

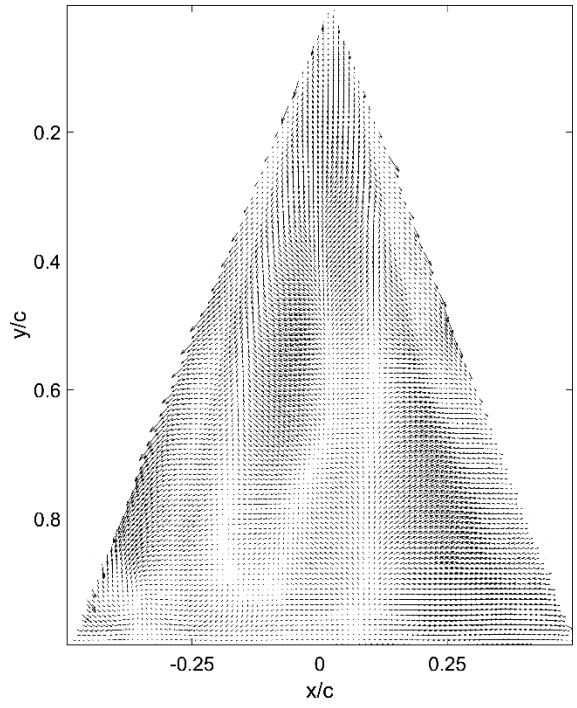

(d)

Figure 66: (a) initial image, (b) final image, (c) skin-friction lines, and (d) skin-friction vectors for 70° delta wing at 25° AoA

Like all the other delta wings, there is no discernible pattern at a -5° AoA in the skin-friction lines. At 0° AoA in Figure 61 (c), wing-tip vortices and one in the middle can clearly be seen. The fact that these features are clearly seen brings up a question as to whether they are caused by noise. More experiments should be done to see if this phenomenon could be repeated. The geometry of the lines is relatively similar to the other delta wings of different sweep angles. At 5° AoA, the primary and secondary lines are still relatively weak, with a general randomness in their directions. While the other vortices disappear from the skin-friction lines, the wing-tip vortex on the right side persists in the results for this wing geometry. At 10° and 15° AoA, the primary separation line and secondary reattachment lines are straight, and one can see a general symmetry, which is lacking in almost all the results above. Since the span is small, there is no space for the secondary separation line to form. The most likely explanation for this is that the primary vortices are formed above, and far away from the surface, which coincides with theoretical delta wing aerodynamics at high sweep angles. At 20° AoA, the primary separation line breaks down at y/c = 0.65, and the presence of wing-tip vortices are again apparent in the skin-friction lines. As with the non-slender delta wings, the lines for 25° AoA is largely asymmetric and weak.

Liu et al [30] performed tests on a 70° delta wing with Pressure Sensitive Paint (PSP), at a Mach number of 0.55 and an AoA of 20°. The geometry of the lines is similar, but that is the extent of similarities. The main difference is that the line down the middle is a primary reattachment line for the experiment done with PSP, while the line down the middle is a primary separation line for the experiment done with GLOF. Although the location of the lines is similar, both cases experience very different flows. For one, the experiments above can be considered incompressible at a Mach number of 0.06. For the PSP experiment, since the Mach number was set at 0.55, the flow enters compressible aerodynamics, as PSP is not sensitive to low-speed flows, thus making

it more complex. There have not been many publications that study the topology of skin-friction on delta wings; most of the research done have been on flow visualization of the vortices that are generated by the delta wing geometry.

Similarly, for the 70° delta wing, force measurements were obtained experimentally and compared with known C_L and C_D data.

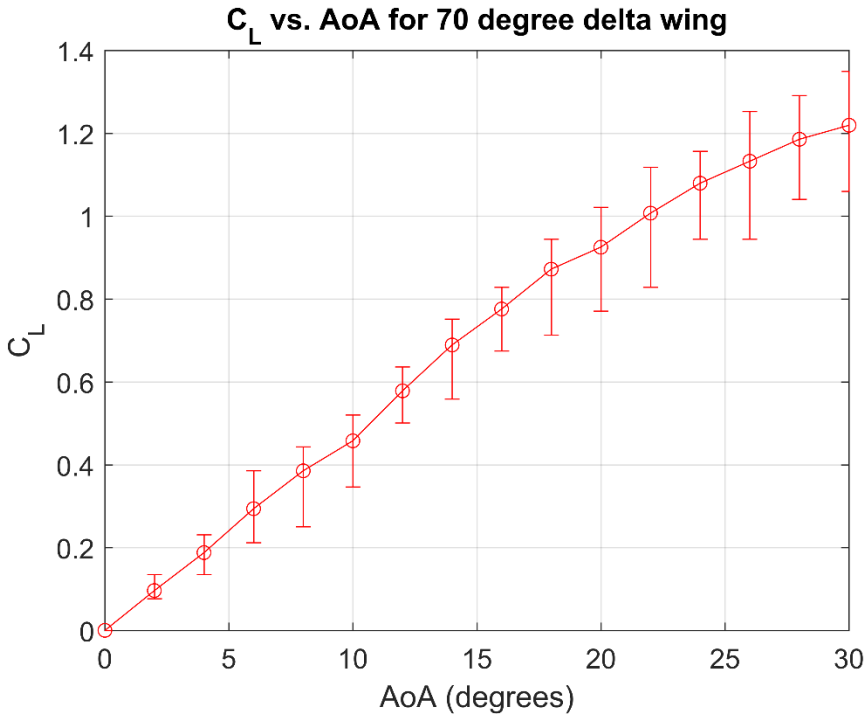

Figure 67: C_L vs. Alpha graph for 70° delta wing

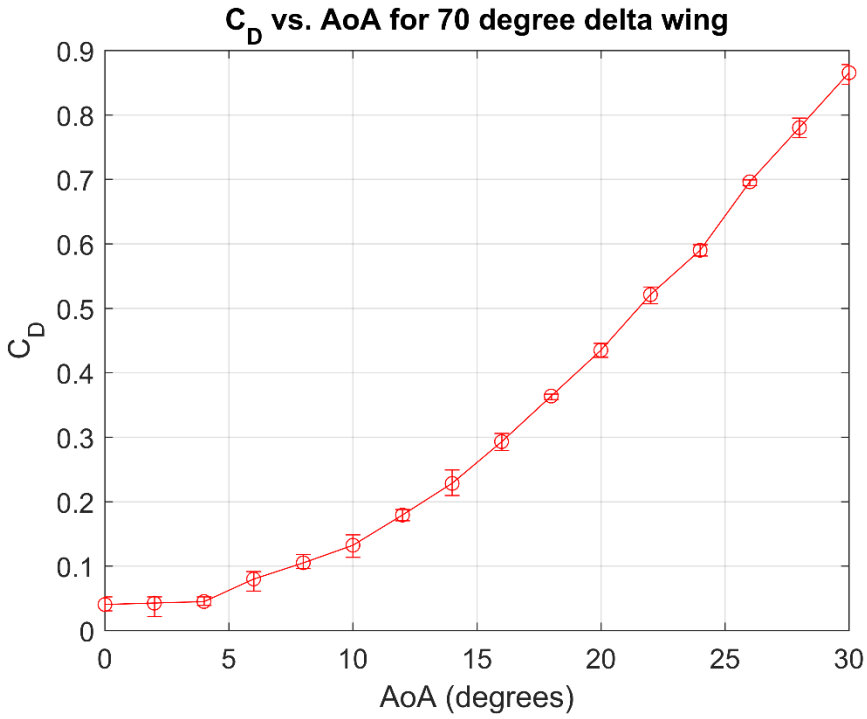

Figure 68: C_D vs. Alpha graph for 70° delta wing

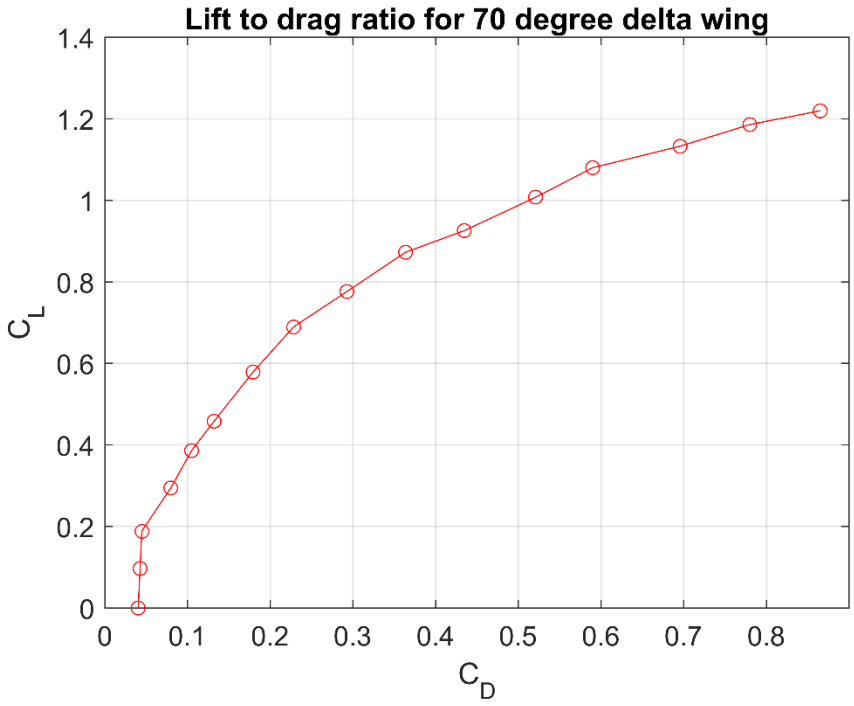

Figure 69: C_L vs. C_D graph for 70° delta wing

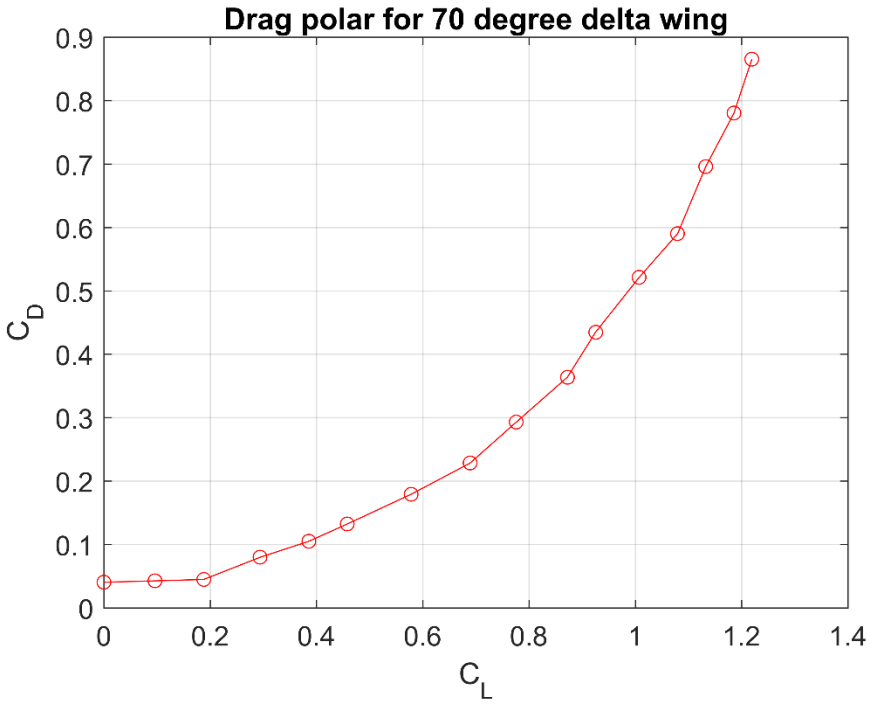

Figure 70: C_D vs. C_L graph for 70° delta wing

The trend for the C_L vs. Alpha curve is similar to that of the 65° delta wing. However, the magnitude of maximum C_L seems to be higher for the 70° delta wing. This observation is collaborated with Traub et al [28] where the maximum C_L increased by around 0.1 to 0.2 between delta wings of 60° and 70° sweep angles. The trend for the C_D vs. Alpha curve also corresponds with published data, with a slight variation in magnitude.

CONCLUSION

Drag is an important aspect of aerodynamics and there is a need for researchers to completely understand the factors that affect it. Skin-friction, especially, is not easily measured. The GLOF technique offers a non-intrusive and global method to extract high-resolution skin-friction fields as shown in the results shown above. These fields allowed for the relatively easy identification of critical features such as separation and reattachment lines, which are crucial for the understanding of flow separation and the interaction between vortices and the surface's boundary layer. A study of step size, sample size, and oil viscosity showed that the extracted skin-friction fields are sensitive to these variables. It is hard to optimize each of the above variable just by observation alone, as they are not mutually independent. A change of the oil viscosity will require a change in the step size and sample size of the analysis and so on. Future work will include the need for a qualitative method to optimize all three variables at the same time, and most importantly, the need for a numerical simulation to be done with the exact model dimensions, Reynolds number, and Mach number as that for the experiments to allow a better comparison between the two to be made. The discussion above were mostly observational as there have not been many research focused on the topology of skin-friction lines for both slender and non-slender delta-wings at low-speeds. In a nutshell, GLOF is able to quantitatively measure skin-friction on a global scale, which is desirable when trying to understand the interaction between the flow and the surface boundary layer for complex flows.

REFERENCES

[1] Cleynen, O. (2016, October 1). Drag curves for a body in steady flight [Digital Image]. Retrieved October 10, 2017, from https://commons.wikimedia.org/wiki/File:Drag_curves_for_aircraft_in_flight.svg

[2] Boundary layers on an airfoil. (n.d.). Retrieved October 10, 2017, from https://history.nasa.gov/SP-367/f35.htm

[3] Johansson, G., Naughton, J., Mehdi, F., & Shiri, F. (2005). Skin Friction Measurements using Oil Film Interferometry and Laser Doppler Anemometry. *4th AIAA Theoretical Fluid Mechanics Meeting*. doi:10.2514/6.2005-4673

[4] Murphy, J. D., & Westphal, R. V. (1986). The laser interferometer skin-friction meter: a numerical and experimental study. *Journal of Physics E: Scientific Instruments, 19*(9), 744-751. doi:10.1088/0022-3735/19/9/020

[5] Naughton, J. W., & Sheplak, M. (2002). Modern developments in shear-stress measurement. *Progress in Aerospace Sciences, 38*(6-7), 515-570. doi:10.1016/s0376-0421(02)00031-3

[6] Liu, T., & Sullivan, J. P. (1998). Luminescent Oil-Film Skin-Friction Meter. *AIAA Journal, 36*(8), 1460-1465. doi:10.2514/2.538

[7] Liu, T., Montefort, J., Woodiga, S., Merati, P., & Shen, L. (2008). Global Luminescent Oil-Film Skin-Friction Meter. *AIAA Journal, 46*(2), 476-485. doi:10.2514/1.32219

[8] Anderson, J. D. (2001). *Fundamentals of aerodynamics*. Boston: Mc-Graw Hill.

[9] Monson, D. J., Mateer, G. G., & Menter, F. R. (1993). Boundary-Layer Transition and Global Skin Friction Measurement with an Oil-Fringe Imaging Technique. *SAE Technical Paper Series*. doi:10.4271/932550

[10] Mateer, G. G., Monson, D. J., & Menter, F. R. (1996). Skin-friction measurements and calculations on a lifting airfoil. *AIAA Journal, 34*(2), 231-236. doi:10.2514/3.13055

[11] Tanner, L. H., & Blows, L. G. (1976). A study of the motion of oil films on surfaces in air flow, with application to the measurement of skin friction. *Journal of Physics E: Scientific Instruments, 9*(3), 194-202. doi:10.1088/0022-3735/9/3/015

[12] Zilliac, G. G. (1996). *Further Developments of the Fringe-Imaging Skin Friction Technique* (United States of America, National Aeronautics and Space Administration, Ames Research Center, Moffett Field, California). Retrieved from https://ntrs.nasa.gov/archive/nasa/casi.ntrs.nasa.gov/19970010467.pdf.

[13] Brown, J. L., & Naughton, J. W. (1999). *The Thin Oil Film Equation* (United States of America, National Aeronautics and Space Administration, Ames Research Center, Moffett Field, California). Retrieved from https://ntrs.nasa.gov/archive/nasa/casi.ntrs.nasa.gov/19990047906.pdf

[14] Horn, B. K., & Schunck, B. G. (1981). Determining optical flow. *Artificial Intelligence, 17*(1-3), 185-203. doi:10.1016/0004-3702(81)90024-2

[15] Lighthill, M. J. (1963). Attachment and separation in three-dimensional flow. *Laminar Boundary Layers*, 2(6), 72-82, Oxford Univ. Press

[16] Tobak, M., & Peake, D. J. (1981). *Topology of Three-Dimensional Separated Flows* (United States of America, National Aeronautics and Space Administration, Ames Research Center, Moffett Field, California). Retrieved from https://ntrs.nasa.gov/archive/nasa/casi.ntrs.nasa.gov/19810014504.pdf

[17] Johnson, T. A., & Patel, V. C. (1993). Skin-friction topology over a surface mounted semi-ellipsoidal wing at incidence. *AIAA Journal, 31*(10), 1842-1849. doi:10.2514/3.11857

[18] Chapman, G. T., & Yates, L. A. (1991). Topology of Flow Separation on Three-Dimensional Bodies. *Applied Mechanics Reviews, 44*(7), 329-345. doi:10.1115/1.3119507

[19] Wang, K. C. (1974). Boundary Layer Over a Blunt Body at High Incidence with an Open-Type of Separation. *Proceedings of the Royal Society A: Mathematical, Physical and Engineering Sciences, 340*(1620), 33-55. doi:10.1098/rspa.1974.0139

[20] Foss, J. F. (2004). Surface selections and topological constraint evaluations for flow field analyses. *Experiments in Fluids, 37*(6), 883-898. doi:10.1007/s00348-004-0877-0

[21] Délery, J. M. (1992). Physics of vortical flows. *Journal of Aircraft, 29*(5), 856-876. doi:10.2514/3.46256

[22] Kohlman, D., & Wentz, J. W. (1969). Vortex breakdown on slender sharp-edged wings. *Astrodynamics Conference*. doi:10.2514/6.1969-778

[23] Gursul, I. (2004). Recent developments in delta wing aerodynamics. *The Aeronautical Journal, 108*(1087), 437-452. doi:10.1017/s0001924000000269

[24] Gursul, I., Gordnier, R., & Visbal, M. (2005). Unsteady aerodynamics of nonslender delta wings. *Progress in Aerospace Sciences, 41*(7), 515-557. doi:10.1016/j.paerosci.2005.09.002

[25] Woodiga, S. A. (2013). *Global skin friction diagnostics: the GLOF technique and measurements of complex separated flows*. Western Michigan University. Retrieved from http://scholarworks.wmich.edu/dissertations/173

[26] Woodiga, S. A., & Liu, T. (2009). Skin friction fields on delta wings. *Experiments in Fluids, 47*(6), 897-911. doi:10.1007/s00348-009-0686-6

[27] Chen, L., & Wang, J. (2009). Numerical simulations of leading-edge vortex core axial velocity for flow over delta wings. *Science in China Series E: Technological Sciences, 52*(7), 2029-2036. doi:10.1007/s11431-009-0082-8

[28] Traub, L. W., Moeller, B., & Rediniotis, O. (1998). Low-Reynolds-Number Effects on Delta-Wing Aerodynamics. *Journal of Aircraft, 35*(4), 653-656. doi:10.2514/2.2352

[29] Roy, J. L., Rodriguez, O., & Kurun, S. (2008). Experimental and CFD Contribution to Understanding Delta Wing Vortical Flow. *46th AIAA Aerospace Sciences Meeting and Exhibit*. doi:10.2514/6.2008-380

[30] Liu, T., Misaka, T., Asai, K., Obayashi, S., & Wu, J. (2016). Feasibility of skin-friction diagnostics based on surface pressure gradient field. *Measurement Science and Technology, 27*(12), 125304. doi:10.1088/0957-0233/27/12/125304

[31] Payne, F. M., Ng, T., Nelson, R. C., & Schiff, L. B. (1988). Visualization and wake surveys of vortical flow over a delta wing. *AIAA Journal, 26*(2), 137-143. doi:10.2514/3.9864

[32] Yavuz, M. M., Elkhoury, M., & Rockwell, D. (2004). Near-Surface Topology and Flow Structure on a Delta Wing. *AIAA Journal, 42*(2), 332-340. doi:10.2514/1.3499

[33] Liu, T., Woodiga, S., Montefort, J., Conn, K. J., & Shen, L. (2009). Global Skin Friction Diagnostics In Separated Flows Using Luminescent Oil. *Journal of Flow Visualization and Image Processing, 16*(1), 19-39. doi:10.1615/jflowvisimageproc.v16.i1.20

[34] Liu, T., & Woodiga, S. (2011). Feasibility of global skin friction diagnostics using temperature sensitive paint. *Measurement Science and Technology, 22*(11), 115402. doi:10.1088/0957-0233/22/11/115402

[35] Liu, T., Woodiga, S., & Ma, T. (2011). Skin friction topology in a region enclosed by penetrable boundary. *Experiments in Fluids, 51*(6), 1549-1562. doi:10.1007/s00348-011-1171-6

[36] Fonov, S., Jones, G., Crafton, J., Fonov, V., & Goss, L. (2006). The development of optical techniques for the measurement of pressure and skin friction. *Measurement Science and Technology, 17*(6), 1261-1268. doi:10.1088/0957-0233/17/6/s05

[37] Chu, J., & Luckring, J. M. (1996). *Experimental Surface Pressure Data Obtained on 65° Delta Wing Across Reynolds Number and Mach Number Ranges* (United States of America, National Aeronautics and Space Administration, Langley Research Center, Hampton, Virginia).

[38] Délery, J. M. (2001). Robert Legendre and Henri Werlé: Toward the Elucidation of Three-Dimensional Separation. *Annual Review of Fluid Mechanics, 33*(1), 129-154. doi:10.1146/annurev.fluid.33.1.129

[39] Délery, J. (2013). Reconsideration of the Two-Dimensional Separation. *Three-dimensional Separated Flow Topology,* 121-142. doi:10.1002/9781118578544.ch6

[40] Patel, V. C. (1993). Three-dimensional flow separation. *Sadhana, 18*(3-4), 553-574. doi:10.1007/bf02744368

[41] Furman, A., & Breitsamter, C. (2013). Turbulent and unsteady flow characteristics of delta wing vortex systems. *Aerospace Science and Technology, 24*(1), 32-44. doi:10.1016/j.ast.2012.08.007

[42] Rockwell, D. (1993). Three-dimensional flow structure on delta wings at high angle-of-attack - Experimental concepts and issues. *31st Aerospace Sciences Meeting*. doi:10.2514/6.1993-550

[43] Huang, X., & Hanff, E. (2000). Evolution of the surface flow topology on a 65 delta wing and its correspondence to the critical states. *38th Aerospace Sciences Meeting and Exhibit*. doi:10.2514/6.2000-790

[44] Leroy, J., Mary, I., & Rodriguez, O. (2003). CFD Solutions of 70-deg Delta Wing Flows. *21st AIAA Applied Aerodynamics Conference*. doi:10.2514/6.2003-4219

[45] Gaffuri, M., Brezillon, J., Kwak, D., Ohira, K., & Carrier, G. (2013). Comparison of CFD solvers for low speed vortex dominated flows. *31st AIAA Applied Aerodynamics Conference*. doi:10.2514/6.2013-2914

[46] Wang, J. & Zhang, W. (2008). Experimental Investigations on Leading-Edge Vortex Structures for Flow over Non-Slender Delta Wings. *Chinese Physics Letters, 25*(7), 2550-2553. doi:10.1088/0256-307x/25/7/060

[47] Miau, J., Kuo, K. T., Liu, W. H., Hsieh, S. J., Chou, J. H., & Lin, C. K. (1995). Flow developments above 50-deg sweep delta wings with different leading-edge profiles. *Journal of Aircraft, 32*(4), 787-794. doi:10.2514/3.46792

[48] Gursul, I. (2005). Review of Unsteady Vortex Flows over Slender Delta Wings. *Journal of Aircraft, 42*(2), 299-319. doi:10.2514/1.5269

[49] Verhaagen, N. (2010). Effects of Leading-Edge Radius on Aerodynamic Characteristics of 50º Delta Wings. *48th AIAA Aerospace Sciences Meeting Including the New Horizons Forum and Aerospace Exposition*. doi:10.2514/6.2010-323

[50] Verhaagen, N. G. (2012). Leading-Edge Radius Effects on Aerodynamic Characteristics of 50-Degree Delta Wings. *Journal of Aircraft, 49*(2), 521-531. doi:10.2514/1.c031550

[51] Gordnier, R. E. (1997). Numerical Simulation of a 65-Degree Delta-Wing Flowfield. *Journal of Aircraft, 34*(4), 492-499. doi:10.2514/2.2218